Semiconductors, Vol. 37, No. 8, 2003, pp. 867–871. Translated from Fizika i Tekhnika Poluprovodnikov, Vol. 37, No. 8, 2003, pp. 897–900.
Original Russian Text Copyright © 2003 by Emel'yanenko, Kolchanova, Mikhaĭlova, Yakovlev.

The Role of Dmitriĭ Nikolaevich Nasledov in the Formation and Development of the Physics and Technology of III–V Semiconductors

O. V. Emel'yanenko, N. M. Kolchanova, M. P. Mikhaĭlova, and Yu. P. Yakovlev
Ioffe Physicotechnical Institute, Russian Academy of Sciences,
Politekhnicheskaya ul. 26, St. Petersburg, 194021 Russia

Submitted February 10, 2003; accepted for publication February 17, 2003

Studies of III–V compounds in the Soviet Union were started in the early 1950s at the Ioffe Physicotechnical Institute, USSR Academy of Sciences. Dmitriĭ Nikolaevich Nasledov, a deputy director of the institute and the head of the semiconductor laboratory, decided to uphold the efforts of N.A. Goryunova in her studies of indium antimonide and to expand these studies to the entire class of III–V materials (III = In, Ga, Al; V = Sb, As, P). It required great scientific courage and foresight for D.I. Nasledov to make such a decision. The only other laboratory in the world which was engaged in studies of III–V compounds at that time was the laboratory headed by Professor Welker (Federal Republic of Germany). All scientists in the field of semiconductors concentrated almost exclusively on germanium and silicon. It seemed that these elemental semiconductors, which brought electronics to a new level, could not be surpassed by any compound semiconductor. However, time showed that this notion was not true.

The first significant report on studies of III–V semiconductors (InSb, InAs) at the Physicotechnical Institute was delivered by Nasledov at the First All-Union Conference on Semiconductors (Leningrad, 1956) [1]. He mentioned (among other phenomena) that neither electrical conductivity nor the Hall voltage depend on temperature in new III–V compounds. Many scientists considered this observation strange and even accidental. However, it was found shortly afterwards that the above temperature independence is the consequence of profound degeneracy in the electron gas, which is typical of heavily doped (then, simply "impure") III–V crystals. Fundamentally new phenomena in these crystals gave rise to a new field in the physics of semiconductors, specifically, the physics of heavily doped semiconductors. The contribution of the laboratory headed by Nasledov to this field is reported in [2, 3].

In general, the issue concerning the potentialities of doping and purification was central to the fate of the new compounds. Deviations from stoichiometry, high reactivity of constituents (As, P), and uncertainty in the pattern of incorporation and removal of impurities sometimes created an impression that all efforts were vain. All the problems that were encountered had to be solved for the first time. Close cooperation between physicists and chemists in the laboratory headed by Nasledov played an important role in the scientific progress; the team of chemists was headed by Goryunova. Physicists developed the zone-melting (purification) and Czochralski methods [4], whereas chemists quite successfully grew ingots in cells.

By the end of the 1950s and the beginning of the 1960s, the joint efforts yielded the first results. The purification, doping, and growth of III–V crystals could be performed as in the case of Ge and Si; other technological problems were also solved step by step. The world's purest InSb crystals were grown and studied; these crystals featured an electron concentration of $n \approx 10^{12}$ cm^{-3} and an electron mobility of $\mu \approx 10^6$ cm^2 V^{-1} s^{-1} at a temperature of $T = 77$ K [5]. The team headed by O.V. Emel'yanenko continued to study transport phenomena in a wider class of III–V compounds. The results of studying the impurity band [6, 7], the discovery of a giant magnetoresistance when charge carriers move via impurities [8], the investigation of the metal–semiconductor transition in various materials, and the determination of the origin of negative (quantum) magnetoresistance (discovered by the Emel'yanenko team even earlier, in 1958 [2]) were of greatest interest [9]. In all of these studies, the simplicity and accuracy of analysis relied on the basic special feature of III–V compounds (consisting in the sphericity of the conduction band, which represents the simplest model of a semiconductor's energy-band structure). The impurity properties, transport phenomena, and photoelectric properties of InSb, InAs, GaAs, AlSb, and InP were studied [10–15]. Diffused and fused p–n junctions and also photodiodes based on n-GaAs [16–18] were fabricated and studied. These and other results have shown conclusively that III–V compounds have a much wider range of controllable semiconductive properties in comparison with Ge and Si and are much more attractive for both the technology and physics of semiconductors.

The number of researchers engaged in the studies of III–V semiconductors has steadily increased. The team investigating III–V sermiconductors at the Physocotechnical Institute was transformed into the laboratory of electronic semiconductors in 1957. Centers of research in the field of III–V semiconductors were founded in other cities of the USSR (Baku, Kishinev, Ordzhonikidze, and so on) under the guidance of Nasledov. Institutes in Moscow and Ukraine, as well as foreign laboratories, became involved and competed in this field. Under these conditions of growing competition, the laboratory headed by Nasledov obtained striking results that clearly showed the intrinsic worth of III–V semiconductors. Specifically, it was shown in 1962 that the luminescence spectrum of GaAs *p–n* junctions narrows appreciably with increasing current, which can only be attributed to the appearance of stimulated emission [19–21]. This was the first observation ever of stimulated emission from semiconductors.[1] Gallium arsenide, as well as a number of other III–V compounds, has a spherical conduction band with a center at the same point, $k = 0$, as for the valence band. This important special feature of III–V semiconductors distinguishes them from a great many indirect-gap semiconductors (including Ge and Si) and brings the probability of obtaining recombination radiation in the former close to 100%.

D.N. Nasledov, S.M. Ryvkin, A.A. Rogachev, and B.V. Tsarenkov were awarded the Lenin Prize in 1964 for their studies that led to the development of semiconductor lasers. In the laboratory headed by Nasledov, a new, revolutionary line in solid-state physics and technology was initiated; this line was related to optoelectronics, and a major contribution was made by the team headed by Tsarenkov. In order to fabricate optoelectronic devices based on binary compounds and graded-gap III–V structures, the method of liquid-phase epitaxy (LPE) for both the open and closed systems was developed by A.T. Gorelenok and Yu.P. Yakovlev at Nasledov's laboratory at the Ioffe Physicotechnical Institute [22, 23]. In the following years, the LPE method was widely used at other semiconductor laboratories at the same institute. Studies of radiative recombination and those aimed at the fabrication of lasers and light-emitting diodes (LEDs) based on GaAs and GaP and of graded-gap *p–n* structures in systems of GaAlAs and GaAlSb solid solutions were actively pursued by the team headed by Tsarenkov. The first surface-barrier structures based on III–V compounds were fabricated by Yu.A. Gol'dberg and E.A. Posse; the characteristics of these structures were consistent with an idealized theoretical model.

A high level of research and development (R & D) in the field of light-emitting devices at the laboratory headed by Nasledov provided the basis for the commercial production of these devices. The Council of Ministers of the USSR decided in 1960 to intensify the efforts aimed at developing devices based on GaAs and GaP. The laboratories headed by Nasledov and Goryunova (Ioffe Physicotechnical Institute) and the Start plant were included into the R & D program. A short time later, researchers and technologists of the Start plant (S.S. Meskin, V.N. Ravich, L.M. Kogan, I.T. Rassokhin, and A.L. Gofshtein-Gardt) with the creative support of scientists from Nasledov's laboratory (B.V. Tsarenkov, A.T. Gorelenok, A.N. Imenkov, V.V. Evstropov, and Yu.P. Yakovlev) developed the commercial production technology for (the first in the USSR) lasers based on GaAs and also LEDs for the infrared (GaAs) and visible (GaP) regions of the spectrum.

Studies on the recombination of nonequilibrium charge carriers and the development of important components (photodetectors and photoemitters) for optoelectronics became one of the leading lines of research in the laboratory headed by Nasledov [24–27].

Between 1964 and 1966, D.N. Nasledov, Yu.S. Smetannikova, and Yu.G. Popov discovered and studied a new physical phenomenon (oscillations of photoconductivity and photomagnetic effect) in InSb narrow-gap semiconductors at low temperatures [28]. As was shown by I.N. Yassievich [29], the oscillations were caused by illumination-induced heating of the electron subsystem. Between 1966 and 1968, D.N. Nasledov and N.M. Kolchanova discovered the heating of an electron subsystem in GaAs and GaSb wide-gap semiconductors. These studies on the heating and cooling of electron–hole plasma received international recognition and have been widely cited in articles and monographs.

Extensive studies of the photoconductivity and photomagnetic effect in all III–V compounds were undertaken in laboratories with the aim of determining the lifetime of carriers and ascertaining the recombination mechanisms of nonequilibrium charge carriers. The response speed, detectability, and photosensitivity were the parameters that were of prime interest to designers of new photodetectors and, consequently, to the scientists at Nasledov's laboratory. The studies on photoelectric phenomena in III–V semiconductors found practical applications: the first (in the USSR) InSb and InAs photodetectors for the middle-infrared region of the spectrum were developed (studies by the team headed by S.V. Slobodchikov and M.P. Mikhaĭlova) and were then produced on a commercial scale by the Institute of Applied Physics.

In the 1960s, not only was the scope of studies in Nasledov's laboratory widened, but new experimental methods were also rapidly introduced. Nasledov's laboratory promptly responded to intense worldwide interest in oxygen and iron-Group impurities, which made it possible to obtain semi-insulating GaAs single crystals. In a very short period of time, Nasledov's laboratory became one of the well-known leading teams in the sci-

---

[1] The lasing effect in GaAs was also reported by Hall *et al.*, Phys. Rev. Lett. **9**, 366 (1962).—*Translator's note.*

entific world concerned with this line of research. At that time, Nasledov made an unexpected but quite reasonable decision: he decided to join the forces of his laboratory at the Ioffe Physicotechnical Institute (N.M. Kolchanova and G.N. Talalakin) with the department headed by V.F. Masterov at the Leningrad Polytechnical Institute. This collaboration made it possible to widen the range of experimental methods and use new methods for comprehensive and in-depth studies of deep-level centers, first in GaAs and then in other III–V compounds. The employment of resonance-based methods (electron spin resonance and nuclear magnetic resonance) made it possible to make considerable and rapid progress in understanding the aforementioned centers. Ferromagnetic properties of GaAs crystals doped with Fe were discovered and studied at that time [30–32]. The assertion that the ordering of impurity atoms belonging to the Fe Group is caused by the exchange interaction via the host atoms without the involvement of conduction electrons was bold and innovative.

Returning to the scientific activity of Nasledov's laboratory, we may state that the 1960s and 70s were fruitful years of learning for the scientists at this laboratory. Nasledov allowed his coworkers more and more freedom in their research; he believed that self-realization was the best method for the mobilization of creative energy. The stored potential yielded striking results, which contributed to the international science and technology of III–V semiconductors in diverse fields.

At that time, Nasledov's laboratory became a genuine training center for scientists: hundreds of postgraduate students, as well as candidates and doctors of science from every part of the Soviet Union, from Novosibirsk to Riga and Vilnius, began working at this laboratory. Research workers from Nasledov's laboratory, who joined it upon graduation from university, have become self-reliant scientists, who are well-known for their contribution to the science and technology of III–V semiconductors in the USSR and around the world. The list of references in this article gives only a rough idea of this process. Below, we list the most outstanding young scientists who gained experience under Nasledov's guidance and went on to collaborate with Nasledov as heads of individual teams working in different lines of research. They were G.N. Talalakin (purification, doping, and growth of crystals, first by zone melting and then by liquid-phase epitaxy); Yu.M. Burdukov (solution of the same problems by the Czochralski methods); O.V. Emel'yanenko and T.S. Lagunova (fundamental studies of transport phenomena in III–V compounds, solid solutions, and structures on them); B.V. Tsarenkov, A.N. Imenkov, V.V. Evstropov, T.N. Danilova, and Yu.P. Yakovlev (fundamental studies and practical applications of *p*–*n* junctions in GaAs, photodiodes, and emitters based on graded-gap III–V compounds); N.V. Zotova (formation of InAs *p*–*n* structures and studies of their electroluminescence); M.P. Mikhaĭlova, Yu.S. Smetannikova, S.V. Slobodchikov, N.M. Kolchanova, and M.A. Sipovskaya (fundamental studies of photoelectromagnetic properties of III–V compounds); and A.A. Gutkin and V.E. Sedov (development and studies of photodiodes based on GaAs). Studies of InSb and GaAs growth technology were awarded State Prizes (for Nasledov and Burdukov). The laboratory headed by Nasledov was repeatedly a participant and prize winner at the Exhibition of Economic Achievements of the USSR, where new structures and devices developed under the guidance of Nasledov were exhibited.

The school of semiconductor science and technology founded by Nasledov put the Soviet Union in the forefront in mastering of III–V compounds. The papers delivered by Nasledov at international conferences attracted much interest.

In 1968, 25 years since the foundation of the Physicotechnical Institute, Doctor of Science (physics and mathematics) Zh.I. Alferov, now a Nobel Prize holder, mentioned the decisive pioneering role of Nasledov in studying and mastering III–V semiconductors, in their technical applications, in fabricating the first semiconductor lasers, and in the development of optoelectronics. In particular, Alferov wrote [33]: "Following the discovery of the semiconducting properties of III–V compounds, scientists from the Physicotechnical Institute took great efforts in the systematic study of the phenomena related to charge transport in these compounds. A natural consequence of these studies at this institute was the creation of the physical prerequisites for the development of an injection laser and a number of other semiconductor devices based on III–V compounds. Nasledov and his coworkers deserve the main credit for these achievements."

It has been 25 years since Nasledov's death. A new laboratory of infrared optoelectronics was founded based on his laboratory. This laboratory is headed by Yu.P. Yakovlev, professor and doctor of science (physics and mathematics); he was a coworker of D.N. Nasledov. In the 1950s, the main objects of investigations performed by Nasledov and his colleagues were the binary III–V compounds, whereas multinary compounds based on III–V semiconductors are now used to solve fundamental and application-oriented problems. Years have passed, the technology has changed, and the range of problems, narrowed. However, traditions established in the middle of the last century have been preserved.

In the 1950s, Nasledov boldly started to study the unknown class of III–V compounds; in the early 1990s, a similar courage, combined with foresight, was exercised by the scientists and technologists of the laboratory when they brought Nasledov's studies to a new level, with the aim of developing quantum-confinement devices based on multinary III–V compounds. As before, enormous scientific potential ensured that the scientific level of the laboratory (in the very difficult conditions of perestroika) remained high; moreover, the laboratory gained wide recognition not only in the commercial market of light-emitting semiconductor devices but also in the scientific community.

Now, the main line of activity of the laboratory is the development and study of optoelectronic devices (lasers, light-emitting diodes, and photodiodes) for the middle-infrared region of the spectrum ($\lambda = 2–5$ μm) on the basis of III–V compounds. The spectral range of 2–5 μm includes a multitude of main absorption lines of natural and industrial gases, such as H_2O, CH_4, CO_2, CO, NH_3, HF, N_2O, and so on; as a result, the use of nondestructive optical methods for the detection of gas molecules in the atmosphere and the determination of their concentration on the basis of coherent and noncoherent emission sources ensure a promising outlook for the monitoring and protection of the environment. The spirit and style of Nasledov's scientific activity, i.e., a sophisticated approach to the problem under investigation, have been preserved in the laboratory. The technology of growing multilayered heterostructures by liquid-phase epitaxy and vapor-phase epitaxy from organometallic compounds is being developed. The transport properties of narrow-gap multicomponent solid solutions based on GaSb and InAs are being studied. Noncoherent and coherent sources of radiation operating in the spectral range of 2–5 μm at room temperature are being developed and studied. Tunable diode lasers, which have been used with good results in diode-laser spectroscopy for the detection of minute amounts (from 1 ppm to 1 ppb) of contaminating substances in a surrounding medium, are being developed. High-efficiency LEDs operating in the spectral range of 2–4 μm and with an emission power exceeding 1 mW in the continuous mode have been developed; these LEDs are being successfully used in portable gas analyzers. In addition, long-wavelength lasers ($\lambda = 3.3$ μm) with an emission power of 6 W have been developed [34]. *p–i–n* diodes and avalanche diodes operating in the spectral range of 1.2–2.4 μm have been fabricated for the first time; these diodes are based on GaInAsSb/GaAlAsSb solid-solution structures and have a quantum efficiency of 0.6–0.7 electron/photon [35]. Thus, the pioneering effort that was started by the prominent scientist and our teacher, Professor Nasledov, with his colleagues more than 50 years ago has found its logical continuation at the Ioffe Physicotechnical Institute in present scientific activity aimed at the development and investigation of nanooptoelectronic devices for the visible and middle-infrared regions of the spectrum. In honoring Nasledov for his prominent scientific achievements, let us follow his motto: "Stay the course!"

REFERENCES

1. D. N. Nasledov and A. Yu. Khalilov, Izv. Akad. Nauk SSSR, Ser. Fiz. **20**, 1494 (1956).
2. O. V. Emel'yanenko and D. N. Nasledov, Zh. Tekh. Fiz. **28**, 1177 (1958) [Sov. Phys. Tech. Phys. **3**, 1094 (1958)].
3. O. V. Emel'yanenko, T. S. Lagunova, and D. N. Nasledov, Fiz. Tverd. Tela (Leningrad) **2**, 192 (1960) [Sov. Phys. Solid State **2**, 176 (1960)].
4. *Gallium Arsenide: Production, Properties, and Applications*, Ed. by F. P. Kesamanly and D. N. Nasledov (Nauka, Moscow, 1973).
5. K. I. Vinogradova, V. V. Galavanov, D. N. Nasledov, and L. I. Solov'eva, Fiz. Tverd. Tela (Leningrad) **1**, 403 (1959) [Sov. Phys. Solid State **1**, 364 (1959)].
6. O. V. Emel'yanenko, T. S. Lagunova, D. N. Nasledov, and G. N. Talalakin, Fiz. Tverd. Tela (Leningrad) **7**, 1315 (1965) [Sov. Phys. Solid State **7**, 1063 (1965)].
7. F. P. Kesamanly, É. É. Klotyn'sh, T. S. Lagunova, and D. N. Nasledov, Fiz. Tverd. Tela (Leningrad) **6**, 958 (1964) [Sov. Phys. Solid State **6**, 741 (1964)].
8. O. V. Emel'yanenko, T. S. Lagunova, D. N. Nasledov, *et al.*, Fiz. Tekh. Poluprovodn. (Leningrad) **7**, 1919 (1973) [Sov. Phys. Semicond. **7**, 1280 (1973)].
9. T. I. Voronina, O. V. Emel'yanenko, T. S. Lagunova, *et al.*, Fiz. Tekh. Poluprovodn. (Leningrad) **17**, 1841 (1983) [Sov. Phys. Semicond. **17**, 1174 (1983)].
10. V. V. Galavanov, D. N. Nasledov, and A. S. Filipchenko, Izv. Akad. Nauk SSSR, Ser. Fiz. **28**, 963 (1964).
11. D. N. Nasledov and S. V. Slobodchikov, Fiz. Tverd. Tela (Leningrad) **1**, 748 (1959) [Sov. Phys. Solid State **1**, 681 (1959)].
12. D. N. Nasledov and Lyan Chi-Chao, Fiz. Tverd. Tela (Leningrad) **2**, 793 (1960) [Sov. Phys. Solid State **2**, 729 (1960)].
13. M. P. Mikhaĭlova, D. N. Nasledov, and S. V. Slobodchikov, Fiz. Tverd. Tela (Leningrad) **5**, 1227 (1963) [Sov. Phys. Solid State **5**, 901 (1963)].
14. N. M. Voronkova, D. N. Nasledov, and S. V. Slobodchikov, Fiz. Tverd. Tela (Leningrad) **5**, 3259 (1963) [Sov. Phys. Solid State **5**, 2383 (1964)].
15. N. P. Esina, N. V. Zotova, and D. N. Nasledov, Fiz. Tekh. Poluprovodn. (Leningrad) **3**, 1370 (1969) [Sov. Phys. Semicond. **3**, 1140 (1969)].
16. Yu. M. Burdukov, A. N. Imenkov, D. N. Nasledov, and B. V. Tsarenkov, Fiz. Tverd. Tela (Leningrad) **3**, 991 (1961) [Sov. Phys. Solid State **3**, 721 (1961)].
17. A. A. Gutkin and D. N. Nasledov, Fiz. Tverd. Tela (Leningrad) **4**, 1360 (1962) [Sov. Phys. Solid State **4**, 999 (1962)].
18. A. A. Gutkin, D. N. Nasledov, and V. E. Sedov, Fiz. Tverd. Tela (Leningrad) **7**, 81 (1965) [Sov. Phys. Solid State **7**, 58 (1965)].
19. A. A. Nasledov, A. A. Rogachev, S. M. Ryvkin, and B. V. Tsarenkov, Fiz. Tverd. Tela (Leningrad) **4**, 1062 (1962) [Sov. Phys. Solid State **4**, 782 (1962)].
20. A. A. Nasledov, A. A. Rogachev, S. M. Ryvkin, *et al.*, Fiz. Tverd. Tela (Leningrad) **4**, 3346 (1962) [Sov. Phys. Solid State **4**, 2449 (1962)].
21. D. N. Nasledov and B. V. Tsarenkov, in *Proceedings of International Conference on the Physics of Semiconductors* (Kyoto, 1966), p. 302.
22. A. T. Gorelenok and B. V. Tsarenkov, USSR Inventor's Certificate No. 196,177 (1965).

23. B. V. Tsarenkov and Yu. P. Yakovlev, USSR Inventor's Certificate No. 383,122 (1970).
24. D. N. Nasledov and S. V. Slobodchikov, Fiz. Tverd. Tela (Leningrad) **4**, 3161 (1962) [Sov. Phys. Solid State **4**, 2315 (1962)].
25. D. N. Nasledov and Yu. S. Smetannikova, Fiz. Tverd. Tela (Leningrad) **4**, 110 (1962) [Sov. Phys. Solid State **4**, 78 (1962)].
26. M. P. Mikhaĭlova, D. N. Nasledov, and S. V. Slobodchikov, Fiz. Tverd. Tela (Leningrad) **4**, 1227 (1962) [Sov. Phys. Solid State **4**, 890 (1962)].
27. N. M. Voronkova and D. N. Nasledov, Fiz. Tverd. Tela (Leningrad) **6**, 2196 (1964) [Sov. Phys. Solid State **6**, 1736 (1964)].
28. D. N. Nasledov, Yu. G. Popov, and Yu. S. Smetannikova, Fiz. Tverd. Tela (Leningrad) **6**, 3728 (1964) [Sov. Phys. Solid State **6**, 2989 (1964)].
29. D. N. Nasledov, Yu. G. Popov, Yu. S. Smetannikova, and I. N. Yassievich, Fiz. Tverd. Tela (Leningrad) **8**, 475 (1966) [Sov. Phys. Solid State **8**, 377 (1966)].
30. V. V. Isaev-Ivanov, N. M. Kolchanova, V. F. Masterov, *et al.*, in *Abstracts of II All-Union Conference on Physicochemical Fundamentals of Semiconductor Doping* (Moscow, 1972).
31. V. V. Isaev-Ivanov, N. M. Kolchanova, V. F. Masterov, *et al.*, Fiz. Tekh. Poluprovodn. (Leningrad) **7**, 414 (1973) [Sov. Phys. Semicond. **7**, 299 (1973)].
32. V. V. Isaev-Ivanov, N. M. Kolchanova, V. F. Masterov, *et al.*, Fiz. Tverd. Tela (Leningrad) **16**, 1044 (1974) [Sov. Phys. Solid State **16**, 674 (1974)].
33. Zh. I. Alferov, V. I. Ivanov-Omskiĭ, L. G. Paritskiĭ, and V. Ya. Frenkel', Fiz. Tekh. Poluprovodn. (Leningrad) **2**, 1397 (1968) [Sov. Phys. Semicond. **2**, 1169 (1969)].
34. M. Aidaraliev, N. V. Zotova, S. A. Kasandashov, *et al.*, Appl. Phys. Lett. **81**, 1166 (2002).
35. I. A. Andreev, E. V. Kunitsina, M. P. Mikhaĭlova, and Yu. P. Yakovlev, Fiz. Tekh. Poluprovodn. (St. Petersburg) **33**, 249 (1999) [Semiconductors **33**, 216 (1999)].

Translated by A. Spitsyn

Semiconductors, Vol. 37, No. 8, 2003, pp. 872–875. Translated from Fizika i Tekhnika Poluprovodnikov, Vol. 37, No. 8, 2003, pp. 901–904.

ELECTRONIC AND OPTICAL PROPERTIES OF SEMICONDUCTORS

ESR of Interacting Manganese Centers in Gallium Arsenide

K. F. Shtel'makh, M. P. Korobkov, and I. G. Ozerov
St. Petersburg State Technical University, ul. Politekhnicheskaya 29, St. Petersburg, 195251 Russia
e-mail: shtelmah@spes.stu.neva.ru
Submitted February 3, 2003; accepted for publication February 3, 2003

Abstract—ESR of Mn-doped GaAs is studied. The results indicate the presence of an interstitial impurity state in GaAs:Mn which is involved in the Coulomb interaction with the substitutional Mn states. Analysis of the temperature variations of ESR spectra and the values of the g factor shows that the interstitial center has a d^5 electron configuration. The substitutional Mn create a strong random crystal field at the interstitial Mn ion. The results can be explained by assuming the existence of a nonzero dipole moment in the neutral state of Mn. *© 2003 MAIK "Nauka/Interperiodica".*

1. INTRODUCTION

The magnetism of Mn-doped gallium arsenide with an Mn concentration of about 10^{20} cm^{-3} is characterized by high values of the Curie temperature [1]. At certain levels of doping, gallium arsenide remains semiconducting, which shows promise for the fabrication of electronic devices that utilize the interaction of polarized charge carriers with the magnetic field of impurity atoms.

The existing theories describing impurity ferromagnetism of Mn-doped GaAs [1] suggest the existence of exchange interaction between substitutional centers. This study aims to show that high-resistivity samples contain interstitial centers that are involved in the interaction with other states even at low Mn content.

It has long been known that Mn introduced into the lattice sites of GaAs forms two charge states [2]. The first state with zero (neutral) charge relative to a crystal is formed if a chemical bond is not completely filled with electrons, i.e., when only two Mn electrons are involved in bonding, instead of three, as occurs when other transition-element atoms enter a crystal. A hole generated in the bond becomes involved in the exchange interaction with the d electrons of Mn, which results in the formation of a ground state with a spin $S = 1$ [3]. Henceforth, we denote such a center as Mn^0. In addition, in highly compensated samples, or in samples with n-type conductivity, one always observes states with an almost cubic environment and which possess the d^5 electron configuration with a spin $S = 5/2$. In accordance with commonly accepted terminology, we will call such states "ionized" and denote them as Mn^-. Finally, another state has been found quite recently by the ENDOR method in neutron-irradiated GaAs doped lightly with Mn. This state corresponds to the interstitial manganese centers $\mathrm{Mn}_{\mathrm{int}}$ with a d^5 electron configuration [4]. The ENDOR spectrum is characterized by g values equal to 2.0006 and by a constant of hyperfine structure $A = 266$ MHz $\equiv 88.9 \times 10^{-4}$ cm^{-1}.

In samples of GaAs highly compensated with Mn, apart from the ESR spectra of individual dopant centers, a transition was observed which is characterized by anomalous temperature behavior of the signal intensity and an unusual g value ($g = 4.18 \pm 0.03$ [5]). These features were attributed to a strong exchange interaction between Mn centers. However, in light of the data discussed below, this explanation seems incorrect.

In actual fact, such a spectrum has not been observed in GaAs:Mn samples with n-type conductivity [6] or in Zn-compensated samples with p-type conductivity [7], in spite of almost the same concentration of Mn introduced into the crystal. This means that only the paramagnetic centers having different states are involved in the interaction. Strong exchange interaction between various ions implies that the resulting values of g should be intermediate between the values for the isolated states [8]. In our case, $g_{\mathrm{neu}} = 2.81$ and $g_{\mathrm{ion}} = 2.002$ [7, 5], which is in contradiction with the observed value $g \approx 4$.

2. RESULTS

ESR spectra were measured using a Bruker ER 220D spectrometer in the temperature range 3.8–100 K. Highly compensated samples similar to those studied in [5] were used in the measurements.

The entire ESR spectrum which includes the transition of interest to us is shown in Fig. 1. The spectrum consists of two almost isotropic lines with $g \approx 4.07 \pm 0.03$ and $g \approx 2.0$ (compare with the data in [5]). In contrast to [5], the value of g was determined from the position of the center in a poorly resolved hyperfine structure with a constant $A = (99 \pm 4) \times 10^{-4}$ cm^{-1} ($T = 7.3$ K). Rotating a sample in a magnetic field at low temperatures ($T < 7.3$ K) leads to the disappearance of the hyperfine structure at certain orientations. The intensity of this spectra differs appreciably for various samples cut from the same crystal. This feature, as well as the superposition of the transition with $g \approx 2$ on the lines of the individual states of the ionized Mn^- center, explains why the transition with $g \approx 2.0$ is not mentioned in [5], and also why the g factor is determined with low accuracy.

The measurements of the samples with an Mn concentration from 10^{16} to 10^{18} cm^{-3} show that the values of g for the first spectral component in the absence of a hyperfine structure can vary within the range from 4.00 to 4.2, all other factors being the same. Therefore, the temperature variations of the intensity of transition and the values of g are in contradiction with the conclusion made in [9] that the line with $g = 4.07$ ($g = 4.0$, according to [9]) corresponds to a forbidden ESR transition of the ionized state of Mn (Mn^-) in a cubic coordination of the lattice site.

All transitions are characterized by an unusual line shape with a structure that becomes more pronounced with increasing temperature (see inset in Fig. 1). The temperature dependences of the relative intensity for both transitions, which is proportional to the population of states [8], are virtually identical, which is seen from Fig. 2 (sample A57 [5]). This observation allows one to conclude that the transitions with the g factors mentioned above correspond to the ESR spectrum of a single state. The specific hyperfine structure indicates that this state is an Mn state. The possibility of observing ESR up to temperatures of about 100 K shows that the spin-lattice relaxation rate is low; i.e, we are dealing with a nondegenerate orbital state. The values of the constant of the hyperfine structure are only slightly larger than the value obtained for Mn in the crystals with predominantly ionic bonds, i.e., in cadmium and barium fluorides, e.g., $A \leq 93 \times 10^{-4}$ cm^{-1} [10]. In other words, hybridization of the d functions with the functions of the valence band is virtually equal to zero.

All of the above-mentioned features show that Mn enters the crystal as an interstitial ion (Mn_{int}) with a $3d^5$ electron configuration. It should be noted that the values of the parameters of the spectrum differ from the values given in [4] (see above).

3. DISCUSSION

The observed features of the spectrum can be explained by using the idea of the combined action of strong axial and orthorhombic crystal fields which are random in magnitude and in the orientation of the Z axes. In this case, the isotropy of transitions under consideration, the unusual line shape, and the unresolved hyperfine structure are determined by averaging the spectrum over all possible rotation angles of the Z axis, while the nonmonotonic temperature dependence of population can be explained by the fact that this state is not the lowest one.

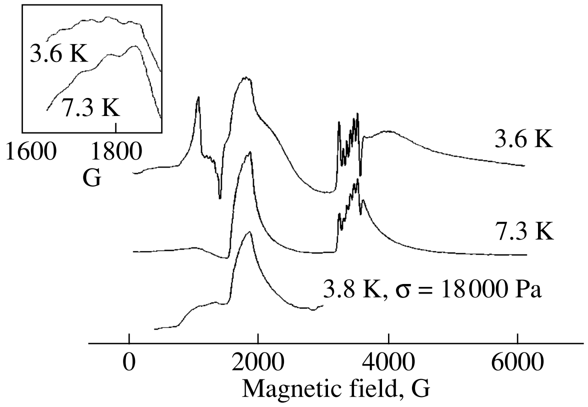

Fig. 1. ESR spectra of sample A57 at several temperatures. The lower spectrum is measured at $T = 3.8$ K under the effect of uniaxial pressure. The inset shows the fragments of the spectrum.

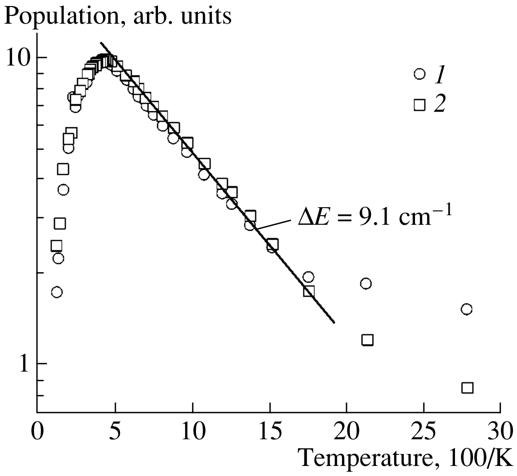

Fig. 2. Temperature dependence of the relative magnetization of the components of the ESR spectra with the g factors equal to (*1*) ~ 2.0 and (*2*) 4.07 for sample A57.

In the crystal studied, the most commonly encountered impurity is Mn; therefore, random crystal fields at low impurity concentrations should most probably be created by the neutral Mn^0 states and the substitutional Mn^- centers that have an excessive negative charge with respect to the crystal matrix. The ratio of the concentrations of these centers as a function of the total Mn concentration in a crystal is given in [5].

An axial crystal field can be created by any charged impurity center, including Mn^-. Using the operators-equivalents, this field can be represented in the form of $D_Z S_Z^2$. Correspondingly, the Mn^0 states can create a field of orthorhombic symmetry, provided they have a nonzero electric dipole moment. This assumption is supported by the data obtained in [9], which are indic-

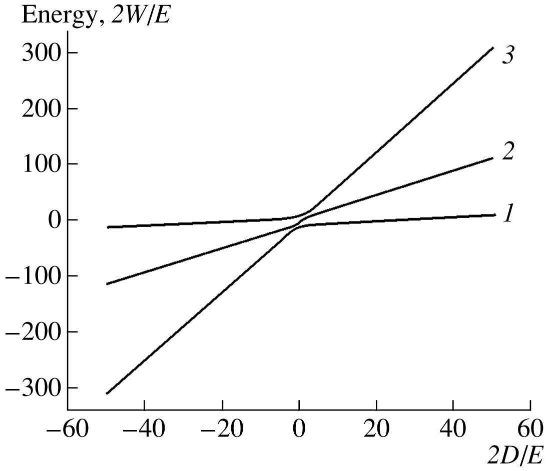

Fig. 3. Position of the ^6S-state levels in a strong crystal field (Hamiltonian (*1*)) in units of *E*/2 as a function of the ratio of parameters *D* and *E*. The numbering corresponds to the numbers of levels. The values of *D* and *E* in the figure are positive.

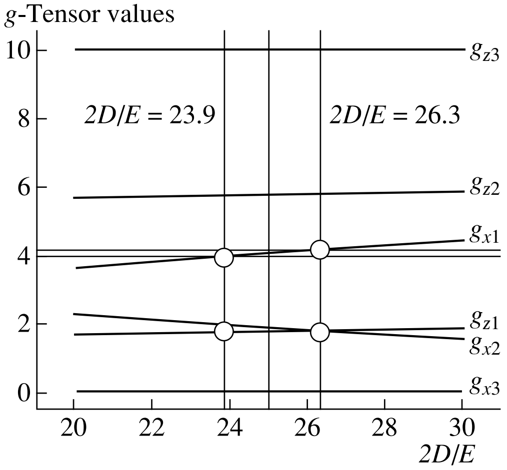

Fig. 4. Calculated values of the components of the *g* tensor for the states shown in Fig. 3 in relation to the ratio of parameters *D* and *E*. Vertical lines mark the limiting values of 2*D*/*E* (open circles) and the value $g_x = 4.07$ (central line). The values of *D* and *E* in the figure are negative.

ative of the electric-dipole nature of the magnetic resonance spectrum of Mn^0. Stabilization of the electric-dipole axis can be attributed to the effect of the Coulomb potential which is created by charged centers and acts on a neutral center; the positive potential of an Mn_{int} center is especially important. This potential can change the orientation of a dipole in such a way that its positive charge will be located farther from the Mn_{int} than the negative one. It is of significance that the orthorhombic electric field can be created under the condition that the axis joining the dipole charges does not coincide with the axis joining the Mn^0 and MN_{int} centers. Using the commonly used notation [8] for the operators-equivalents, this field can be written as $(D_x - D_y)(S_x^2 - S_y^2)$.

The ideas discussed above about interacting states make it possible to determine the signs of the potentials acting on the interstitial Mn center. The potential formed by Mn^- is negative, which corresponds to its charge with respect to the crystal matrix. If we accept the mechanism discussed above on the spatial fixation of the electric dipole of an Mn^0 center, then the potential difference created by the individual components of a dipole also turns out to be negative.

Of course, other combinations of charges of different nature with similar symmetry can also contribute to the spectrum of Mn states. For example, a dipole structure can be formed by an Mn^-–D^+ pair with *D* as a donor [5]. However, the change in the shape of the ESR line with temperature in the range 3.8–8 K is indicative of the dynamics in crystal-field sources. As an analogue, we can use the motion of particles in a liquid, which results in the narrowing of the NMR (or ESR) line due to the rapid oscillations of a local field acting at a magnetic center, provided that the rate of the spin–lattice relaxation of the source of this field is high [8]. Here, it is worth mentioning that the ESR spectrum of Mn^0 at the temperatures $T \leq 8$ K broadens with increasing temperature until it totally disappears [7]. Therefore, the most probable source of the orthorhombic field seems to be the Mn^0 state.

Thus, the spectrum of interacting Mn centers can be described by the Hamiltonian of the form

$$H = DS_Z^2 + E(S_X^2 - S_Y^2) + g\beta\mathbf{HS}, \qquad (1)$$

where *D* and *E* are the constants that characterize axial and orthorhombic fields acting on the center, β is the Bohr magneton, **H** is the vector of the magnetic field strength, and $S = 5/2$ is the spin of Mn_{int}. The terms that describe hyperfine interaction and that are responsible for the conservation of the centroid of the split lines are omitted in (1), as they are not necessary for the analysis.

The results of the numerical diagonalization of the Hamiltonian (1) and the calculation of the components g_z and g_x of the *g* factor [6] are shown in Figs. 3 and 4. From these figures, it is seen that the values of $g \sim 4.00$–4.18 and ~2.0, which characterize the Zeeman splitting of only one of the levels, are obtainable under the condition $24 < 2D/E < 26$. The value of the g_x component of the upper level at $D < 0$ and $E < 0$ varies from 4.00 to 4.18. The corresponding values of g_z are equal to 1.8–1.88. The values of the components of the *g* tensors are $g_z \sim 10$ and $g_x \sim 0$ for the lower level, and $g_z \sim 6$ and $g_x \sim 2$ for the level of the intermediate state.

Verification of the calculations presumes observation of the transitions at least with the characteristic values $g_z \sim 10$ and $g_z \sim 6$. In the region of $T = 3.8$ K, the application of an external pressure to a crystal, as noted in [11], results in the disappearance of the ESR spectrum of a neutral Mn center. In this region, a transition with a peculiar ESR line shape is observed (Fig. 1). The corresponding value $g = 8.3 \pm 0.5$ is determined at the half-height of the line; i.e., the results of calculation correlate quite well with the observed ESR spectra.

Thus, analysis of the features of the EPR spectrum shows that the interstitial Mn centers can exist not only in neutron-irradiated samples, but also in highly compensated samples. The electron configuration of such centers is d^5; they experience a strong crystal field of arbitrary orientation.

The relative intensity of this state is described by the exponential law (Fig. 2). The index of the exponential function ΔE should obviously be related to the energy spacing of the levels shown in Fig. 3. A rough estimate of these values can be obtained from the following considerations. The average distance between impurity centers in GaAs crystal with an impurity concentration of about 10^{17} cm^{-3} is approximately equal to 34 lattice constants. Treating a crystal as a medium with a permittivity ε ($\varepsilon_{\mathrm{GaAs}} = 12$), we can estimate the potential W_{dipole} created by Mn^0 at a site occupied by the $\mathrm{Mn}_{\mathrm{int}}$ ion using the classical approach.

The potential can be written as $W_{\mathrm{dipole}} \le q^2 l/\varepsilon r^2$, where l is the characteristic length of a dipole. Assuming $l = (\sqrt{3}/4)a_{\mathrm{lattice}}$, i.e., equal to the distance to the nearest-neighbor atom with tetrahedral bonds; the charge q, equal to the elementary charge; and r, equal to the average distance between Mn centers, we obtain $W_{\mathrm{dipole}} \sim E \le 0.32$ cm^{-1} for the Mn concentration of 5×10^{16} cm^{-3}.

The temperature dependence of the relative intensity of the ESR line with $g_x = 4.07$ and $g_z = 2.0$ allows us to conclude that this state is the upper one in the calculated spectrum at $D < 0$ and $E < 0$. Denoting the spacings between levels as ΔE_1 and ΔE_2 (the energy and indices are reckoned from the bottom), the calculation with regard to the estimated value E yields the following results: $\Delta E_1 = 8.3$–8.9 cm^{-1} and $\Delta E_2 = 15.1$–16.7 cm^{-1}, which, in view of the crudeness of the approach used, is quite close to the value $\Delta E = 9.1$ cm^{-1} obtained from the temperature dependence of the populations of states (Fig. 2).

4. CONCLUSION

The features of the ESR of interacting Mn centers in gallium arsenide show that the ESR spectrum at low temperatures originates from the interstitial manganese ions $\mathrm{Mn}_{\mathrm{int}}$.

The $\mathrm{Mn}_{\mathrm{int}}$ ions interact with the neutral and ionized states of Mn. The interaction between $\mathrm{Mn}_{\mathrm{int}}$, Mn^0, and Mn^- has a Coulomb nature.

The results can be interpreted by assuming that the neutral Mn^0 state (d^5 + hole) has a nonzero electric dipole moment; i.e., a hole is spatially shifted with respect to the electron core with d^5 configuration.

REFERENCES

1. T. Jungwirth, W. A. Atkinson, B. H. Lee, and A. H. MacDonald, Physica E (Amsterdam) **6**, 794 (2000); T. Dietl, H. Ohno, F. Matsukura, *et al.*, Science **287**, 1019 (2000).
2. V. F. Masterov, Fiz. Tekh. Poluprovodn. (Leningrad) **18**, 3 (1984) [Sov. Phys. Semicond. **18**, 1 (1984)].
3. I. Ya. Karlik, I. A. Merkulov, D. N. Mirlin, *et al.*, Fiz. Tverd. Tela (Leningrad) **24**, 3550 (1982) [Sov. Phys. Solid State **24**, 2022 (1982)].
4. S. J. C. H. M. van Gisbergen, M. Godlewski, T. Gregorkiewicz, and C. A. J. Ammerlaan, Phys. Rev. B **44**, 3012 (1991).
5. V. F. Masterov, S. B. Mikhrin, B. E. Samorukov, and K. F. Shtel'makh, Fiz. Tekh. Poluprovodn. (Leningrad) **17**, 1259 (1983) [Sov. Phys. Semicond. **17**, 796 (1983)].
6. V. F. Masterov, S. B. Mikhrin, and K. F. Shtel'makh, Fiz. Tekh. Poluprovodn. (Leningrad) **19**, 1867 (1985) [Sov. Phys. Semicond. **19**, 1150 (1985)].
7. V. F. Masterov, K. F. Shtel'makh, and M. N. Barbashov, Fiz. Tekh. Poluprovodn. (Leningrad) **22**, 654 (1988) [Sov. Phys. Semicond. **22**, 408 (1988)].
8. A. Abragam and B. Bleaney, *Electron Paramagnetic Resonance of Transition Ions* (Clarendon Press, Oxford, 1970; Mir, Moscow, 1972), Vol. 1.
9. N. P. Baran, V. Ya. Bratus', V. M. Maksimenko, *et al.*, Pis'ma Zh. Éksp. Teor. Fiz. **55** (2), 108 (1992) [JETP Lett. **55**, 101 (1992)].
10. S. A. Al'tshuler and B. M. Kozyrev, *Electron Paramagnetic Resonance in Compounds of Transition Elements* (Nauka, Moscow, 1972; Halsted, New York, 1975).
11. J. Schneider, U. Kaufmann, W. Wilkening, *et al.*, Phys. Rev. Lett. **59**, 240 (1987).

Translated by A. Zalesskiĭ

Semiconductors, Vol. 37, No. 8, 2003, pp. 876–883. Translated from Fizika i Tekhnika Poluprovodnikov, Vol. 37, No. 8, 2003, pp. 905–911.
Original Russian Text Copyright © 2003 by Lagunova, Voronina, Mikhaĭlova, Moiseev, Samokhin, Yakovlev.

Interaction of Charge Carriers with the Localized Magnetic Moments of Manganese Atoms in *p*-GaInAsSb/*p*-InAs:Mn Heterostructures

T. S. Lagunova, T. I. Voronina, M. P. Mikhaĭlova, K. D. Moiseev, E. Samokhin, and Yu. P. Yakovlev

Ioffe Physicotechnical Institute, Russian Academy of Sciences,
Politekhnicheskaya ul. 26, St. Petersburg, 194021 Russia

Submitted February 3, 2003; accepted for publication February 4, 2003

Abstract—Transport properties of *p*-$Ga_{1-x}In_xAs_ySb_{1-y}$/*p*-InAs:Mn heterostructures with undoped layers of solid solutions similar in composition to GaSb ($x \lesssim 0.22$) grown by liquid-phase epitaxy on substrates with a Mn concentration of $(5–7) \times 10^{18}$ cm^{-3} are studied. It is ascertained that there is an electron channel at the interface (from the InAs side). The anomalous Hall effect and negative magnetoresistance are observed at relatively high temperatures (77–200) K. These phenomena can be attributed to the *s*–*d*-exchange interaction between Mn ions of the substrate and *s* electrons of the two-dimensional channel. The effective magnetic moment of Mn ions was evaluated as $\mu = 200\mu_B$ at $T = 77$ K. © *2003 MAIK "Nauka/Interperiodica".*

1. INTRODUCTION

It was shown by Voronina *et al.* [1–3] that, in individual *p*-$Ga_{1-x}In_xAs_ySb_{1-y}$/*p*-InAs heterostructures with undoped layers similar in composition to GaSb ($x \lesssim 0.22$), an electron channel with semimetal properties exists at the interface. This channel features high electron mobility at 77 K: $\mu_{77} = (3–7) \times 10^4$ cm^2 V^{-1} s^{-1}. In these studies, the Hall effect, the mobility, and the magnetoresistance were investigated as functions of temperature and magnetic field. It was shown that the Hall coefficient and the electron mobility observed in the electron channel remain constant in the temperature range from 77 to 200 K and are independent of the magnetic field strength. The magnetoresistance has a positive sign and is governed by the mobility. Heavily compensated *p*-InAs:Zn or *p*-InAs:Mn samples with a hole density of $p_{300} \lesssim 10^{17}$ cm^{-3} were used as high-resistivity substrates. However, at a high degree of compensation, the conductivity of *p*-InAs begins to change to intrinsic at $T > 200$ K and the substrate shunts all charge transport in the *p*-GaInAsSb/*p*-InAs:Mn heterostructure.

This study is aimed at investigating the transport properties of *p*-GaInAsSb/*p*-InAs:Mn heterostructures grown on substrates doped heavily with manganese ($p = (5–7) \times 10^{18}$ cm^{-3}). This problem is of interest since manganese, which behaves as an acceptor impurity in InAs, is used in the fabrication of various optoelectronic devices. It is well known that Mn is a transition element; Mn atoms have unfilled 3*d* and filled 4*s* shells (electron configurations $3d^5$ and s^2, respectively). Manganese dissolves easily in InAs, occupying sites in the indium sublattice. When the Mn concentration in InAs becomes sufficiently high, Mn exhibits specific properties: at low temperatures, it is in the Mn^{3+} charge state (the $3d^4$ electron configuration) and provides *n*-type conductivity. At higher temperatures, Mn atoms can capture electrons from the valence band (one electron per Mn atom). Thus, Mn atoms change their charge state to Mn^{2+} (the $3d^5$ electron configuration), due to which the *p*-type conductivity arises.

Thus, the purpose of this study was to investigate the behavior of the Mn impurity in *p*-$Ga_{1-x}In_xAs_ySb_{1-y}$/*p*-InAs:Mn heterostructures ($x = 0.04, 0.09, 0.22$) and in heavily doped ($p = (5–7) \times 10^{18}$ cm^{-3}) *p*-InAs:Mn substrates. The effect of the exchange interaction between charge carriers and the magnetic moments of Mn atoms on the transport properties of the heterostructures under investigation was analyzed.

2. EXPERIMENTAL RESULTS

Epitaxial layers (epilayers) of $Ga_{1-x}In_xAs_ySb_{1-y}$ solid solutions with an In content $x = 0.04$, 0.09, and 0.22 were grown by liquid-phase epitaxy on *p*-InAs:Mn substrates 350 μm thick with a hole density $p = (5–7) \times 10^{18}$ cm^{-3}. The thickness of epilayers ranged from 1 to 2 μm. Using transmission electron microscopy, we showed that the InAs/GaInAsSb interface is sharp (the width of the transition layer was about three to four monolayers). The epilayers were nominally undoped; they had *p*-type conductivity with a hole density $p \approx 10^{16}$ cm^{-3} and mobility $\mu_H \approx 2000$ cm^2 V^{-1} s^{-1} at $T = 77$ K. Six indium contacts were formed on the epilayer

Characteristics of $p\text{-Ga}_{1-x}\text{In}_x\text{As}_y\text{Sb}_{1-y}/p\text{-InAs:Mn}$ heterostructures at $T = 77$ K

Sample no.	Content of In, x	Hole density p, cm^{-3}	R_H, cm^2/C		μ_H, cm^2 V^{-1} s^{-1}		$\Delta\rho/\rho$, %	
			$H = 2$ kOe	$H = 20$ kOe	$H = 2$ kOe	$H = 20$ kOe	$H = 2$ kOe	$H = 20$ kOe
1	0.04	10^{17}	-7×10^5	-7×10^5	−44000	−40000	+4	+140
2	0.09	10^{17}	-9×10^5	-9×10^5	−48000	−46000	+2	+110
3	0.22	10^{17}	-6×10^5	-6×10^5	−30000	−30000	+5	+170
4	0.04	5×10^{18}	−220	+5.4	−440	+14	−1.3	−9.2
5	0.09	6×10^{18}	−1170	−12	−2800	−20	−4	−30
6	0.22	7×10^{18}	−390	+4	−1200	+13	−1.5	−10.3

surface to measure the parameters of the $p\text{-Ga}_{1-x}\text{In}_x\text{As}_y\text{Sb}_{1-y}/p\text{-InAs:Mn}$ heterostructures; specifically, the Hall coefficient R_H, the conductivity σ, the Hall mobility μ_H, and the transverse magnetoresistance $\Delta\rho/\rho$ in magnetic fields of strength 0–20 kOe in the temperature range of 77–300 K were measured. These parameters were also measured from the substrate side. The table contains the main parameters of the $p\text{-Ga}_{1-x}\text{In}_x\text{As}_y\text{Sb}_{1-y}/p\text{-InAs:Mn}$ heterostructures measured from the epilayer side at $T = 77$ K.

Figures 1a and 1b show the results of measurements of the Hall coefficient R_H and the Hall mobility μ_H as functions of the magnetic field strength H at $T = 77$ in the $p\text{-Ga}_{1-x}\text{In}_x\text{As}_y\text{Sb}_{1-y}/p\text{-InAs:Mn}$ heterostructures. The measurements were performed from the epilayer side; the hole density in the substrate was $p = 10^{17}$ cm^{-3} (samples 1–3) and $p \gtrsim 5 \times 10^{18}$ cm^{-3} (samples 4–6). As can be seen from Figs. 1a and 1b, for a hole density in the substrate, $p = 10^{17}$ cm^{-3} (samples 1–3), large values of the Hall coefficient R_H and the electron mobility μ_H are observed and are virtually independent of the magnetic field strength up to 20 kOe. In the case of a high hole density in the substrate ($p \gtrsim 5 \times 10^{18}$ cm^{-3}) for the solid solutions of any composition studied ($x = 0.04$, 0.09, 0.22, samples 4–6), the field dependences of the Hall coefficient and mobility radically differ from the corresponding dependences for samples 1–3: the values of R_H and μ_H become two orders of magnitude smaller, decrease slightly with magnetic field increasing to 5 kOe, and abruptly decrease with further increase in the magnetic field; at $H \gtrsim 18$ kOe, the conductivity changes from n- to p-type.

In contrast to the measurements performed from the epilayer side, the measurements performed from the substrate side for samples 4–6 showed p-type conductivity at $T = 77$ K and an increase in the Hall coefficient R_H and hole mobility μ_H with increasing magnetic field over the entire range of the magnetic fields studied. Since the dependences measured for samples 4–6 from the substrate side were almost identical, they are shown in Figs. 1a and 1b by a dotted line only for sample 6, whose with hole density $p = 7 \times 10^{18}$ cm^{-3}.

Figures 2a and 2b show the temperature dependences of the Hall coefficient R_H and the mobility μ_H measured from the epilayer side at $H = 3$ kOe. In samples 1–3, which were grown on substrates with an Mn concentration $p = 10^{17}$ cm^{-3}, the Hall coefficient and the mobility remain constant up to 200 K; above this temperature, R_H and μ_H decrease abruptly due to the appearance of intrinsic conductivity in the substrate. In samples 4–6, which were grown on substrates with an Mn concentration $p = (5\text{–}7) \times 10^{18}$ cm^{-3}, R_H and μ_H decrease gradually in the temperature range $T = 77$–200 K (by approximately a factor of 2); above 200 K, as in samples 1–3, an abrupt decrease in R_H and μ_H is observed.

The measurements for samples 4–6 at $H = 3$ kOe from the substrate side (the dashed lines in Figs. 2a, 2b) indicate p-type conductivity over the entire temperature range. The Hall coefficient and the mobility increase with increasing temperature up to 200 K. Above 200 K, these quantities tend toward constant values.

Figure 3 shows the temperature dependence of the Hall coefficient R calculated per unit volume for the p-InAs:Mn substrate with an Mn concentration $p = 7 \times 10^{18}$ cm^{-3} (sample 6) at magnetic-field values of $H = 3$ and 10 kOe. It can be seen that, at $H = 3$ kOe, the Hall coefficient decreases with decreasing temperature much faster than at $H = 10$ kOe. At $T = 77$ K, the values of the Hall coefficient at $H = 3$ kOe become smaller than those at $H = 10$ kOe by an order of magnitude. The temperature dependence of the Hall coefficient at $H = 10$ kOe for InAs:Mn with approximately the same hole density as that in [4] is also shown in Fig. 3 by the dashed line. An abrupt decrease in R_H at $H = 10$ kOe occurred at $T < 77$ K and, at $T \approx 50$ K, the Hall coefficient changed its sign.

Figure 4 shows the dependences of the transverse magnetoresistance on the magnetic field strength in the $p\text{-Ga}_{1-x}\text{In}_x\text{As}_y\text{Sb}_{1-y}/p\text{-InAs:Mn}$ heterostructures at $T = 77$ K. As can be seen, for all solid solution compositions grown on substrates with an Mn concentration $p = 10^{17}$ cm^{-3} (samples 1–3), the ordinary Lorentz positive magnetoresistance is observed. Positive magnetoresis-

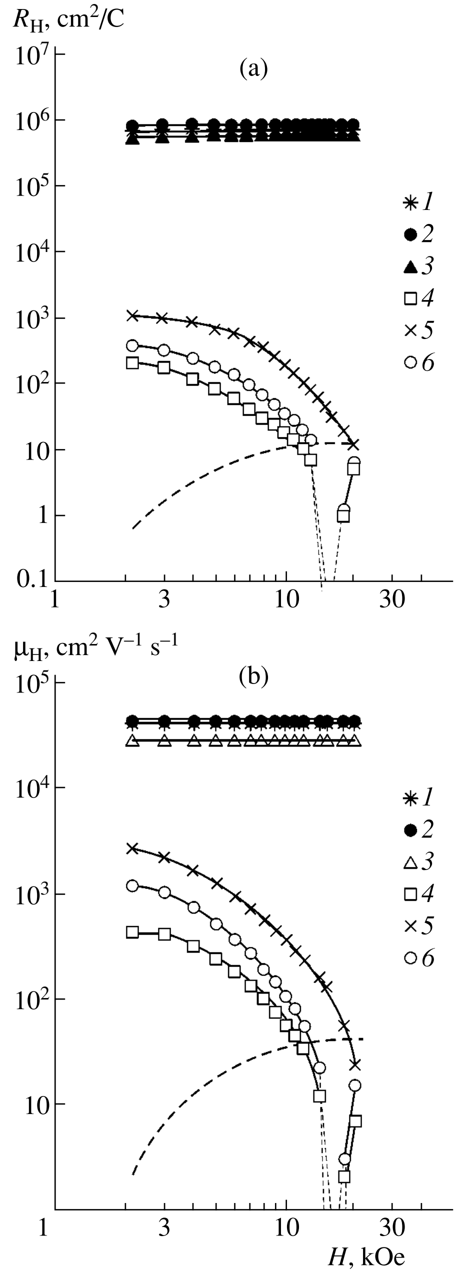

Fig. 1. Dependences of (a) the Hall coefficient R_H and (b) the Hall mobility μ_H on the magnetic field strength H at T = 77 K. The curve numbers correspond to the sample numbers in the table. Dashed lines represent the values of R_H and μ_H measured for sample 6 from the substrate side.

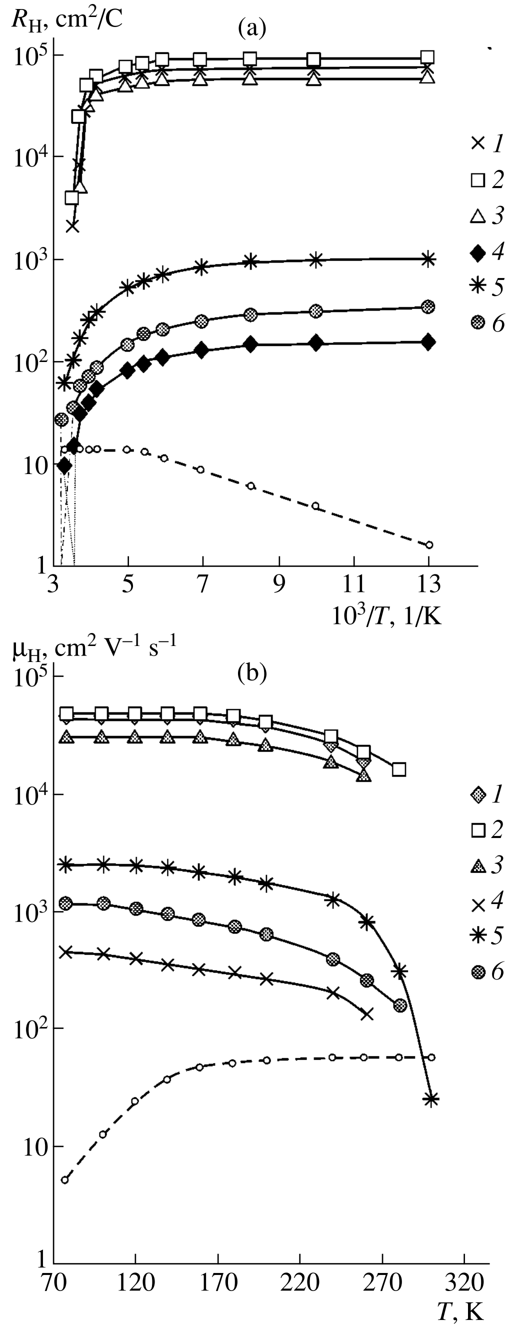

Fig. 2. Temperature dependences of (a) the Hall coefficient R_H and (b) the Hall mobility μ_H at a magnetic field strength H = 3 kOe. The curve numbers correspond to the sample numbers in the table. Dashed lines represent the values of R_H and μ_H measured for sample 6 from the substrate side.

tance increases proportionally with increasing magnetic field strength to H^2. The small value of the magnetoresistance coefficient $B_r = (\Delta\rho/\rho)(c/\mu^2H^2) = 0.1$–$0.2$ is due to scattering from impurity ions, which is dominant because the quality of the interface is high (roughness, dislocation loops, and other defects are absent).

In the p-$Ga_{1-x}In_xAs_ySb_{1-y}$/p-InAs:Mn heterostructures grown on substrates with a hole density $p = (5$–$7) \times 10^{18}$ cm^{-3} (samples 4–6), in contrast to samples 1–3, negative magnetoresistance (NMR) is observed for all of the studied solid solutions compositions. NMR increases proportionally to H^2 up to 5 kOe, and, in stronger fields ($H > 10$ kOe), it tends toward a constant

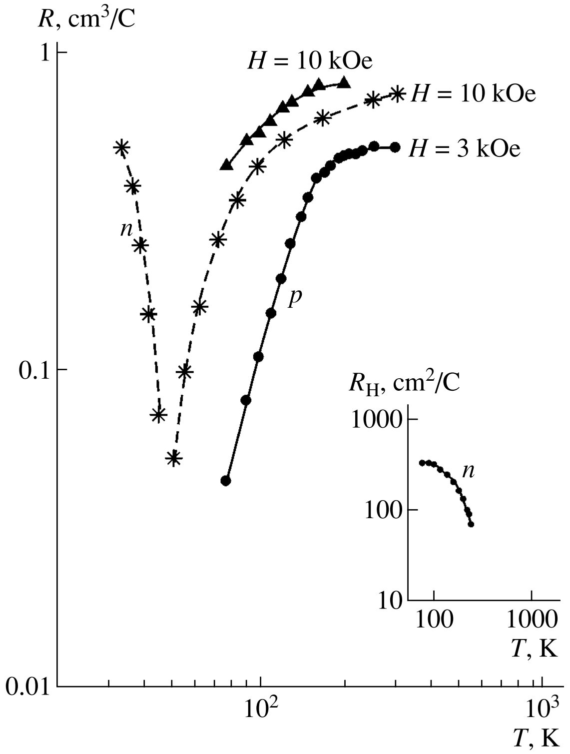

Fig. 3. Temperature dependences of the Hall coefficient R for the substrate of sample 6 at H = 10 and 3 kOe (solid lines) and for InAs:Mn with $p = 8 \times 10^{18}$ cm^{-3} at H = 10 kOe [4] (dashed line). The inset shows the temperature dependence of R_H for the heterostructure of sample 6 at H = 3 kOe.

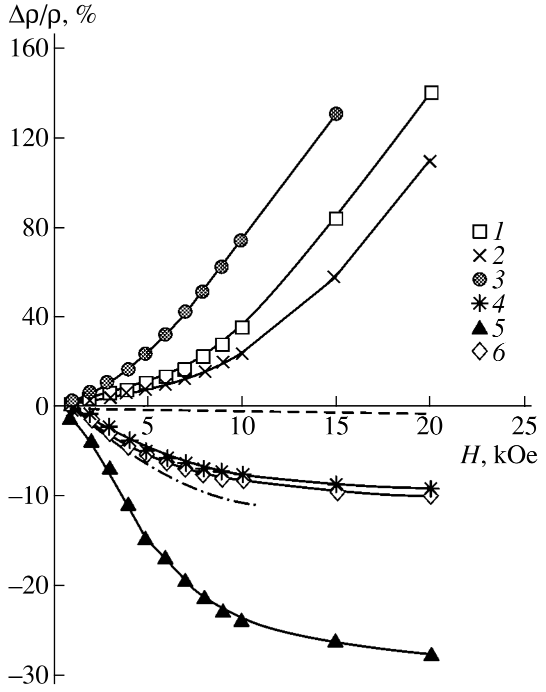

Fig. 4. Dependences of the transverse magnetoresistance $\Delta\rho/\rho$ on the magnetic field strength H at T = 77 K. The curve numbers correspond to the sample numbers in the table. The dashed line represents $\Delta\rho/\rho$ for the case of measurement of sample 6 from the substrate side. The dash–dot line represents the results of [4], $p = 8 \times 10^{18}$ cm^{-3}, T = 4.2 K.

value. When samples 4–6 were measured from the substrate side (the dashed curve in Fig. 4), NMR was also observed, but it was considerably lower (smaller than 1%).

The temperature dependences of NMR for samples 4–6 measured from the epilayer side at H = 3 kOe are shown in Fig. 5. It can be seen that the temperature dependence of the NMR is weak below 200 K and that NMR abruptly decreases at higher temperatures; however, even at T = 300 K, the contribution of NMR is noticeable (about 1%). The measurements of the temperature dependence of NMR from the substrate side were hindered due to the small magnitude of this effect.

Thus, the experimental data shown in Figs. 1–3 indicate that the transport properties of the p-GaInAsSb/p-InAs:Mn heterostructures grown on substrates with a hole density $p = (5–7) \times 10^{18}$ cm^{-3} (samples 4–6) radically differ from the properties of similar heterostructures grown on lightly doped substrates with a hole density $p = 10^{17}$ cm^{-3} (samples 1–3). This phenomenon can be attributed only to the different properties of the substrates.

3. DISCUSSION

Let us consider first the transport properties of the p-InAs:Mn substrate with a hole density $p = (5–7) \times 10^{18}$ cm^{-3} and then those of the electron channel in the p-GaInAsSb/p-InAs:Mn heterostructure with a Mn concentration of $(5–7) \times 10^{18}$ cm^{-3}.

3.1. Properties of the p-InAs:Mn Substrate with a Hole Density $p = 7 \times 10^{18}$ cm^{-3}

We will now analyze the substrate parameters shown in Figs. 1–4 using the substrate of sample 6 as an example. The values of the Hall coefficient at T = 300 K and H = 20 kOe (Fig. 3) indicate that the hole density in the substrate of sample 6 is $p = 7 \times 10^{18}$ cm^{-3}. At a hole density $p = 7 \times 10^{18}$ cm^{-3}, the Hall coefficient should be independent of the magnetic field in the temperature range of 77–300 K due to the degeneracy of the electron–hole gas, as was observed in p-InAs:Zn with a similar hole density [5]. A decrease in the Hall coefficient with decreasing temperature and magnetic field is indicative of the anomalous dependence of the Hall coefficient, i.e., the anomalous Hall effect (AHE), which is typical of semiconductors with magnetic

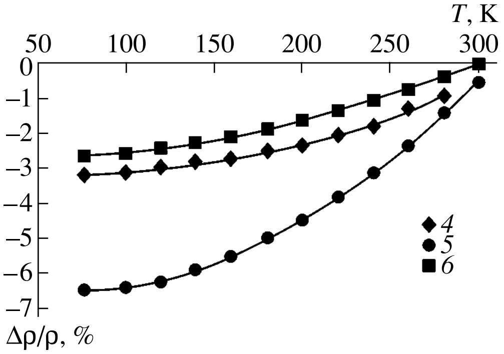

Fig. 5. Temperature dependences of the magnetoresistance at $H = 3$ kOe. The curve numbers correspond to the sample numbers in the table.

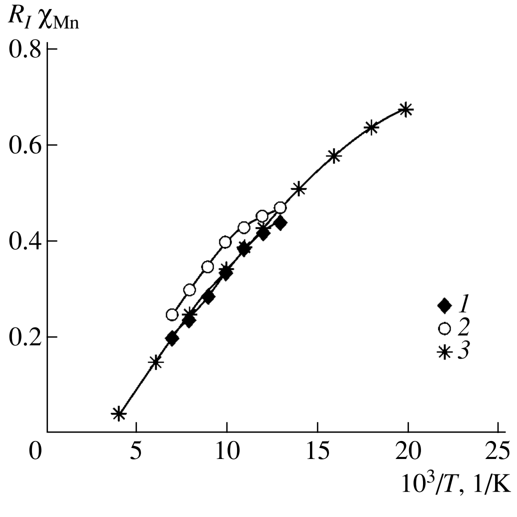

Fig. 6. Dependence of $R_I\chi_{Mn}$ on inverse temperature for (*1*) the substrate of sample 6 at $H = 10$ kOe, (*2*) the substrate of sample 6 at $H = 3$ kOe, and (*3*) InAs:Mn with $p = 8 \times 10^{18}$ cm^{-3} at $H = 10$ kOe [4].

impurities. A similar AHE was observed previously in [4] for single-crystal InAs:Mn with an Mn concentration of $(5–8) \times 10^{18}$ cm^{-3}. The Hall coefficient measured decreased abruptly with decreasing temperature, and its temperature dependence changed from that typical of a *p*-type material to that typical of an *n*-type material in the temperature range of 45–90 K (the dashed line in Fig. 3). It was shown in [4] that, when the Mn concentration in InAs exceeds 10^{18} cm^{-3}, the state of the Mn ions may change from Mn^{3+} to Mn^{2+} with a decrease in temperature; in this case, the relationship between the $3d^4$ and $3d^5$ configurations changes, which leads to a decrease in the hole density in the valence band and the appearance of Mn ions with the $3d^5$ configuration. With respect to the III–V semiconductors, such a phenomenon occurs only in InSb [6] and InAs [7, 8], in which Mn, being an acceptor impurity, has an activation energy $E_A \lesssim 0.03$ eV, which is close to the value obtained in terms of the hydrogen-like model; by contrast, in GaAs and InP, Mn forms a multiply charged, deep acceptor level with $E_A \approx 0.1$ eV [8]. In *p*-InAs:Mn, manganese forms a shallow impurity level with an energy (according to the hydrogen-like model) $E_A = (0.028 - aN^{1/3})$ eV, where $a = 1.31 \times 10^{-8}$ eV cm. At $p = 4 \times 10^{18}–10^{19}$ cm^{-3}, overlap of electronic shells of closely located atoms occurs and the impurity levels approach the valence band.

The AHE observed is attributed to the specific exchange interaction of charge carriers with the magnetic Mn impurity. At lower temperatures, the Hall coefficient R_{exp} measured is governed by the algebraic sum of the ordinary Hall coefficient R, related to the effect of the Lorentz force on charge carriers, and the anomalous Hall coefficient $R_I\chi_{Mn}$, related to the magnetization of a sample and the spin–orbit interaction [9]:

$$R_{exp} = R + R_I\chi_{Mn}. \quad (1)$$

Here, χ_{Mn} is the magnetic susceptibility and $R_I\chi_{Mn}$ is the Hall coefficient controlled by the magnetism of manganese.

Figure 6 shows the dependence of $R_I\chi_{Mn}$ on inverse temperature for a sample analyzed in [4] (Fig. 6, curve *3*) and for the substrate of sample 6 at $H = 10$ and 3 kOe (curves *1*, *2*, respectively). It can be seen that, at $H = 10$ kOe, all these dependences are linear in the temperature range of 77–200 K. At low temperatures ($T \lesssim 77$ K), when a large number of Mn ions in the Mn^{3+} charge state (the d^4 configuration) appear, a deviation from the linear dependence is observed (curve *3*).

We may suggest that, at high temperatures, the linear dependence of $R_I\chi_{Mn}$ on inverse temperature is controlled mainly by the magnetic susceptibility χ_{Mn}, which also linearly depends on inverse temperature. The Curie law, which characterizes the magnetic susceptibility of doubly charged Mn^{2+} ions (the d^5 configuration), is defined by the formula [4]

$$\chi_{Mn} = N\mu_B g^2 S(S+1)/3kT. \quad (2)$$

Here, N is the concentration of Mn ions, $S = 5/2$ is the spin moment, $g = 2$ is the Landé g-factor, and μ_B is the Bohr magneton.

At low temperatures, when Mn^{3+} ions (the d^4 configuration) arise in great number, a deviation from the Curie law is observed. The energy diagram of the Mn ion with the $3d^4$ configuration is significantly affected by the splitting of the energy levels by the crystal field and by the spin–orbit interaction. In this temperature range, the average value of the magnetic moment of the Mn ion depends on the population of different levels of its multiplet and, therefore, on temperature. The linear dependence of the magnetic susceptibility at low temperatures is determined by the formula [7]

$$\chi = ng^2\mu_B^2 S_Z^2/kT, \tag{3}$$

where the oriented spin moment $S_Z = \pm 2$ and $g = 2$. The investigations of [7] showed a weak dependence of χ on orientation, and the value of the product $dS_Z = 2.3$ was obtained for formula (3); in this case, $n = N$ (N is the total concentration of Mn ions).

Comparing the results of our studies for $R_I\chi_{\mathrm{Mn}}$ for the substrate of sample 6 at $H = 10$ and 3 kOe (Fig. 6, curves *1*, *2*, respectively), we can see that, with a decrease in the magnetic field, the deviation from the linear dependence that characterizes the Curie law is observed at higher temperatures due to the increase in the concentration of Mn in the Mn^{3+} state (d^4). We may suggest that, at $H = 3$ kOe, the effect of spin–orbit interaction begins to manifest itself at higher temperatures.

The existence of negative magnetoresistance also indicates spin interaction between charge carriers and magnetic Mn ions. For the substrate of sample *6*, the value of the negative magnetoresistance at $T = 77$ K is less than 1% (Fig. 4, dashed line). A high value of negative magnetoresistance was observed in [4] only at liquid-helium temperature (Fig. 4, dash–dot line).

3.2. Properties of the Electron Channel at the p-GaInAsSb/p-InAs:Mn heterojunction

The experimental data shown in Figs. 1–4 indicate that the transport properties of the *p*-GaInAsSb/*p*-InAs:Mn heterostructures grown on substrates with a hole density $p \gtrsim 5 \times 10^{18}$ cm^{-3} (samples 4–6) differ radically from the transport properties of heterostructures grown on lightly doped substrates with $p = 10^{17}$ cm^{-3} (samples 1–3). This phenomenon cannot be attributed to simple shunting by a substrate, as in the case of doping with nonmagnetic impurities, for example, with Zn [5].

Let us analyze the results obtained for samples 4–6, which were measured from the epilayer side, in terms of the three-layer model by the formula

$$\mu_H nh = \mu_1^2 p_1 h_1 + \mu_2^2 p_2 h_2 - \mu_3^2 n_3 h_3, \tag{4}$$

where h is the total thickness of a sample; and n, p, and μ_H are the experimental values of the concentrations and mobility of charge carriers, respectively. The subscripts 1, 2, and 3 are related to the epilayer of the solid solution, substrate, and electron channel, respectively. We ascertained that, in samples 4–6, which were measured from the epilayer side, at $H \lesssim 5$ kOe in the temperature range of 77–200 K, *n*-type conductivity is dominant and the contributions of the epilayer of the *p*-type solid solution and *p*-type substrate to the total effect measured become noticeable only at higher temperatures and in stronger magnetic fields.

Thus, we may conclude that, in magnetic fields with $H \lesssim 5$ kOe at $T \lesssim 200$ K, in measurements from the side of the solid solution, we analyze the electron channel at the *p*-GaInAsSb/*p*-InAs:Mn heterojunction for all compositions of the solid solution.

In the *p*-GaInAsSb/*p*-InAs:Mn heterostructures grown on substrates with an Mn concentration $p = (5–7) \times 10^{18}$ cm^{-3}, the Hall coefficient R_H and the mobility μ_H in the electron channel (samples 4–6) are an order of magnitude lower than in similar structures grown on substrates with an Mn concentration $p = 10^{17}$ cm^{-3} (samples 1–3). This circumstance may be due to a change in the energy structure of the heterojunction caused by the splitting of the levels of the Mn atom by the crystal field and the spin–orbit interaction. On the basis of previous estimates of the energy channel and the dependence of the electron-channel width on mobility [2], we conclude that the value of mobility, 500–3000 cm^2 V^{-1} s^{-1}, corresponds to an effective channel width of 100–200 Å.

The dependence of R_H on inverse temperature for sample 6 (Fig. 6) in the electron channel at $T = 77–200$ K is similar to that in the case of measurements of the Hall coefficient in bulk InAs:Mn with a hole density $p = 8 \times 10^{18}$ cm^{-3} at lower temperatures ($T < 50$ K), where the charge state of manganese Mn^{3+} (d^4) is dominant. This fact, as discussed above, is attributed to the spin–orbit interaction. On the basis of this circumstance, we may suggest that the AHE in the structures with an electron channel that is observed at $H = 3$ kOe in the temperature range of 77–200 K may be due to the magnetic properties of the substrate and to the interaction of Mn^{3+} ions (d^4) with electrons at the interface.

As we have seen previously (Figs. 4, 5), in the *p*-GaInAsSb/*p*-InAs:Mn heterostructures grown on substrates heavily doped with manganese (samples 4–6), negative magnetoresistance (NMR) is observed, in contrast to similar heterostructures grown on substrates lightly doped with manganese (samples 1–3), where positive magnetoresistance is observed. The appearance of NMR in heterostructures with an electron channel, as well as in substrates heavily doped with manganese, is observed simultaneously with AHE. However, NMR in structures with an electron channel attains 30% at 77 K, whereas, in bulk InAs heavily doped with manganese, such an effect is observed only at $T = 4.2$ K (Fig. 4, dash–dot line).

Figure 4 shows that, at $T = 77$ K, the dependence of the NMR on the magnetic field strength is of classical type: the NMR is proportional to H^2 in weak magnetic fields ($H \lesssim 5$ kOe) and tends toward a constant value at $H > 10$ kOe. Notably, even in the case of *p*-type conductivity, at $H \gtrsim 18$ kOe, no other effects arise, except NMR. The appearance of NMR at the interface can be related only to the interaction of charge carriers with the magnetic moments of Mn ions in InAs:Mn. The

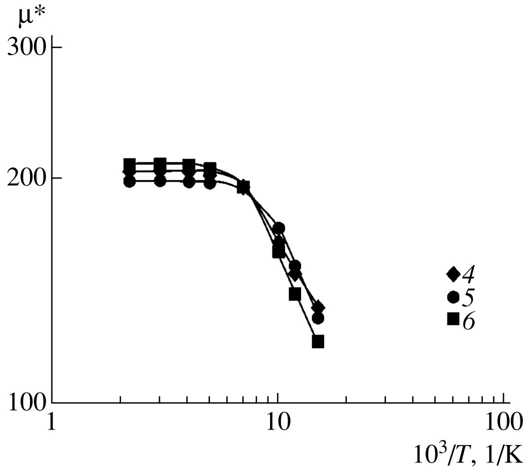

Fig. 7. Dependences on the effective magnetic moment of Mn ions $\mu^* = \mu/\mu_B$ on the magnetic field strength H. The curve numbers correspond to the sample numbers in the table.

experimental results obtained for all solid solution compositions are well described by the formula [10]

$$\Delta\rho/\rho_{\text{exp}} = \Delta\rho/\rho_{\text{sat}}\tanh^2(\mu H/kT), \qquad (5)$$

where μ is the magnetic moment of Mn ions.

If we know the dependence of $\Delta\rho/\rho$ on the magnetic field strength, we can calculate the magnetic moment μ. Figure 7 shows that, for all solid solution compositions, at $T = 77$ K in magnetic fields $H \lesssim 5$ kOe, where NMR quadratically depends on the magnetic field, the magnetic moment $\mu = 200\mu_B$. The large value of the magnetic moment results in a high magnetic energy μH, which becomes comparable with the thermal energy kT at temperatures up to 200 K in a magnetic field with $H = 5$ kOe. The appearance of such high NMR at T = 77 K is observed only in the electron channel of a heterostructure. In bulk *p*-InAs:Mn doped with manganese to the same level, such a value of NMR was observed only at $T = 4.2$ K [4].

The quantity $\Delta\rho/\rho_{\text{sat}}$ controls the concentration of magnetic centers N_m [9]. The experiments we carried out show that the concentration of magnetic centers increases with increasing electron mobility at the interface.

Thus, we may conclude that NMR is governed by the spin–orbit exchange interaction of Mn ions with *s* electrons in the channel. The spin–orbit interaction is equivalent to the effect of a high-power quasi-magnetic molecular field [11] on the spins of external *s* electrons in the channel. The strong quasi-magnetic field generated by Mn ions orients the spins of electrons and, when an external magnetic field is applied, high NMR is observed so long as the conductivity related to the electron channel is dominant.

The obtained value of the magnetic moment $\mu = 200\mu_B$ allows us to estimate the magnetic susceptibility χ at the interface by formula (4): $\chi = 10^{-2}$ esu cm^3, which is three orders of magnitude larger than in the substrate.

4. CONCLUSIONS

The results of the experimental study of the transport properties of *p*-GaInAsSb/*p*-InAs:Mn heterostructures with a high concentration of manganese in the substrate allows us to conclude the following.

(i) In the *p*-$Ga_{1-x}In_xAs_ySb_{1-y}$/*p*-InAs:Mn heterostructures with undoped layers of solid solutions similar in composition to GaSb ($x \leq 0.22$), grown on substrates with a hole density $p = (5–7) \times 10^{18}$ cm^{-3}, an electron channel exists at the interface (on the InAs side), in which the electron mobility μ_H = 500–3000 cm^2 V^{-1} s^{-1}.

(ii) In the structures with an electron channel, the AHE and NMR are observed. Their magnitudes are controlled by the *s*–*d* exchange interaction of Mn ions of the substrate with *s* electrons in the channel at the interface.

(iii) The AHE and NMR are observed in the heterostructures at higher temperatures than in InAs:Mn substrates. In particular, these phenomena manifest themselves in the heterostructures with an electron channel at $T = 77$ K, whereas, in bulk samples, the AHE and NMR are observed only at $T < 30$ K and at $T = 4.2$ K, respectively.

(iv) The large magnitude of the effective magnetic moment ($\mu = 200\mu_B$), determined from NMR, indicates a high degree of magnetization of the interface, which is related to the specific features of interaction between electrons in the electron channel and magnetic Mn impurity atoms of the substrate.

ACKNOWLEDGMENTS

This study was supported in part by the Russian Foundation for Basic Research, project no. 02-02-17633.

REFERENCES

1. T. I. Voronina, T. S. Lagunova, M. P. Mikhaĭlova, *et al.*, Fiz. Tekh. Poluprovodn. (St. Petersburg) **30**, 985 (1996) [Semiconductors **30**, 523 (1996)].
2. T. I. Voronina, T. S. Lagunova, M. P. Mikhaĭlova, *et al.*, Fiz. Tekh. Poluprovodn. (St. Petersburg) **32**, 215 (1998) [Semiconductors **32**, 195 (1998)].
3. T. I. Voronina, T. S. Lagunova, M. P. Mikhaĭlova, *et al.*, Fiz. Tekh. Poluprovodn. (St. Petersburg) **34**, 194 (2000) [Semiconductors **34**, 189 (2000)].

4. D. G. Andrianov, V. V. Karataev, G. V. Lazareva, *et al.*, Fiz. Tekh. Poluprovodn. (Leningrad) **11**, 1252 (1977) [Sov. Phys. Semicond. **11**, 738 (1977)].
5. F. P. Kesamanly, T. S. Lagunova, D. N. Nasledov, *et al.*, Fiz. Tekh. Poluprovodn. (Leningrad) **2**, 56 (1968) [Sov. Phys. Semicond. **2**, 47 (1968)].
6. D. G. Andrianov, G. V. Lazareva, A. S. Savel'ev, and V. I. Fistul', Fiz. Tekh. Poluprovodn. (Leningrad) **10**, 568 (1976) [Sov. Phys. Semicond. **10**, 339 (1976)].
7. D. G. Andrianov and A. S. Savel'ev, Fiz. Tekh. Poluprovodn. (Leningrad) **14**, 539 (1980) [Sov. Phys. Semicond. **14**, 317 (1980)].
8. É. M. Omel'yanovskiĭ and V. I. Fistul', *Transition-Metal Impurities in Semiconductors* (Metallurgiya, Moscow, 1983).
9. S. V. Vonsovskiĭ, *Modern Theory of Magnetism* (GITTL, Moscow, 1952).
10. É. I. Zavaritskaya, I. D. Voronova, and N. V. Rozhdestvenskaya, Fiz. Tekh. Poluprovodn. (Leningrad) **6**, 1945 (1972) [Sov. Phys. Semicond. **6**, 1668 (1972)].
11. H. Ohno, Phys. Rev. Lett. **68**, 2664 (1992).

Translated by Yu. Sin'kov

Semiconductors, Vol. 37, No. 8, 2003, pp. 884–888. Translated from Fizika i Tekhnika Poluprovodnikov, Vol. 37, No. 8, 2003, pp. 912–916.
Original Russian Text Copyright © 2003 by Gutkin, Ermakova.

ELECTRONIC AND OPTICAL PROPERTIES OF SEMICONDUCTORS

Analysis of the Emission Band of $V_{Ga}Te_{As}$ Complexes in *n*-GaAs under Uniaxial Pressure

A. A. Gutkin* and A. V. Ermakova

Ioffe Physicotechnical Institute, Russian Academy of Sciences, Politekhnicheskaya ul. 26, St. Petersburg, 194021 Russia
**e-mail: Agut@defect.ioffe.ru*

Submitted February 3, 2003; accepted for publication February 4, 2003

Abstract—For approximating the insignificant deviation of the axes of radiating optical dipoles of $V_{Ga}Te_{As}$ complexes in GaAs from one of the ⟨111⟩ directions, the shape of the structureless photoluminescence band of these defects at a pressure of 10 kbar along the [111] axis is analyzed. For separating split components of this band, which belong to centers with different orientations, a procedure is developed which uses the laws of the piezospectroscopic behavior of anisotropic centers. According to this procedure, spectral measurements are carried out when the electric vector of the optical wave is either parallel or normal to the pressure axis. The model suggested for analysis is verified. It is determined that the splitting of the energies of the centers with different orientations at a pressure of 10 kbar is approximately equal to 38 meV. In this case, the relative fraction of the rotator that describes the polarization properties of light emitted by an individual complex in a classical dipole approximation is equal to 0.15. This fact is indicative of the comparability of the roles of spin–orbit and Jahn–Teller interactions in the formation of the emitting state of the complex. *© 2003 MAIK “Nauka/Interperiodica”.*

1. INTRODUCTION

It is known that the complex defects (complexes) in GaAs, which consist of a Ga vacancy (V_{Ga}) and a Te atom replacing an As atom in its sublattice (Te_{As}), are effective centers of hole trapping. In *n*-type material, these complexes are responsible for a broad photoluminescence (PL) band peaked at the photon energy $\hbar\omega$ of about 1.2 eV. This band is due to the recombination of *c*-band electrons with holes localized at complexes [1–5].

Both the piezoelectric properties of this band in the case of PL excitation due to the generation of electron–hole pairs and its polarization in the case of resonance polarized excitation were investigated [4–8]. These investigations revealed the distortions of the $V_{Ga}Te_{As}$ complex responsible for this band. The distortions are caused by the interaction of localized carriers with nontotally atomic vibrations which are not fully symmetric (the Jahn–Teller effect). These distortions reduce the initial trigonal symmetry of the complex to a monoclinic one and have several possible orientations in an individual defect. The external uniaxial pressure along the [111] or [110] direction at low temperature leads to the alignment of such distortions in a significant fraction of all centers responsible for the emission band at 1.2 eV.

The directions of the axes of optical dipoles, which are used to describe the emitting and absorbing states of the defects under consideration in terms of the classical dipole approximation, were determined from a quantitative analysis of the results of the investigations mentioned [5]. It was revealed that the relative contribution of the rotator to the absorption and emission of light by these centers (μ_1 and μ_2, respectively) lies in the range of 0–0.26. A more exact estimate of these quantities could not be obtained mainly because of the large width of the PL band and relatively small splitting of its components, which belong to the centers with different orientations, under uniaxial strain [9]. Owing to this circumstance, the direct observation of these components was impossible, and the existing method of decomposition of the complex band into its components [10] turned out to be inapplicable. The reason for this fact is that the band spectrum did not contain any portion caused by a single component. In view of the circumstances mentioned, the magnitude of the integrated polarization of the emission band of complexes was determined and analyzed [4–8]. Knowing this magnitude only for the case of partial alignment of distortions, the degree of which is unknown [5], made it impossible to determine μ_2 and, consequently, μ_1 more exactly [5].

Meanwhile, the values of these parameters allow us to estimate the properties of optical transitions in an individual center and may be used for the estimation of the relative role of various intracenter interactions in the formation of the electron state of a defect.

The purpose of this study is to apply the laws of piezospectroscopic behavior of anisotropic centers to the separation of the components of the emission band at 1.2 eV for *n*-GaAs:Te under uniaxial pressure and to determine the optical characteristics of the $V_{Ga}Te_{As}$ complex in terms of the classical dipole approximation.

2. MODEL OF THE CENTERS RELATED TO THE BAND AT 1.2 EV AND MAIN APPROXIMATIONS

It was previously shown that all investigated properties of the PL band can be explained on the basis of the assumption that the set of centers responsible for the band consists of two types of defects. These defects have identical optical properties and similar distortions which are not fully symmetric and lead to the monoclinic symmetry of the defect [5]. In the centers of the first type, the distortions may reorient and align due to uniaxial pressure, whereas such variation in the distortion orientation does not occur in the defects of the second type. The first-type defects apparently represent $V_{Ga}Te_{As}$ isolated complexes, whereas the second-type ones are assumed to also contain V_{Ga} and Te_{As} associated with some third-type center, for example, an additional Te atom. A hole bounded to such a defect is in the vacancy state. Such a hole strongly interacts with phonons which are not fully symmetric; this interaction leads to distortion (Jahn–Teller effect), whereas the influence of Te_{As} and associated centers is relatively weak. It is assumed that the environment of an isolated vacancy has the trigonal symmetry due to the Jahn–Teller effect. Therefore, the simultaneous influence of the donor and this effect on the vacancy state of the hole in the complex leads to the deviation of the axis of the radiating dipole of the complex from one of the ⟨111⟩ axes being relatively small. The direction of the latter does not coincide with the initial trigonal axis at which (or close to which) V_{Ga} and Te_{As} are located. For any isolated $V_{Ga}Te_{As}$ complex, three equivalent directions of the dipole axis exist (Fig. 1) and the reorientation of the distortion and dipole is possible. For defects of the second type, one of the directions is fixed due to the influence of the associated center and reorientation is impossible. However, the distribution of all possible directions over complexes of this type is also uniform. The direction of the optical-dipole axis is characterized by the angle φ, which is reckoned from a ⟨110⟩-type axis in the symmetry plane of the monoclinic complex (Fig. 1). According to [5], $\varphi \approx 28°40'$; i.e., the dipole axis deviates from the trigonal axis closest to it by 6°–7°.

A broad emission band can be resolved relatively easily if it contains only two components. Such a situation occurs for monoclinic centers if an external-strain axis is parallel to the [001] axis [9]. However, the experiments demonstrated that the splitting of the emission bands, when the electric vector of the optical wave ε is either parallel or normal to the strain axis, is small. Correspondingly, the shape of the bands is virtually the same as in the absence of strain.[1] Under these conditions, the reliable separation of the components of the luminescence band, with allowance made for experimental error, is impossible. Therefore, we performed experiments with the uniaxial strain along the [111] direction. A pressure P along this axis violates the equivalence of distortions in those isolated complexes in which the primary axis V_{Ga}–Te_{As} does not coincide with the direction of pressure. At low temperatures, this circumstance leads to the alignment of distortions and radiating dipoles of these complexes. Thus, all of the isolated complexes can be divided into two groups: in the first group, the axes of radiating dipoles deviate by the same (low) angle from the pressure axis, and, in the second group, the primary axis of the complex coincides with the pressure axis. Therefore, for a pressure along the [111] axis, at low temperatures, the emission band of isolated complexes splits into two components, which correspond to these groups. In this case, in general, the emission band of the isolated complexes is polarized due to the alignment [5]. It should be also noted that, for both groups of complexes considered above, the pressure axis lies in the plane of the defect symmetry, i.e., in the plane that contains both the dipole axis and the primary axis of the complex.

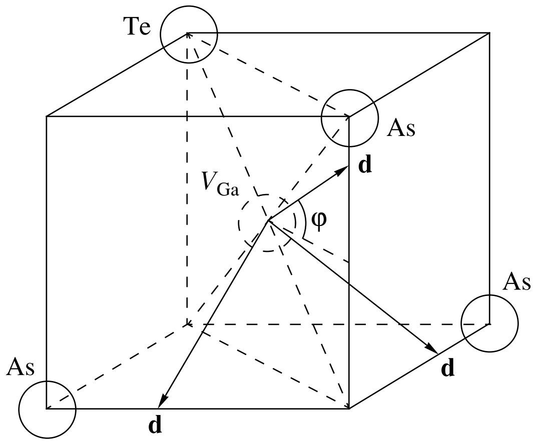

Fig. 1. Initial arrangement of the components of the $V_{Ga}Te_{As}$ complex and possible directions of the **d** axis of the emitting dipole.

The complexes with directions of the dipole axis that fail to reorient, as well as common defects with the monoclinic symmetry at **P** ∥ [111], are divided into three groups. Concerning the orientation of dipoles relative to the pressure axis, the first two of these groups are similar to the groups of the isolated complexes, whereas, in the third group, the pressure axis does not lie in the symmetry plane of the defect. In the case of complexes with reorientable distortions, this group of centers vanished due to the alignment. Thus, strictly speaking, the emission band of complexes with distortions that fail to reorient is split into three components at **P** ∥ [111] [9]. However, the axes of the dipoles of complexes of the third group, similarly to the axes of the dipoles of complexes of the second group, are directed closely to the ⟨111⟩ axes, which are not parallel

---

[1] This fact is caused by the proximity of the direction of the dipole axis in the centers under investigation to that of the ⟨111⟩ axes, i.e., to the dipole direction in the centers with trigonal symmetry, in which no splitting is observed for the strain direction noted.

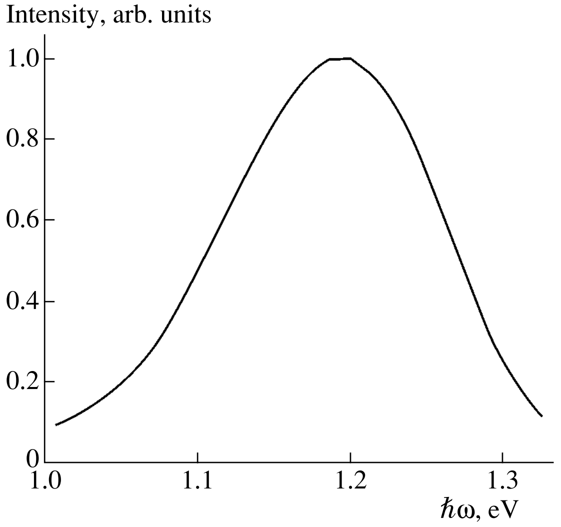

Fig. 2. Photoluminescence spectrum of $V_{Ga}Te_{As}$ complexes in the unstrained crystal n-GaAs:Te ($n \approx 10^{18}$ cm^{-3}) at 2 K.

to the pressure axis. Therefore, one might expect that the difference between the positions of their emission bands is small at **P** || [111]. In this case, the entire emission spectrum of all centers at low temperature includes virtually only two components, which coincide with the components of the emission band of isolated complexes. We previously used a similar model to describe the temperature dependence of the integrated polarization of PL for the band studied for the case of uniaxial pressure [11]. The model yielded reasonable agreement between calculations and experiment. This model corresponds to the limiting case, where it is possible to disregard the influence of Te_{As} on the vacancy state of a hole which is bounded to a complex, compared to the influence of the tetragonal distortion. Therefore, in further quantitative analysis of the PL spectra, we will also assume that the axis of the radiating dipole of the complex is directed along one of the trigonal axes of the crystal which do not coincide with the primary axis of the defect.

Let us consider the emission of defects of the two above-mentioned groups in n-GaAs at **P** || [111] and low temperature under conditions of equal probability of excitation of all centers due to their trapping of holes, which appear due to the generation of electron–hole pairs in the classical dipole approximation. In this case, it is possible to derive the following ratios for the intensities of the split components of the emission band for different directions of optical polarization:

$$\frac{I_1(\|)}{I_1(\perp)} = \frac{1-\mu_2}{\mu_2}, \tag{1}$$

$$\frac{I_2(\|)}{I_2(\perp)} = \frac{1+7\mu_2}{4+\mu_2}, \tag{2}$$

$$\frac{I_1(\|)}{I_2(\perp)} = \frac{1-\mu_2}{1+7\mu_2}\frac{9(1+2A)}{3-2A}, \tag{3}$$

$$\frac{I_1(\perp)}{I_2(\perp)} = \frac{\mu_2}{4+\mu_2}\frac{9(1+2A)}{3-2A}. \tag{4}$$

Here, A is the fraction of aligning centers and $I_i(\|)$ and $I_i(\perp)$ are the intensities of the emission with the electrical vector of the optical wave ε parallel and normal to the pressure axis, respectively. The emission is due to the ith group of complexes; the emission direction is perpendicular to the pressure axis.

3. EXPERIMENTAL RESULTS AND ANALYSIS

In order to separate the components of the PL band that split under the uniaxial pressure, we measured the PL spectra for two directions of polarization, which were mentioned in the previous section. The experiments were carried out at 2 K for the Czochralski-grown n-GaAs:Te samples with an electron density of ~10^{18} cm^{-3}, which were similar to the samples investigated by us previously [4–8, 11].

The emission spectrum of the $V_{Ga}Te_{As}$ complexes at $P = 0$ is shown in Fig. 2. No optical polarization is observed in the band, which is indicative of the equal probability of distribution of anisotropic emission centers over all possible orientations. A pressure of 10 kbar along the [111] direction caused the polarization of the band; the degree of polarization varied within the spectrum. This phenomenon manifested itself in differences in the spectral shifts, depending on the direction of the electrical vector of the optical wave of the emission detected (Fig. 3), and is indicative of the splitting of the spectrum into several components with various degrees of polarization. These components were not observed directly, and the procedure for separating them was based on the following.

1. According to the approximate model developed in Section 2, the number of split components is equal to 2.

2. The energy position of the components does not vary upon varying the orientation of the plane of polarization of the emission detected, and their spectral shapes are identical and coincide with the shape of the entire band at zero pressure (the zero spectrum). It is the latter circumstance, in particular, that allows one to substitute the ratios of the component intensities by the ratios of the peaked values of the components in relations (1)–(4).

3. Component *1*, related to the centers for which the direction of the dipole axis is close to that of the pressure axis, is shifted to lower photon energies compared with Component *2*. The reason for this is that the excited (bounding the hole) state of these centers at **P** || [111] has a lower energy; the alignment of distortions occurs due to this fact [5].

In this case, the photon energy $\hbar\omega_{\max}(\perp)$, which corresponds to the peak of the emission band with $\boldsymbol{\varepsilon} \perp \mathbf{P}$ shifted to higher energies (Fig. 2), specifies the lower limit of the position of the peak of component *2* on the energy scale. As the starting point for separating the components of the band corresponding to $\boldsymbol{\varepsilon} \parallel \mathbf{P}$, let us assume that the position of the peak of component *2* coincides with $\hbar\omega_{\max}(\perp)$ and its magnitude for $\boldsymbol{\varepsilon} \parallel \mathbf{P}$ is such that the highest energy part of the entire experimental spectrum with the polarization mentioned is completely controlled by component *2*. The difference between the entire spectrum and this component should represent component *1* (its spectral shape should also coincide with that of the zero spectrum). If the initial stage does not yield such a representation, agreement between the difference spectrum and the zero spectrum may be obtained by decreasing the magnitude of component *2* and shifting it to higher photon energies.

The possibility of describing the experimental spectrum with $\boldsymbol{\varepsilon} \perp \mathbf{P}$ by the same two components may serve as a criterion of the accuracy of component determination and the applicability of the model used. In this case, the peaks of the components determined should satisfy relations (1)–(4), which include only two parameters (μ_2 and A).

The results of such a separation of components are shown in Fig. 2. Splitting of the components at P = 10 kbar is ~38 meV, and their peak positions correspond to $\hbar\omega_1 \approx 1.192$ eV and $\hbar\omega_2 \approx 1.230$ eV. The relative magnitudes of the peaks were $I_{1\,\max}(\parallel) \approx 0.85$, $I_{2\,\max}(\parallel) \approx 0.19$, $I_{1\,\max}(\perp) \approx 0.15$, and $I_{2\,\max}(\perp) \approx 0.385$.

Using these values, we can derive $\mu_2 = 0.15$ and $A = 0.57$ from relations (1) and (3). Relations (2) and (4) yield the same values of these parameters.

4. DISCUSSION

First of all, we should note that the obtained values of μ_2 and A lie within the ranges of possible values of these parameters determined in [5, 11]. Let us estimate the error introduced by neglecting the dipole-axis deviation from the $\langle 111\rangle$ direction. Considering the emission of the centers of the first group with allowance made for this deviation, it is possible to derive the following relation (which does not include the parameter A, similarly to relation (1)):

$$\frac{I_1(\parallel)}{I_1(\perp)} = \frac{3\mu_2 + (1-2\mu_2)(2b+a)^2}{3\mu_2 + (1-2\mu_2)(b-a)^2}. \qquad (5)$$

Here, $a = \sin\varphi$ and $b = (1/\sqrt{2})\cos\varphi$ are the absolute values of the components of the unit vector of the dipole axis in the $\langle 100\rangle$ axes of the crystal. Using $\langle 100\rangle$ $\varphi = 28°40'$ [5] and substituting the above magnitudes of the component peaks from relation (5), we obtain the value of μ_2, which does not differ from the one reported in Section 3.

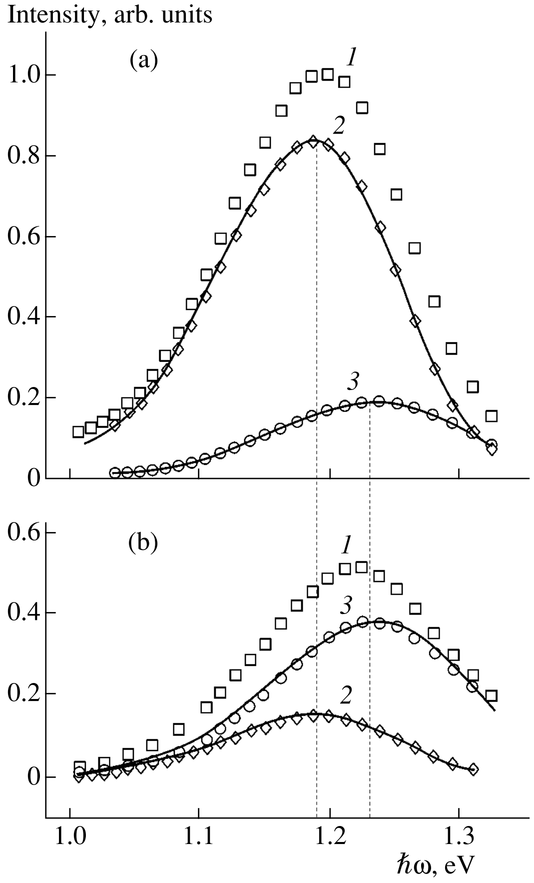

Fig. 3. Photoluminescence spectra of $V_{\mathrm{Ga}}\mathrm{Te}_{\mathrm{As}}$ complexes at a temperature of 2 K and a pressure of 10 kbar along the [111] direction. (a) $\boldsymbol{\varepsilon} \parallel \mathbf{P}$, (b) $\boldsymbol{\varepsilon} \perp \mathbf{P}$. (*1*) Experimental spectrum; curves (*2*) and (*3*) represent components *1* and *2*, whose shape coincides with the shape of the spectrum at zero pressure; diamonds (*2*) and circles (*3*) indicate the values of the emission intensities which yield the experimental values in sum and best coincide with curves *1* and *2*.

In order to calculate A talking the deviation mentioned into account let us use the expression relating this magnitude with the integrated polarization ratio of the emission band in the case of pressure along the [111] axis, which ensures the maximum possible alignment of distortions r^*_{111} [5]:

$$A = \frac{r^*_{111}-1}{r^*_{111}+2}\frac{1}{(a+b)b}\frac{1+\mu_2}{1-2\mu_2}. \qquad (6)$$

Since

$$r^*_{111} = \frac{I_{1\,\max}(\parallel) + I_{2\,\max}(\parallel)}{I_{1\,\max}(\perp) + I_{2\,\max}(\perp)}, \qquad (7)$$

it follows from the results of Section 3 that $r^*_{111} = 1.91$. In this case, according to expression (6), for the sample investigated, $A = 0.56$, which virtually coincides with the value obtained from expressions (3) or (4).

Consequently, neglecting the deviation of the dipole axis from the $\langle 111 \rangle$ direction does not lead to substantial error in determining the model parameters.

The values of μ_2 obtained is substantially lower than the value of 0.2, which is typical of dipoles characterizing the emission upon recombination of a *c*-band electron with a hole localized at an acceptor, which is in a state with a total momentum of 3/2 and its component ±1/2. Such a state is formed due to the spin–orbit interaction and the effect of the intracenter distortion (or external uniaxial pressure) if the spin–orbit interaction is dominant. If μ_2 is smaller than 0.2, but substantially differs from 0, the distortion and spin–orbit splitting of the initial vacancy t_2 state of the complex will be on the same order of magnitude; i.e., in this case, the roles of the spin–orbit and Jahn–Teller interactions in the formation of the ground state of the localized hole are comparable. According to estimates [12], in the emitting state of the complex, the Jahn–Teller splitting attains several tenths of an eV. Consequently, the spin–orbit splitting is on the same order of magnitude.

From an analysis of the data on the polarization of the band at 1.2 eV in the case of polarized resonance excitation, an empiric expression relating the relative contributions of the rotator to the absorption and emission of light by the $V_{Ga}Te_{As}$ complexes was derived [5]:

$$\mu_1 = \frac{0.91 - 3.5\mu_2}{3.5 - 5.32\mu_2}. \qquad (8)$$

Using this relation and $\mu_2 = 0.15$, we derive $\mu_1 = 0.14$.

It is also worth noting that the magnitude of splitting of the components of the emission band determined in Section 3 is in agreement with the range of possible values of the difference in activation energies of the thermal emission of holes by complexes with different orientations at the same pressure [11].

5. CONCLUSIONS

Thus, the results reported show that a model considering a set of reorientable and nonreorientable complexes with identical optical parameters and directions of the axis of the emitting dipole close to one of the $\langle 111 \rangle$ axes [5, 11] describes well the shape of the photoluminescence band of *n*-GaAs:Te, which is due to these centers, at uniaxial pressure and low temperature. In this case, the emission band can be presented with a rather high accuracy as the sum of two components, whose spectral shapes coincide with the shape of the band at zero pressure, whereas the intensities of these components are related by expressions that are valid for emitting dipoles with a trigonal axis. This means that the variations in the energies of both types of complexes with pressure are similar and depend only on the dipole direction relative to the pressure axis, whereas a slight deviation of the defects from trigonality, which should lead to the emergence of a third emission component, is insignificant.

The separation of the emission components, which belong to complexes with various orientations, along with the results of [5], made it possible to determine the optical parameters of complexes in the dipole approximation. The relative role of the spin–orbit and Jahn–Teller interactions in the formation of the ground state of the hole bounded to the $V_{Ga}Te_{As}$ complex was also estimated.

The analysis presented also demonstrates the possibility of separating components of the broad emission band of anisotropic centers under uniaxial strain by the procedure that makes use of the laws of the piezospectroscopic behavior of such defects. This method can be applied to centers with tetragonal, trigonal, orthorhombic, and monoclinic symmetries, since with the corresponding directions of strain, their emission bands split into only two components [9].

REFERENCES

1. E. W. Williams, Phys. Rev. **168**, 922 (1968).
2. F. N. Vorobkalo, K. D. Glinchuk, and A. V. Prokhorovich, Fiz. Tekh. Poluprovodn. (Leningrad) **7**, 896 (1973) [Sov. Phys. Semicond. **7**, 610 (1973)].
3. H. G. Guislain, L. De Wolf, and P. Clauws, J. Electron. Mater. **7**, 83 (1978).
4. N. S. Averkiev, A. A. Gutkin, E. B. Osipov, *et al.*, Fiz. Tekh. Poluprovodn. (St. Petersburg) **26**, 1269 (1992) [Sov. Phys. Semicond. **26**, 708 (1992)].
5. A. A. Gutkin, M. A. Reshchikov, and V. E. Sedov, Fiz. Tekh. Poluprovodn. (St. Petersburg) **34**, 1201 (2000) [Semiconductors **34**, 1151 (2000)].
6. A. Gutkin, M. Reshchikov, V. Sedov, and V. Sosnovski, Proc. Est. Acad. Sci., Phys. Math. **44**, 212 (1995).
7. A. A. Gutkin, N. S. Averkiev, M. A. Reshchikov, and V. E. Sedov, in *Proceedings of 18th International Conference on Defects in Semiconductors*, Ed. by M. Suezawa and H. Katayama-Yoshida (Sendai, 1995), Mater. Sci. Forum **196–201**, 231 (1995).
8. N. S. Averkiev, A. A. Gutkin, E. B. Osipov, *et al.*, in *Proceedings of 1st National Conference on Defects in Semiconductors*, Ed. by N. T. Bagraev (St. Petersburg, 1992), Defect Diffus. Forum **103–106**, 31 (1993).
9. A. A. Kaplyanskii, J. Phys. (Paris) **28** (8–9), 4 (1967).
10. M. V. Fok, Tr. Fiz. Inst. im. P.N. Lebedeva, Akad. Nauk SSSR **59**, 3 (1972).
11. A. A. Gutkin and M. A. Reshchikov, Fiz. Tekh. Poluprovodn. (St. Petersburg) **37**, 287 (2003) [Semiconductors **37**, 271 (2003)].
12. A. A. Gutkin, M. A. Reshchikov, and V. E. Sedov, Fiz. Tekh. Poluprovodn. (St. Petersburg) **31**, 1062 (1997) [Semiconductors **31**, 908 (1997)].

Translated by N. Korovin

Semiconductors, Vol. 37, No. 8, 2003, pp. 889–893. Translated from Fizika i Tekhnika Poluprovodnikov, Vol. 37, No. 8, 2003, pp. 917–921.
Original Russian Text Copyright © 2003 by Seregin, Stepanova, Kozhanova, Volkov.

A Mössbauer Study of Fe Impurity Atoms in Gallium Arsenide

P. P. Seregin, T. R. Stepanova, Yu. V. Kozhanova, and V. P. Volkov
St. Petersburg State Technical University, ul. Politekhnicheskaya 29, St. Petersburg, 195251 Russia

Submitted February 3, 2003; accepted for publication February 4, 2003

Abstract—Mössbauer emission spectroscopy of the ^{57}Co(^{57m}Fe) isotope was used to find the dependence of the charge state of Fe impurity atoms in GaAs on the Fermi level position in the band gap. Neutral and ionized states of impurity atoms both in the surface region (where impurity atoms form associations with lattice vacancies) and in the bulk region (where an impurity exists in the form of isolated substitutional atoms) are identified. In the bulk region of partially compensated samples, fast electron exchange between neutral and ionized acceptor Fe centers performed by holes via the valence band is revealed. © *2003 MAIK "Nauka/Interperiodica".*

1. INTRODUCTION

The behavior of Fe impurity atoms in GaAs repeatedly attracted the attention of D.N. Nasledov (see, for example, "The Properties of Gallium Arsenide Doped with Iron and Nickel" [1], which is now considered a classical study). The investigations of Fe impurity atoms in GaAs by absorption Mössbauer spectroscopy were initiated specifically by Nasledov [2, 3]. In this spectroscopic method, the material under investigation serves as an absorbent (in the case of the ^{57}Fe isotope, the material studied contains Fe atoms) and a conventional source of radiation with a single emission line is used (for ^{57}Fe, radioactive nuclei of ^{57}Co introduced into the lattice of a cubic nonmagnetic crystal serve as such a source). The main drawback of absorption spectroscopy as applied to impurity atoms is that limiting sensitivity does not exceed 10^{18} cm^{-3}. Since the Fe concentration in GaAs:Fe samples obtained by the floating-zone method amounted to ~10^{20} cm^{-3} (which significantly exceeds the solubility limit of Fe in GaAs: 2×10^{18} cm^{-3} [1]), the Mössbauer spectra were attributed to precipitates of the $FeGa_{1.3}$ type [2, 3], rather than to Fe impurity atoms. Thus, it was evident that emission Mössbauer spectroscopy of the ^{57}Co(^{57m}Fe) isotope should be used for such investigations

In emission Mössbauer spectroscopy, the sample under investigation serves as a source of gamma-ray photons (in the case of the ^{57}Fe isotope, the radioactive isotope ^{57}Co is introduced into a sample) and its radiation is analyzed using a conventional absorbent with a single absorption line (for ^{57}Fe, the absorbent $K_4Fe(CN)_6 \cdot 3H_2O$ is used most often). The sensitivity of the emission Mössbauer spectroscopy to the ^{57}Co(^{57m}Fe) isotope can be as high as 10^{13} cm^{-3}. However, one should bear in mind that the data obtained from the emission Mössbauer spectra are related to the parent atom (^{57}Co), with respect to the site of the probe atom in the lattice, and to the daughter atom (^{57m}Fe), with respect to the electronic state of the probe atom. In particular, Masterov *et al.* demonstrated the efficiency of this technique through studying Fe impurity atoms in GaP [4, 5]: neutral and ionized Fe impurity centers were identified and fast electron exchange between neutral and ionized Fe centers was revealed. However, the latter phenomenon was not observed for ^{57}Co(^{57m}Fe) impurity atoms in GaAs [5]. In addition, it is noteworthy that two regions (surface and bulk) can be distinguished in the diffusion distribution of cobalt and iron in III–V compounds; notably, the concentration of impurity atoms and vacancies is higher in the surface region [6]. Therefore, we should expect differing behaviors from Fe impurity atoms in the surface and bulk regions of a crystal. This question also remains open.

In this study, the potentials of the emission Mössbauer spectroscopy of the ^{57}Co(^{57m}Fe) isotope are used to identify neutral and ionized states of Fe impurity atoms in the surface and bulk regions of GaAs, as well as to observe fast electron exchange between neutral and ionized Fe centers in the bulk region.

2. EXPERIMENTAL

The emission Mössbauer spectra of the ^{57}Co(^{57m}Fe) isotope were measured using a commercial CM-22201 spectrometer at 295 and 78 K. As a conventional absorbent, we used $K_4Fe(CN)_6 \cdot 3H_2O$ with a surface density of 0.05 mg/cm^2 with respect to the ^{57}Fe isotope. The instrumental width of the ^{57}Fe spectral line was assumed to be equal to the width of the Mössbauer spectrum of the above absorbent with the use of the ^{57}Co source in Pd: $\Gamma = 0.26(2)$ mm/s. The GaAs samples under study doped with ^{57}Co served as sources. The isomer shifts δ of the ^{57}Co(^{57m}Fe) Mössbauer spec-

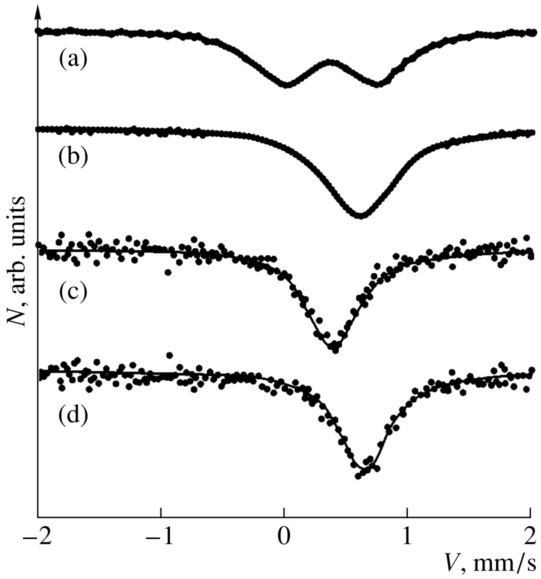

Fig. 1. Emission Mössbauer spectra of ^{57}Co(^{57m}Fe) impurity atoms in GaAs measured at 295 K in the (a, b) surface and (c, d) bulk regions of *n*- and *p*-type samples ((a, c) $p = 2 \times 10^{18}$ cm^{-3} and (b, d) $n = 2 \times 10^{18}$ cm^{-3}). The spectra are measured for samples (a) I, (b) II, (c) III, and (d) IV.

tra are reported with respect to the $K_4Fe(CN)_6 \cdot 3H_2O$ absorbent.

In order to identify neutral and ionized Fe centers, we used single-crystal samples of GaAs with *n*- and *p*-type conductivity ($p = n = 1.6 \times 10^{18}$ cm^{-3} at 295 K). Cobalt was electrolytically deposited on the sample surface from an ammonium solution of the noncarrying preparation $^{57}CoCl_2$; samples were then subjected to homogenizing in evacuated quartz cells in the presence of GaAs powder (to reduce evaporation of As) for 24 h at 1025°C. After homogenizing, the samples were treated in a mixture of HF and HNO3 to remove the remaining ^{57}Co (which failed to diffuse); a layer ~20 μm thick was also removed (the Co concentration in this layer, determined by the radioactive-tracer technique, was equal to 10^{18} cm^{-3}). This layer served as a Mössbauer source for studying the state of ^{57}Co(^{57m}Fe) impurity atoms in the surface layer (samples I and II with the concentrations of charge carriers $p = 2 \times 10^{18}$ cm^{-3} and $n = 2 \times 10^{18}$ cm^{-3}, respectively). Then, a second layer (~150 μm thick) was removed, and the rest of the sample (where the Co concentration was ~5×10^{16} cm^{-3}) served as a Mössbauer source for studying the state of ^{57}Co(^{57m}Fe) impurity atoms in the bulk region (samples III and IV with concentrations of charge carriers $p = 2 \times 10^{18}$ cm^{-3} and $n = 2 \times 10^{18}$ cm^{-3}, respectively). The conductivity type of the samples did not change after their homogenization.

In order to investigate the fast electron exchange between neutral and ionized Fe centers in the bulk region, we used a sample of single-crystal *n*-GaAs ($n = 5 \times 10^{16}$ cm^{-3} at 295 K) into which the ^{57}Co isotope was introduced according to the technique described above (the homogenizing time was equal to 5 min). The remaining ^{57}Co that failed to diffuse was removed from the sample surface; then, a layer ~40 μm thick was removed following which layers with a Co concentration of ~1.5×10^{17}, ~8×10^{16}, and ~5×10^{16} cm^{-3} (samples V, VI, VII, respectively) were successively removed to be used as Mössbauer sources.

In order to reveal the fast electron exchange between neutral and ionized Fe centers in the surface region, we prepared a Mössbauer source on the basis of single-crystal *n*-GaAs ($n = 3 \times 10^{17}$ cm^{-3} at 295 K) into which the ^{57}Co isotope was introduced according to the technique described above (the homogenizing time was equal to 24 h). The remaining ^{57}Co that failed to diffuse was removed from the sample surface; then, a layer ~20 μm thick was removed (the Co concentration in this layer was ~10^{18} cm^{-3}). This layer was used as a Mössbauer source (sample VIII).

3. RESULTS AND DISCUSSION

As was noted above, due to the low solubility of Fe in GaAs, only emission Mössbauer spectroscopy can be used to study the state of Fe impurity atoms. In this method, the radioactive isotope ^{57}Co is introduced into GaAs by diffusion doping. After the decay of ^{57}Co, the ^{57m}Fe isotope appears, which serves as a Mössbauer probe. When analyzing experimental results, one should bear in mind that $N_{Co} \gg N_{Fe}$ (N_{Co} and N_{Fe} are the concentrations of Co and Fe impurity in GaAs, respectively); hence, the position of the Fermi level in the band gap is governed by the concentrations of Co impurity atoms and dopant atoms, as well as by the type of their electric activity (Zn and Te are used as dopants to fabricate *p*- and *n*-type GaAs, respectively).

According to the electrical measurements, Fe and Co impurity atoms form deep acceptor levels in the band gap of GaAs, which lie at 0.59(2) and 0.54(3) eV above the valence-band top [7]. Therefore, only neutral iron centers $[Fe]^0$ should contribute to the spectra of *p*-type samples (where the Fermi level is near the valence-band top), and only ionized iron centers $[Fe]^-$ should be observed in *n*-type samples (where $N_{Te} > N_{Co}$ and the Fermi level lies near the conduction-band bottom; N_{Te} is the concentration of donors).

As can be seen from Fig. 1, the fine structure of the Mössbauer spectra depends both on the conductivity type of an initial sample and on the location of ^{57}Co(^{57m}Fe) impurity atoms (either at the surface or in the bulk region). The Mössbauer spectrum of ^{57}Co(^{57m}Fe) impurity atoms in the surface region of the *p*-type sample *I* consists in a quadrupole doublet ($\delta = 0.45(2)$ mm/s, the quadrupole splitting $E_Q = 0.95(3)$ mm/s, the width of the components of the quadrupole doublet $\Gamma = 0.55(3)$ mm/s; spectrum I, Fig. 1a);

by contrast, for the *n*-type sample II ($N_{Te} > N_{Co}$), the spectrum involves a single broadened line (δ = 0.60(2) mm/s, E_Q = 0.20(3) mm/s, Γ = 0.56(2) mm/s; spectrum II, Fig. 1b). The parameters of spectra I and II depend only slightly on the measurement temperature (295 or 78 K). The presence of quadrupole splitting in spectrum I is indicative of the formation of Co atom–vacancy associations in the surface region; notably, after the radioactive decay of ^{57}Co, the daughter ^{57m}Fe atoms remain in such associations. The isomeric shift of spectrum I corresponds to the trivalent state of iron ^{57m}Fe^{3+} with the electronic configuration 3d^5. Therefore, the parent Co atoms incorporated in these associations are in the trivalent state ^{57}Co^{3+}. The dependence of the isomeric shift of the spectra of Fe impurity atoms in the surface region on the conductivity type of samples is indicative of electrical activity of the aforementioned associations. In the *p*-type sample I, the associations are in the neutral state, and they contain ^{57}Co^{3+}(^{57m}Fe^{3+}) ions with incomplete systems of tetrahedral bonds, which leads to a large quadrupole splitting of the Mössbauer spectrum I. In the *n*-type sample II, the associations under consideration are ionized and they contain the ^{57}Co^{2+}(^{57m}Fe^{2+}) ions with complete systems of tetrahedral bonds. As a result, the quadrupole splitting of spectrum II is significantly smaller than that of spectrum I.

The Mössbauer spectra of ^{57}Co(^{57m}Fe) impurity atoms in the bulk regions of the *p*-type sample III (spectrum III, Fig. 1c) and the *n*-type sample IV (spectrum IV, Fig. 1d) consist of single, somewhat broadened lines (Γ = 0.50(2) mm/s) with different isomeric shifts: the smallest shift is observed for the *p*-type sample (δ = 0.38(2) mm/s), and the largest shift is observed for the *n*-type sample (δ = 0.63(2) mm/s). The parameters of the spectra depend weakly on the measurement temperature. Evidently, spectrum III should be attributed to isolated neutral acceptor iron centers [^{57m}Fe]^0 that formed after the radioactive decay of isolated neutral-acceptor cobalt centers [^{57}Co]^0 (the isomeric shift δ_n) and spectrum IV should be attributed to isolated ionized-acceptor iron centers [^{57m}Fe]$^-$ that formed after the radioactive decay of isolated ionized-acceptor cobalt centers [^{57}Co]$^-$ (the isomeric shift δ_i). The value of δ_n is typical of isomeric shifts in the Mössbauer spectra of compounds containing trivalent iron with the electronic configuration 3d^5. Such a conclusion is in agreement with the results of studying GaAs:Fe by the ESR method [8].

The increase in the isomeric shift of the ^{57}Co(^{57m}Fe) Mössbauer spectra upon passage from the [^{57m}Fe]^0 centers to the [57mFe]$^-$ centers indicates that the electron density at the ^{57m}Fe nuclei decreases. Apparently, the ionization of the [^{57m}Fe]^0 center is accompanied with an increase in the population of the 3*d* shell of the iron atom. For quantitative estimation of the variation in the isomeric shift, the following relation should be used:

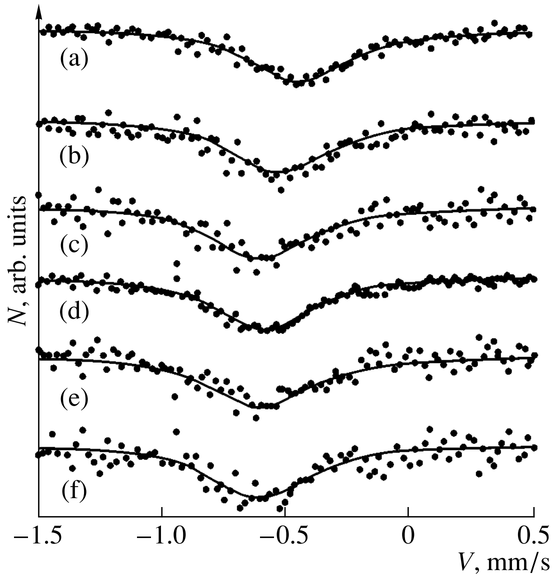

Fig. 2. Emission Mössbauer spectra of ^{57}Co(^{57m}Fe) impurity atoms in the bulk region of GaAs measured at (a–c) 295 and (d–f) 78 K. The Co concentration is (a, b) 1.5×10^{17}; (b, e) 8×10^{16}; and (c, f) 5×10^{16} cm^{-3}. The spectra are measured for samples (a, d) V; (b, e) VI; and (c, f) VII.

$$\Delta = \delta_n - \delta_i = \alpha(|\Psi_n(0)|^2 - |\Psi_i(0)|^2). \qquad (1)$$

Here, α is the calibration constant ($\alpha = 0.23a_0^{-3}$ mm/s [9]); $|\Psi_n(0)|^2$ and $|\Psi_i(0)|^2$ are the electron densities at the nuclei of the centers [^{57m}Fe]^0 and [^{57m}Fe]$^-$, respectively (they were calculated in [10]); and a_0 is the Bohr radius.

If the centers [^{57m}Fe]^0 and [^{57m}Fe]$^-$ have electronic configurations 3d^5 and 3d^6, respectively, the theoretical value of Δ_{theor} = 0.58 mm/s. This value differs significantly from the experimental value of Δ_{exptl} = 0.25(2) mm/s. The differences between the measured and calculated values of Δ are attributed to the fact that the nonzero population of the 4*s* orbital of the Fe atom, which changes upon passing from the [^{57m}Fe]^0 center to the [^{57m}Fe]$^-$ center, is disregarded in the calculations.

The Mössbauer spectra of ^{57}Co(^{57m}Fe) impurity atoms in the bulk region of partially compensated samples V, VI, and VII (spectra V, VI, VII in Figs. 2a, 2b, 2c, respectively) at room temperature consist of individual, somewhat broadened lines (Γ = 0.50(2) mm/s) whose isomeric shifts steadily vary with increasing degree of compensation (0.50(2), 0.56(2), 0.63(2) mm/s for spectra V, VI, VII, respectively). However, at 78 K, the isomeric shifts of the spectra of these samples turned out to be identical (0.62–0.63 mm/s) and to correspond to ionized centers [^{57m}Fe]$^-$ (see Figs. 2d, 2e, 2f).

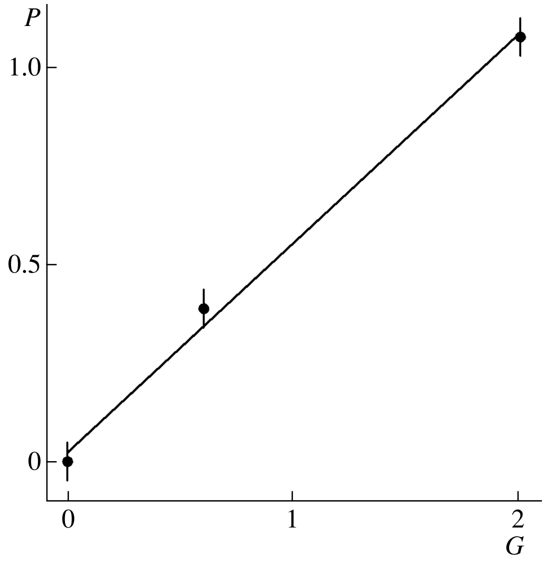

Fig. 3. Dependence of $P = N_n/N_i$ on $G = (N_{Co} - N_{Te})/N_{Te}$ (here N_{Co}, N_{Te}, N_n, and N_i are the concentrations of Co atoms, Te atoms, neutral Fe centers, and ionized Fe centers, respectively). The straight line corresponds to the value of $(\beta_{Co}/\beta_{Fe})\exp[(E_{Fe} - E_{Co})/kT] = 0.53(3)$.

In order to explain the features in spectra V, VI, and VII, we should take into account that, when the condition $N_{Co} > N_{Te}$ is satisfied, the Fermi level is related to the level of the Co atom with the energy E_{Co} as follows:

$$\mu = E_{Co} - kT\ln\beta_{Co}G. \quad (2)$$

Here, β_{Co} is the degeneracy factor of the Co-atom level; $G = (N_{Co} - N_{Te} - p + n)/(N_{Te} + p - n) \approx (N_{Co} - N_{Te})/N_{Te}$; and n and p are the electron and hole densities, respectively.

Hence,

$$P = N_n/N_i = G[\beta_{Co}/\beta_{Fe}]\exp[(E_{Fe} - E_{Co})/kT], \quad (3)$$

where N_n and N_i are the concentrations of neutral and ionized iron centers, respectively; β_{Fe} is the degeneracy factor of the Fe-atom level; and E_{Fe} is the energy of the Fe-atom level.

Thus, if the values of E_{Fe} and E_{Co} are rather close to each other one can satisfy the condition $P \approx 1$ by varying the concentrations of cobalt (N_{Co}) and tellurium (N_{Te}). In this case, the fine structure of the emission Mössbauer spectra will depend on the relation between the lifetime of the Mössbauer level of the ^{57m}Fe isotope ($\tau_0 \approx 10^{-7}$ s) and the time τ of electron exchange between $[^{57m}Fe]^0$ and $[^{57m}Fe]^-$ centers.

If $\tau \ll \tau_0$, a single line with the isomeric shift

$$\delta = (\delta_i + P\delta_n)/(P + 1), \quad (4)$$

will be observed in the Mössbauer spectrum. This line is related to some averaged state of iron, which appears due to the fast electron exchange between $[^{57m}Fe]^0$ and $[^{57m}Fe]^-$ centers.

If $\tau \gg \tau_0$, then, under the condition that parent Co atoms be electrically active, a single line (related to neutral $[^{57m}Fe]^0$ centers) will be observed in the Mössbauer spectrum, whereas, under the condition that Co atoms be electrically inactive, two lines (related to the neutral $[^{57m}Fe]^0$ and ionized $[^{57m}Fe]^-$ centers) will be observed.

Evidently, spectra V, VI, and VII are indicative of fast electron exchange between neutral and ionized iron centers in the bulk region of the material; this exchange arises when the Fermi level μ is located near the energy level of the iron atom E_{Fe}. Samples III, IV, and V satisfy the condition $P \approx 1$. Indeed, since the Te concentration in all of these samples was 5×10^{16} cm^{-3}, the value of G for these samples ranged from 2 to 0 and the Fermi level shifted from the midgap (at $G = 0$) to the position a few kT below the level E_{Co} (at $G = 2$). Figure 3 shows the calculated dependence $P(G)$, which corresponds to the value of $(\beta_{Co}/\beta_{Fe})\exp[(E_{Fe} - E_{Co})/kT] = 0.53(3)$. Assuming that $\beta_{Co}/\beta_{Fe} \approx 1$ (since this value cannot differ greatly from unity), we obtain $E_{Fe} = E_{Co} - 0.016(3)$ eV. This value is consistent with the data of [7].

Thus, fast ($\tau \ll \tau_0$) electron exchange between the neutral and ionized acceptor iron centers in the bulk region of partially compensated GaAs is ascertained. This exchange occurs via the trapping of a hole by a $[^{57m}Fe]^-$ center with subsequent transfer of the trapped hole to the valence band. For this process, the lifetime of the ionized $[^{57m}Fe]^-$ center τ_i is governed by the rate of trapping of a hole by this center

$$\tau_i = 1/p\sigma V, \quad (5)$$

where p is the hole density, V is the thermal velocity of holes, and σ is the cross section of trapping of a hole by a $[Fe]^-$ center.

According to the Hall measurements, for the samples under investigation, $p = 10^{15}$ cm^{-3}; thus using $V = 10^7$ cm/s and, $\sigma = 10^{-13}$ cm^2 (the lower limit for the cross section of the trapping of a hole by a Coulomb center), we obtain $\tau_n = \tau_i = 10^{-9}$ s (here, τ_n is the lifetime of the $[^{57m}Fe]^0$ center); i.e., during the time interval τ_0, more than 10^2 events of recharging of iron centers occur, and some averaged state of the impurity iron centers is observed in the Mössbauer spectrum.

We can try to reduce the electron-exchange rate by decreasing the measurement temperature. However, at 78 K, the spectra of samples V, VI, and VII are related to centers $[^{57m}Fe]^-$ (see Fig. 2). This fact indicates a temperature shift of the Fermi level rather than deceleration of the electron exchange (in the latter case, only the state of $[^{57m}Fe]^0$ would manifest itself in the emission Mössbauer spectrum).

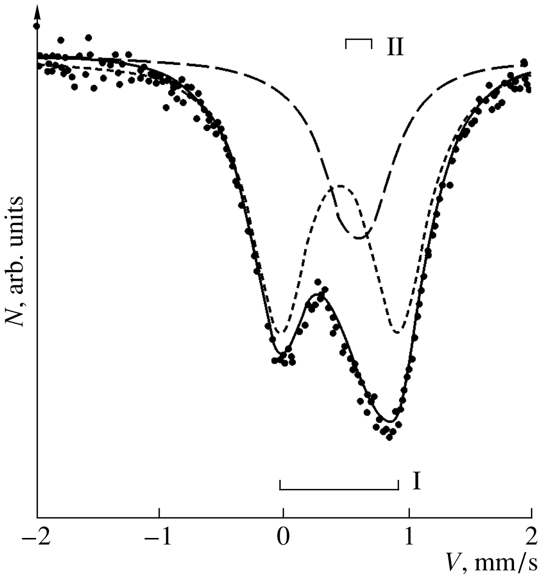

Fig. 4. Emission Mössbauer spectrum of ^{57}Co(^{57m}Fe) impurity atoms in the surface region of *n*-type GaAs (sample VIII, $n = 3 \times 10^{17}$ cm^{-3}, the measurement temperature is 295 K). The positions of the quadrupole doublets corresponding to spectra I and II for samples I and II are indicated.

We have also tried to reveal the electron exchange between neutral and ionized iron centers in the surface region of partially compensated GaAs (sample VIII). However, as can be seen from Fig. 4, the Mössbauer spectrum of this sample at 295 K (spectrum VIII, Fig. 4) represents a superposition of spectra of type I (related to ^{57m}Fe^{3+} ions incorporated in associations with vacancies) and type II (related to ^{57m}Fe^{2+} ions incorporated in associations with vacancies).

In order to explain the features of spectrum VIII, we should take into account that trapping of electrons by the ^{57}Co center is accompanied by emission of Auger electrons and the Fe atom turns out to be multiply ionized: ^{57m}Fe^{n+} ($n \approx 7$). Such an ion is an effective trapping center for Auger electrons (the maximum energy of Auger electrons does not exceed 100 eV, which corresponds to the average free path $\lambda_0 \approx 20$ Å). Notably, neutralization of the ^{57m}Fe^{n+} ion into the stable valence states occurs over ~10^{-12} s. However, the type of state of the daughter atom (^{57m}Fe^{2+} or ^{57m}Fe^{3+}) depends both on the nature of the electrical activity of the iron center and on the concentration of electron-trapping centers in the lattice. Taking into account that both states of iron manifest themselves in spectrum VIII, we may conclude that this spectrum demonstrates the nonequilibrium situation ($\tau \gg \tau_0$), which arises during the neutralization of ^{57m}Fe^{n+} ions in the GaAs lattice, and that the contribution of ^{57m}Fe^{3+} ions to spectrum VIII is controlled by the fraction of ^{57}Co^{3+} ions that have electron-trapping centers in the nearest neighborhood (within the distance λ_0), whereas ^{57}Co^{2+} ions have no electron-trapping centers in the neighborhood within the distance λ_0.

4. CONCLUSIONS

The emission Mössbauer spectroscopy of the ^{57}Co(^{57m}Fe) isotope was used to show that Fe impurity centers in the surface and bulk regions of single-crystal GaAs have different local structures. In the surface region, where the impurity concentration is about 10^{18} cm^{-3}, Fe centers form associations with lattice vacancies, whereas, in the bulk region, where the impurity concentration does not exceed 5×10^{16} cm^{-3}, they exist in the form of isolated substitutional impurity atoms. It is shown that the charge state of Fe impurity atoms in GaAs depends on the position of the Fermi level in the band gap. The neutral and ionized acceptor states of impurity atoms both in the surface and bulk regions of the material are identified: in the *p*- and *n*-type materials, iron atoms are stabilized with the electronic configurations $3d^5$ and $3d^6$, respectively. In partially compensated samples of GaAs, fast electron exchange between neutral and ionized acceptor iron centers is revealed in the bulk region in the temperature range of 78–295 K; this exchange is carried out by holes via the valence band.

REFERENCES

1. N. M. Kolchanova, D. N. Nasledov, and G. N. Talalakin, Fiz. Tekh. Poluprovodn. (Leningrad) **4**, 134 (1970) [Sov. Phys. Semicond. **4**, 106 (1970)].
2. G. B. Il'menkov, I. F. Mironov, D. N. Nasledov, *et al.*, Fiz. Tverd. Tela (Leningrad) **13**, 1407 (1971) [Sov. Phys. Solid State **13**, 1176 (1971)].
3. V. K. Isaev-Ivanov, V. F. Masterov, D. N. Nasledov, and V. K. Yarmarkin, Fiz. Tverd. Tela (Leningrad) **16**, 2068 (1974) [Sov. Phys. Solid State **16**, 1342 (1974)].
4. V. F. Masterov, F. S. Nasredinov, S. A. Nemov, and P. P. Seregin, Fiz. Tekh. Poluprovodn. (St. Petersburg) **30**, 840 (1996) [Semiconductors **30**, 450 (1996)].
5. V. F. Masterov, F. S. Nasredinov, S. A. Nemov, and P. P. Seregin, Fiz. Tekh. Poluprovodn. (St. Petersburg) **30**, 884 (1996) [Semiconductors **30**, 472 (1996)].
6. A. I. Blashku, Candidate's Dissertation (Polytechnical Inst., Chisinau, 1973).
7. V. I. Fistul' and A. M. Ageev, Fiz. Tverd. Tela (Leningrad) **7**, 3681 (1965) [Sov. Phys. Solid State **7**, 2975 (1965)].
8. M. de Wit and T. L. Estle, Phys. Rev. **132**, 195 (1963).
9. K. T. Duff, Phys. Rev. B **9**, 66 (1974).
10. J. Blomquist, J. Chem. Phys. **55**, 141 (1971).

Translated by Yu. Sin'kov

Semiconductors, Vol. 37, No. 8, 2003, pp. 894–914. Translated from Fizika i Tekhnika Poluprovodnikov, Vol. 37, No. 8, 2003, pp. 922–940.

ELECTRONIC AND OPTICAL PROPERTIES OF SEMICONDUCTORS

Rare-Earth Elements in the Technology of III–V Compounds and Devices Based on These Compounds

A. T. Gorelenok*, A. V. Kamanin, and N. M. Shmidt
Ioffe Physicotechnical Institute, Russian Academy of Sciences,
Politekhnicheskaya ul. 26, St. Petersburg, 194021 Russia
**e-mail: algor@mail.ioffe.ru*

Submitted February 3, 2003; accepted for publication February 4, 2003

Abstract—The results of our studies concerned with the use of rare-earth elements in the liquid-phase epitaxial technology of the InP, InGaAsP, InGaAs, and GaP compounds and with the fabrication of various optoelectronic and microelectronic devices and structures based on these compounds are summarized. The results related to the surface gettering of GaAs with the films of rare-earth elements in order to obtain a high-resistivity material for various purposes are also reported. *© 2003 MAIK “Nauka/Interperiodica”.*

1. INTRODUCTION

The use of rare-earth elements (REEs) (lanthanides) in the technology of semiconducting materials was reported for the first time in 1964 [1]. Mandelkorn *et al.* [1] used doping with REEs to enhance the radiation resistance of silicon solar cells. It was shown in subsequent publications that REEs behave in silicon similarly to Group III elements and are acceptors. In addition, it was shown [2] that doping of silicon with REEs leads to a decrease in the carbon concentration by a factor of about 10–30, whereas doping of germanium with REEs [3] reduces the oxygen concentration.

Using REEs in III–V compounds was suggested for the first time in Nasledov’s laboratory at the Ioffe Physicotechnical Institute in 1967; Pyshkin *et al.* [4] introduced lanthanides into GaP crystals grown from a solution–melt in attempts to reduce the background impurity concentration in these crystals. However, high REE concentrations in the liquid phase were apparently used [4], so that the gettering effect was not observed; the GaP crystals had *p*-type conductivity with a rather high concentration of holes.

Intensive studies related to the use of REEs in the technology of III–V compounds were started in the 1980s and encompassed the growth of both bulk single crystals [5] and epitaxial layers [6]. Two fields of REE applications were recognized almost at once.

The first field is related to the introduction of high concentrations (10^{17}–10^{20} cm^{-3}) of REE impurities into single crystals of III–V compounds. In this case, REEs behave as isovalent impurities and replace Group III elements in the crystal lattice. The presence of REEs in the host of III–V compounds gives rise to intracenter luminescence in the spectral regions of 1.0 and 1.54 μm [7–12]. Recently, this effect has been actively studied also in a silicon host with the aim of developing emitters in the infrared region of the spectrum.

The second field of applications is related to the introduction of small amounts of REEs into the solution–melt in growing both bulk crystals [5] and epitaxial layers [6]. In this case, REEs act as getters of background impurities and ensure purification of the growing single crystal or epitaxial layer.

The phenomenon of purification of III–V compounds (by the example of InP and InGaAs) as a result of doping solutions–melts with La or Mg was reported for the first time by Factor and Haigh [13]. The InP and InGaAs compounds with an electron concentration $n = 10^{16}$ and $n = 10^{15}$ cm^{-3}, respectively, were obtained; however, the data on the mobility were not reported since it was apparently low [13]. It was noted [13] that the material is purified mainly owing to the effect of Group III impurities, as a result of formation of high-melting chalcogenides, which precipitate as slags in the liquid phase and do not enter into the solid phase.

The phenomenon of profound purification of InP and InGaAs solid solutions (which are lattice-matched to InP) in the course of liquid-phase epitaxy (LPE) as a result of doping with REEs was reported by us for the first time in 1983 [14, 15]. The electron concentration in the layers was reduced to ~10^{13} cm^{-3}; the electron mobility was as high as 6.5×10^4 cm^2 V^{-1} s^{-1} in InP and 10^5 cm^2 V^{-1} s^{-1} in InGaAs at 77 K. Later on, these results were reproduced by Körber *et al.* [16].

In what follows, we will summarize the results of studying the behavior of REEs in the liquid and solid phases during LPE, the electrical properties of undoped and doped materials, the luminescent properties of undoped material and its photoexcitation spectra, the properties of structures with two-dimensional electron gas, metal–insulator–semiconductor (MIS) structures, Schottky barriers, photoresistors, *p*–*i*–*n* photodiodes, field-effect transistors (both vertical and with the Schottky gate), light-emitting diodes based on GaP, and the Gunn diodes; we will also report the data on surface gettering in GaAs using REE films.

2. EXPERIMENTAL

Epitaxial InP, InGaAsP, InGaAs, and GaP layers, as well as structures based on these compounds, were grown by LPE on InP:Fe, InP:Sn, and GaP:Sn substrates with (100) orientation in an atmosphere of purified hydrogen (with the amount of impurities less than 0.01 ppm) in graphite sliding boats. The REE charges (Y, Nd, Gd, Ho, Yb, and such) were put into a boat along with In and Ga. The REE charges were 99.9% pure, while the Ga and In charges were 99.999 and 99.9999% pure, respectively. The REE content in the liquid phase was varied from 0.001 to 0.1 at. %. Epitaxial growth of InP and InGaAs(P) was performed at 645°C, and that of GaP, at 860°C; the temperature of supersaturation of the solution–melt with respect to phosphorus was $\Delta T \approx 5$ K; and the cooling rate of the system was ~0.5 K/min. We used Si, Ge, Sn, S, Se, and Te as donors and Mg and Cd as acceptors.

The initial material for the surface gettering was GaAs grown by the Czochralski method [17] using Ga and As of 99.99999% purity. This GaAs compound had an electron concentration of $n = (1\text{–}3) \times 10^{15}$ cm^{-3} and a mobility of 1500–2000 cm^2 V^{-1} s^{-1} at 300 K; the orientation of the wafers was (111), and the thickness was 1.6 mm. The GaAs wafers were coated with Y film from one or both sides using vacuum thermal deposition; the Y film thickness was ~1000 Å. The wafers were then subjected to heat treatment for 0.25–0.5 h at temperatures of 700 or 800°C in the atmosphere of pure hydrogen. The Y films were removed by plasma etching after the heat treatment [18].

In order to determine the concentration and mobility of charge carriers, we used the conventional method of Hall effect measurements. X-ray diffraction studies were performed using a double-crystal spectrometer, and the carrier-concentration profiles were measured using an electrolytic *C*–*V* profilometer [18]. The content of REE atoms was assessed quantitatively using an IMS-4F ion microanalyzer. The luminescence and photoexcitation spectra were also measured using conventional methods.

3. SPECIAL FEATURES OF REE BEHAVIOR IN THE CASE OF LIQUID-PHASE EPITAXY OF INP AND INGAAS(P)

We found in our first experiments with LPE InP growth from solutions–melts doped with REEs that the addition of an REE to the solution–melt increases the In solubility [6]. The influence of the REE concentration in solutions–melts on the solubility of InP in In or in In–Ga–As was studied using the loss of weight of the InP substrate. Figure 1 shows the dependences of phosphorus solubility on the composition of the liquid phase in the solutions–melts, with these compositions ensuring the formation of InGaAsP solid solutions with corresponding values of λ_g for various concentrations of Ho in the solutions–melts; here, λ_g is the wavelength corresponding to the band gap E_g of the solid solution.

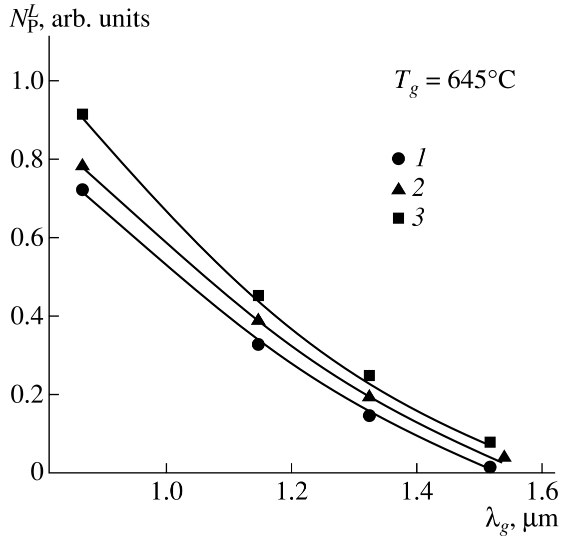

Fig. 1. Solubility of phosphorus (N_P^L) in liquid phases of a solid solution of various compositions corresponding to different values of λ_g for an Ho content equal to (*1*) 0, (*2*) 0.01, and (*3*) 0.1 at. %; T_g is the growth temperature.

It can be seen from Fig. 1 that, as the content of phosphorus and holmium increases in solutions–melts, the solubility of InP in the melts increases. This fact can be attributed to formation and precipitation of high-melting compounds of P with Ho (HoP) as a slag in the solution–melt. The resulting deficit of phosphorus in the solution–melt is compensated by dissolution of the substrate; thus, equilibrium is established the system consisting of In–P(In–Ga–As–P) (liquid) and InP substrate. Such an explanation is consistent with the fact that the enthalpy of InP formation is much lower than the enthalpy of formation for compounds consisting of Group V elements and REEs [19].

In Fig. 2, we show the dependence of supersaturation of the solution–melt with respect to phosphorus on the Ho content in the In-P and In-Ga-As-P liquid solutions corresponding to $\lambda_g = 1.55$ µm. It can be seen that this effect becomes less pronounced as the content of phosphorus in the melt decreases. It is noteworthy that this fact should be taken into account when growing multilayered structures in order to avoid etching of the previous layer while growing the next layer. Almost similar dependences were obtained when the solutions–melts were doped with other REEs, in particular, with Yb, Gd, and Dy.

The following situation is observed in the solid phase. If the REE content in the liquid phase N_{REE}^L varies in the range of 0–0.005 at. %, epitaxial InP layers are,

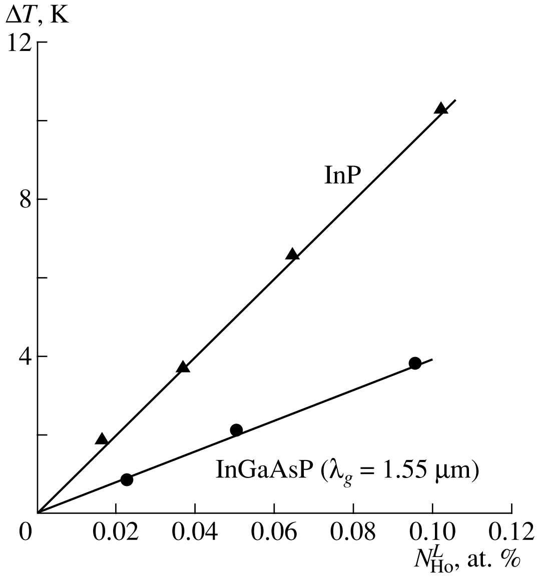

Fig. 2. Dependence of the degree of supersaturation of the solution–melt ΔT with respect to phosphorus on the Ho content in the liquid phase ($N^L_{\rm Ho}$) for InP and InGaAsP.

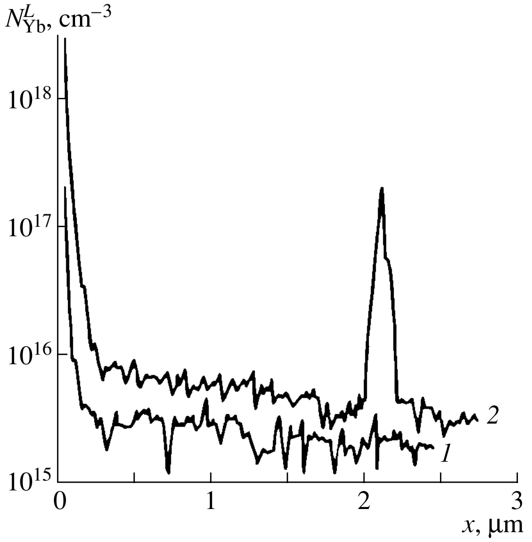

Fig. 3. The SIMS profiles of Yb in epitaxial InP layers at an Yb content in the liquid phase equal to (*1*) 0.001 and (*2*) 0.01 at. %.

as a rule, homogeneous over the depth and area. In contrast, inclusions of the second phase [20] are formed if $N^L_{\rm REE} \gtrsim 0.005$ at. %; these inclusions consist of compounds involving phosphorus, oxygen, elements of Group I, and REE. A sharp increase in the density of inclusions (to 10^4 cm^{-2}) is observed for $N^L_{\rm REE} \gtrsim 0.01$ at. %. The sizes of inclusions range from 5 to 200 μm, depending on $N^L_{\rm REE}$.

A quantitative estimate of the concentration of Yb atoms in epitaxial InP layers was obtained by secondary-ion mass spectrometry (SIMS) using an IMS-3F (CAMECA) mass spectrometer; the results are shown in Fig. 3. It can be seen that the concentration profile is almost flat at low concentrations of Yb in the liquid phase (curve *1*). By contrast, a peak in the Yb concentration is observed near the layer–substrate interface at $N^L_{\rm Yb}$ = 0.01 at. % (curve *2*); this peak is possibly related to either an inclusion of the second phase or the commonly observed buildup of impurities at the interface. An increase in the Yb concentration near the layer surface is related to error in the SIMS method [21]. It can be seen from Fig. 3 that the concentration of Yb atoms in homogeneous samples does not exceed the method's sensitivity, which amounts to (2–4) × 10^{15} cm^{-3}. Estimation of the distribution coefficient for Yb in GaAs according to the data represented in Fig. 3 shows that this coefficient is no larger than 10^{-4}, which differs from the values of (4–8) × 10^{-2} obtained previously for Dy, Gd, and Sm in GaAs [22].

Studies of the influence of $N^L_{\rm Dy}$ on the mismatch between the lattice parameters of the layer and InP substrate (Fig. 4) showed that the lattice parameter of the layer did not change when the Dy content introduced into the liquid phase was in the range of $N^L_{\rm Dy}$ = 0–0.015 at. %. This fact can also indicate that the concentration of REE atoms in the solid phase is low (at a level of ~10^{13} cm^{-3}). Studies of Raman scattering in InP doped with REEs are also indicative of the absence of lattice distortions [23].

4. MECHANISM OF PURIFICATION OF INP AND INGAAS(P) EPITAXIAL LAYERS AS A RESULT OF DOPING WITH RARE-EARTH ELEMENTS

Typically, the REE atoms in InP replace In atoms in the course of LPE and behave as isoelectronic impurities [9], so that the effects of doping with REEs generally amounts to purification of the material. Our studies concerned with the doping of InP and InGaAs(P) with various REEs in the course of LPE showed that, as the concentration of REE atoms in the liquid phase increases [6], the charge-carrier concentration (equal to N_D–N_A) first decreases (Fig. 5) and then the conductivity-type inversion takes place. A large spread in REE concentrations corresponding to the conductivity-type inversion is related to the dissimilar reactivity of different REEs and their purity, the purity both of initial components of the solution–melt (varying donor and acceptor background) and of graphite boats, and the dew point of hydrogen.

In order to clarify the mechanism of interaction between REEs and background impurities, we performed experiments with joint doping of the solution–

melt with REEs and donors of Groups IV (Si, Ge, Sn) and VI (S, Te, Se) [24] and acceptors of Group II (Mg, Cd) [6]. The concentration of donors introduced into the liquid phase was such that the electron concentration in the layers was ~5×10^{18} cm^{-3}, which exceeds the typical background concentration by at least an order of magnitude. Following doping with donors, various amounts of Dy were added to the solution–melt.

The results of the aforementioned studies are illustrated in Fig. 6, where the relative electron concentration in the layers is shown as a function of the Dy content in the solution–melt. The concentration n_0 in the layers that were not doped with REEs was used as the normalization parameter. It can be seen from Fig. 6 that the concentration of electrons (and, consequently, of donors) in the layers doped with elements of Group IV depends only slightly on the amount of Dy added to the solution–melt. By contrast, the donor concentration in the solid phase decreases appreciably (by an order of magnitude and more) as a result of addition of Dy to the solution–melt doped with donor elements of Group VI. This decrease is more pronounced if the atomic weight of the donor is lower and the donor's reactivity is higher. In our opinion, the reported experimental data indicate that a chemical reaction of donors with REEs occurs in the solution–melt after addition of REEs; chalcogenides of REEs are mainly formed as a result of this reaction. The well-known fact that doping with REEs gives rise to oxygen drain is consistent with the above model [25]. In fact, oxygen belongs to Group VI and has the lowest atomic weight among the elements of this Group. Therefore, the addition of an REE to the solution–melt brings about the intense bonding of oxygen, which prevents oxygen from entering into the solid phase.

In Fig. 6, crosses represent the dependence of the electron concentration on the Dy content in InP:Dy layers without additional introduction of donors into the solution–melt. It can be seen that this dependence coincides with the curve obtained for the samples which were additionally doped with sulfur. This fact suggests that sulfur and oxygen are the main background impurities in the InP layer under investigation and is consistent with the results of our studies of the photoexcitation spectra of shallow-level donors [26].

The results obtained in experiments with the doping of InGaAsP with Yb + Mg and Yb + Cd are listed in Table 1. It can be seen that, in contrast to the combined doping with donors and REEs, doping with both acceptors and REEs brings about an increase in the charge-carrier concentration rather than a decrease. This fact indicates that REEs virtually do not react with Cd and Mg in the liquid phase, in contrast to REE reactivity with the donors of Group IV. An increase in the hole concentration in the layers in the case of doping with both acceptors and REEs is apparently caused by the deoxidation of acceptors by REEs, which leads to an increase in the acceptor concentration in the liquid phase according to the reactions

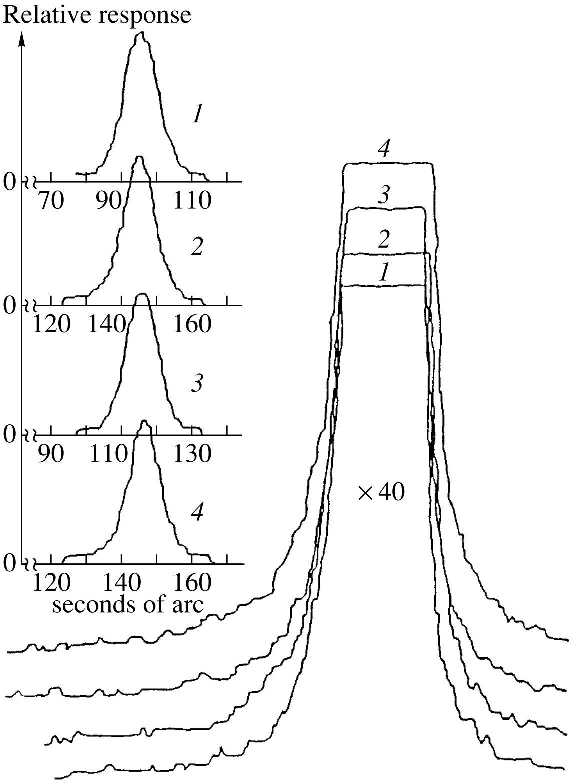

Fig. 4. Diffraction patterns for InP layers with N^L_{Dy} concentrations amounting to (*1*) 0, (*2*) 0.007, (*3*) 0.01, and (*4*) 0.015 at. %.

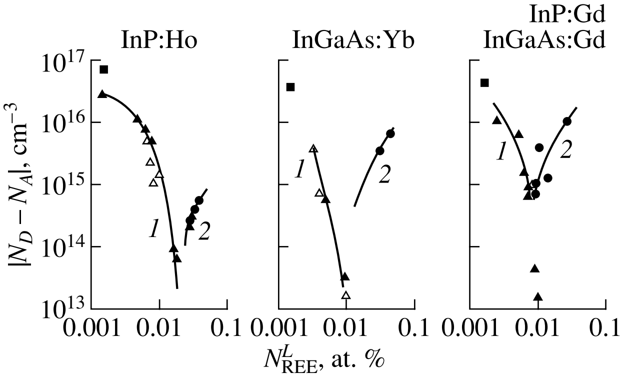

Fig. 5. The net $N_D - N_A$ concentration in epitaxial layers as a function of REE content in the liquid phase (N^L_{REE}) for (*1*) *n*- and (*2*) *p*-type layers. The filled square represents the background concentration.

$$3MgO + 2Yb = Yb_2O_3 + 3Mg,$$

$$3CdO + 2Yb = Yb_2O_3 + 3Cd$$

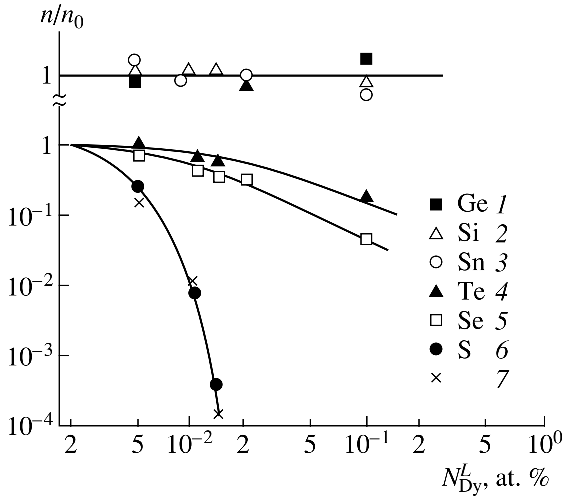

Fig. 6. Dependences of relative electron concentration in InP epitaxial layers doped with elements of Group IV ((*1*) Ge, (*2*) Si, and (*3*) Sn) and Group VI ((*4*) Te, (*5*) Se, and (*6*) S) elements on the Dy content in the liquid phase; the curve represented by crosses corresponds to doping of the liquid phase only with Dy.

and, correspondingly, to an increase in the hole concentration. This phenomenon can be used advantageously in the formation of contact layers in device structures.

Taking the above into account, we may conclude that the mechanism of purification of a material as a result of doping the solution–melt with REEs consists in the interaction of REEs mainly with elements of Group VI via the formation of high-melting chalcogenide compounds which precipitate in the liquid phase and do not enter into the solid phase; this phenomenon results in a reduction of the donor-concentration background by several orders of magnitude. In the situation where the concentration of background donors in the layers becomes lower than the concentration of background acceptors, conductivity-type inversion occurs (Fig. 5). In this case, the REE concentration in the solid phase is no higher than 10^{15} cm^{-3} (Fig. 3) and does not give rise to distortion of the crystal lattice (Fig. 4).

We note in the conclusion of this section that, since the acceptor background in the initial materials can vary in the course of the liquid-phase formation, the dependence of carrier concentration in the layers on the REE content in the solution–melt can be irreproducible. In order to increase the reproducibility of the results, we suggested using combined doping with REEs and Sn [6], taking into account the fact that Sn virtually does not react with REEs in the liquid phase. Thus, it is possible to control the electron concentration in epitaxial layers by introducing an amount of REE into the liquid phase so that the condition $N_A > N_D$ is definitely satisfied and then by the proper dosing of the Sn concentration in the solution–melt.

The results of these studies are shown in Fig. 7, which illustrates the control over electron concentration $n = N_D - N_A$ in InGaAs layers within the range of $n = 2 \times 10^{14}$–3×10^{17} cm^{-3} for a Dy concentration in the solution melt equal to 0.006 at. % and for variation of the Sn content in the liquid phase from 0.001 to 0.4 at. %. A typical electron-concentration profile in an InGaAs:(Dy, Sn) epitaxial layer is shown in Fig. 8.

Such a necessity for controlling the electron concentration arises, for example, in the development of photodetectors, field-effect transistors, and structures with two-dimensional (2D) electron gas, which will be considered in the following sections.

5. ELECTRICAL AND OPTICAL PROPERTIES OF INP AND INGAAS(P) EPITAXIAL LAYERS DOPED WITH RARE-EARTH ELEMENTS

The temperature dependence of the Hall electron mobility in the InP and InGaAs(P) layers was analyzed in detail by Gorelenok *et al.* [24]. Doping with REEs makes it possible to reduce the electron concentration in the layers to ~10^{13} cm^{-3} both in InP and in InGaAs. The electron mobility in InGaAs can be as high as

Table 1. Joint doping of InGaAs solid solutions with Yb and Mg and with Yb and Cd

Solid solutions	Acceptors		Yb, at. %	Characteristics at 300 K	
	impurity	at. %		p, 10^{19} cm^{-3}	μ, cm^2 V^{-1} s^{-1}
$In_{0.77}Ga_{0.23}As_{0.48}P_{0.52}$	Mg	0.05	0	3.5	185
$In_{0.77}Ga_{0.23}As_{0.48}P_{0.52}$	Mg	0.05	0.01	4.1	230
$In_{0.53}Ga_{0.47}As$	Mg	0.05	0	1.8	140
$In_{0.53}Ga_{0.47}As$	Mg	0.05	0.01	6.5	150
$In_{0.54}Ga_{0.46}As_{0.92}P_{0.08}$	Mg	0.05	0	2.0	100
$In_{0.54}Ga_{0.46}As_{0.92}P_{0.08}$	Mg	0.05	0.01	4.5	110
$In_{0.54}Ga_{0.46}As_{0.92}P_{0.08}$	Cd	1.0	0	4.1×10^{-2}	76
$In_{0.54}Ga_{0.46}As_{0.92}P_{0.08}$	Cd	2.0	0.08	3.1×10^{-1}	47

1.54×10^4 cm^2 V^{-1} s^{-1} at 300 K and as high as 10^5 cm^2 V^{-1} s^{-1} at 77 K (7×10^4–10^5 cm^2 V^{-1} s^{-1} in InP) [6].

5.1. Lifetime of Nonequilibrium Charge Carriers

The lifetime of nonequilibrium charge carriers (τ_p) in n^0-InGaAs was determined from the diffusion component of the dark current in a reverse-biased *p*–*n* junction fabricated on the basis of the above material [27]. The diffusion component of the dark current was determined experimentally from the temperature dependence of reverse current at low reverse-bias voltages ~0.1 V in the temperature range from 300 to 400 K. It was found that τ_p in InGaAs layers obtained by prolonged annealing of the solution–melt without REEs in a hydrogen atmosphere was about 300 ns and was as long as 10 μs for the material obtained from the solution–melt doped with REEs. Thus, doping the solution–melt with REEs makes it possible to appreciably increase the lifetime of nonequilibrium charge carriers (to ~10 μs]) in InGaAs ($E_g = 0.73$ eV) and in InGaAsP ($E_g = 0.8$ eV). Apparently, this phenomenon is caused by the fact that REEs reduce the concentration not only of shallow-level background donor impurities but also of the impurities which introduce deep-level centers into the materials under consideration.

5.2. Drift Velocity of Electrons

It is well known that the ultimate response speed of field-effect devices is limited not only by the mobility but also by the drift velocity (v_d) of the charge carriers. Therefore, it is of interest to ascertain the field dependence of v_d in InGaAsP solid solutions obtained by doping the solutions–melts with REEs. In order to determine the dependence $v_d(E)$, we measured the current–voltage characteristics using a setup with optoelectronic strobing ultrashort electrical pulses with a time resolution of ~25 ps [28] and ~10 ps [29]. The dependence $v_d(E)$ was calculated using the formula

$$v_d(E) = I(E)/en_0s,$$

where E is the electric-field strength, e is the elementary charge, n_0 is the electron concentration, s is the cross section of the sample, and I is the current through the sample.

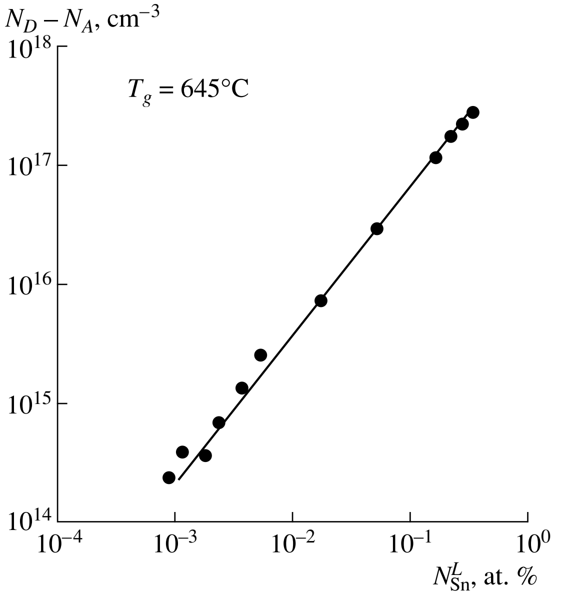

Fig. 7. Dependence of $N_D - N_A$ concentration in InGaAsP epitaxial layers on the Sn content in the liquid phase for a constant Dy content $N^L_{\text{Dy}} = 0.006$ at. %. T_g corresponds to the growth temperature.

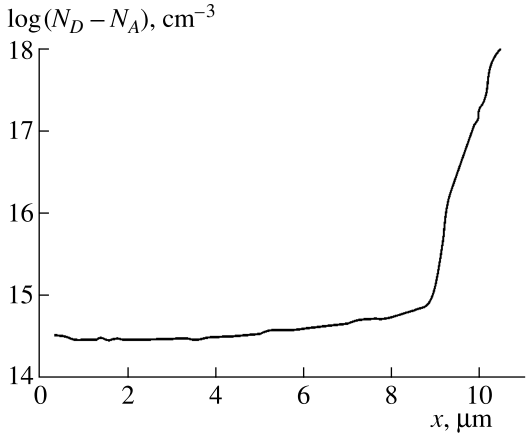

Fig. 8. A typical concentration profile of the electron concentration in InGaAs:(Dy, Sn) epitaxial layer; N^L_{Dy} = 0.006 at. % and N^L_{Sn} = 0.001 at. %.

In Fig. 9, we show the field dependences of v_d for InGaAsP solid solutions with different compositions. The highest drift velocity (2.8×10^7 cm/s) is observed in the $\text{In}_{0.53}\text{Ga}_{0.47}\text{As}$ ternary compound, for which the experimental dependence $v_d(E)$ is in good agreement with the corresponding dependence calculated using the Monte Carlo method [29]. The obtained large values of v_d are indicative of the high structural quality of the material and of its efficient purification as a result of doping the solution–melt with REEs. It is also noteworthy that the obtained dependence of $v_d(E)$ runs higher for InGaAs than for GaAs; as a result, the field-effect devices based on InGaAs are expected to have a higher response speed than those based on GaAs.

5.3. Low-Temperature Edge Photoluminescence

The photoluminescence (PL) of InP and InGaAs was excited by a helium–neon laser at a temperature of

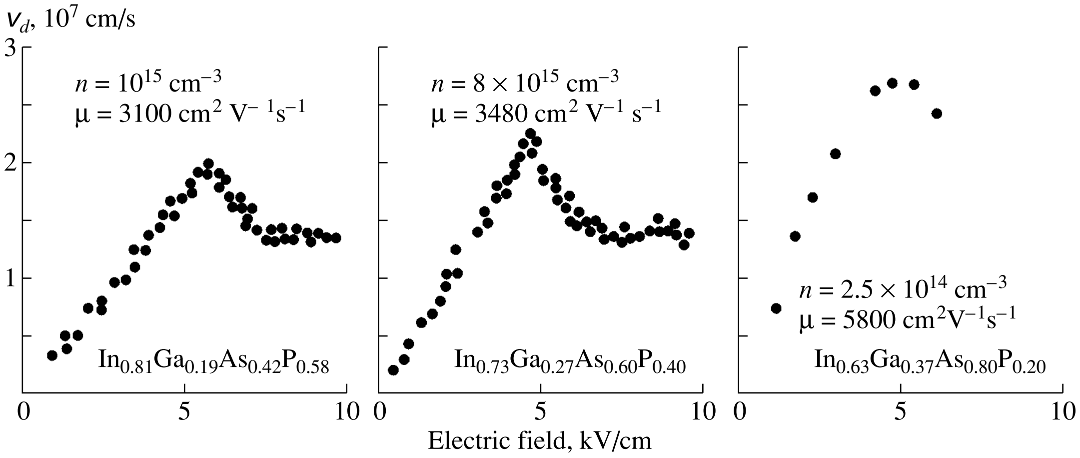

Fig. 9. Dependences of the electron drift velocity (v_d) on the electric-field strength for different compositions of InGaAsP solid solutions at 300 K.

2 K. The low-temperature edge PL can be used to assess the degree of purity of the material. The PL spectra of nominally undoped *n*-InP and *n*-InGaAs layers with $n \approx 10^{16}$ cm^{-3} consisted of an edge band peaked at 1.415–1.418 eV for InP and at 0.81–0.82 eV for InGaAs and of a weaker (with an intensity lower than that of the edge band by two orders of magnitude) impurity band related to donor–acceptor recombination. The edge band has a half-width of 6–8 meV for InP and 8–10 meV for InGaAs; these half-widths were caused by recombination from the states which belonged to free and bound excitons and were broadened owing to the effect of a random electric field induced by background impurities (Fig. 10). The introduction of a relatively small amount of REE (no larger than 0.001 at. %) into the solution–melt resulted in the narrowing of the line that was related to the neutral exciton–donor complex D^0X and which was dominant in the spectrum; in addition, a line related to an exciton bound to a neutral acceptor A^0X appeared in the spectrum. In the long-wavelength spectral region, which has a relatively low intensity, the A^0e band corresponding to recombination of free electrons at shallow-level acceptors is intensified. Simultaneously, the electron mobility measured at 77 K increases to the values which twice exceed the initial values (before an introduction of REEs) and approach the values characteristic of very pure samples. A further increase in the level of doping of the solution–melt with REE (Fig. 10) also brings about appreciable changes in the PL spectra.

If 0.01 at. % of Gd is introduced into the melt, the intensity of the line A^0X increases drastically, whereas the spectral step feature X caused by emission from free excitons transforms into a line whose intensity exceeds that of the D^0X line. Simultaneously, the integrated intensity of the entire excitonic portion of the spectrum and the A^0e band increase. A further increase in the Gd content (from 0.01 to 0.03 at. %) results in an appreciable quenching of D^0X and X lines combined with continuing increase in the intensities of the A^0e and A^0X lines. The charge-carrier mobility in corresponding samples is found to be much lower than in the samples which were not doped with Gd. The evolution of InP PL spectra with increasing REE content in the solution–melt results in the successive obtainment first of material [11] purer than the initial undoped InP and then compensated, high-resistivity, and pure *p*-type material. A similar evolution of PL spectra is also observed for InGaAs. In Fig. 10b, we show a typical PL spectrum of *n*-InGaAs with $n = 5 \times 10^{14}$ cm^{-3}. It can be seen that the line corresponding to the exciton–donor complex D^0X with a half-width of 2.5 meV and the A^0X and A^0e lines are dominant in the spectrum. Thus, the PL spectra of InP and InGaAs indicate that the material is purified as a result of doping the solution–melt with REEs; this doping reduces the internal random field of charged impurity centers, which gives rise to a fine excitonic structure in the spectra.

5.4. Photoexcitation Spectra

The photoexcitation spectra were measured using a submillimeter laser magnetospectrometer with a high resolution (~1 μeV). The emission source was a submillimeter CH_3OH-vapor laser with optical pumping provided by a CO_2 laser. The photoconductivity spectra were recorded at fixed frequencies of laser radiation with a varied magnetic field (**H**) at 4.2 K under Voigt's geometric conditions (**q** ⊥ **H**, where **q** is the wave vector of radiation). In order to enhance the sensitivity, the spectra were measured using additional illumination with photons whose energy corresponded to the fundamental-absorption range; the intensity of this illumination was kept constant [30].

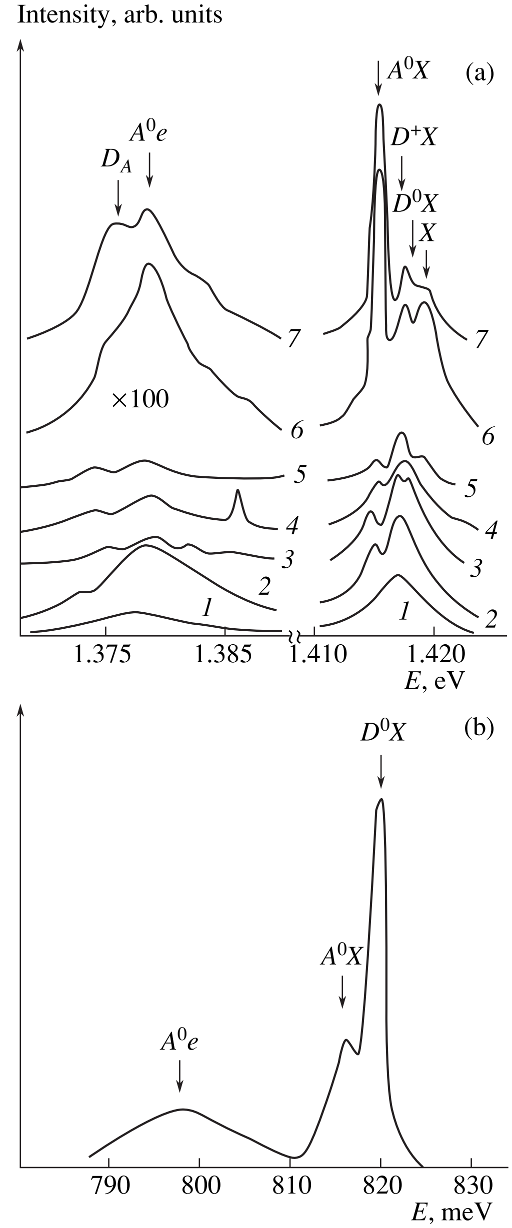

Fig. 10. The spectra of low-temperature edge photoluminescence in (a) InP with the Gd (N^L_{Gd}) content equal to (*1*) 0, (*2*) 0.001, (*3*) 0.004, (*4*) 0.007, (*5*) 0.009, (*6*) 0.01, AND (*7*) 0.02; and in InGaAs with (N^L_{Gd}) = 0.06 at. %.

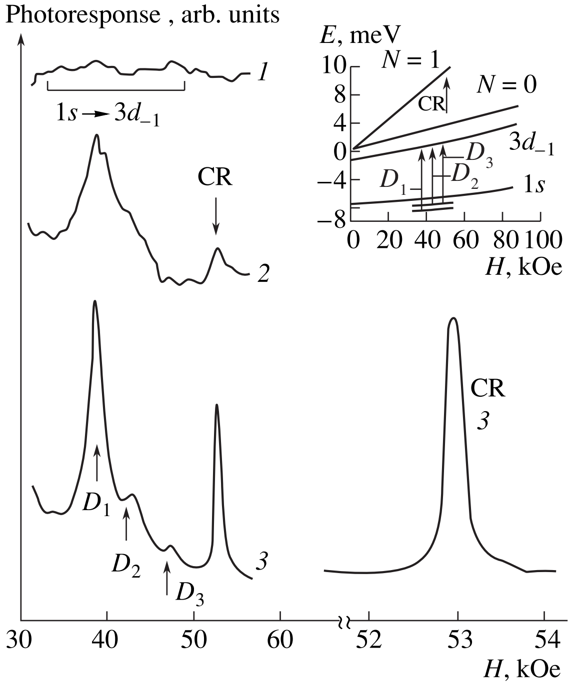

Fig. 11. Photoexcitation spectra for the $1s$–$3d_{-1}$ transition and the cyclotron resonance (CR) at a wavelength λ = 1.6 μm for the samples doped with (*1*) Gd (0.001 at. %), (*2*) Gd (0.04 at. %), and Yb (0.01 at. %). The field dependences of the shift for donor levels $3d_{-1}$ and Landau levels $N = 0$ and $N = 1$ are shown in the inset. The arrows indicate the transitions observed at 4.2 K.

We studied the epitaxial InP layers obtained by doping the solution–melt with Yb or Gd; the electron concentration in these layers was (0.2–2.0) × 10^{14} cm^{-3} and the mobility was (4–7) × 10^4 $\mathrm{cm}^2\ \mathrm{V}^{-1}\ \mathrm{s}^{-1}$ at 77 K.

In Fig. 11, we show the photoresponse which corresponds to a $1s$–$3d_{-1}$ transition and the cyclotron resonance (CR). There are no resonance lines in spectrum *1* for the sample with a Gd content of 0.001 at. % in the liquid phase and after 1-h annealing of the solution–melt. Three lines corresponding to the excitation of three donors and a CR line can be resolved in spectra *2* and *3*. The magnetic-field dependences of levels $1s$ and $3d_{-1}$ are shown in the inset and correspond to calculations performed in the effective-mass approximation [31]. In calculations, values of the effective Rydberg energy Ry^* = 7.31 meV and $m^* = 0.08m_0$ were used. The chemical shift of the $1s$ state of donors D_1–D_3, i.e., the difference between the energy of the ground state of donors of different chemical origin, is enlarged in the inset to Fig. 11 for the sake of better illustration. It can be concluded from comparing the intensities of donor-related lines in the photoexcitation spectra $1s \longrightarrow 2p_{+1}$ [30] and $1s \longrightarrow 3d_{-1}$ that the donor D_1 corresponds to sulfur, whereas donors D_2 or D_3 correspond to silicon. In Fig 11, we show the narrowest CR line observed in spectrum *3* separately and on an enlarged scale.

The cyclotron electron mass $m^* = (0.0806 \pm 0.0003)m_0$ is in good agreement with the value of m^* in the layers of pure InP obtained by vapor-phase epitaxy. The effective electron mobility at the CR frequency in the sample with spectrum *3* is as high as ~10^6 $\mathrm{cm}^2\ \mathrm{V}^{-1}\ \mathrm{s}^{-1}$, which is comparable to the effective electron mobility in ultrapure GaAs layers.

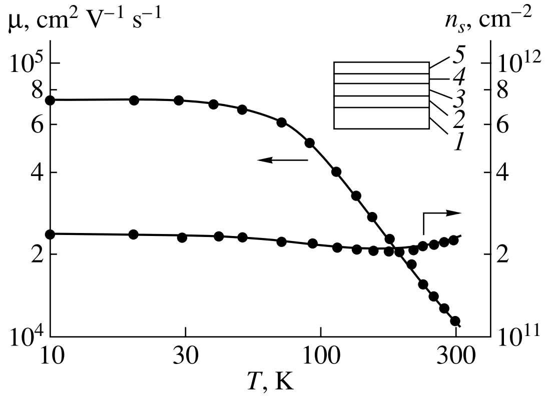

Fig. 12. Temperature dependences of the electron concentration and mobility in an $In_{0.88}Ga_{0.12}As_{0.23}P_{0.77}/In_{0.53}Ga_{0.47}As$ structure with a buffer layer and a spacer as shown in the inset: (*1*) the InP:Fe substrate; (*2*) an n^0-InGaAsP buffer layer (λ_g = 1.06 μm) with $n = 6 \times 10^{14}$ cm^{-3} and d = 0.5 μm; (*3*) an InGaAsP (λ = 1.06 μm) buffer layer (an electron source) with $n = 6 \times 10^{16}$ cm^{-3} and d = 0.1–0.35 μm; (*4*) an n^0-InGaAsP layer (λ = 1.06 μm) with d = 100–300 Å; and (*5*) an n^0-$In_{0.53}Ga_{0.47}As$ layer with $n = 6 \times 10^{14}$ cm^{-3} and d = 0.7–1 μm.

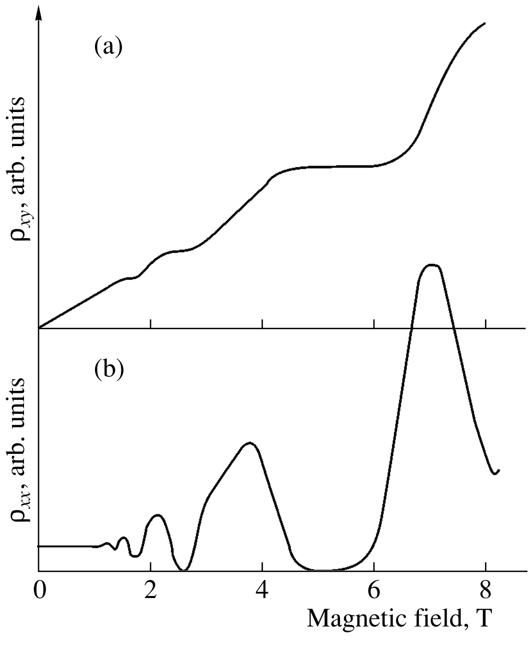

Fig. 13. (a) Quantum Hall effect and (b) the Shubnikov–de Haas oscillations for two-dimensional structures shown in Fig. 12.

Thus, the photoexcitation spectra indicate that InP is efficiently purified as a result of doping the solution–melt with REEs.

5.5. Structures with a Two-Dimensional Electron Gas

The developed technology for obtaining InP layers and InGaAsP solid solutions, which are lattice-matched to InP, allowed us to be the first to use LPE to develop structures that involved a 2D electron gas and were based on InGaAsP [32]. These structures were formed by the consecutive epitaxial growth first of 1.2-μm-thick InP layers with $n \approx 10^{16}$ cm^{-3} and then of 2.7-μm-thick $In_{0.53}Ga_{0.47}As$ layers with $n = 6 \times 10^{13}$ cm^{-3} on a semi-insulating InP:Fe substrate. The Shubnikov–de Haas oscillations were observed in such structures at 4.2 K; the 2D electron concentration determined from the analysis of these oscillations was $n_s = 2.6 \times 10^{13}$ cm^{-2} and did not coincide with the results of Hall measurements, which indicated that the 2D channel was shunted. Another disadvantage of the structure under consideration consists in the fact that it is very difficult to obtain a perfect InGaAs/InP interface owing to dissociation of InP at the epitaxy temperature prior to growth of a narrow-gap InGaAs layer.

In order to obtain a perfect heterointerface, $In_{0.88}Ga_{0.12}As_{0.23}P_{0.77}$ solid solution was used as a wide-gap material; a spacer was also introduced in order to eliminate the shunting of the 2D channel [33]. In addition, a buffer layer of InGaAsP solid solution was grown between the InP:Fe substrate and the wide-gap solid-solution layer (the source of electrons) in order to prevent Fe diffusion from the substrate into the channel (see Fig. 12, the inset). The electron concentration in the 0.7-μm-thick narrow-gap $In_{0.53}Ga_{0.47}As$ layer and also in the 200-Å-thick spacer and in the 0.5-μm-thick InGaAs buffer layer was reduced to $n < 10^{15}$ cm^{-3} as a result of doping with REEs. The electron concentration was equal to 6×10^{16} cm^{-3} in the 0.2-μm-thick wide-gap InGaAs layer (the source of electrons). The temperature dependences of the electron concentration and mobility in the structure under consideration are shown in Fig. 12; the magnetotransport parameters of these structures measured at 4.2 K in strong magnetic fields are shown in Fig. 13. The horizontal plateaus in the quantum Hall effect and the portions with zero resistivity, which correspond to these plateaus, and also the agreement between the 2D electron concentration obtained from the analysis of the Shubnikov–de Haas oscillations and the results of the Hall measurements in weak fields indicate that there is no shunting effect in the structures under consideration. The electron mobility was equal to 1.23×10^4 cm^2 V^{-1} s^{-1} at 300 K and 7.3×10^4 cm^2 V^{-1} s^{-1} at 4.2 K (Fig. 12), which are apparently the best results ever obtained for structures obtained by LPE. The fact that the transport characteristics are not affected by illumination [34] indicates that the structures under consideration hold promise for application in the technology of high electron mobility transistors (HEMTs).

6. RARE-EARTH ELEMENTS IN DEVICE TECHNOLOGY

The developed technology for the formation of epitaxial layers containing REEs was used to fabricate light-emitting diodes based on GaP, Gunn diodes, photodetectors based on InP and InGaAsP, and field-effect transistors of various types.

6.1. Light-Emitting Diodes Based on GaP

One of the topical problems in the development of light-emitting diodes (LEDs) consists in the fabrication of a LED with pure green emission. At room temperature, such LEDs should emit light with a wavelength $\lambda = 555$ nm ($h\nu \approx 2.23$ eV), which corresponds to the highest sensitivity of the human eye.

The GaP band gap at room temperature is very close to the desired photon energy $h\nu$. However, attempts to obtain the pure green emission from a GaP LED fabricated by conventional technology have failed. As a rule, bands related to the presence of Group II and VI impurities in the material are observed in the spectrum in addition to the emission caused by band-to-band transitions. These additional bands can be most easily observed in the spectra of low-temperature luminescence, in which case the corresponding spectral lines are reliably resolved.

In Fig. 14a, we show a typical PL spectrum of lightly doped *n*-GaP ($n_0 \approx 4 \times 10^{16}$ cm^{-3}) at a temperature of 2 K. The material was grown using conventional LPE. The *n*-type layers with the aforementioned electron concentration are typically used as active regions in the GaP LEDs. When discussing the spectra shown in Fig. 14, we should bear in mind that the band gap increases with decreasing temperature. The band with $h\nu \approx 2.32$ eV corresponds to the band-to-band emission at 2 K (peak *1* in Fig. 14a). It can be seen from Fig. 14a that the spectrum includes undesirable impurity-related peaks *2* and *3*, which have appreciable intensities, in addition to peak *1*. These undesirable peaks are caused by recombination via donor–acceptor pairs related to the background impurities of Groups II and VI.

Doping of the liquid phase with yttrium in the course of growing the active region makes it possible to significantly reduce the donor background. The purification effect is clearly illustrated by the PL spectrum of GaP grown under the conditions where ytterbium (N_Y^L = 0.005 at. %) was introduced into the liquid phase (Fig. 14b). The level of doping of the epitaxial layer is approximately the same as that of the sample whose spectra are shown in Fig. 14a. It can be seen that the edge-emission band ($h\nu = 2.307$ eV at 2 K) is dominant in the spectrum of the sample grown with yttrium added to the liquid phase. The impurity-related bands are found to be suppressed to a great extent. Virtually only the pure-green band-to-band emission with a line half-width of ~80 meV is observed at 300 K in the PL spectra of the samples under consideration (Fig. 14c). It is noteworthy that the energy position $h\nu$ of the peak corresponding to the edge-emission band is equal to 2.24 eV at 300 K.

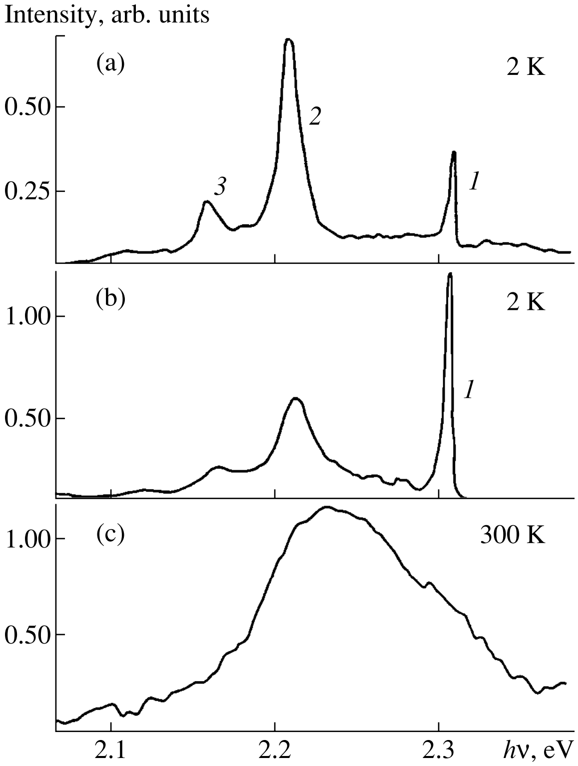

Fig. 14. Photoluminescence spectra of epitaxial GaP layers ($n = 4 \times 10^{16}$ cm^{-3}): (a) the layer grown without doping the solution–melt with REEs; and (b) and (c) the layer doped with yttrium (N_Y^L = 0.005 at. %).

However, it is not sufficient to suppress the impurity-related emission from the active (base) LED region for obtaining the pure-green emission. It is also necessary to suppress the impurity-related emission from the p^+-type region of a LED.

Therefore, we used the method of joint doping of the liquid phase with magnesium and yttrium to form a p^+-type region in a GaP LED in order to obtain the pure-green emission. In Fig. 15, we show a typical PL spectrum of a *p*-GaP layer, which has a hole concentration of ~10^{18} cm^{-3} at 300 K and is formed using the aforementioned method. The emission spectrum consists virtually of only a single band with $h\nu = 2.234$ eV at 300 K.

The electroluminescence spectra of emitting *p*–*n* structures formed using the developed LPE method and based on GaP were similar to the PL spectra shown in Figs. 14 and 15 and consisted of a single pure-green band at 300 K. Thus, the use of REEs in LPE makes it possible to easily fabricate GaP-based LEDs with pure-green emission ($\lambda = 555$ nm) [35, 36].

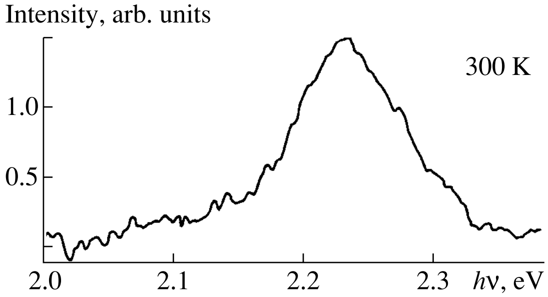

Fig. 15. The photoluminescence spectrum of an epitaxial p-GaP layer ($p \approx 10^{18}$ cm^{-3}) doped heavily with Mg and Y (N^L_{Mg} = 0.05 at. % and N^L_{Y} = 0.005 at. %).

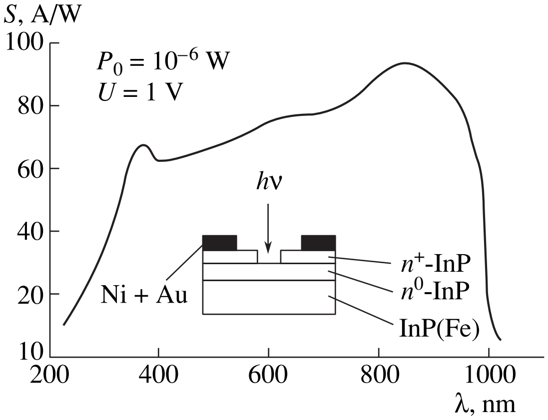

Fig. 16. The photoresponse spectrum of a photoresistor based on InP.

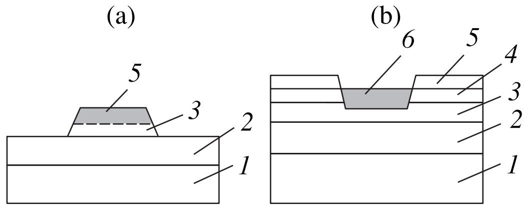

Fig. 17. Schematic representation of p–i–n photodiodes with (a) mesa and (b) planar structure: (*1*) the n^+-InP:Sn substrate, (*2*) an undoped n-InP buffer layer, (*3*) a narrow-gap n^0-InGaAs(InGaAsP):REE layer ($n^0 < 10^{15}$ cm^{-3}) with E_g = 0.73(0.8) eV, (*4*) an n-InGaAsP layer with E_g = 1.0 eV, (*5*) a p-InGaAs(InGaAsP) layer, and (6) a SiO$_2$ layer.

6.2. Gunn Diodes Based on InGaAs

The developed technology for obtaining pure layers was used to form the structures for the Gunn diodes on n^+-InP(100) substrates with $n = 10^{18}$ cm^{-3}. The electron concentration in the InGaAs active region was 10^{15}–10^{16} cm^{-3}, and the corresponding mobility was 9×10^3–10^4 cm^2 V^{-1} s^{-1}. The diodes were fabricated in the form of cellular structures [37] with a contact diameter of 12 μm, which ensured the possibility of performing the measurements in the continuous mode without additional measures for improving heat removal. Generation with an efficiency of 2.5% in the 8-mm band of wavelengths was obtained.

A special feature of the Gunn diodes based on InGaAs is the fact that, when compared with conventional Gunn diodes based on n-GaAs and n-InP, the generation frequency is found to be much higher for the same thickness of the n-type layer since the peak drift mobility of electrons in n-InGaAs is higher than in GaAs and InP [29].

6.3. Photodetectors

The InP and InGaAs layers doped with REEs were used to fabricate various types of photodetectors: photoresistors, p–i–n diodes, avalanche photodiodes, and field-effect and bipolar phototransistors.

In order to fabricate the photoresistors, we used lightly doped InP and InGaAs layers that had a net concentration of $N_D - N_A \approx 10^{13}$–$10^{15}$ cm^{-3} and were grown on semi-insulating InP:Fe substrates ($\rho = 10^7$ Ω cm) [38, 39]. The dark resistance of photoresistors was 10^6–10^8 Ω for InP and 10^3–10^6 Ω for InGaAs. The initial portions of the current–voltage characteristics were linear ($j \propto E$). As the applied voltage increased so that the electric-field strength exceeded $E \approx 2 \times 10^3$ V/cm for InGaAs and $E = 10^4$ V/cm for InP, a deviation from Ohm's law was observed. A typical special feature of the spectral characteristics of photoresistors based on InP and InGaAs is a wide range of spectral sensitivity that extended to the ultraviolet spectral region. The photosensitivity was as high as 40 A/V even at a wavelength of λ= 300 nm (Fig. 16) [38]. The long-wavelength edge was governed by the material's band gap. Photoresistors based on InGaAs had a response speed of 10^{-10} s and an amplification of 8–10 when the contacts were spaced by 5 μm.

The technology of obtaining pure layers doped with REEs was also used to develop two types of p–i–n photodiodes: mesa-type [40] and planar [41]. Both variants are shown in Fig. 17. In the case of a mesa structure (Fig. 17a), passivation with poliimide varnish was used to stabilize the dark currents [41]. The spectral-sensitivity range was 0.92–1.67 μm. The current sensitivity was 0.5–0.7 A/W in the wavelength range from 1.3 to 1.55 μm. The dark-current density was about 10^{-7} A/cm^2 at a bias voltage of 1–5 V. When the p–i–n diodes with an active area 50–100 μm in diameter were exposed to laser radiation with a wavelength of 1.3 μm and an optical-pulse duration of 25 ps, the rise and decay times for the photoresponse were ~50 ps [42].

Previously, there had been many attempts to fabricate avalanche photodiodes (APDs) based on InGaAs/InP heterostructures with dark currents and noise levels that were much lower than in Ge APDs. The APD design in which the regions of the avalanche multiplication and optical absorption are separated (i.e., the *p–n* junction is formed in the InP emitting layer at a certain distance from the InGaAsP/InP interface [43]) is found to be most successful. The formation of a *p–n* junction in InP made it possible to reduce the APD dark currents, owing to the smaller values of the diffusion, generation–recombination, and tunneling currents in InP than in InGaAsP (InGaAs) [43, 44]. The smallest dark current in such APDs was attained in the planar structure with the *p–n* junction outcrop at the surface being protected with SiO_2 film and amounted to 3×10^{-6} A/cm^2 at $0.9U_f$. The largest multiplication factor of 5500 was attained [45] in the mesa structure; the dark-current density was equal to 8×10^{-5} A/cm^2 at a breakdown voltage U_f.

The heterostructures were formed by LPE [46] on *n*-InP:Sn(100) substrates with $n = (1–2) \times 10^{18}$ cm^{-3}. Prior to epitaxial growth, the melts were subjected to long-term annealing (for more than 20 h) in a hydrogen atmosphere or were doped with Dy. Indium was of 6N purity. This circumstance made it possible to reduce the carrier concentration in *n*-InP and *n*-InGaAsP to 2×10^{15} cm^{-3}. A 2- to 3-μm-thick buffer layer of undoped *n*-InP with $n = (5–8) \times 10^{15}$ cm^{-3}, a 1.5- to 2-μm-thick layer of undoped *n*-InGaAsP ($E_g \approx 0.95$ eV) with $n \approx 5 \times 10^{15}$ cm^{-3}, and a 3- to 4-μm-thick layer of undoped *n*-InP with $n = (2–5) \times 10^{15}$ cm^{-3} were successively grown on the *n*-InP substrate. Finally, Cd was diffused into the upper *n*-InP layer to a depth of 1.5–2.0 μm. Mesas with a diameter of ~100 μm were then formed on the above structures using photolithography; the Au–Te and Au–Zn contacts to the *n*- and *p*-type regions were formed by vacuum deposition and subsequent fusing at 450°C in the hydrogen atmosphere. In the inset in Fig. 18, we show a schematic representation of an APD with a mesa structure. Antireflection and protective coating films were not deposited.

We studied the spectral sensitivity of diodes illuminated from the mesa side, as well as the dark currents, avalanche multiplication, and capacitance–voltage (*C–V*) characteristics. The studies of the *C–V* characteristics showed that the capacitance was equal to 1–2 pF in zero-biased diodes. The capacitance was reduced to 0.6 pF when reverse bias was applied.

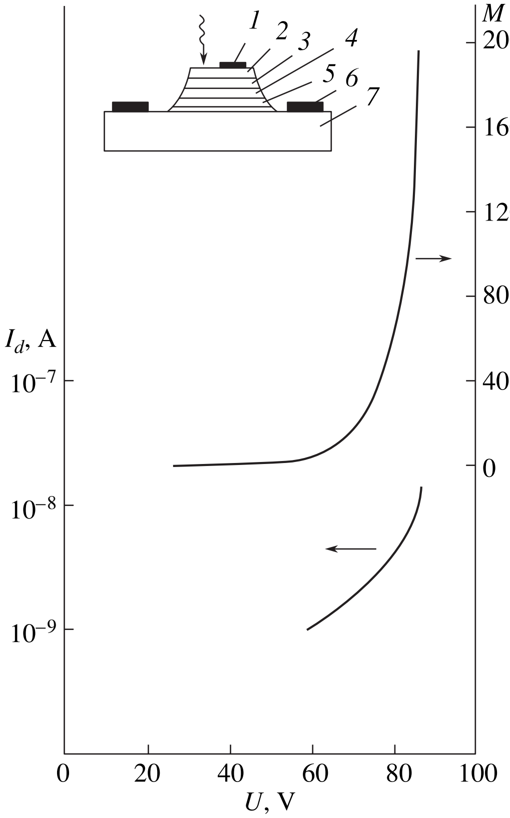

Fig. 18. Dependences of the avalanche-multiplication factor M and the dark current I_d on the reverse bias U. Schematic representation of a LED with a mesa structure is shown in the inset: (*1*) an ohmic Au–Zn contact, (*2*) a *p*-InP:Cd layer, (*3*) an *n*-InP layer, (*4*) an *n*-InGaAsP layer, (5) an *n*-InP layer, (*6*) an ohmic Au–Te contact, and (*7*) the *n*-InP substrate.

Figure 18 shows the dependences of the dark current I_d and the avalanche-multiplication factor M on the reverse bias. Avalanche multiplication set in at $U \approx 50$ V; the value of M was as large as 200 at 86 V. The distance between the *p–n* junction and the heterointerface was ~2 μm for the diode under consideration. The shape of the spectral characteristics is typical of double heterostructures illuminated from the mesa side. At $M = 1$, the spectral sensitivity is observed in the range from 0.9 to 1.35 μm; this range is limited by the fundamental-absorption edges for the InP window and for the narrow-band material. The photosensitivity was as high as 0.7 A/W at $\lambda \approx 1.3$ μm.

Vertical field-effect phototransistors were fabricated on the basis of developed technology for obtaining purified layers. The operation of these transistors is based on modulation of the built-in potential barrier by absorbed light [47]. The structure of such a field-effect phototransistor with a buried gate is shown schematically in Fig. 19a. A ~3-μm-thick InP undoped buffer layer with $n \approx 5 \times 10^{16}$ cm^{-3} and then a 4-to 6-μm-thick InGaAs(InP) active layer with $n = (1–10) \times 10^{14}$ cm^{-3} were successively formed on the n^+-InP:Sn substrate in the course of fabrication of the transistors under consideration. The next technological operation consisted in the formation of a ~1-μm-thick buried gate using selective diffusion of Zn through windows in SiO_2, which had areas of 5×5 or 10×10 μm^2 and were spaced by 5 μm. After subsequent removal of SiO_2, the structure was overgrown first with a 3- to 4-μm-thick pure

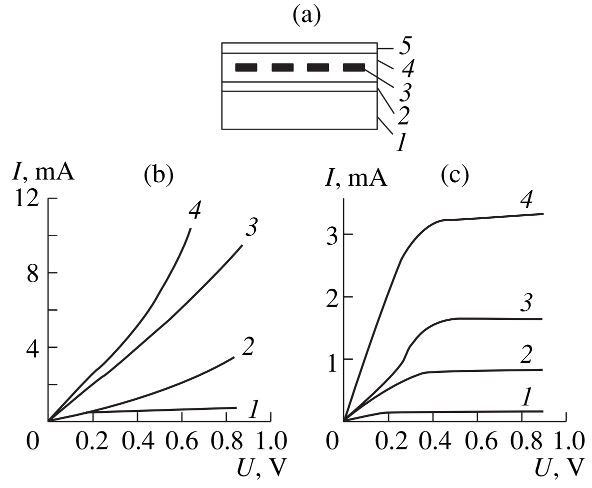

Fig. 19. A vertical field-effect phototransistor. (a) Schematic representation of a structure with a buried gate: (*1*) the InP substrate, (*2*) an InP buffer layer, (*3*) a p^+-InGaAs buried gate, (*4*) an n^0-InGaAs:REE layer, and (*5*) an n^+-InGaAs layer. (b and c) Current–voltage characteristics of the (b) triode and (c) pentode types. The illumination power was equal to (*1*) 0, (*2*) 5×10^{-6}, (*3*) 3×10^{-4}, and (*4*) 2×10^{-2} W.

n^0-InGaAs(InP) layer and then with a ~1-μm-thick n^+-InGaAs(InP) contact layer. Contacts to the structure were formed by vacuum deposition of metal through the mask of eutectic Au–Ge alloy.

Figures 19b and 19c show the output current–voltage (*I*–*V*) characteristics of the phototransistors under consideration; these characteristics were either of the triode (Fig. 19b) or pentode (Fig. 19c) type, depending on the doping level of n^0-InGaAs(InP) and on the geometric parameters of the structure. The triode-type *I*–*V* characteristics were commonly observed when the total thickness of the space-charge region (SCR) for p^+–n^0 junctions was larger than (or equal to) the geometric width of the channel, whereas the pentode-type characteristics were observed if the SCR thickness was smaller than the channel width.

Studies of the effect of illumination on *I*–*V* characteristics showed that the current increased linearly with increasing source–drain voltage in the triode-type structures as the illumination intensity became higher. The leveling-off of current in a wide range of illumination intensities is observed for the pentode-type *I*–*V* characteristics (Fig. 19c), much the same as in conventional planar field-effect transistors. In the triode-type structures, the amplification coefficient first increased with increasing illumination intensity, then reached a maximum, and finally decreased; at the same time, the above coefficient remained virtually constant in the pentode-type structures in a wide range of illumination intensities. Studies of pulse-response characteristics showed that the rise times depended heavily on the illumination intensity, geometric parameters of the structures, and applied voltage. The rise and decay times were equal to ~10 ns at high incident-light power (10 mW), whereas these times increased to 100–200 ns at the levels of illumination power lower than 0.1 mW. The spectral range of photosensitivity amounted to 1.0–1.6 μm. The static amplification coefficient was as large as 100 when the illumination power was lower than 0.1 mW and at a bias of 1.5 V.

The method of joint doping of a material with Cd and REEs was used to fabricate bipolar *N*–*p*–*N* phototransistors with a heavily doped thin base [48] (Fig. 20a). In the completed transistor, the base was in fact composite; i.e., a 100- to- 200-Å-thick *p*-InGaAsP ($E_g = 0.8$ eV) layer with a hole concentration of 10^{18} cm^{-3} was grown in such a way that a thin 100- to 500-Å-thick *p*-type layer was formed in the adjacent wide-gap *n*-InGaAsP ($E_g = 1.1$ eV) layer [48]. The use of a composite base makes it possible to control the transistor's dark-current density in a wide range (from 10^{-4} to 10^{-6} A/cm^2). By varying the thickness of the narrow-gap region in the base from 100 to 1000 Å, one can vary the current gain from 100 to 1000 (Fig. 20b); simultaneously, the rise and decay times vary from 20 to 100 ns.

Strong dependences of the gain and response speed on the illumination intensity are observed for structures whose bases differ in thickness. These dependences are caused by the presence of a barrier at the heterointerface. It was possible to obtain the highest gain, equal to 1000 (at $\tau \approx 100$ ns), at an illumination power of 10 mW and relatively high bias voltages.

6.4. Schottky Barriers

The idea of using REEs to form high-quality Schottky barriers was based on the assumption that the high reactivity with respect to oxygen, arsenic, and phosphorus would make it possible to reduce the probability of the formation of unstable conducting phases for native InP and InGaAs oxides. In addition, it was assumed that the presence of REEs would also reduce the migration of As and P at the metal–InP(InGaAs) and insulator–InP(InGaAs) interfaces. This effect of REEs would ensure large values of the Schottky barrier height, a low density of states at the insulator–InP(InGaAs) interface, and temporal stability of the above parameters.

In order to form Schottky barriers based on InP and InGaAs with an electron concentration $n = (1–2) \times 10^{16}$ cm^{-3}, multilayered metallization was used; layers of ytterbium (with a thickness of 200–300 Å), nickel (200–300 Å), and gold (5000 Å) were used. The multilayered barrier was formed by deposition aided by thermal evaporation in vacuum. The forward portions of the *I*–*V* characteristics of the Schottky barriers were almost ideal, with the ideality factor being equal to 1.05–1.1; the barrier heights were 0.76 and 0.55 eV for InP and InGaAs, respectively. In Fig. 21, we show the reverse *I*–*V* characteristics of these barriers (curves *1*, *2*) and the

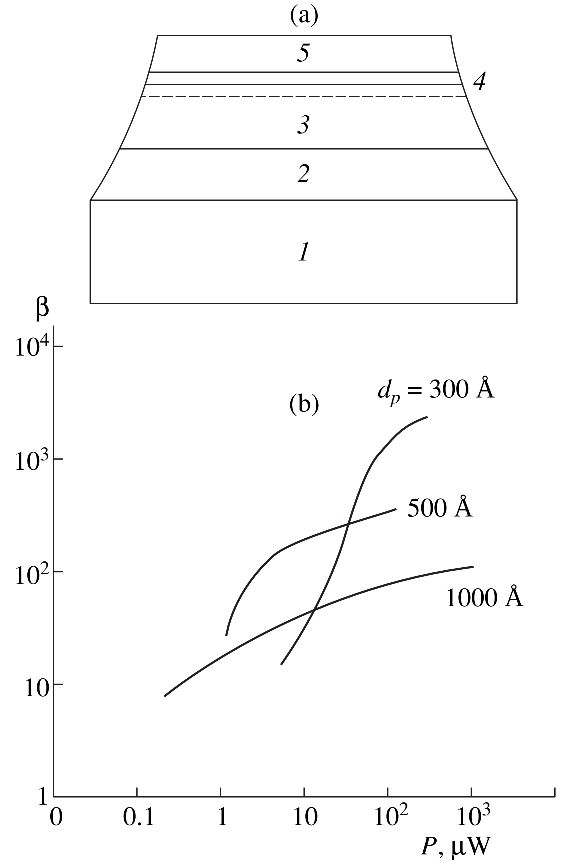

Fig. 20. A bipolar *N–p–N* phototransistor. (a) Schematic representation of the mesa structure: (*1*) the n^+-InP substrate, (*2*) a buffer *n*-InP layer, (*3*) the emitter (undoped, $n \approx 10^{17}$ cm^{-3}), (*4*) the composite base consisting of *p*-InGaAsP:(REE, Cd) (with E_g = 0.8 eV, $p = 10^{18}$ cm^{-3}, and a thickness of 100–200 Å) and InGaAsP (E_g = 1.1 eV, 100–200 Å), and (*5*) the *n*-InGaAsP collector (E_g = 1.1 eV, $n \approx 10^{17}$ cm^{-3}). (b) Dependences of the current gain β on the incident-light power *P* for several values of the thickness d_p of the *p*-type region.

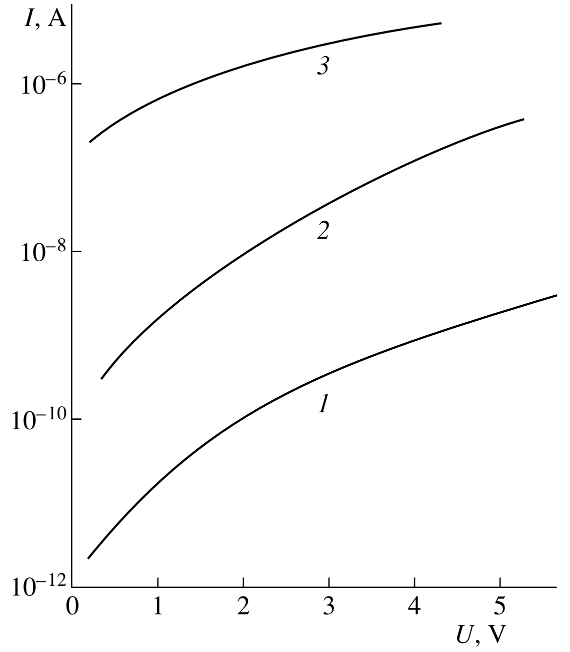

Fig. 21. Reverse current–voltage characteristics of Schottky barriers with an area of 9×10^{-4} cm^2 (the characteristics were measured at 300 K): (*1*) for an InP–Yb–Ni–Au structure, (*2*) for an InGaAs–Y–Ni–Au structure, and (*3*) for an InP–Au structure.

Au–*n*-InP barrier (curve *3*) for the sake of comparison [49]. It can be seen that the leakage currents under a reverse voltage of 1 V are smaller for multilayered metallization than for conventional Au–*n*-InP barriers by several orders of magnitude at a reverse bias of 1 V.

Our preliminary studies of REE oxides have shown that REE oxides such as Sc_2O_3 and Y_2O_3 have a resistivity of 10^{15}–10^{16} Ω cm. These values of resistivity almost coincide with the resistivity of thermal silicon dioxide. The REE oxides were formed by thermal evaporation of scandium or yttrium in vacuum with controlled introduction of oxygen. Studies of InP-based metal–insulator–semiconductor structures incorporating the above insulators showed that the fixed charge at the interface is smaller than 10^{11} electron/cm^2, the density of surface states at the minimum is lower than 10^{11} eV^{-1} cm^{-2}, and the hysteresis of the capacitance–voltage characteristic is no larger than 0.2 V (Fig. 22) [6].

6.5. Field-Effect Transistors with Schottky Barriers

The developed technology for obtaining Schottky barriers and doped layers with high mobility (dual doping with Sn and REE) was used to fabricate field-effect transistors with Schottky barriers [50]. The InGaAs layers with electron concentrations $n = (1–2) \times 10^{17}$ cm^{-3} had an electron mobility as high as 7000 cm^2 V^{-1} s^{-1} at room temperature. The structure and typical *I–V* characteristics of field–effect transistors are shown in Fig. 23 [50]. For a gate area of 1.5 × 290 μm, the transconductance was 180 mS/mm at 300 K and the power gain was equal to 17 dB at a frequency of 4 GHz.

In Fig. 24, we show the frequency dependence of the power gain. For the sake of comparison, the frequency dependence measured for a GaAs field-effect transistor with the same topology, the same gate size, and under the same conditions is also shown (curve *2*). It can be seen that a field-effect transistor based on InGaAs features a higher operating frequency.

7. SURFACE GETTERING OF GAAS USING FILMS OF RARE-EARTH ELEMENTS

The surface gettering of high-resistivity ($\rho = 10^8$ Ω cm) GaAs(111) and GaAs(100) doped with chromium was

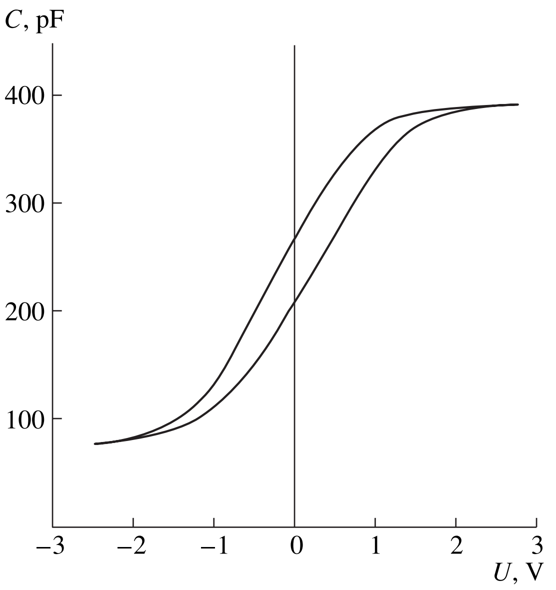

Fig. 22. A typical capacitance–voltage characteristic of a Sc_2O_3–InP MIS structure (the Sc_2O_3 thickness is 250 Å).

reported previously. The 0.3-mm-thick wafers of this GaAs compound were coated with ~100-nm-thick SiO_2, Si–W, Cr, or Si–Cr films and were subjected to heat treatment for 15–45 h at 826–926°C. As a result, it was found that the dislocation density and stresses decreased, whereas the resistivity and carrier mobility increased somewhat [51].

In this paper, we report the results of surface gettering of impurities and defects in comparatively thick (1.6 mm) wafers of GaAs(111) grown from initial Ga and As of 7*N* purity by the Czochralski method [17]; these wafers had an electron concentration of $n = (1–3) \times 10^{15}$ cm^{-3} and a mobility of 1500–2000 cm^2 V^{-1} s^{-1} at 300 K. This was a material in which the charge-carrier concentration was controlled by the ratio between the concentration of intrinsic defects such as V_{Ga}, V_{As}, I_{Ga}, I_{As}, As_{Ga}, Ga_{As} and of various complexes containing these defects, rather than by the background concentration of residual impurities. An analysis of the temperature dependence of the charge-carrier concentration in the initial material (Fig. 25) showed that this dependence was governed by a shallow acceptor level with an activation energy of 10–12 meV and by a deep donor level with an activation energy of 150 meV. In this case, the compensation degree was 40% and the acceptor concentration was 10^{15} cm^{-3} [52, 53].

Surface gettering was accomplished using thin (~100 nm) yttrium films deposited either on one side (OSC, one-side coating) or both sides (TSC, two-side coating) of the wafer (Fig. 26) using thermal evaporation or plasma sputtering. The wafers were then subjected to thermal annealing (TA) in the atmosphere of purified hydrogen at 700–800°C; the duration of

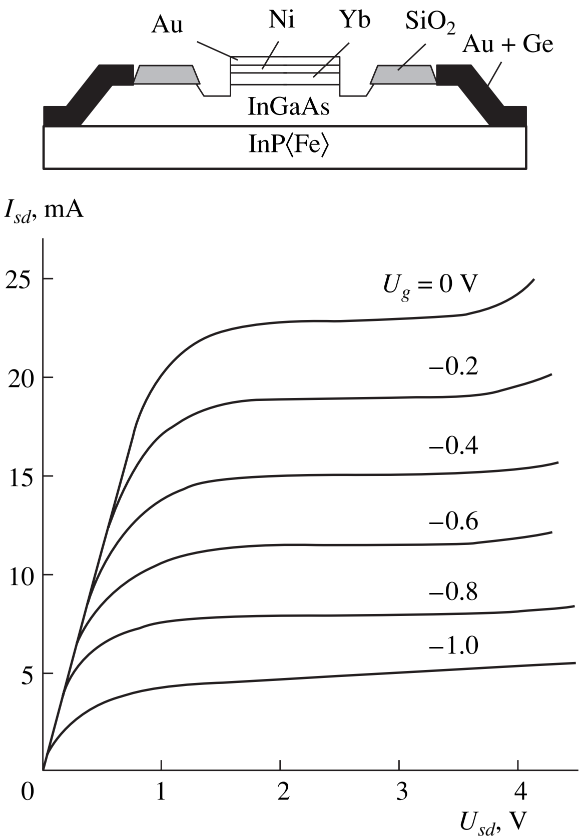

Fig. 23. Schematic representation of a Schottky barrier field-effect transistor and the current–voltage characteristics of this transistor at 300 K.

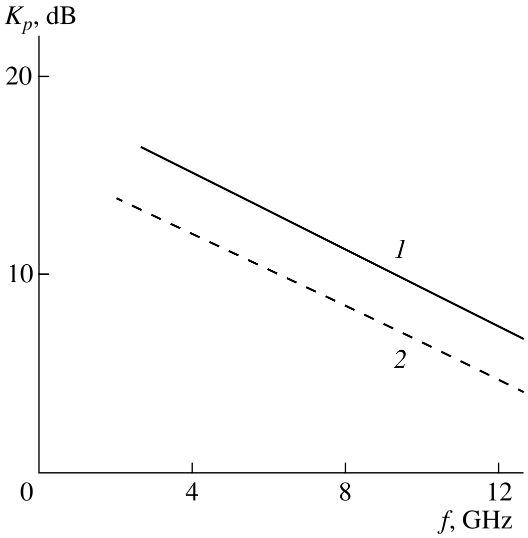

Fig. 24. Frequency dependences of the power gain for Schottky barrier field-effect transistors which are based on (*1*) InGaAs and (*2*) GaAs and have identical geometric parameters.

annealing ranged from 5 min to 38 h. It was shown that the use of TA makes it possible to control the charge-carrier concentration in the range from 10^8 to 10^{14} cm^{-3} and attain an electron mobility as high as 7000 cm^2 V^{-1} s^{-1} at 300 K; the above results depend on the duration and temperature of TA.

A decrease in the degree of compensation to 30% and an increase in the electron mobility to 7000 cm^2 V^{-1} s^{-1} were observed [52–54] once the initial GaAs wafer with a two-sided Y coating was subjected to TA for 5 h at 800°C. The temperature dependence of the electron concentration in the resulting material is governed only by a donor level with an activation energy of 430 meV (Fig. 25, curve *2*).

The carrier-concentration distribution over depth in gettered wafers was determined from capacitance–voltage measurements using Hg–GaAs Schottky barriers and an electrolyte–GaAs system in a chemical cell; it was possible to illuminate the electrolyte–semiconductor interface [50, 51]. A sulfuric acid etchant H_2SO_4 : H_2O_2 : H_2O (1 : 8 : 1) was used as the electrolyte; the latter ensured a constant etching rate of 4 μm/min for several days. When the electrolyte–semiconductor interface is exposed to light with $h\nu > E_g$, the photocurrent produced in the electrolyte–semiconductor system is proportional to the effective hole lifetime. Consequently, measurements of photocurrent during chemical etching of high-resistivity GaAs make it possible to qualitatively determine the distribution of the effective lifetime of nonequilibrium charge carriers.

It is noteworthy that we preliminarily studied the carrier-concentration profile in the samples using the Hg–GaAs Schottky barrier and layer-by-layer etching of GaAs in the H_2SO_4 : H_2O_2 : H_2O (1 : 8 : 50) etchant (the etching rate was 100 nm/min); the results showed that the wafer surface had the *p*-type conductivity with $p \approx 10^{16}$ cm^{-3} down to a depth of ~0.5 μm after the Y–GaAs structures had been subjected to TA for 0.5 h at 800°C with subsequent etching-off of the Y film in plasma. At the same time, the GaAs surface without a Y film (in the case of OSC gettering, Fig. 26c) also had the *p*-type conductivity with $p \approx 10^{17}$ cm^{-3} after TA for 0.5 h at 800°C [55, 56]. The thickness of the *p*-type layer was several micrometers; at a larger depth, inversion of the conductivity type was observed on both sides of the wafer and the electron concentration was no higher than ~10^{12} cm^{-3}.

The concentration profiles for majority charge carriers $N_D - N_A$ and the effective-lifetime (τ_{eff}) profiles for nonequilibrium charge carriers in gettered GaAs after TA (800°C, 0.5 h) are shown in Fig. 27. The profiles are virtually flat.

The surface layer had the *n*-type conductivity with $n \approx 10^{13}$–10^{14} cm^{-3} after TA for 0.25 h at 700°C and subsequent removal of Y films by plasma etching both in the case of OSC and TSC gettering. The thickness of the surface layer was several micrometers; at a larger depth, the concentration decreased to 10^{12} cm^{-3} or lower, depending on TA conditions (Fig. 27). It can be seen that gettering encompasses the entire volume of the sample even if the wafer is coated with a Y film only from one side. However, it is apparent that the uncoated surface also contributes to the gettering effect. It can be seen from Fig. 27 that the τ_{eff} profile is also flat after TA both at 700°C and at 800°C; the value of τ_{eff} is 30% larger after TA at 700°C than after TA at 800°C.

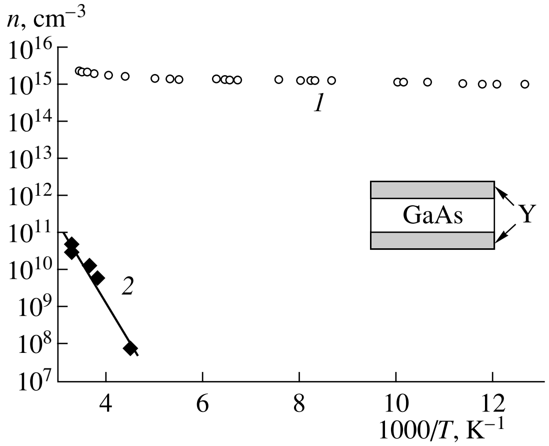

Fig. 25. Temperature dependences of electron concentration (*1*) in initial GaAs and (*2*) in GaAs after removal of a two-sided Y coating and heat treatment for 3 h.

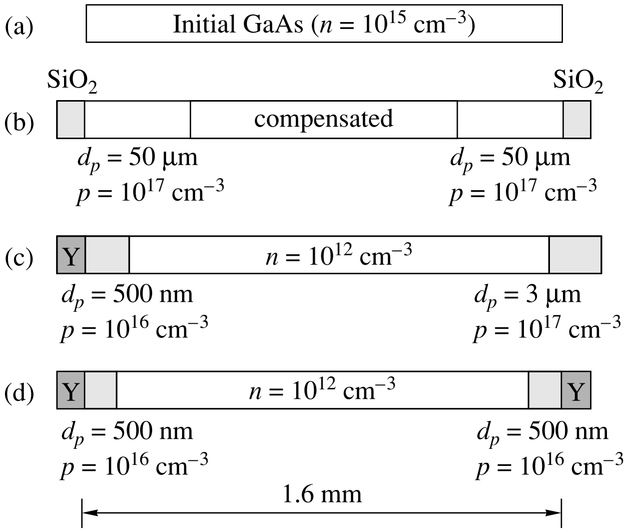

Fig. 26. Schematic representation of treated GaAs substrates: (a) initial GaAs, (b) GaAs with TSC using SiO_2 films, (c) GaAs with OSC using a Y film, and (d) GaAs with TSC using Y films.

The PL spectra measured at 2 K for the TSC-gettered samples prior to and after TA at 800°C are shown

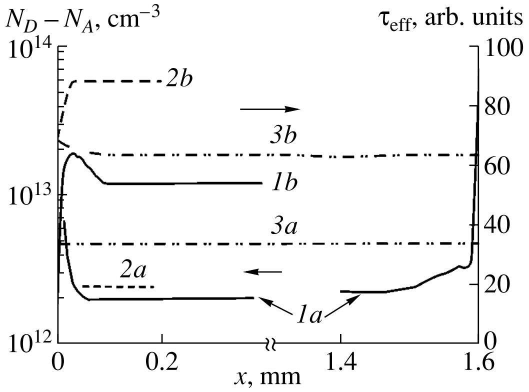

Fig. 27. (*1a–3a*) The charge-carrier concentration profiles and (*1b–3b*) hole-lifetime profiles after OSC gettering (*1a*, *1b*) for 0.5 h at 800°C and (*2a*, *2b*) for 0.25 h at 700°C and (*3a*, *3b*) after TSC gettering for 0.5 h at 800°C. The points x = 0 and 1.6 mm correspond to wafer surfaces after removal of the Y film and to an uncoated surface, respectively.

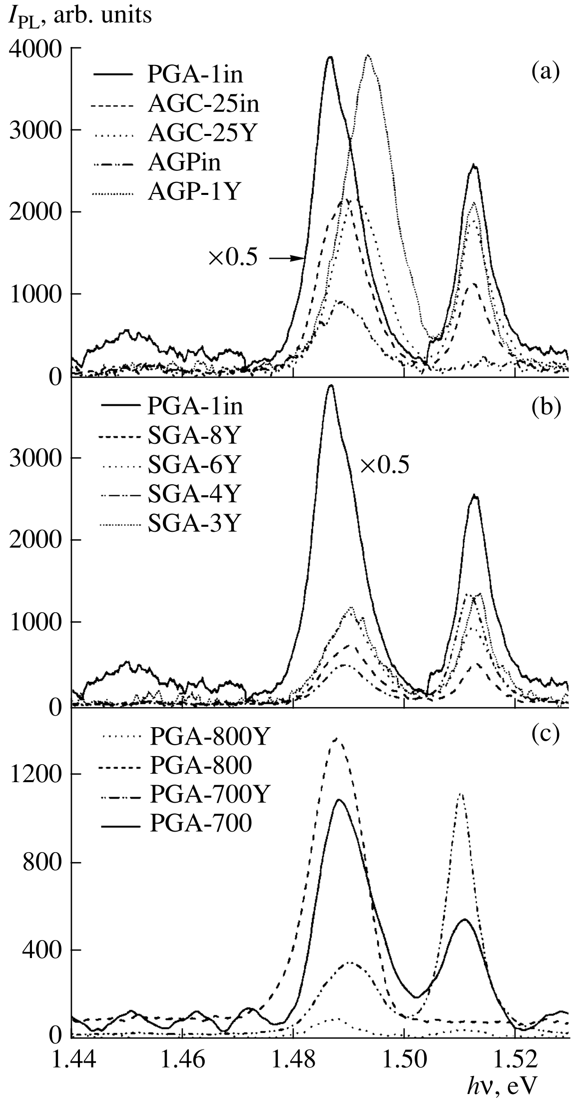

Fig. 28. Photoluminescence spectra of GaAs at 2 K for the samples before and after thermal annealing: (a, b) the TSC gettering after removal of a 50-μm-thick layer and (c) the OSC gettering. The annealing conditions are listed in Table 2.

in Figs. 28a and 28b. As can be seen from Fig. 28a and the data listed in Table 2, the PL spectrum of initial GaAs (PGA-1in) includes three bands peaked at 1.512, 1.487, and 1.45 eV. The band peaked at 1.512 eV corresponds to the exciton bound to a neutral acceptor (A^0X), and the band peaked at 1.487 eV corresponds to the two-hole transition of the exciton bound to the Si neutral acceptor [57]. The band peaked at 1.487 eV was dominant before gettering; the intensity of this band decreased significantly after gettering (sample SGA-8Y). At the same time, the impurity-related band peaked at 1.45 eV, which is apparently associated with intrinsic defects, disappears as a result of gettering [58–60].

The impurity-emission band peaked at 1.45 eV is not observed in the PL spectra of samples AGC-25in and AGPin grown by the Czochralski method under a layer of liquid boron oxide. Two bands peaked at 1.493 eV (related to a transition from the conduction band to the neutral carbon acceptor) and at 1.513 eV (A^0X) are observed in the PL spectra of the AGPin sample (GaAs:Cr) after gettering (sample AGP-1Y). At the same time, only a single band peaked at 1.488 eV and attributed to a transition from a neutral donor to a neutral acceptor (Mg or Be) was observed in the PL spectrum prior to gettering [57]. It is worth noting that the gettering effect for impurities and defects was observed in GaAs at $N_D - N_A < 10^{16}$ cm^{-3}. In this situation, the background concentration of charge carriers is governed by intrinsic defects. The PL spectra after TSC gettering are shown for different conditions of TA in Fig. 28. The edge-emission bands peaked at 1.513 and 1.514 eV are related to the D^+X and D^0X transitions, respectively. The studies have shown that TA for 3 h at 800°C is apparently optimal. The data obtained from microwave photoconductivity made it possible to make a similar conclusion.

The PL spectra measured after TSC gettering with the use of Y–Ni films are similar to those described above; however, the edge-emission band has a higher intensity (see Table 2). Consequently, gettering with the use of Y–Ni films is preferable from the standpoint of device applications. The PL spectra after the OSC gettering of the samples are shown in Fig. 28c. It can be seen that the acceptor-related band is prevalent in the PL spectra for uncoated surfaces at both annealing temperatures; at the same time, the excitonic edge band is dominant in the spectra for coated surfaces and is most intense after TA at 700°C. Thus, as follows from

Table 2. Heat-treatment conditions and the data on photoluminescence (PL) spectra at 2 K

Samples	Coating	T, °C	t, h	Features of the spectra (PL bands)								
				edge-emission band			impurity-emission band 1			I_{ed}/I_{im1}	impurity-emission band 2	
				$h\nu$, eV	I_{ed}	$\Delta h\nu$, meV	$h\nu$, eV	I_{im1}	$\Delta h\nu$, meV		$h\nu$, eV	I_{im2}
PGA-1in	–	–	–	1.512	2586.0	5.910	1.487	7771.2	9.110	0.333	1.450	581.3
SGA-8Y	TSC Y	800	0.25	1.512	1837.4	5.913	1.490	2584.3	9.672	0.711	–	–
SGA-6Y	TSC Y	800	0.5	1.513	3296.5	6.648	1.490	3855.6	9.677	0.855	–	–
SGA-4Y	TSG Y	800	3	1.512	46419.6	6.283	1.489	17724.4	9.312	2.619	–	–
PGA-4Y-370	TSC Y	800	3	1.512	10683.1	6.091	1.490	7715.0	8.241	1.385	–	–
SGA-3Y	TSC Y	800	28	1.514	1400.7	7.444	1.490	1235.8	9.679	1.133	–	–
AGC-25in	–	–	–	1.513	3765.5	6.463	1.489	7234.6	9.841	0.520	1.453	546.7
AGC-25Y	TSC Y	800	0.5	1.512	6303.5	6.281	1.491	7223.0	10.417	0.873	–	–
AGPin	–	–	–	–	–	–	1.488	925.8	10.199	–	–	–
AGP-1-Y	TSC Y	800	0.5	1.513	2120.3	5.170	1.493	3905.0	10.084	0.543	–	–
PGA1-10-3YNi	TSC YNi	800	0.25	1.511	6279.9	6.488	1.487	3578.9	10.435	1.755	–	–
PGA1-10-2YNi	TSC YNi	800	0.5	1.511	7289.3	6.558	1.488	2616.3	9.249	2.786	–	–
PGA1-6-1YNi	TSC YNi	800	1	1.512	2594.4	6.450	1.489	963.7	9.448	2.692	–	–
PGA1-6-2YNi	TSC YNi	800	2	1.512	2467.7	6.193	1.488	860.3	9.009	2.868	–	–
PGA1-SiO_2	TSC SiO_2	850	5	1.511	199.1	5.601	1.488	270.4	7.152	0.736	–	–
PGA1-SiO_2	TSC SiO_2	850	38	1.511	1223.7	5.449	1.486	3830.1	8.772	0.320	1.444	737.7
PGA-800Y	OSC Y	800	0.25	1.510	49.2	9.132	1.488	101.2	8.280	0.487	1.444	28.5
PGA-800	–	800	0.25	–	–	–	1.488	1368.3	10.863	–	–	–
PGA-700Y	OSC Y	700	0.25	1.511	1121.5	5.889	1.490	352.2	10.034	3.184	–	–
PGA-700	–	700	0.25	1.511	546.5	8.950	1.488	1091.6	11.160	0.501	–	–
SGA-1Y (*p*-type)	TSC Y	800	0.25	1.511	1070.4	7.225	1.489	1209.5	9.729	0.885	1.453	114.5
PGA1-6-2YNi (*p*-type)	TSC YNi	800	2	1.512	4571.0	6.341	1.489	1346.3	9.163	3.395	–	–
PGA1-10-2YNi (*p*-type)	TSC YNi	800	0.5	1.512	222.1	5.756	1.489	159.1	10.900	1.396	1.444	53.0
PGA1-10-1YNi (*p*-type)	TSC YNi	800	0.25	1.512	563.2	6.492	1.489	503.8	9.581	1.118	–	–

Fig. 28c and Table 2, gettering at a temperature of 700°C is preferable.

Spectral data for the *p*-type samples with $p \approx 10^{16}$–10^{17} cm^{-3} after gettering by Y and Y–Ni films are also listed in Table 2.

8. CONCLUSION

It is shown that doping of the solutions–melts with REEs in the course of LPE leads to the cleaning of InP, InGaAsP, and GaAs epitaxial layers of background impurities, mainly elements of Group VI; this cleaning is caused by interaction of the above impurities with REEs in the liquid phase, the formation of high-melting chalcogenides, and the precipitation of these chalcogenides from the solution–melt. Cleaning of the material is corroborated by (i) a decrease in the charge-carrier concentration in the layers to ~10^{13} cm^{-3} with a simultaneous increase in the carrier mobility to (7–10) × 10^4 cm^2 V^{-1} s^{-1} at 77 K, (ii) excitonic structure of the edge-luminescence spectra, (iii) the narrow lines in the spectra of photoexcitation of shallow-level donors, (iv) high values of the lifetime for nonequilibrium charge carriers (~10 μs), (v) high drift velocity of electrons in InGaAs (2.8 × 10^7 cm/s), and (vi) pure-green luminescence in GaP (λ = 555 nm).

It is ascertained that, as the content of isovalent REEs in the liquid phase increases from 0.001 to 0.1 at. %, inversion of the conductivity type occurs in InP and InGaAs epitaxial layers when the content of REEs is in the range of 0.001–0.008 at. %, depending on the background of acceptor impurities.

It is shown that the ultimate soluble concentration of REEs in the solid phase is no higher than 10^{15} cm^{-3} at the epitaxy temperature of 645°C; estimation of the distribution coefficient yielded the value of $<10^{-4}$.

It is ascertained that REEs, in addition to their interaction with background impurities in the liquid phase, interact with the main components of the solution–melt, particularly with phosphorus; as a result, supersaturation of the solution–melt with respect to phosphorus decreases, which should be taken into account when growing multilayered structures.

It is shown that joint doping of solutions–melts with an REE and Sn makes it possible to vary the electron concentration in the layers within 10^{14}–10^{17} cm^{-3}; the electron mobility is as high as 7000 cm^2 V^{-1} s^{-1} at 300 K in InGaAs doped with an REE and Sn (n = (1–2) × 10^{17} cm^{-3}).

The use of REEs in the technology of optoelectronic and microelectronic devices based on InGaAs/InP made it possible to develop the following structures and devices:

(I) structures with two-dimensional electron gas that feature an electron mobility of 1.23×10^4 cm^2 V^{-1} s^{-1} at 300 K and 7.3×10^4 cm^2 V^{-1} s^{-1} at 4.2 K and are not affected by irradiation with white light, which is very important for field-effect transistors with high electron mobility (HEMTs);

(II) photodetectors of various types: planar photoresistors based on InGaAs and InP for the spectral range of 0.2–1.6 μm; *p–i–n* photodiodes for the spectral range of 1–1.6 μm with a sensitivity of 0.7 A/W, a response speed of ~50 ps, and a dark-current density of 10^{-7} A/cm^2; avalanche photodiodes with sensitivity in the spectral range of 0.9–1.35 μm, a multiplication factor $M = 200$, and a dark-current density of ~10^{-5} A/cm^2 at $0.9U_f$; and vertical field-effect phototransistors, which are designed for the spectral range of 1.0–1.6 μm and have a static amplification coefficient of ~100;

(III) Schottky barriers based on *n*-InP and *n*-InGaAs with leakage currents that are smaller than those for Au–*n*-InP(InGaAs) Schottky barriers by several orders of magnitude;

(IV) MIS structures based on InP with the density of surface states at the insulator–semiconductor interface $<10^{11}$ eV^{-1} cm^{-2}, a fixed charge amounting to $<10^{11}$ electron/cm^2, and hysteresis voltage lower than 0.2 V;

(V) Schottky barrier field-effect transistors based on *n*-InGaAs ($n \approx 2 \times 10^{17}$ cm^{-3}) with a transconductance of 180 mS/mm at 300 K and power gain of 17 dB at 4 GHz for the gate area of 1.5 × 290 μm;

(VI) LED *p–n* structures based on GaP and designed for the pure-green (λ = 555 nm) emission; and

(VII) Gunn diodes based on *n*-InGaAs/n^+-InP with a generation efficiency of 2.5% in the 8-mm wavelength band of microwaves.

The results of studying the surface gettering of GaAs by REE films can be summarized as follows.

(i) Surface gettering of 1.6-mm-thick GaAs wafers with an initial carrier concentration of 2×10^{15} cm^{-3} and mobility of 1500–2000 cm^2 V^{-1} s^{-1} made it possible to decrease the carrier concentration to 10^8 cm^{-3} and increase the mobility to 7000 cm^2 V^{-1} s^{-1}.

(ii) The surface gettering of GaAs by Y films for one- and two-sided coating of the wafer surface is a volume effect.

(iii) It is shown that the gettering effect manifests itself even after annealing at a comparatively low temperature (700°C).

(iv) Flat profiles of the carrier concentration $N_D - N_A$ and effective lifetime are extraordinary results.

(v) Generation of antipodal $\mathrm{As_{Ga}}$ and $\mathrm{Ga_{As}}$ antisite defects and, possibly, various intrinsic defects (such as V_{Ga}, V_{As}, I_{Ga}, and I_{As}) occurs in the course of gettering. Apparently, spatial separation of antipodal defects and formation of complexes containing these defects are more important during gettering than direct annihilation of antipodal defects; as a result of this spatial separation and complex formation, the charge-carrier concentration decreases and the carrier mobility increases.

(vi) Gettered GaAs can be promising as a material for high-voltage high-power devices; for X-ray and nuclear-radiation detectors and detectors of nuclear particles (including neutrinos); and for very large-scale and very high-speed integrated circuits in microelectronics and optoelectronics. It is important that the technology for production of gettered GaAs is simple and is compatible with conventional technology for preparation of substrates; there are only two additional operations: deposition of gettering films and heat treatment.

Thus, the results of studies reported in this paper show that the use of REEs in the technology of III–V compounds and optoelectronic and microelectronic devices based on these compounds is efficient and promising.

REFERENCES

1. J. Mandelkorn, L. Schwartz, J. Broder, and H. Kautz, J. Appl. Phys. **35**, 2258 (1964).
2. N. T. Bagraev, E. P. Bochkarev, L. S. Vlasenko, *et al.*, Izv. Akad. Nauk SSSR, Neorg. Mater. **14**, 614 (1978).
3. G. V. Lashkarev, A. I. Dmitriev, G. A. Sukach, and V. A. Shershel’, Fiz. Tekh. Poluprovodn. (Leningrad) **5**, 2075 (1971) [Sov. Phys. Semicond. **5**, 1808 (1971)].

4. S. I. Pyshkin, S. I. Radutsan, and S. V. Slobodchikov, Fiz. Tekh. Poluprovodn. (Leningrad) **1**, 1013 (1967) [Sov. Phys. Semicond. **1**, 847 (1967)].
5. L. F. Zakharenkov, V. V. Kozlovskii, A. T. Gorelenok, and N. M. Shmidt, in *Semiconductor Technology. Processing and Novel Fabrication Techniques* (Wiley, New York, 1997), p. 91.
6. A. T. Gorelenok, A. V. Kamanin, and N. M. Shmidt, Microelectron. J. **26**, 705 (1995).
7. V. A. Kasatkin, F. P. Kesamanly, V. G. Makarenko, and N. S. Tselishcheva, Fiz. Tekh. Poluprovodn. (Leningrad) **15**, 2432 (1981) [Sov. Phys. Semicond. **15**, 1414 (1981)].
8. H. Ennen and J. Schneider, J. Electron. Mater. **13**, 114 (1984).
9. V. F. Masterov and L. F. Zakharenkov, Fiz. Tekh. Poluprovodn. (Leningrad) **24**, 610 (1990) [Sov. Phys. Semicond. **24**, 383 (1990)].
10. H. Nakagome and K. Takahei, Jpn. J. Appl. Phys. **28**, L2098 (1989).
11. K. Thonke, H. U. Hermann, and J. Schneider, J. Phys. C: Solid State Phys. **21**, 5881 (1988).
12. D. L. Adler, D. C. Jacobson, D. J. Eaglesham, *et al.*, Appl. Phys. Lett. **61**, 2181 (1992).
13. M. M. Factor and J. Haigh, U.S. Patent No. 4339302 (1982).
14. K. A. Gatsoev, A. T. Gorelenok, S. I. Karpenko, *et al.*, Fiz. Tekh. Poluprovodn. (Leningrad) **17**, 2148 (1983) [Sov. Phys. Semicond. **17**, 1373 (1983)].
15. N. T. Bagraev, L. S. Vlasenko, K. A. Gatsoev, *et al.*, Fiz. Tekh. Poluprovodn. (Leningrad) **18**, 83 (1984) [Sov. Phys. Semicond. **18**, 49 (1984)].
16. W. Körber, J. Weber, A. Hangleiter, *et al.*, J. Cryst. Growth **79**, 741 (1986).
17. A. V. Markov, A. Y. Polyakov, N. B. Smirnov, *et al.*, Nucl. Instrum. Methods Phys. Res. A **439**, 651 (2000).
18. V. F. Andrievskiĭ, A. T. Gorelenok, N. A. Zagorel'skaya, *et al.*, Fiz. Tekh. Poluprovodn. (St. Petersburg) **36**, 404 (2002) [Semiconductors **36**, 382 (2002)].
19. F. Hulliger, in *Handbook on the Physics and Chemistry of Rare Earth*, Ed. by K. A. Schneider and L. Eyring (North-Holland, Amsterdam, 1979), Vol. 4, p. 153.
20. H. Nakagome, K. Takanei, and Y. Homma, J. Cryst. Growth **85**, 345 (1987).
21. O. Aina, M. Mattingly, S. Steinhauser, *et al.*, J. Cryst. Growth **21**, 215 (1988).
22. V. N. Romanenko and V. S. Kheĭfets, Izv. Akad. Nauk SSSR, Neorg. Mater. **9**, 190 (1973).
23. V. Kh. Baĭramov, L. F. Zakharenkov, G. V. Il'menkov, *et al.*, Fiz. Tekh. Poluprovodn. (Leningrad) **23**, 1496 (1989) [Sov. Phys. Semicond. **23**, 927 (1989)].
24. A. T. Gorelenok, V. G. Gruzdov, R. Kumar, *et al.*, Fiz. Tekh. Poluprovodn. (Leningrad) **22**, 35 (1988) [Sov. Phys. Semicond. **22**, 21 (1988)].
25. Yu. A. Karpov, V. V. Mazurenko, V. V. Petrov, *et al.*, Fiz. Tekh. Poluprovodn. (Leningrad) **18**, 368 (1984) [Sov. Phys. Semicond. **18**, 230 (1984)].
26. V. G. Golubev, A. T. Gorelenok, V. I. Ivanov-Omskiĭ, *et al.*, Pis'ma Zh. Tekh. Fiz. **11**, 347 (1985) [Sov. Tech. Phys. Lett. **11**, 143 (1985)].
27. A. T. Gorelenok, V. V. Mamutin, D. V. Pulyaevskiĭ, *et al.*, Fiz. Tekh. Poluprovodn. (Leningrad) **21**, 1498 (1987) [Sov. Phys. Semicond. **21**, 912 (1987)].
28. A. Galavanauskas, A. T. Gorelenok, Z. Dobrovol'skis, *et al.*, Fiz. Tekh. Poluprovodn. (Leningrad) **22**, 1672 (1988) [Sov. Phys. Semicond. **22**, 1055 (1988)].
29. V. Balinas, A. T. Gorelenok, A. Krotkus, *et al.*, Fiz. Tekh. Poluprovodn. (Leningrad) **24**, 848 (1990) [Sov. Phys. Semicond. **24**, 534 (1990)].
30. V. G. Golubev, A. T. Gorelenok, V. I. Ivanov-Omskiĭ, *et al.*, Izv. Akad. Nauk SSSR, Ser. Fiz. **50**, 282 (1986).
31. C. Aldreich and R. L. Greene, Phys. Status Solidi B **93**, 343 (1979).
32. Zh. I. Alferov, A. T. Gorelenok, A. V. Kamanin, *et al.*, Fiz. Tekh. Poluprovodn. (Leningrad) **18**, 1230 (1984) [Sov. Phys. Semicond. **18**, 768 (1984)].
33. A. T. Gorelenok, D. N. Rekhviashvili, M. Yu. Nadtochiĭ, and V. M. Ustinov, Pis'ma Zh. Tekh. Fiz. **16** (8), 47 (1990) [Sov. Tech. Phys. Lett. **16**, 302 (1990)].
34. A. T. Gorelenok, D. N. Rekhviashvili, M. Yu. Nadtochiĭ, and V. M. Ustinov, Fiz. Tekh. Poluprovodn. (Leningrad) **25**, 908 (1991) [Sov. Phys. Semicond. **25**, 549 (1991)].
35. A. T. Gorelenok and M. V. Shpakov, Fiz. Tekh. Poluprovodn. (St. Petersburg) **30**, 488 (1996) [Semiconductors **30**, 269 (1996)].
36. A. T. Gorelenok, A. V. Kamanin, and M. V. Shpakov, Inst. Phys. Conf. Ser. **155**, 385 (1997).
37. V. I. Borisov, A. T. Gorelenok, S. G. Dmitriev, *et al.*, Fiz. Tekh. Poluprovodn. (St. Petersburg) **26**, 607 (1992) [Sov. Phys. Semicond. **26**, 345 (1992)].
38. Zh. I. Alferov, A. T. Gorelenok, V. G. Dal'nichenko, *et al.*, Pis'ma Zh. Tekh. Fiz. **9**, 1516 (1983) [Sov. Tech. Phys. Lett. **9**, 649 (1983)].
39. A. T. Gorelenok, V. G. Danil'chenko, Z. P. Dobrovol'skis, *et al.*, Fiz. Tekh. Poluprovodn. (Leningrad) **19**, 1460 (1985) [Sov. Phys. Semicond. **19**, 898 (1985)].
40. V. M. Andreev, M. S. Bogdanovich, A. T. Gorelenok, *et al.*, Zh. Tekh. Fiz. **55**, 1566 (1985) [Sov. Phys. Tech. Phys. **30**, 907 (1985)].
41. V. M. Andreev, A. T. Gorelenok, M. Z. Zhingarev, *et al.*, Fiz. Tekh. Poluprovodn. (Leningrad) **19**, 668 (1985) [Sov. Phys. Semicond. **19**, 411 (1985)].
42. V. A. Volkov, A. T. Gorelenok, V. N. Luk'yanov, *et al.*, Pis'ma Zh. Tekh. Fiz. **13**, 1059 (1987) [Sov. Tech. Phys. Lett. **13**, 442 (1987)].
43. K. Nishida, K. Taguchi, and Y. Matsumoto, Appl. Phys. Lett. **35**, 251 (1979).
44. S. R. Forrest, IEEE J. Quantum Electron. **17**, 217 (1981).
45. O. K. Kim, S. R. Forrest, W. A. Bonner, and R. G. Smith, Appl. Phys. Lett. **39**, 402 (1981).
46. Zh. I. Alferov, M. G. Vasil'ev, A. T. Gorelenok, *et al.*, Pis'ma Zh. Tekh. Fiz. **8**, 722 (1982) [Sov. Tech. Phys. Lett. **8**, 312 (1982)].
47. M. S. Bogdanovich, V. I. Korol'kov, N. Rakhimov, and T. S. Tabarov, Pis'ma Zh. Tekh. Fiz. **11**, 89 (1985) [Sov. Tech. Phys. Lett. **11**, 35 (1985)].
48. A. T. Gorelenok, V. G. Gruzdov, V. G. Dal'nichenko, *et al.*, Pis'ma Zh. Tekh. Fiz. **10**, 1294 (1984) [Sov. Tech. Phys. Lett. **10**, 546 (1984)].
49. S. Loualiche, H. L'Haridon, A. Le Corre, *et al.*, Appl. Phys. Lett. **52**, 540 (1988).

50. Zh. I. Alferov, V. I. Bosyĭ, A. T. Gorelenok, *et al.*, Pis’ma Zh. Tekh. Fiz. **14**, 2001 (1988) [Sov. Tech. Phys. Lett. **14**, 784 (1988)].
51. A. T. Gorelenok, V. L. Kryukov, and G. P. Furmanov, Pis’ma Zh. Tekh. Fiz. **20** (13), 60 (1994) [Tech. Phys. Lett. **20**, 546 (1994)].
52. N. Shmidt, A. Gorelenok, V. V. Emtsev, *et al.*, Solid State Phenom. **69–70**, 279 (1999).
53. L. S. Vlasenko, A. T. Gorelenok, V. V. Emtsev, *et al.*, Fiz. Tekh. Poluprovodn. (St. Petersburg) **35**, 184 (2001) [Semiconductors **35**, 177 (2001)].
54. L. S. Vlasenko, A. T. Gorelenok, V. V. Emtsev, *et al.*, Pis’ma Zh. Tekh. Fiz. **27** (1), 19 (2001) [Tech. Phys. Lett. **27**, 9 (2001)].
55. V. F. Andrievskiĭ, A. T. Gorelenok, N. A. Zagorel’skaya, *et al.*, Fiz. Tekh. Poluprovodn. (St. Petersburg) **36**, 404 (2002) [Semiconductors **36**, 382 (2002)].
56. V. F. Andrievskiĭ, A. T. Gorelenok, N. A. Zagorel’skaya, *et al.*, Pis’ma Zh. Tekh. Fiz. **27** (23), 67 (2001) [Tech. Phys. Lett. **27**, 1013 (2001)].
57. L. Pavesi and M. Guzzi, J. Appl. Phys. **75**, 4779 (1994).
58. A. T. Gorelenok, V. F. Andrievskii, A. V. Kamanin, *et al.*, J. Phys.: Condens. Matter **14**, 13105 (2002).
59. A. T. Gorelenok, V. F. Andrievskii, A. V. Kamanin, *et al.*, Nucl. Instrum. Methods Phys. Res. B **186**, 240 (2002).
60. A. T. Gorelenok, V. F. Andrievskii, A. V. Kamanin, *et al.*, in *Proceedings of 2001 European Microwave Week: GaAs’2001 Conference* (London, 2001), p. 13.

Translated by A. Spitsyn

Semiconductors, Vol. 37, No. 8, 2003, pp. 915–917. Translated from Fizika i Tekhnika Poluprovodnikov, Vol. 37, No. 8, 2003, pp. 941–942.
Original Russian Text Copyright © 2003 by Prikhod'ko.

ELECTRONIC AND OPTICAL PROPERTIES
OF SEMICONDUCTORS

Electromagnetic Effect in High-Temperature Superconductivity: 15 Years of Investigations (1987–2002) at the Department of Experimental Physics of St. Petersburg State Technical University

A. V. Prikhod'ko

St. Petersburg State Technical University, ul. Politekhnicheskaya 29, St. Petersburg, 195251 Russia

Submitted February 3, 2003; accepted for publication February 4, 2003

Abstract—A review of the experimental investigations of high-temperature superconductivity performed at the Department of Experimental Physics of St. Petersburg State Technical University (SPTU) under the direction of Professor V.F. Masterov, Doctor of Physics and Mathematics, is presented. The emphasis will be on the investigation of the weak-superconductivity effect discovered in samples composed of a high-temperature superconductor (HTSC) and selenium. In 1975, Masterov became the Head of the Solid-State Spectroscopy Laboratory on the recommendation of the Head of the Department Professor D.N. Nasledov. Since 1987, one of the successful lines of research in the laboratory has been the investigation of high-temperature superconductivity. *© 2003 MAIK "Nauka/Interperiodica".*

Twelve years have elapsed since V.F. Masterov published a review devoted to the macroscopic effects in HTSCs and 15 years have passed since the investigations of high-temperature superconductivity began at the department of experimental physics of SPTU. All of the macroscopic phenomena in HTSCs are related to the so-called electromagnetic effect, which was discovered virtually simultaneously by Masterov and by the research teams of Osip'yan, Müller, and Bednortz in 1987. We mean the electromagnetic-energy absorption by a HTSC sample. The effects of magnetic-flux quantization observed in this case when samples are cooled in a magnetic field make it possible to obtain information about the structure of the superconducting state and the transition to this state. Masterov investigated the nature of electromagnetic-energy absorption and concluded that it is the multiply connected Josephson medium that is crucial for the appearance of the superconducting state in granular samples. The characteristic size of the smallest individual circuit with a weak-coupling section is assumed to be controlled by the linear size of a grain. In this case, it is possible to observe the magnetic-flux quantization for a reasonably uniform crystal-size distribution. It was established that weak coupling occurs via intercrystalline regions. A significant conclusion was also made: the circuit-size distribution has to be narrow. This circumstance leads to absorption of microwave power in a narrow temperature interval. The artificial variation in the circuit area while increasing the fraction of the nonsuperconducting phase performed by Masterov confirmed the model suggested. In this case, individual circuits are weakly coupled because an increase in the magnetic field does not lead to superconductivity decay in an individual circuit but only reduces the Meissner effect. The result obtained in the form of a dependence of the magnetic-field strength on circuit area agrees well with known concepts about flux quantization in a superconducting ring.

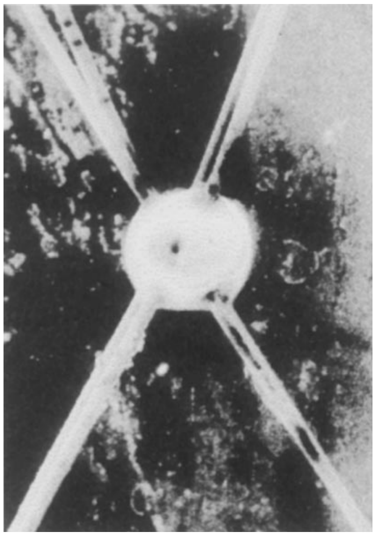

Fig. 1. HTSC–Se bulk sample; the diameter of each of the four tungsten electrodes is 50 μm.

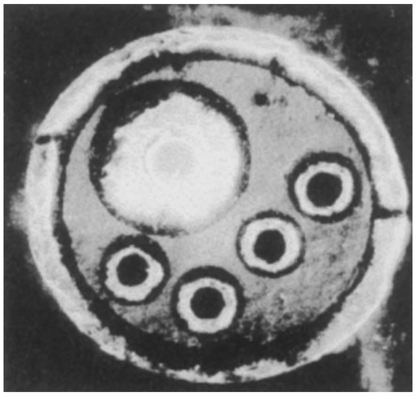

Fig. 2. Cross section of a quasi-one-dimensional sample. The inner diameter of the basic capillary is 110 μm. Five capillaries each with an inner diameter of 20 μm and 10 mm long are placed inside this capillary. The HTSC–Se medium is placed inside the capillaries.

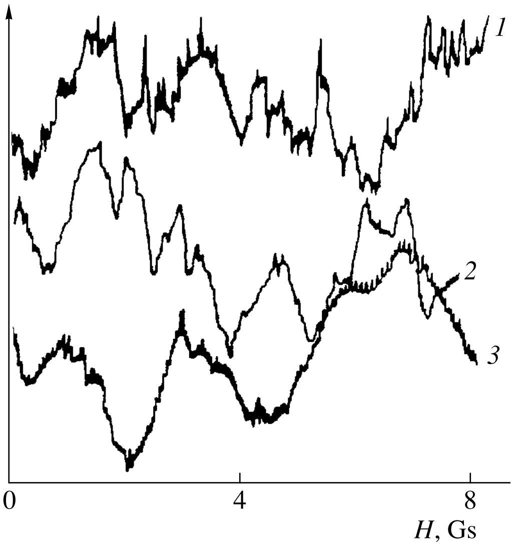

Fig. 3. Mesoscopic structure of the microwave-absorption signal: the dependence of the first derivative of the microwave-absorption signal with respect to the magnetic field on magnetic field.

In the early 1990s, studies of HTSC–semiconductor composites [2–4] began at the aforementioned department. Bulk HTSC–selenium structures were fabricated, and a cycle of investigations, which served as the basis for the continuation of the studies in the late 1990s, was performed. The successful realization of the studies was due to several reasons. The first of these was the appropriate choice of the semiconductor—amorphous selenium. This semiconductor was chosen because Masterov had a good understanding of the object of investigation, since he had investigated the electron spin resonance in selenium, while researching his Candidate dissertation [5]. Second, the microwave method (the basic one in experiments) was also well known by Masterov. In Figs. 1 and 2, we show two objects fabricated at that time: an HTSC–Se bulk sample and an HTSC–Se capillary. When processing the current–voltage characteristics obtained for the HTSC–Se bulk samples, Masterov called attention to the existence of a Josephson current in the structures with the size of weak coupling exceeding the critical one by an order of magnitude. It was suggested that a new mechanism of current transport forming the Josephson medium manifests itself in this case. When discussing the results, attention was drawn to alternative mechanisms of superconductivity, in particular, to the model of superconductivity in structures with U^- centers. Unfortunately, Masterov passed away before the results of studies in this field were published [6].

Let us consider the electromagnetic experiment with HTSC–Se capillaries. In Fig. 3, we show the field dependence of absorption at 77 K. The observation of a signal in the mesoscopic form makes it possible to estimate the areas of the Josephson circuits and compare these areas with the known size distribution of HTSC crystals in the selenium bulk. Our attention is drawn to the following fact: the appearance of circuits whose size is larger than that of an individual HTSC crystal (14 μm; the magnetic field strength $B = 0.4$ G). After several temperature cycles, these features disappear (compare curves *1* and *3* in Fig. 3). At the same time, conventional magnetic-flux quantization ($B = 6$–2 G) is observed in circuits related to the size of an individual HTSC crystal (approximately 3 μm). Statistical processing of the results of X-ray scanning of the surface yields a distribution with a mean grain size of 3 μm. The mechanism of the appearance of unconventional circuits is now investigated in terms of a new model of superconductivity.

The next cycle of investigations was started at the Department with the discovery of fullerenes and the detection of superconductivity in structures based on them. The investigations in this field were described in detail in the review devoted to the investigations of fullerenes at the Department [7]. The microwave investigations of single-crystal HTSCs are described in [8].

REFERENCES

1. V. F. Masterov, in *High-Temperature Superconductivity: Fundamental and Applied Studies*, Ed. by A. A. Kiselev (Mashinostroenie, Leningrad, 1990), No. 1, p. 405.

2. A. V. Prikhod’ko and V. F. Masterov, Pis’ma Zh. Tekh. Fiz. **19** (14), 17 (1993) [Tech. Phys. Lett. **19**, 440 (1993)].

3. A. V. Prikhod'ko, S. B. Kozyrev, and V. F. Masterov, Sverkhprovodimost: Fiz. Khim. Tekh. **3**, 1130 (1989).
4. A. V. Prikhod'ko, L. Z. Dapkus, and V. F. Masterov, Pis'ma Zh. Tekh. Fiz. **19** (12), 34 (1993) [Tech. Phys. Lett. **19**, 369 (1993)].
5. V. F. Masterov, Candidate's Dissertation (Leningrad Polytechnical Inst., 1971).
6. A. V. Prikhod'ko, K. D. Tsendin, and B. P. Popov, Fiz. Tekh. Poluprovodn. (St. Petersburg) **35**, 707 (2001) [Semiconductors **35**, 677 (2001)].
7. A. V. Prikhod'ko and O. I. Kon'kov, Fiz. Tekh. Poluprovodn. (St. Petersburg) **36**, 1286 (2002) [Semiconductors **36**, 1204 (2002)].
8. A. V. Prikhod'ko and N. M. Shibanova, Nauchn.-Tekh. Vedomosti Peterb. Gos. Tekh. Univ., No. 4, 118 (2001).

Translated by V. Bukhanov

Semiconductors, Vol. 37, No. 8, 2003, pp. 918–922. Translated from Fizika i Tekhnika Poluprovodnikov, Vol. 37, No. 8, 2003, pp. 943–946.
Original Russian Text Copyright © 2003 by Masterov, Shtel'makh, Maslov, Mikhrin, Samorukov.

ELECTRONIC AND OPTICAL PROPERTIES OF SEMICONDUCTORS

The Relaxation of the Neutral State of Manganese in Gallium Arsenide

V. F. Masterov†**, K. F. Shtel'makh, V. P. Maslov, S. B. Mikhrin, and B. E. Samorukov**

St. Petersburg State Technical University, Politekhnicheskaya ul. 29, St. Petersburg, 195251 Russia

e-mail: shtelmah@spes.stu.neva.ru

Submitted February 3, 2003; accepted for publication February 4, 2003

Abstract—Results of investigations of the longitudinal magnetic relaxation of the neutral state of the Mn^0 center in GaAs are presented. Relaxation mechanisms were determined from the broadening of the electron-spin-resonance line in the temperature range of 3.4–8.2 K and from the variation in the nuclear relaxation rate in the range of 36–310 K. The nuclear relaxation investigation demonstrates that the electron relaxation is governed by the interaction between lattice vibrations and local vibrations of the center. This allows one to represent the electron relaxation at low temperatures as the consequence of anharmonicity of local vibrations of the electron dipole moment of the Mn^0 center. *© 2003 MAIK "Nauka/Interperiodica".*

1. INTRODUCTION

The results of investigating the spin-lattice relaxation (SLR) of a paramagnetic center are of great help in interpreting the results of electron spin resonance (ESR), studies especially when the structure of the spectrum, which allows one to determine the true spin of the paramagnetic state, is absent. Furthermore, the manifestation of the excited state of the center in the spectrum of acoustic vibrations of the lattice (the Debye spectrum) is possible. This makes it possible, using SLR investigations, to independently determine the relatively small energy spacing between the ground and excited states of the center [1].

A direct investigation of effects related to the manifestation of the spin-lattice relaxation, specifically, the saturation of the signal and the relaxation broadening of the ESR line [2, 3], is often possible only in a limited temperature range due to the high rate of SLR. Therefore, the investigation of nuclear SLR makes it possible to study electron relaxation at higher temperatures [4]. This is possible since the nuclear SLR time τ_1 is substantially longer than the electron-relaxation time T_1. If the dependence of the time of correlation between the nuclear and electronic subsystems on temperature is sufficiently weak, it will then be possible to assume that the nuclear relaxation rate is proportional to the electron relaxation rate.

In various publications, the results of [5], which was devoted to the investigation of the temperature dependence of ultrasonic absorption, were discussed. Ultrasonic absorption is of the relaxation type, which makes it possible to determine the relaxation time from the frequency at which the absorption is strongest. The results of [5] admit ambiguous interpretation of the temperature dependences of the relaxation time, which was considered in detail in [6]. The second-order Raman process with the participation of a weakly split multiplet of the ground state of a neutral Mn center (the Orbach–Blum mechanism) and the first-order process in which phonons are involved were compared. A phonon is in resonance with the spacing between the ground state of the center and the level that manifests itself in the Debye spectrum and is due to the impurity (the Orbach–Aminov mechanism). Comparison has demonstrated that the rate of the Raman process in the temperature range $7 \text{ K} < T < 10 \text{ K}$ should be substantially higher, even with allowance made for the random stresses affecting the center.

In this study, we report the results of investigating relaxation in a wide temperature range. The use of a wide temperature range allowed us to obtain a considerable range of variation in the value of T_1. The results demonstrate that the relaxation of the Mn^0 center cannot be considered in terms of conventional concept of interaction of the magnetic moment of a center with lattice vibrations.

Sample A59 was used for measurements. The sample properties are described in [7]. In the low-temperature region, the measurements were carried out using an ER-220D Brucker ESR spectrometer. At higher temperatures, we used a nuclear magnetic resonance (NMR) relaxometer, operating at a frequency of 10 MHz, with the same parameters as those described in [8]. The NMR relaxation was measured using the nuclei of the Ga^{71} isotope.

---

† Deceased.

2. RESULTS OF LOW-TEMPERATURE MEASUREMENTS

The magnetic-resonance spectrum of a neutral Mn center in GaAs is due to two transitions which correspond to the selection rules $\Delta m = 1$ and $\Delta m = 2$. The g-factor is $g = 2.82$. The main spectral features are reported in [9].

The SLR investigations of the neutral state of manganese Mn^0 were carried out in the temperature range of 3.8–8 K for the transition with $\Delta m = 2$ [10]. Above 8.3 K, the ESR spectrum of the Mn^0 state is not observed due to strong broadening of the line. This circumstance, first, unambiguously points to a high SLR rate and, second, suggests the method of its estimation from the measurement of the line width. For the centers with a spin larger than 1/2, it is assumed that the probabilities of relaxation transitions for various spin states are equal to each other.

The SLR rate may be estimated from the uncertainty relation $\Delta E \Delta t \approx h$ [3]. In this case, the energy uncertainty ΔE controls the variation in the ESR-line width. Specifically, $\Delta E = g\mu_B\delta(\Delta H)$, where ΔH is the ESR-line width, $\delta(\Delta H)$ is the variation in ΔH relative to the temperature-independent value, and μ_B is the Bohr magneton. The time uncertainty Δt is comparable with the longitudinal relaxation time T_1. Since the width of an individual ESR line of the Mn^0 center at 3.8 K is approximately equal to the hyperfine-interaction constant ~50 G [9], substantial broadening of the spectrum should be expected even for $\delta(\Delta H) \approx \Delta H/2$. Substituting these quantities into the uncertainty relation, we can demonstrate that, for the transition with $\Delta m = 2$, the variation in ΔH by 25 G corresponds to $\Delta t \equiv T_1 \approx 5 \times 10^{-9}$ s, which is in good agreement with [5].

The line width cannot be determined directly from the inflection point of the line due to poor spectral resolution. Therefore, with allowance made for the fact that the concentration of the states of Mn is constant in this temperature range, the line width was determined from the relation [2]

$$N = KI(\Delta H)^2, \qquad (1)$$

where N is the number of corresponding paramagnetic centers, K is the constant, and I is the intensity of the ESR signal.

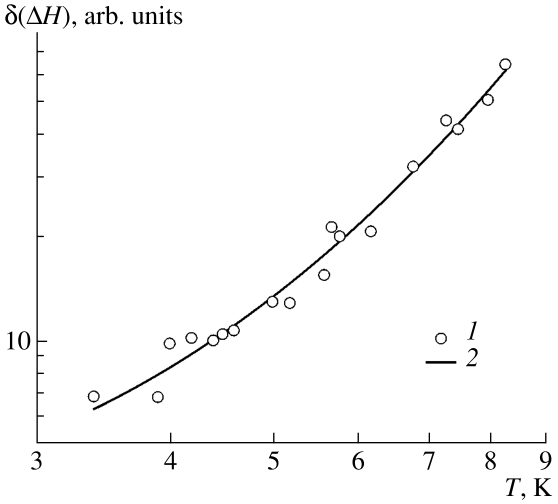

Fig. 1. Temperature dependence of the variation in the ESR-line width for the Mn^0 center on a double logarithmic scale. (*1*) Results of interpretation of the experimental data; (*2*) approximation by polynomial (2). The parameters are given in the text.

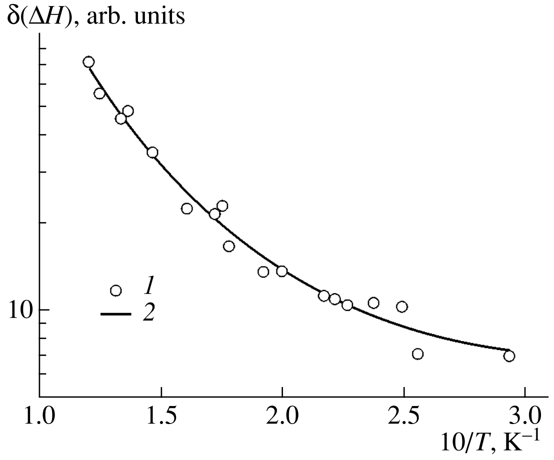

Fig. 2. Temperature dependence of the variation in the ESR-line width for the Mn^0 center on a semilogarithmic scale. (*1*) Results of interpretation of the experimental data; (*2*) results of approximation by formula (3).

The measurement results are shown in Figs. 1 and 2. Since the absolute value of the SLR rate is unimportant (admittedly high) and only the temperature dependence $1/T_1$ is of interest, the magnitude of $\delta(\Delta H)$ is plotted along the ordinate axis. As can be seen from Figs. 1 and 2, the dependence obtained may be approximated with the same accuracy either as a polynomial,

$$T_1^{-1} = aT + bT^3 + cT^5, \qquad (2)$$

or as an exponential function

$$T_1^{-1} = d\exp(-\Delta E/kT) + eT. \qquad (3)$$

The parameters characterizing the dependences were determined from the minimum squared deviation of the calculated dependence from the experimental data (minimum of χ^2).

The minima of χ^2 coincide irrespective of the chosen approximation. The values of the factors a, b, and c, which characterize the polynomial representation of

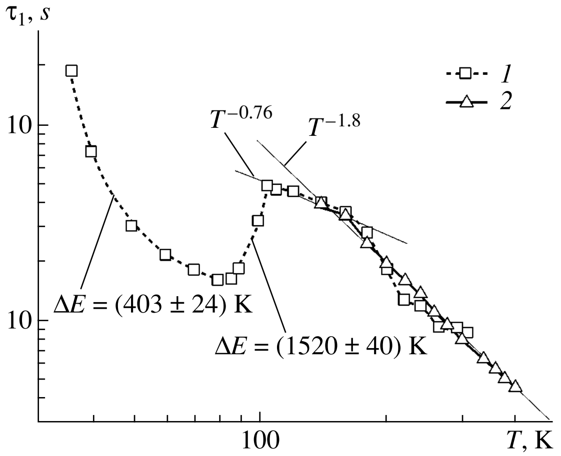

Fig. 3. Temperature dependences of the nuclear spin-lattice relaxation time: (*1*) Ga^{71} nuclei in the sample A59; (*2*) results of [14] obtained in a high-temperature region for a similar sample. It can be seen that, at $T < 105$ K, the dependences cannot be described by polynomials. Solid lines represent the results of a polynomial approximation in the range of $105\text{ K} < T < 310$ K. Designations correspond to the temperature dependences of τ_1 or to the powers of exponentials for different temperature ranges.

the results, are equal to 1.08 ± 0.59, 0.05 ± 0.03, and $(7 \pm 4) \times 10^{-4}$ arbitrary units, respectively. This means that virtually over the entire temperature range, the dependence is determined by the bT^3 term, and, only at 8 K are the contributions to the relaxation of the second and third terms comparable. This fact somewhat disagrees with the results of [5, 6]. The values of ΔE determined from our measurements are virtually equal to those obtained in [5]: $\Delta E = (3.0 \pm 0.3)$ meV.

The exponential temperature dependence of the SLR rate is indicative of the Orbach–Aminov mechanism. The essence of this mechanism is in the successive absorption and emission of phonons that are in resonance with the energy gap Δ between the ground-state level of a paramagnetic center and the level of another state located within the Debye spectrum [1]. The nature of this state does not affect the temperature dependence of the relaxation time. However, it affects the absolute value of T_1; i.e., it can be either the excited state of the impurity center or the state related to one of the modes of the optical lattice vibrations or a local vibration [10].

In the Raman process, the SLR represents a sequence of events of absorption–emission of any pair of phonons with the difference of resulting energies of the pairs equal to the energy of the microwave quantum. In the case of the Orbach–Blum process, closely located levels of the center, which correspond to different components of the momentum, are involved in the relaxation and $1/T_1 \propto T^5$. For non-Kramers ions, whose energy structure has low initial splitting in a zero magnetic field, a similar temperature dependence was predicted by Walker [11].

The dependence $T_1 \propto T^{-3}$ likely represents a first-order process describing the relaxation of the non-Kramers ion, in which one acoustic and one optical phonon with an energy $\hbar\omega$ are involved. This energy is lower than the energy of the higher lying level, which is in resonance with the Debye spectrum [10].

For a conventional paramagnetic center, the SLR rate controlled by any Raman process should be substantially higher that the value of $1/T_1$, which is governed by the Orbach–Aminov mechanism. This follows from the fact that the number of phonons involved in the Raman process is incommensurably larger (almost the entire Debye spectrum) compared with the number of phonons that are in resonance with the energy interval Δ in the Orbach–Aminov process [1].

However, it should not be forgotten that the resonance absorption detected in the ESR measurements is of the electric-dipole type [12]. The presence of the dipole moment of the center should lead to at least two consequences. First, the natural frequencies of dipole vibrations should differ from the frequencies of optical lattice phonons. Second, the efficiency of the resonance absorption is comparable with the efficiency of relaxation in which local vibrations are involved, i.e., considerably exceeds the efficiency of any Raman process [10]. Therefore, we may assume that $T_1 \propto \exp(-\Delta E/kT)$, where the value of ΔE is on the order of a few meV.

The value of ΔE can be presented as the result of mixing of vibrations corresponding to optical phonons of the GaAs lattice. Indeed, the energies of longitudinal (E_{LO}) and transverse (E_{TO}) optical phonons are equal to 36.69 and 33.84 meV, respectively. According to [13], the difference between E_{LO} and E_{TO} is 2.89 meV, which agrees with the results presented.

The assumption on the effect of local vibrations during the electron relaxation of the Mn^0 center is confirmed by the results of investigations of the nuclear magnetic relaxation.

3. RESULTS OF HIGH-TEMPERATURE MEASUREMENTS

The results of measurements of the nuclear SLR rate are shown in Fig. 3. In the range of 310–105 K, the mechanisms associated with the effect of lattice vibrations on nuclei manifest themselves. These are the Raman $\tau_1^{-1} \propto T^2$ ($140\text{ K} < T < 310$ K) and direct $\tau_1^{-1} \propto T$ ($105\text{ K} < T < 140$ K) processes.

For comparison, Fig. 3 also shows the results of high-temperature investigations of the nuclear relaxation in Mn-doped GaAs [14].

In the temperature range of 105–86 K, a change in the mechanisms of spin diffusion occurs: the fast diffusion becomes restricted [4]. In this case, the magnetic atoms begin to play a decisive role in the energy exchange between the nuclear spins and the lattice.

In the case of fast diffusion (the temperature is high enough), the SLR rate equals

$$\tau_1^{-1} = \frac{4}{3\pi}(N_p\bar{C}/b^3). \quad (4)$$

In the case of restricted diffusion (low temperatures), the SLR rate is described by the equation [4]

$$\tau_1^{-1} = \frac{8}{3}\pi N_p \bar{C}^{1/4} D^{3/4}. \quad (5)$$

Here

$$\bar{C} = \frac{2}{5}\gamma_n^2\gamma_p^2\hbar^2 s(s+1)\frac{T_1}{1+\omega_1^2 T_1^2},$$

ω_1 is the frequency of the nuclear resonance; T_1 is the time of longitudinal electron relaxation; γ_n is the gyromagnetic ratio, which corresponds to the electron spin s; N_p is the concentration of paramagnetic centers; and D is the spin diffusivity.

The parameters that have the dimensionality of length control the effect of the diffusion mechanism:

$$b = (3a\langle\mu_p\rangle/B_1)^{1/4},$$

$$\beta = \left(\frac{\bar{C}}{D}\right)^{1/4},$$

where b is the diffusion barrier radius; a is the distance between nuclei; $\langle\mu_p\rangle$ is the average thermodynamic momentum of a magnetic atom involved in the diffusion of the nuclear magnetization; and B_1 is the field induced by the magnetic center at distances where it is comparable with the field induced by neighboring nuclei.

For $b \gg \beta$, fast diffusion occurs, and, for $b \ll \beta$, diffusion is restricted.

If the electron-relaxation time is short, i.e., the temperature is high, $\omega_1 T_1 \ll 1$ and $\tau_1^{-1} \propto T_1^{\alpha}$; for $\omega_1 T_1 \gg 1$ (the low-temperature region), $\tau_1^{-1} \propto T_1^{-\alpha}$, where $\alpha = 1$ or 1/4, depending on the diffusion mechanism.

The aforesaid explains the behavior of the temperature dependence of the nuclear relaxation rate in the temperature region below 105 K. In the range 80 K < T < 105 K, $\tau_1^{-1} \propto T_1^{-\alpha}$, and, for 36 K < T < 80K, $\tau_1^{-1} \propto T_1^{\alpha}$. For the low-temperature portion of the dependence, it should be assumed that $\alpha = 1/4$. In this case, the behavior of τ_1 is described by the exponential function with the energy $\Delta E_{\text{low}} = (403 \pm 24)$ K in the power of the exponential. Under the assumption that $\alpha = 1/4$, this form of the function yields for the electron relaxation rate $\Delta E_{\text{low}} = (1600 \pm 100)$ K $\equiv (0.138 \pm 0.009)$ eV. The value obtained coincides with the power of the exponential that describes the behavior of τ_1 in the range of 80–105 K: $\Delta E_{\text{high}} = (1520 \pm 40)$ K $\equiv (0.131 \pm 0.003)$ eV. In this case, $\alpha = 1$. Formally, the shape of the dependences and the equality of the powers of exponentials are indicative of the manifestation of the mechanism of electron relaxation similar to the Orbach–Aminov mechanism. However, first, the value of $\Delta E \approx 1560$ K $\equiv 134$ meV is close to the ionization energy of a neutral Mn center in GaAs and even exceeds it, and, second, this value substantially exceeds the Debye temperature for GaAs. Depending on the crystal temperature, the latter can take values from 275 to 341 K. Hence, the Orbach–Aminov mechanism, as primarily defined, cannot occur in the GaAs:Mn crystal. Therefore, the large value of ΔE is indicative of the existence of the vibrational state of the center, which confirms the suggestion based on the analysis of electron relaxation. We can refer to the results of the investigation of optical absorption and photoconductivity in the GaAs:Mn crystals, in which vibrations with an energy ~140 meV were detected [13].

CONCLUSION

Thus, the results of investigations of the temperature dependence of the SLR rate primarily show that the mechanisms of fast relaxation should manifest themselves even at relatively low temperatures (as low as 8–10 K). These mechanisms are based on the interaction of the electric-dipole moment of a neutral Mn center with lattice vibrations. Otherwise, the passage from highly efficient Raman mechanisms to the mechanism of the Orbach–Aminov type with increasing temperature cannot be explained.

The interaction of the Mn^0 center with lattice vibrations is to a large extent controlled by the presence of the electric-dipole moment of the center.

REFERENCES

1. A. Abragam and B. Bleaney, *Electron Paramagnetic Resonance of Transition Ions* (Clarendon Press, Oxford, 1970; Mir, Moscow, 1972), Vol. 1.
2. C. P. Poole, *Electron Spin Resonance: a Comprehensive Treatise on Experimental Techniques* (Wiley, New York, 1966; Mir, Moscow, 1970).
3. S. A. Altshuler and B. M. Kozyrev, *Electron Spin Resonance in Compounds of Transition Elements* (Nauka, Moscow, 1972; Halsted, New York, 1975).
4. C. D. Jeffries, *Dynamical Nuclear Orientation* (Interscience, New York, 1963; Mir, Moscow, 1965).
5. K. Lassmann and H. Schad, Solid State Commun. **18**, 449 (1976).
6. N. S. Averkiev, A. A. Gutkin, O. G. Krasikova, *et al.*, Solid State Commun. **68**, 1025 (1988).
7. V. F. Masterov, S. B. Mikhrin, B. E. Samorukov, and K. F. Shtel'makh, Fiz. Tekh. Poluprovodn. (Leningrad) **17**, 1259 (1983) [Sov. Phys. Semicond. **17**, 796 (1983)].

8. M. N. Barbashov, V. P. Maslov, and V. F. Masterov, Fiz. Tverd. Tela (Leningrad) **25**, 1130 (1983) [Sov. Phys. Solid State **25**, 648 (1983)].
9. J. Schneider, U. Kauffmann, W. Wilkening, *et al.*, Phys. Rev. Lett. **59**, 240 (1987); V. F. Masterov, K. F. Shtel'makh, and M. N. Barbashov, Fiz. Tekh. Poluprovodn. (Leningrad) **22**, 654 (1988) [Sov. Phys. Semicond. **22**, 408 (1988)].
10. K. N. Shrivastava, Phys. Status Solidi B **117**, 437 (1983).
11. M. B. Walker, Can. J. Phys. **46**, 1347 (1968).
12. N. P. Baran, V. Ya. Bratus', V. M. Maksimenko, *et al.*, Pis'ma Zh. Éksp. Teor. Fiz. **55** (2), 108 (1992) [JETP Lett. **55**, 101 (1992)].
13. M. Linnarsson, E. Janzen, B. Monemar, *et al.*, Phys. Rev. B **55**, 6938 (1997).
14. T. H. Yeom, I. G. Kim, S. H. Choh, *et al.*, Solid State Commun. **111**, 229 (1999).

Translated by N. Korovin

Semiconductors, Vol. 37, No. 8, 2003, pp. 923–926. Translated from Fizika i Tekhnika Poluprovodnikov, Vol. 37, No. 8, 2003, pp. 947–950.

Photosensitive Structures Based on Boron Phosphide Single Crystals

Yu. A. Nikolaev*, V. Yu. Rud', Yu. V. Rud'*, and E. I. Terukov***
** Ioffe Physicotechnical Institute, Russian Academy of Sciences, Politekhnicheskaya ul. 26, St. Petersburg, 194021 Russia*
e-mail: yuryrud@mail.ioffe.ru
*** St. Petersburg State Polytechnical University, Politekhnicheskaya ul. 29, St. Petersburg, 195251 Russia*
Submitted February 3, 2003; accepted for publication February 4, 2003

Abstract—Boron phosphide single crystals are grown by steady-state crystallization. New photosensitive structures, In/*p*-BP and H_2O/*p*-BP, are suggested and fabricated. Steady-state *I–V* characteristics and spectra of the relative quantum efficiency of photoconversion of the structures obtained are studied. The type and energy of direct and indirect interband transitions are determined. It is concluded that the boron phosphide structures produced can be used in practice. *© 2003 MAIK "Nauka/Interperiodica".*

Recently, interest in solids composed of elements with low atomic numbers have sharply increased [1–4]; this is due to the unique properties of such compounds, which offer potential for use in high-temperature applications and development of electrooptical systems operating in the short-wavelength spectral range. Among the diamond-like III–V semiconductors, borides BN, BP, and BAs have not been adequately studied rather due to technological problems [5, 6]. It should also be mentioned that the lattice parameter of BP crystals is such that they are the most suitable materials for fabricating lasers on silicon substrates [7]. The photoelectric properties of the boron compound structures have been virtually unstudied [6]. This study is aimed at expanding the range of photosensitive structures based on BP single crystals and the experimental study of their optoelectronic properties.

The structures were formed on BP single crystals grown by steady-state crystallization from liquid solutions. The single crystals grown were shaped as octahedra with native mirror faces about 0.5 × 0.5 mm in size. Such crystals are dark orange colored in transmitted white light. According to the thermopower sign, the BP single crystals grown are characterized by *p*-type conductivity. Their resistivity is ~10^3 Ω cm at $T = 300$ K, which, as a rule, increases no more than two times as the temperature decreases to 77 K. This suggests that the conductivity of the *p*-BP single crystals grown is controlled by acceptor centers with shallow levels.

Rectifying In/*p*-BP structures were obtained by the vacuum thermal deposition of thin layers of pure indium (~0.05 mm) onto the native mirror planes of BP crystals. The typical steady-state *I–V* characteristic of one of such structures at $T = 300$ K is shown in Fig. 1. The forward direction corresponds to a positive external voltage *U* applied to the BP crystal. The initial portion ($U < 0.6$ V) of the forward *I–V* characteristics is described by the diode equation; however, the ideality factor is high ($n' \cong 5$–10) due to a high series resistance of the structures. At bias voltages higher than the cutoff voltage U_0, the forward *I–V* characteristics begin to obey the law

$$U = U_0 + R_0 I, \tag{1}$$

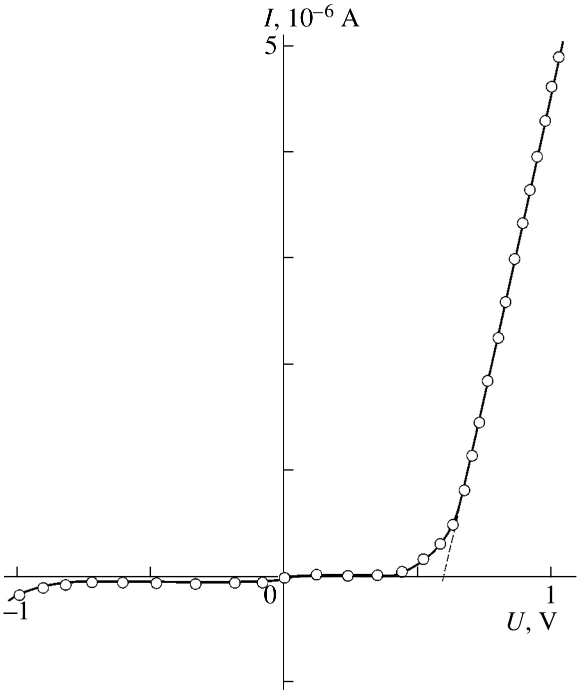

Fig. 1. Steady-state *I–V* characteristic of the In/*p*-BP structure (sample *5*) at $T = 300$ K. The forward direction corresponds to the positive polarity of external bias at the *p*-BP substrate.

Photoelectric properties of the structures based on *p*-BP single crystals at $T = 300$ K

Structure type	R_0, Ω	U_0, V	φ_B, eV	$\hbar\omega^m$, eV	S_U^m, V/W
In/*p*-BP	10^3–10^5	0.6–3	1.7–1.84	3.2–3.6	180
H_2O/*p*-BP	5×10^4			3.1–3.6	30

where R_0 is the residual resistance. The table lists the values of U_0 and R_0 for the barriers obtained. The rather wide ranges of variation of these values suggest that the conditions of crystal growth and barrier formation affect the *I–V* characteristics of the structures grown. The rectification factor, defined as the forward-to-reverse current ratio at $U \cong 1$ V, is $K \cong 25$ at $T = 300$ K for the highest quality structures. The reverse current obeys the power law $I \propto U^{1.2-1.4}$ with increasing voltage at $U \leq 1$–1.5 V, which can be explained by the rather poor quality of the structure periphery, caused by the small size (≤1 mm) and specific habitus of the single crystals.

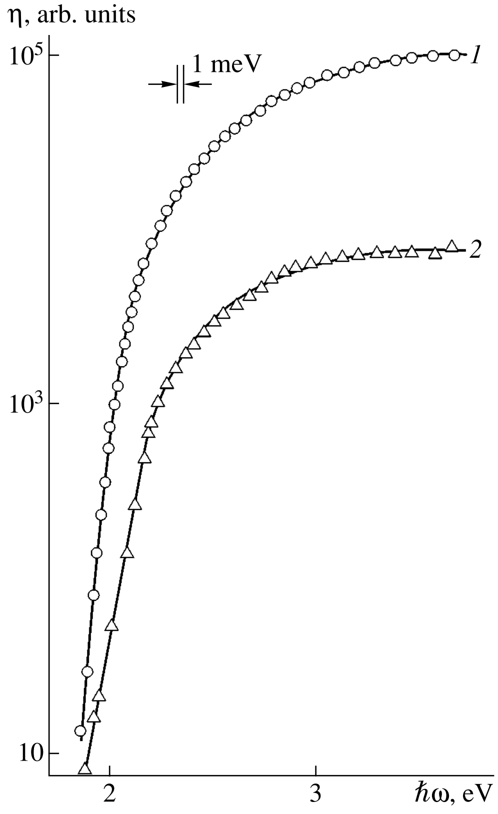

Fig. 2. Spectral dependences of the relative quantum efficiency of photoconversion of (*1*) the surface-barrier In/*p*-BP structure and (*2*) the photoelectrochemical cell H_2O/*p*-BP in nonpolarized light at $T = 300$ K (illumination from the side of the barrier contact and electrolyte).

Upon illumination of the In/*p*-BP structures, the photovoltaic effect arises. The photovoltage sign is independent of the photon energy and the light beam (~0.2 mm in diameter) position on the structure surface. The *p*-BP substrates in the In/*p*-BP structures are charged positively under illumination, which corresponds to the forward direction.

In addition to the Schottky barriers, the possibility of developing photosensitive structures by bringing the *p*-BP single crystal surface into contact with a liquid electrolyte was also studied. Distilled water was used as an electrolyte; a platinum-wire tip (~0.2 mm in diameter) immersed into the electrolyte in front of the BP single crystal surface exposed to light was used as a counterelectrode. It turned out that photoelectrochemical H_2O/*p*-BP cells, as well as solid-state In/*p*-BP structures, exhibit both rectification and the photovoltaic effect. The rectification factor of the cells obtained is $K \cong 10^2$ at $U \cong 10$ V; the forward direction and the photovoltage sign correspond to the positive polarity of *p*-BP. The highest photo voltaic sensitivity of the best cells is $S_U^m = 30$ V/W at $T = 300$ K; it does not exhibit pronounced degradation, which is typically caused by photocorrosion of the semiconductor surface.

The spectral dependences of the relative quantum efficiency $\eta(\hbar\omega)$ of photoconversion for typical In/*p*-BP and H_2O/*p*-BP structures illuminated from the side of the barrier contacts are shown in Fig. 2. We can see that the spectra $\eta(\hbar\omega)$ for different barriers are similar. This circumstance may be caused by the fact that the photosensitivity is controlled by the photoabsorption in the same BP semiconductor. As is evident from Fig. 2, the steep increase in η for the grown structures begins at photon energies $\hbar\omega \geq 1.9$–2.0 eV, which is close to the energy of indirect optical transitions $E_G^{in} \cong 2$ eV in the *p*-BP crystals [5]. It is worth noting that the photosensitivity drops at $\hbar\omega < E_G^{in}$ in all of the structures obtained, which can be caused by a low lattice defect concentration in the grown crystals. At the same time, significant structured photosensitivity is typically observed in the long-wavelength region ($\hbar\omega < E_G$) of the spectra η for the structures on GaP and InP, which is caused by the transitions in which lattice-defect levels are involved [8, 9]. Therefore, the low photosensitivity of the BP structures in the region $\hbar\omega < 2$ eV may be considered as an important difference between these and the well-studied structures on GaP and InP.

Another important feature of the In/*p*-BP and H_2O/*p*-BP structures is the fact that their photosensitivity increases by two to three orders of magnitude as the photon energy increases ($\hbar\omega > E_G$) and has a constant (highest) value of S_U^m in the range of 3.1–3.6 eV (see table), without exhibiting a distinct short-wavelength falloff. It is pertinent to emphasize that the photosensitivity of Au/*p*-BP structures was studied in [5] only at

$\hbar\omega \leq 2.3$ eV. We note that, in practice, it is impossible to obtain thin plates with an area necessary for the application of absorption spectroscopy because of the limited size of the BP single crystals (≤1 mm). Therefore, the spectra $\eta(\hbar\omega)$ of photosensitive structures formed on such small *p*-BP crystals is, for the time being, only practical possibility for analyzing the energy spectrum of such a material in the short-wavelength region of fundamental absorption of BP ($\hbar\omega > E_G^{in}$).

Figure 3 shows the results of the analysis of the photosensitivity spectra on the basis of the theory of interband absorption in semiconductors [8, 9]. The analysis suggests that the long-wavelength edge of the photosensitivity of the H_2O/*p*-BP structures obtained obeys the law

$$\eta\hbar\omega \propto (E_G^{in} - \hbar\omega)^2. \tag{2}$$

Indeed, the photosensitivity spectra are straightened in the coordinates $\eta(\hbar\omega)^{1/2} - \hbar\omega$ in the energy range of 1.9–2.2 eV. Therefore, taking into account and results of [8, 10], the long-wavelength increase in η at $\hbar\omega >$ 1.9 eV may be attributed to indirect interband transitions in BP. Extrapolation of the dependences $(\eta\hbar\omega)^{1/2} \longrightarrow 0$ allows determination of $E_G^{in} \cong$ 1.9–2.0 eV for the structures on various BP crystals at T = 300 K. Apparently, the observed change in E_G^{in} may be related to changes in deviations from BP stoichiometry within the homogeneity region. This assumption is confirmed by the observations [4, 11, 12] of changes in the BP-lattice parameter in a fairly wide range.

In the high-energy region $\hbar\omega > 2.3$ eV, the spectra $(\eta\hbar\omega)$ of the Schottky barriers and photoelectrochemical cells (Fig. 3, curve *2*) obey the law

$$\eta\hbar\omega \propto (E_G^{dir} - \hbar\omega)^{1/2}, \tag{3}$$

where E_G^{dir} is the energy of direct interband transitions. The validity of the law (3) may indicate the occurrence of direct interband transitions in BP crystals; the energy of these transitions is determined by the extrapolation $(\eta\hbar\omega)^2 \longrightarrow 0$. The obtained $\eta(\hbar\omega)$ spectra allow us to estimate the direct band gap of the BP crystals as $E_G^{dir} \cong$ 2.5 eV. We should note that thus estimated value for BP differs from the very contradictory data available in the literature [5, 11]. Therefore, the question of the BP band gap calls for further study.

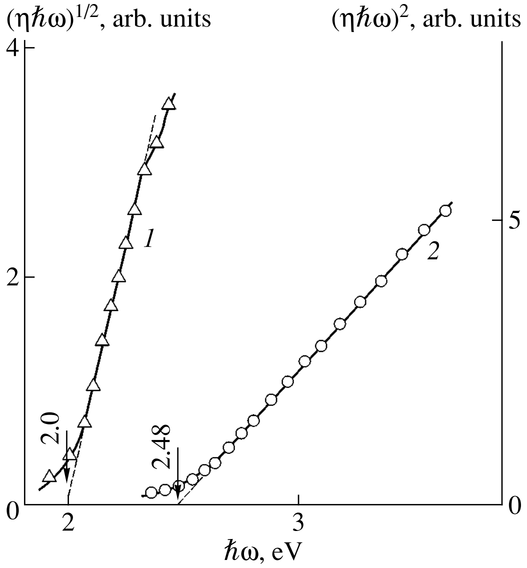

Fig. 3. Dependences of (*1*) $(\eta\hbar\omega)^{1/2}$ and (*2*) $(\eta\hbar\omega)^2$ on the photon energy $\hbar\omega$ for the H_2O/*p*-BP photoelectrochemical cell at T = 300 K.

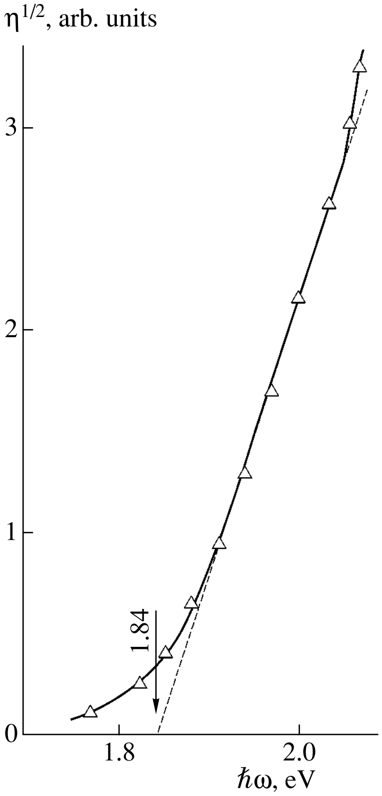

Fig. 4. Dependences of $\eta^{1/2}$ on the photon energy $\hbar\omega$ for the In/*p*-BP structures at T = 300 K (sample 1).

In the case of In/*p*-BP barriers, the long-wavelength increase in the photosensitivity is characteristic of photogenerated-carrier emission from a metal into boron phosphide (Fig. 4). The results of estimating the metal–semiconductor barrier height φ_B are listed in the table. The extrapolation $\eta^{1/2} \longrightarrow 0$ yields φ_B = 1.7–1.84 eV for various structures. The change observed in φ_B can be caused by the dependence of the In/*p*-BP-barrier height on the conditions of the barrier formation and the quality of the BP-crystal surface.

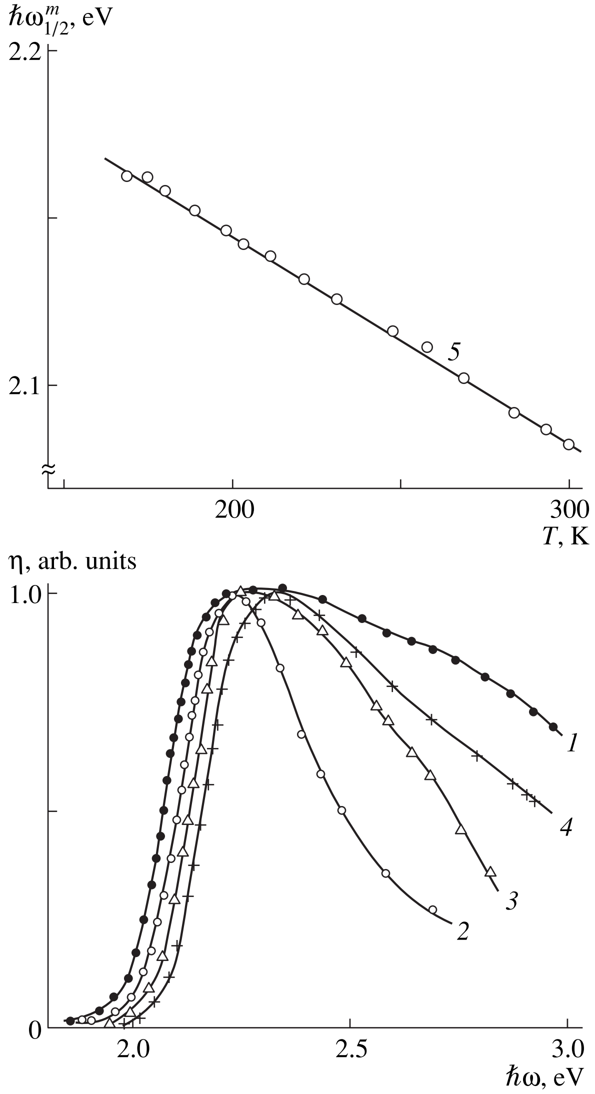

Fig. 5. Spectra of the relative quantum efficiency of photoconversion of the In/*p*-BP structure versus temperature: T = (*1*) 300, (*2*) 289, (*3*) 203, and (*4*) 169 K (the spectra η are normalized to the absolute maximum at each temperature) and the temperature dependence of the energy position of the point $\eta^m_{1/2}$ at the long-wavelength edge of $\eta(\hbar\omega)$.

As temperature decreases (T < 300 K), the long-wavelength edge of the spectra $\eta(\hbar\omega)$ shifts to shorter waves (Fig. 5, curves *1*–*4*). The energy position of the point $\hbar\omega^m_{1/2}$ corresponds to the half falloff $\eta^m_{1/2}$ at the long-wavelength edge of the photosensitivity spectra of the BP structures and linearly depends on temperature (see Fig. 5, curve *5*). This allows us to estimate the temperature coefficient of the band gap variation for the obtained BP crystals as $\beta = -6 \times 10^{-4}$ eV / K.

Thus, new photosensitive structures (In/BP barriers and H_2O/BP photoelectrochemical cells) have been obtained which make it possible to realize the broadband photodetection mode with the highest quantum efficiency of photoconversion in the spectral range of 3.1–3.6 eV. It was ascertained that such structures are virtually insensitive to radiation with the photon energy $\hbar\omega < 2$ eV. The sharp long-wavelength falloff in the photosensitivity of the fabricated structures indicates a low content of lattice defects in the grown single crystals of boron phosphide. The energy of direct interband optical transitions and the temperature coefficient ($\beta \cong (-6 \times 10^{-4}$ eV/K)) of variation in the band gap of single crystals of boron phosphide have been estimated.

REFERENCES

1. J. T. Glass, R. Messier, and N. Fujimori, in *Diamond Silicon and Related Wide Bangap Semiconductors: MRS Symposium Proceedings* (Materials Research Society, Pitsburg, PA, 1990), No. 162.
2. M. Ferhat, A. Zaoui, M. Certier, and M. Aourag, Physica B (Amsterdam) **252**, 229 (1998).
3. B. Bouhafs, H. Aourag, M. Ferhat, and M. Certier, J. Phys.: Condens. Matter **11**, 5781 (1999).
4. A. Zaoui and F. El Hag Hassan, J. Phys.: Condens. Matter **13**, 253 (2001).
5. R. J. Archer, R. Y. Koyama, E. E. Loebner, and R. C. Lucas, Phys. Rev. Lett. **12**, 538 (1964).
6. *Landolt-Bornstein. New Series*, Ed. by O. Madelung (Springer, Berlin, 1982), Vol. 17a.
7. S. Nishimura, S. Matsumoto, and K. Tarashima, Opt. Mater. **19**, 223 (2002).
8. J. I. Pankove, *Optical Processes in Semiconductors* (Prentice-Hall, Englewood Cliffs, N.J., 1971; Mir, Moscow, 1973).
9. S. G. Konnikov, D. Melebaev, V. Yu. Rud’, *et al.*, Pis’ma Zh. Tekh. Fiz. **18** (24), 11 (1992) [Sov. Tech. Phys. Lett. **18**, 798 (1992)].
10. Yu. I. Ukhanov, *Optical Properties of Semiconductors* (Nauka, Moscow, 1977).
11. P. Mori-Sanchez, A. M. Pendas, and V. Luana, Phys. Rev. B **63**, 125103 (2001).
12. L. Lin, G. T. Woods, and T. A. Callcott, Phys. Rev. B **63**, 235107 (2001).

Translated by A. Kazantsev

Semiconductors, Vol. 37, No. 8, 2003, pp. 927–930. Translated from Fizika i Tekhnika Poluprovodnikov, Vol. 37, No. 8, 2003, pp. 951–954.
Original Russian Text Copyright © 2003 by Aĭdaraliev, Zotova, Karandashev, Matveev, Remennyĭ, Stus', Talalakin.

SEMICONDUCTOR STRUCTURES, INTERFACES, AND SURFACES

Negative Luminescence at 3.9 μm in InGaAsSb-Based Diodes

M. Aĭdaraliev, N. V. Zotova, S. A. Karandashev, B. A. Matveev, M. A. Remennyĭ, N. M. Stus', and G. N. Talalakin

Ioffe Physicotechnical Institute, Russian Academy of Sciences, Politekhnicheskaya ul. 26, St. Petersburg, 194021 Russia

Submitted February 10, 2003; accepted for publication February 17, 2003

Abstract—Current–voltage characteristics, as well as spectral and power–current characteristics, for the emission of InAsSbP/InGaAsSb double-heterostructure diodes grown on InAs substrates were measured under forward and reverse biases in the temperature range of 25–90°C. It was shown that the conversion efficiency for negative luminescence, which occurs due to the extraction of charge carriers from the regions adjacent to the *p–n* junction at temperatures ~90°C, is higher than the conversion efficiency for electroluminescence. Narrowing of the negative luminescence spectra in diodes with a built-in cavity was observed. *© 2003 MAIK "Nauka/Interperiodica".*

1. INTRODUCTION

The effect of negative luminescence (NL) in semiconductors has been known since 1965, when V.I. Ivanov-Omskiĭ and his colleagues at the Ioffe Physicotechnical Institute observed that the intensity of emission from one of the surfaces of an InSb sample subjected to crossed electric and magnetic fields was lower than the corresponding equilibrium value. A similar effect takes place in a reverse-biased *p–n* junction. Extraction of the charge carriers from the regions adjacent to the junction leads to a reduction of their density below the equilibrium value, so that $(np) < (n_0p_0) = n_i^2$ (here, n_0, p_0, n, and p are equilibrium and nonequilibrium densities of electrons and holes, respectively; and n_i is the intrinsic charge-carrier density). Due to the extraction of charge carriers, the recombination-radiation intensity P decreases and becomes lower than the thermal background level P_0, and absorption dominates over emission; this means that the luminescence appears to be "negative":

$$\Delta P = P - P_0 = P_0\left(\frac{np}{n_i^2} - 1\right) \le 0.$$

Negative luminescence was studied in bulk InAs crystals [2], in InSb- and CdHgTe-based diodes [3, 4], and, recently, in superlattice (SL) structures [5, 6]. Devices utilizing the NL effect are used for shielding photodetectors from a thermal background and for testing photodetector systems [7]. In the latter case, stability of the radiation flux is important; thus, the advantages of NL sources in comparison with electroluminescent (i.e., forward-biased) ones are a uniform distribution of the NL intensity and a weak current dependence of the NL power near the saturation point. More uniform distribution of emission is a consequence of increased resistance of the reverse-biased *p–n* junction, which results in a redistribution of the current flux. Under forward bias, redistribution of the current flux usually leads to a narrowing of the emitting area with increasing current [8].

The power of the NL, or the "thermal contrast", is limited by the power of the blackbody emission at a given temperature. At higher temperatures T and longer wavelengths λ, the power of the NL increases, in contrast to the case of electroluminescence (EL). It was shown that, in a p-InAsSb$_{0.2}$/n-InAsSb$_{0.2}$ homojunction (λ = 5.5 μm), the NL mode of operation becomes more efficient at temperatures exceeding 80°C [9]; for InAs/InAsSb SL structures (λ = 4.3 μm), this threshold was determined as T = 310 K [10]. However, variation in temperature is accompanied by a change in the emission wavelength, which is undesirable for test sources. The wavelength can be stabilized in structures with a built-in cavity, such as resonant-cavity LEDs (see, e.g., [11]). As far as we know, NL sources of this type have not been investigated yet.

In this paper, we report the results of studying the NL in double heterostructures with an *n*-InGaAsSb active region (λ = 3.8 μm at 20°C), which include cavity-coupled diodes, in the temperature range from 20 to 90°C.

2. EXPERIMENTAL

Lattice-matched p-InAsSb$_{0.09}$P$_{0.18}$/n-InGa$_{0.07}$AsSb$_{0.07}$ heterostructures were grown by liquid-phase epitaxy on *n*-InAs(111) substrates at 630–680°C. The substrate thickness was 350 μm, and the electron density was 2×10^{16} cm^{-3}. Next to the InGa$_{0.07}$AsSb$_{0.07}$ active layer of thickness 2–3 μm, a wide-gap *p*-InAsSbP layer (with a band gap E_g = 390 meV at 300 K) of thickness 2–4 μm was grown; it was doped with Zn to obtain a hole density of $(5–7) \times 10^{17}$ cm^{-3}. An *n*-InAsSbP layer of thickness 2–3 μm was grown between the substrate and the

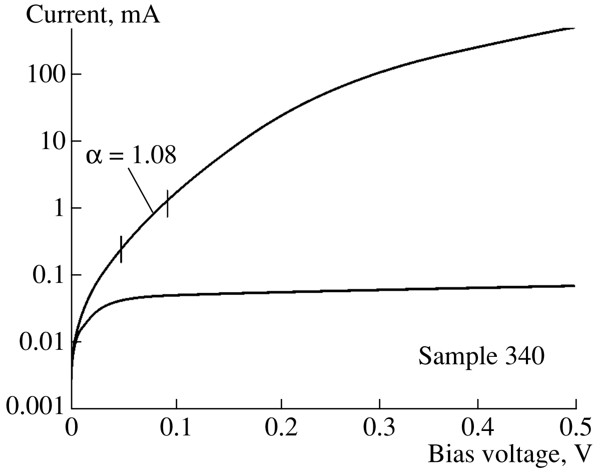

Fig. 1. Forward and reverse room-temperature current–voltage characteristics of a diode with an InGaAsSb active region (3.8 μm at 20°C) 300 μm in diameter.

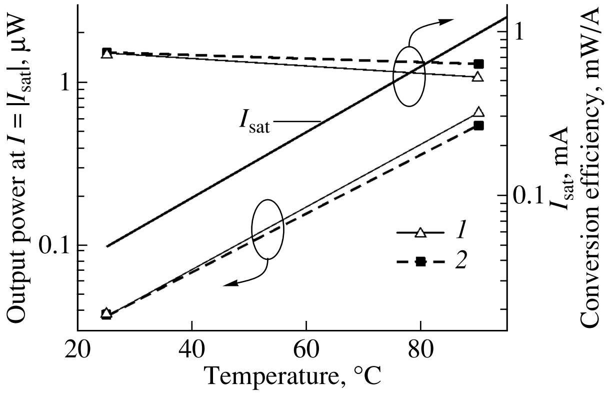

Fig. 2. Temperature dependences of the saturation current I_{sat}, the emission power for $I = |I_{sat}|$, and the conversion efficiency (*1*) in the NL and (*2*) in the EL mode for a diode with an InGaAsSb active region 300 μm in diameter.

active layer. Previously, we used similar structures to fabricate high-power lasers emitting at 3.3 μm [12].

Circular mesa structures 300 μm in diameter and the upper Au:Zn contact to the *p*-region were formed by photolithography. Chips 1×0.9 mm^2 in size were mounted on an Si holder of size $1.1 \times 1.6 \times 0.4$ mm^3 with a U-shaped cathode contact region and a circular anode contact (this arrangement is called "flip chip bonding" or "episide bonding"; see also Fig. 1 in [13]). Radiation was emitted through the wide-gap *n*-InAsSbP layer and the substrate, which had been thinned to 80–120 μm. Some of the experiments were carried out in a configuration with an interference filter attached to the substrate; the filter passband was at 3.9 μm. An optical contact between the surfaces of the filter and the heterostructure was achieved by using chalcogenide glass with a refractive index of 2.6.

Measurements of the EL were carried out in the pulsed mode. The spectra and the absolute power of the emission were measured using a HgCdTe-based diode cooled to 77 K, with the directional pattern of the LED and the spectral sensitivity curve of the photodetector taken into account.

3. RESULTS AND DISCUSSION

Figure 1 represents the room-temperature current–voltage characteristic of a diode with an InGaAsSb active region; the reverse saturation current is equal to 50 μA, and the ideality factor for the forward portion $\alpha = 1.08$. Such a small deviation of α from unity is indicative of the high quality of the *p*–*n* junction and is an advantage of these diodes in comparison with those used in [14], which have $\alpha = 1.3$. At voltages exceeding about 0.35 V, the *p*–*n* junction barrier flattens out and the *I*–*V* curve becomes linear. Around zero bias, the resistance amounts to $R_0 = 560\ \Omega$ ($R_0A = 0.4\ \Omega$ cm^2, with the diode area $A = 0.7 \times 10^{-3}$ cm^2).

Necessary conditions for the observation of NL are the saturation of the reverse current and the absence of leakages, which can heat the structure and lead to a decrease in the radiation contrast. The absence of leakages makes it possible to use the diode as a photodetector. For example, most studies of NL over the last five years have been performed using photodiode structures. The detectability of the diode under study at room temperature ($D^*_{\lambda\max} = 1 \times 10^{10}$ cm Hz$^{1/2}$ W^{-1}) matches the characteristics of the best photodiodes for this spectral range, and we succeeded in observing the negative radiation contrast under reverse bias. Figure 2 plots the saturation current I_{sat} and the emission power for the cases of negative and positive luminescence under a current whose magnitude is equal to I_{sat}; the conversion efficiency for both cases is also shown. At 25°C, the power and the conversion efficiency (0.05 μW and 0.74 mW/A, respectively) are the same in both modes, which is related to the linearity of the power current–ampere characteristics at low currents. The conversion efficiency is lower by more than a factor of two in comparison to that for InAs diodes emitting at 3.4 μm; this observation reflects the general trend of a decrease in the conversion efficiency with decreasing energy gap [15].

It was shown [16, 17] that, above 200 K, the diffusion mechanism is mainly responsible for the current flow in *p*–*n* junctions based on InAs and related alloys; i.e., according to the Shockley theory, recombination in the *p* and *n* regions of the junction determines its current–voltage characteristics. This conclusion is corroborated by our measurements, which indicate that the saturation of the reverse current takes place even at elevated temperatures (up to 200°C) [15]. Evidently, surface treatment in narrow-gap diodes does not play a decisive role for the observation of current saturation, since, at elevated temperatures, the values of I_{sat} consid-

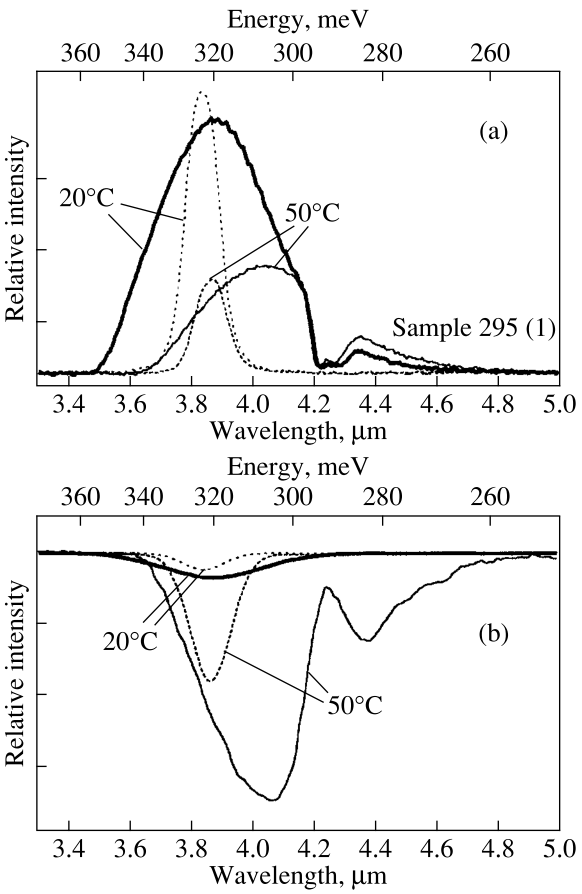

Fig. 3. Spectra of (a) positive and (b) negative luminescence of the diodes with an InGaAsSb active region at 20 and 50°C; solid lines correspond to an open-surface structure and dotted lines, to a structure with a filter. The measurements were carried out (a) with 10 μs, 2 kHz pulses at I = 150 mA and (b) with 200 μs, 2 kHz pulses at $I = |I_{sat}|$.

erably exceed the surface-leakage currents. At 90°C, the saturation current was equal to ~1 mA, which is higher than the expected leakage current. With increasing temperature, the NL power increased as a result of an increase in I_{sat}, but the variation in the conversion efficiency was insignificant. Thus, our results show that, in the temperature range examined, the increase in the rate of nonradiative recombination processes (Auger recombination) depends only slightly on temperature. At the same time, one should note a trend toward the saturation of the positive emission power, which manifests itself in a relative decrease of the conversion efficiency to 0.53 mW/A under high currents. Previously, we established, both for structures similar to those under study [18] and for p-InAs$Sb_{0.2}$/n-InAs$Sb_{0.2}$ diodes (λ = 5.5 μm) [9], that this behavior is not related to thermal effects. It can be suggested that the higher conversion efficiency of the NL in comparison to that of the EL is a general property of narrow-gap III–V structures and is related to the influence of Auger processes at high currents.

Figure 3 represents the spectra of EL and NL recorded at 20 and 50°C; a shift to longer wavelengths with increasing temperature can be seen. Taking the data of Fig. 3 into account, we find that the efficiency in the NL mode η_{NL} = 0.8–0.9, which is close to the highest values reported in the literature [19].

The spectrum of a diode with a filter virtually does not shift with varying temperature, since the change in the filter transmission related to the change in the refractive index of its layers is small. At the peak of the filter transmission, the emission power increases in comparison to the configuration without a filter; this is due to the antireflection effect caused by the presence of the built-in cavity (the filter). In the ideal case, the design of the diode described above makes it possible to increase the radiation output by 40%.

One can see from Fig. 3 that, both for the open-surface diodes and the diodes with filters, the long-wavelength shift of the spectral peak is the same for the EL and the NL, which reflects the symmetry (the interrelation) of the emission and absorption processes. Similarly, the presence of atmospheric carbon dioxide has the same effect on the shape of both spectra: the "hot" luminescence (the EL) is attenuated due to the absorption around 4.3 μm by the "cold" gas in the optical path, while the "cold" luminescence (the NL) is screened by the gas, which appears to be "hot" in this case.

4. CONCLUSION

Thus, we observed intense negative luminescence in the wavelength region λ = 3.9–4.1 μm in reverse-biased diode heterostructures p-InAsSbP/n-In$Ga_{0.07}$As$Sb_{0.07}$. In the temperature range of 25–90°C, its intensity increased with the current and the temperature. The NL efficiency was 0.8–0.9, and the conversion efficiency was 0.74–0.66 mW/A, which is somewhat higher than for positive luminescence. The behavior of the NL reproduced all of the features of the positive luminescence, in particular, a weak temperature dependence of the spectral peak position in the diodes with a built-in cavity and attenuation of the emission by atmospheric carbon dioxide.

ACKNOWLEDGMENTS

We thank N.D. Il'inskaya for her help in carrying out this study.

This study was supported by the Ministry of Science and Technology of the Russian Federation through the program "Development of a Fundamental and Technological Basis for the Creation of Novel Nanostructures for Electronics and Optoelectronics" and by Schlumberger Oilfield Services with the administrative support of the U.S. Civil Research and Development Foundation.

REFERENCES

1. V. I. Ivanov-Omskiĭ, B. T. Kolomiets, and V. A. Smirnov, Dokl. Akad. Nauk SSSR **161**, 1308 (1965) [Sov. Phys. Dokl. **10**, 345 (1965)].
2. S. S. Bolgov, V. K. Malyutenko, and A. P. Savchenko, Fiz. Tekh. Poluprovodn. (St. Petersburg) **31**, 526 (1997) [Semiconductors **31**, 444 (1997)].
3. T. Ashley, C. T. Elliot, N. T. Gordon, *et al.*, J. Cryst. Growth **159**, 1100 (1996).
4. T. Ashley, C. T. Elliot, N. T. Gordon, *et al.*, Infrared Phys. Technol. **36**, 1037 (1995).
5. M. J. Pullin, X. Li, J. D. Heber, *et al.*, Proc. SPIE **3938**, 144 (2000).
6. L. J. Olafsen, I. Vurgaftman, W. W. Bewley, *et al.*, Appl. Phys. Lett. **74**, 2681 (1999).
7. G. R. Nash, N. T. Gordon, T. Ashley, *et al.*, IEE Proc.: Optoelectron. (2003) (in press).
8. V. K. Malyutenko, O. Yu. Malyutenko, A. D. Podoltsev, *et al.*, Appl. Phys. Lett. **79**, 4228 (2001).
9. B. A. Matveev, N. V. Zotova, S. A. Karandashev, *et al.*, IEE Proc.: Optoelectron. **149** (1), 33 (2002).
10. M. J. Pullin, H. R. Hardaway, J. D. Heber, and C. C. Phillips, Appl. Phys. Lett. **75**, 3437 (1999).
11. E. Hadji, J. Bleuse, N. Magnea, and J. L. Pautrat, Appl. Phys. Lett. **67**, 2591 (1995).
12. M. Aydaraliev, N. V. Zotova, S. A. Karandashov, *et al.*, Appl. Phys. Lett. **81**, 1166 (2002).
13. M. Aĭdaraliev, N. V. Zotova, S. A. Karandashev, *et al.*, Fiz. Tekh. Poluprovodn. (St. Petersburg) **34**, 99 (2000) [Semiconductors **34**, 104 (2000)].
14. A. Krier, V. V. Sherstnev, and H. H. Gao, J. Phys. D: Appl. Phys. **33**, 1656 (2000).
15. B. A. Matveev, N. V. Zotova, N. D. Il'inskaya, *et al.*, J. Mod. Opt. **49**, 743 (2002).
16. N. P. Esina, N. V. Zotova, and D. N. Nasledov, Fiz. Tekh. Poluprovodn. (Leningrad) **3**, 1370 (1969) [Sov. Phys. Semicond. **3**, 1140 (1969)].
17. A. Krier and Y. Mao, Infrared Phys. Technol. **38**, 397 (1997).
18. M. Aĭdaraliev, N. V. Zotova, S. A. Karandashev, *et al.*, Fiz. Tekh. Poluprovodn. (St. Petersburg) **35**, 619 (2001) [Semiconductors **35**, 598 (2001)].
19. W. W. Bewley, M. J. Jurkovic, C. L. Felix, *et al.*, Appl. Phys. Lett. **78**, 3082 (2001).

Translated by M. Skorikov

Semiconductors, Vol. 37, No. 8, 2003, pp. 931–935. Translated from Fizika i Tekhnika Poluprovodnikov, Vol. 37, No. 8, 2003, pp. 955–959.
Original Russian Text Copyright © 2003 by L'vova, Berkovits, Dunaevskiĭ, Lantratov, Makarenko, Ulin.

SEMICONDUCTOR STRUCTURES, INTERFACES, AND SURFACES

Wet Chemical Nitridation of (100)GaAs Surface: Effect on Electrical Parameters of Surface-Barrier Au–Ti/GaAs Structures

T. V. L'vova*, V. L. Berkovits, M. S. Dunaevskiĭ, V. M. Lantratov, I. V. Makarenko, and V. P. Ulin

Ioffe Physicotechnical Institute, Russian Academy of Sciences, Politekhnicheskaya ul. 26, St. Petersburg, 194021 Russia
**e-mail: tatiana.lvova@mail.ioffe.ru*

Submitted February 10, 2003; accepted for publication February 17, 2003

Abstract—The influence exerted by wet chemical nitridation of the (100)GaAs substrate surface in hydrazine-sulfide solutions before fabrication of barrier contacts on the parameters of surface-barrier Au–Ti/GaAs structures has been studied. The structures fabricated on nitrided substrates are characterized by lower reverse currents and higher breakdown voltages. The barrier height in structures of this kind is 0.71 ± 0.02 eV, and the ideality factor, 1.06 ± 0.01. The observed improvement in the electrical parameters of the structures is due to replacement of the natural oxide layer on the substrate surface by a thin coherent GaN film. *© 2003 MAIK "Nauka/Interperiodica".*

1. INTRODUCTION

The presence of a natural oxide on the surface of III–V semiconductors largely restricts the possibility of using these compounds in microelectronics and, in particular, poses severe difficulties for the fabrication of surface-barrier (*m*–*s*) structures. A key influence on the electrical parameters of structures of this kind is exerted by the composition and structure of the interface, which must be formed, in the ideal case, by the atomic-flat surface of a semiconductor and the metal layer. At the same time, the existing procedures for cleaning the GaAs surface to remove the oxide necessarily leads to strong disruption of the surface planarity and stoichiometry of the substrate. In particular, thermal cleaning of the GaAs surface in a vacuum leads to the formation of multiple elongated pits with a density of 10^{10} cm^{-2} on the surface and even to the appearance of gallium drops [1]. One of the most efficient and widely used methods for removing the oxide from the (100)GaAs surface is the so-called "dry etching", i.e., cleaning in low-energy plasma [2]. However, bombardment of the semiconductor surface with plasma ions can disrupt the surface layer to a depth of up to a hundred angströms and significantly change its electrical and optical properties [3]. In this case, the interface formed upon deposition of a metal is far from being ideal and its properties strongly depend on the conditions of surface cleaning. This, in turn, impairs the electrical parameters of the structures and leads to a pronounced scatter of these parameters. At the same time, it is the stability and reproducibility of the parameters of *m*–*s* structures that is the necessary condition for the fabrication of high-quality devices. As shown in [4], it is necessary for GaAs integrated circuits with transistors based on *m*–*s* structures that the scatter in the potential barrier heights not exceed ±0.02 eV. However, the real scatter greatly exceeds this value. Technological procedures aimed to deal with this problem consist in the development of techniques for the removal of oxide from the surface and in the stabilization of a given state of the semiconductor surface in the course of metal deposition.

Chemical passivation of the GaAs surface may aid in solving the problem of fabricating *m*–*s* structures with reproducible and stable parameters. Chemical passivation is a method for modifying the semiconductor surface by creating on it an adsorbed film of foreign atoms, which remains chemically stable in air or in some other technological medium. To be compatible with technological processes, such a film must, in addition, be sufficiently stable thermally. It seems appropriate to use GaN layers as stabilizing films because of their thermal and chemical stability. It is known, however, that, owing to large lattice mismatch, when such layers are deposited on the GaAs surface they lose their mechanical stability even at a thickness of two monolayers (ML). Therefore, a nitride film can effectively protect the surface only if it is 1 ML thick. It is very difficult to obtain such films using the existing nitridation techniques, which rely upon surface treatment with nitrogen plasma. In this case, nitride films, which are either amorphous or have crystalline structure with a large density of dislocations, stacking faults, and microcracks, are formed on the surface (see [4]).

In [5, 6], a new technique for GaAs nitridation by treatment of the surface with hydrazine-sulfide solutions was first developed. It was shown that the

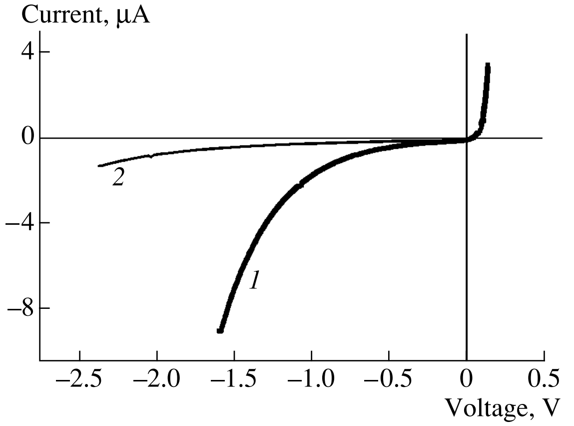

Fig. 1. Typical *I–V* characteristic of Au–Ti/GaAs structures of (*1*) group 1 and (*2*) group 2.

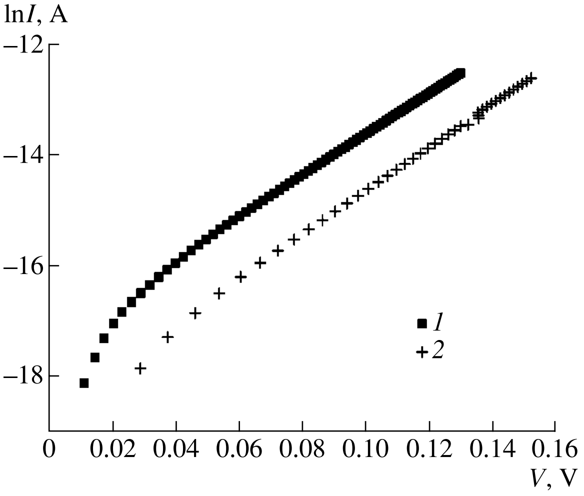

Fig. 2. Forward *I–V* characteristic of Au–Ti/GaAs structures of (*1*) group 1 and (*2*) group 2.

(100)GaAs surface treated with these solutions is free of oxide and is covered with a layer of nitrogen atoms chemisorbed on gallium atoms, i.e., with a nitride monolayer. The continuity of the layer formed is indicated by the surprising stability of the treated surface under atmospheric conditions, which does not become oxidized for at least several months. This, it is hoped that wet chemical nitridation of the surface of GaAs substrates will improve the electrical parameters of surface-barrier structures.

The aim of this study was to analyze the influence exerted by wet chemical nitridation of a GaAs substrate surface on the properties of Au–Ti/GaAs structures.

2. EXPERIMENTAL PROCEDURE

Surface-barrier structures were fabricated on (100) *n*-GaAs substrates with an electron density of 1–2 × 10^{17} cm^{-3}. Two types of structures were studied experimentally. For the first group, the substrate surface was subjected to standard treatment which included the removal of organic contaminants from the surface and subsequent etching in standard sulfuric acid etchant. An ohmic contact was formed on the rear side of a substrate by depositing an Au–Ge layer and subsequent annealing in vacuum at 450°C for of 5 min. Mesa structures with an area 2 × 2 mm^2 were formed by photolithography on the front side. Before depositing the barrier metal, the GaAs surface was treated with 10% HF to remove the thick oxide layer. For structures of the second group, substrates were subjected, after performing the above procedures and immediately before barrier metal deposition, to treatment in a hydrazine-sulfide solution, as described in [5]. Then, the substrates of both groups were annealed at 450°C in a high vacuum for 10 min, and 5-nm-thick Ti and 30-nm-thick Au layers were deposited at 100°C by vacuum evaporation.

To determine the characteristic parameters of the structures under study, the current–voltage (*I–V*) characteristics and dependences of the differential capacitance on voltage were measured at room temperature. In addition, to elucidate the mechanisms of, and reasons for changes in, the structure parameters, atomic-force microscopy (AFM) was applied to study, under atmospheric conditions, the morphology of GaAs substrates before and after treatment with hydrazine-sulfide solutions. The measurements were done on a homemade (NT-MDT Company) device operating in the contact mode with the use of a probe-microcantilever with a rigidity factor of 0.16 and 0.68 N/m and a radius of curvature of the probe tip of less than 20 nm. Statistical processing of the AFM topography was done with SPM Image Magic software [7]. In addition, the influence exerted by annealing on the microprofile of nitrided surfaces was studied with a GPI-300 high-vacuum scanning tunnel microscope (STM) [CENI (Center for Natural-Science Research), Russian Academy of Sciences, Moscow]. In these experiments, the annealing was done at 400–550°C for 60 min at a residual pressure of 2.7 × 10^{-6} Pa in the preparation chamber, with a Chromel–Alumel thermocouple as temperature sensor. After being cooled to room temperature, a sample was transferred with a vacuum manipulator to the measuring chamber and fixed in the STM.

3. EXPERIMENTAL RESULTS

It was found that the *I–V* characteristics of structures of the first and second groups differ markedly, which is particularly pronounced under reverse bias (Fig. 1). The reverse current of structures formed on a nitrided surface was an order of magnitude lower than the current for structures belonging to the first group. Since the carrier density in the substrates used did not exceed 3 × 10^{17} cm^{-3}, then according to [8], the current transport in the surface-barrier structures under study may be due to

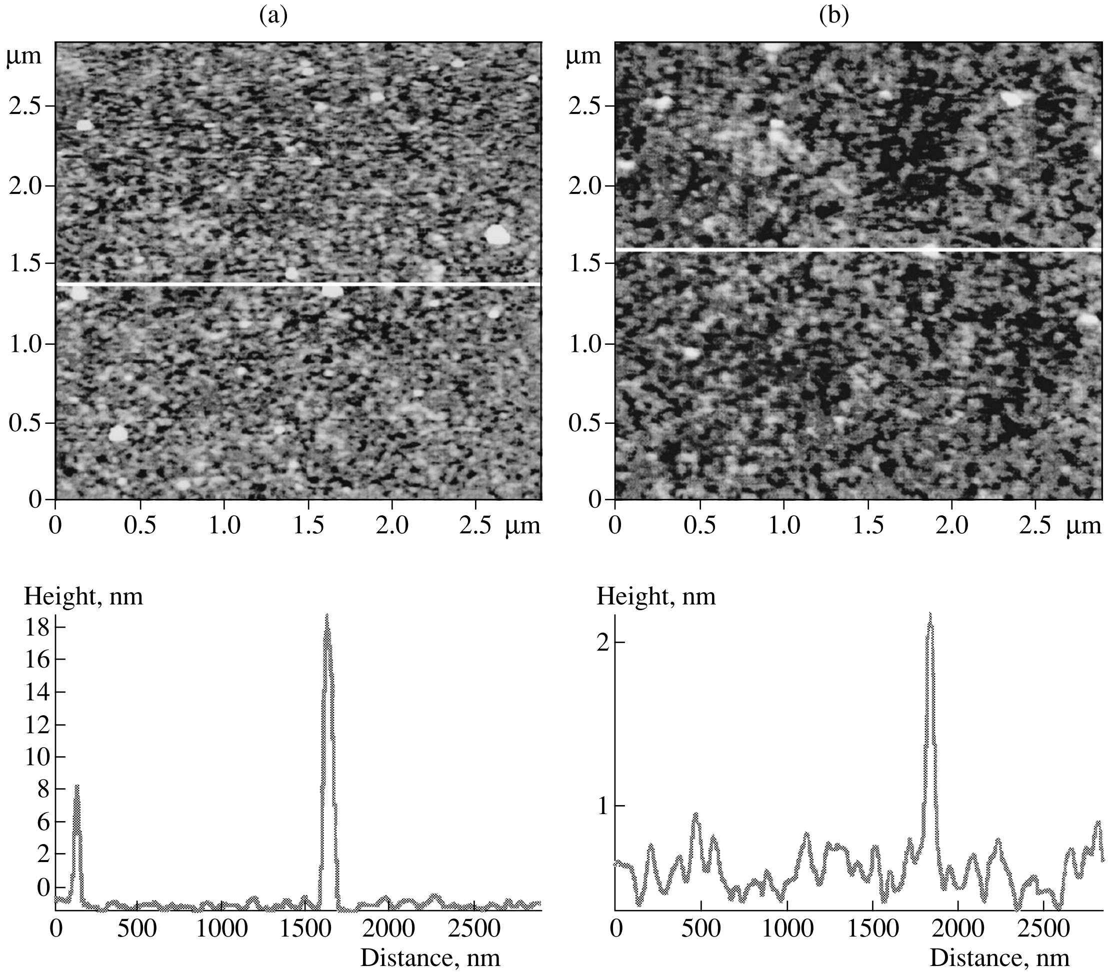

Fig. 3. AFM topographic images of the surface of GaAs substrates: (a) substrate processed using the standard procedure and (b) that treated with a hydrazine-sulfide solution.

thermionic emission, for which the dependence of current I on voltage U has the form

$$I = A^{**}ST^2\exp(-q\Phi/kT)[\exp(qU/nkT)-1],$$

where A^{**} is the Richardson constant, equal to 8.16 A cm^{-2} K^{-2} for GaAs; S, the diode area; T, the measurement temperature (K); Φ, the potential barrier height; k, Boltzmann's constant; q, the elementary charge; and n, the ideality factor.

Using this expression, the ideality factor n was determined from the slope of the ln$I$-vs.-U plot of the forward I–U characteristic and its extrapolation to the Y axis yielded the potential barrier height (Fig. 2). The ideality factors n of the structures formed on the nitrided surface (group 2) are much smaller (1.06 ± 0.01) than the ideality factors for the structure of group 1 (1.2 ± 0.1). In addition, special mention should be made of the insignificant scatter of the potential barrier heights in structures of group 2 (0.71 ± 0.02 eV). The potential barrier in structures fabricated on substrates untreated in a hydrazine-sulfide solution (group 1) is somewhat lower, and the scatter of the barrier heights is much greater than that for group 2 (0.66 ± 0.04 eV). A study of the surface topography by the AFM method before and after nitridation revealed that treatment with a hydrazine-sulfide solution makes the microprofile of the surface smoother. Figure 3 shows typical topographic images of the surface of the substrates under study before and after nitridation. Visually, the initial GaAs substrates have a mirrorlike surface, whose rms microroughness is 0.4 nm according to AFM. After etching, the rms microroughness increases to 0.5 nm. However, in both the first and second cases, there are surface microprofile elements with a small radius of curvature and height of up to 20 nm (Fig. 3a). After nitridation, the rms roughness is 0.3 nm, the density of microprofile elements with a small radius of curvature decreases, and their height does not exceed 2.5 nm (Fig. 3b).

An STM study of the influence exerted by annealing in a vacuum on the microprofile of a nitrided surface demonstrated that prolonged annealing (for 60 min) at 400–500°C does not lead to the development of a

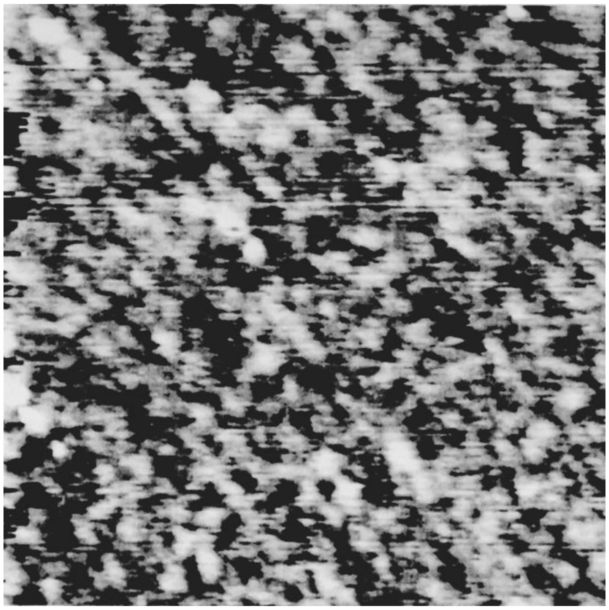

Fig. 4. STM image of the surface of GaAs substrate subjected to nitridation and annealing in a vacuum at T = 500°C. Image field 0.48×0.48 μm^2.

microprofile, contrary to what commonly occurs in the case of a GaAs surface with a natural oxide [1]. The mean microprofile roughness is small, on the order of 1 nm. However, owing to the insignificant number of microprofile elements with a small radius of curvature, the maximum height difference in the image is somewhat greater. For example, it is 4.8 nm in the 0.48×0.48 μm^2 field (Fig. 4). This suggests that the nitride film that formed on the GaAs surface upon treatment in a hydrazine-sulfide solution has sufficient thermal stability.

4. DISCUSSION

It is known that the use of titanium as a barrier metal leads to a decrease in the thickness of the separating oxide film at the interface because of the interaction of the metal with the oxide layer covering the surface of the GaAs substrate. Ti/GaAs structures retain their rectifying properties after high-temperature annealing; however, the potential barrier height changes significantly depending on the annealing temperature and medium, which is probably due to direct interaction of Ti with GaAs and the formation of intermetallic phases at the interface [9]. To make the series resistance of *m–s* structures lower, titanium nitride, which has metallic conductivity, is used instead of the metal. TiN/GaAs structures are commonly fabricated using plasmochemical techniques, which leads to the formation of intermediate GaN layers with poor crystal quality. This is immediately shown by the potential barrier height and ideality factor. In this case, only high-temperature annealing of the structures (759–800°C) can yield an ideality factor close to unity (1.07) [10].

Presumably, the nitridation technique used in the present study makes it possible to diminish the thickness of the separating layer to the maximum possible extent. In addition, AFM studies of the surface topography before and after nitridation revealed that the GaAs surface microprofile is smoothed by treatment in the hydrazine-sulfide solution. After this treatment, the (100)GaAs surface is covered with nitrogen atoms (or, more precisely, with NH groups) chemically bound to gallium atoms in the crystal lattice [5]. Such a surface layer can be regarded as a GaN monolayer coherently bound to the substrate and covered with adsorbed hydrogen atoms. An analysis of electron diffraction (RHEED) patterns of the surface of nitrided samples demonstrated that the type of the diffraction pattern (1×1) remains unchanged in a wide range of temperatures (from room temperature to above 770°C). The diffraction reflections are the strongest at 400–450°C. Therefore, the authors believe that sufficiently complete cleansing of the surface to remove physically sorbed components is achieved at the temperatures used.

It may be assumed that, in the course of deposition by vacuum evaporation, titanium interacts with the nitride layer, which leads to detachment of the nitrogen layer from the GaAs surface. The interface formed in this case can be regarded as a contact of TiN with a GaAs surface terminated with Ga. This conclusion is confirmed by measurements of the *I–V* characteristics of the structures. The ideality factors of groups 1 and 2 differ significantly. This indicates that the interfaces in these groups differ in thickness and composition. In structures formed on the nitrided GaAs surface (structures of group 2), the ideality factor n is close to unity (1.06 ± 0.01). This fact points to the presence of a thin tunnel-transparent layer between the metal and semiconductor, and the small scatter of n suggests that the layer thickness is approximately the same over the entire substrate area.

Comparison of the results obtained in studying the *I–V* characteristics and those furnished by AFM and STM methods suggests that the higher reverse currents and lower breakdown voltages of structures of group 1, compared with structures belonging to group 2, are due to the nonuniform distribution of an electric field over the surface, which results from the presence of microprofile elements with a small radius of curvature and a height that is comparable to the thickness of the barrier metal layer deposited by vacuum evaporation (Fig. 3a).

5. CONCLUSION

A comparative analysis of *I–V* characteristics demonstrated that wet chemical nitridation of the surface of GaAs substrates before fabrication of the barrier contact greatly improves the parameters of surface-barrier

Au–Ti/GaAs structures. This is due to the formation of a high-quality interface between the metal and semiconductor on the nitrided GaAs surface.

Indeed, as follows from a comparison of AFM and STM topographic images of the surface of GaAs substrates with natural oxide and those treated with a hydrazine-sulfide solution, wet chemical nitridation makes the microprofile of the surface smoother and the nitride film formed is thermally stable.

ACKNOWLEDGMENTS

This study was supported by the Ministry of Science program “Physics of Solid-State Nanostructures” (grant no. 99-2035). We thank A.G. Karchevskaya and A.N. Karpenko for assistance with the experiments.

REFERENCES

1. I. V. Sedova, T. V. L’vova, V. P. Ulin, *et al.*, Fiz. Tekh. Poluprovodn. (St. Petersburg) **36**, 59 (2002) [Semiconductors **36**, 54 (2002)].
2. F. Cappasso and G. F. Williams, J. Electrochem. Soc. **20**, 45 (1982).
3. Yu. A. Berashevich, A. L. Danilyuk, A. N. Kholod, and V. E. Borisenko, Fiz. Tekh. Poluprovodn. (St. Petersburg) **36**, 91 (2002) [Semiconductors **36**, 85 (2002)].
4. N. Braslau, J. Vac. Sci. Technol. A **4**, 3085 (1986).
5. V. L. Berkovits, V. P. Ulin, M. Losurdo, *et al.*, Appl. Phys. Lett. **80**, 3739 (2002).
6. V. L. Berkovits, T. V. L’vova, and V. P. Ulin, Vacuum **57**, 201 (2000).
7. A. V. Ankudinov, M. S. Dunaevskiĭ, V. A. Marushchak, *et al.*, Fiz. Tverd. Tela (St. Petersburg) **42**, 1874 (2000) [Phys. Solid State **42**, 1927 (2000)].
8. S. Sze, *Physics of Semiconductor Devices* (Wiley, New York, 1981; Mir, Moscow, 1984).
9. A. K. Sinha, T. E. Smith, M. H. Read, and J. M. Poate, Solid-State Electron. **19**, 489 (1976).
10. L. C. Zhang, S. K. Cheung, C. L. Liang, and N. W. Cheung, Appl. Phys. Lett. **50**, 445 (1987).

Translated by M. Tagirdzhanov

Semiconductors, Vol. 37, No. 8, 2003, pp. 936–939. Translated from Fizika i Tekhnika Poluprovodnikov, Vol. 37, No. 8, 2003, pp. 960–963.
Original Russian Text Copyright © 2003 by Slobodchikov, Salikhov, Samorukov.

On the Charge-Transport Mechanisms in Cr–*n*-InP and Mo–*n*-InP Diode Structures

S. V. Slobodchikov, Kh. M. Salikhov, and B. E. Samorukov

Ioffe Physicotechnical Institute, Russian Academy of Sciences,
Politekhnicheskaya ul. 26, St. Petersburg, 194021 Russia

Submitted February 3, 2003; accepted for publication February 4, 2003

Abstract—Electrical characteristics of Cr–*n*-InP and Mo–*n*-InP diode structures were investigated, and the charge-transport mechanism was estimated. It was established that this is either a thermionic or generation–recombination current that dominates in the Cr–*n*-InP structures, depending on temperature. In Mo–*n*-InP structures, the double injection of charge carriers dominates in the drift transport. © *2003 MAIK “Nauka/Interperiodica”.*

1. INTRODUCTION

Literature data on the technology and investigation of InP-based metal–semiconductor diode structures indicate that the properties of such structures doped with transition metals have virtually not been analyzed. Meanwhile, the electrical characteristics of such structures, which are used in practice, are known to primarily depend on the properties of metals. According to the investigations of the mechanism of formation of the Schottky barrier [1], in which a number of metals (including Cr [2]) were used, it is their chemical activity in particular that plays an important role in interacting with the substrate surface. The Schottky barrier height and its dependence on the interface properties control the efficiency of structures developed for practical purposes. Therefore, it seemed to be of interest to perform measurements that would make it possible to estimate the charge-transport mechanism in *n*-InP-based diode structures using chromium and molybdenum as rectifying contacts.

2. PROCEDURE FOR STRUCTURE FABRICATION

To fabricate Cr–*n*-InP structures, we used Czochralski-grown indium phosphide crystals with an electron concentration $n_0 = 2 \times 10^{16}$ cm^{-3}. The diodes were formed by the vacuum deposition of chromium on a preliminarily cleaned and etched substrate surface. Mo–*n*-InP structures were formed on crystals with $n_0 = 3 \times 10^{17}$ cm^{-3} also by vacuum deposition of molybdenum on a substrate surface, which was preliminarily etched in a Br : C_2H_5OH (1 : 4) mixture for one minute. The Mo-layer thickness amounted to ~1000 Å. Indium contacts were soldered to *n*-InP and Contactol silver paste was used to form contacts with the Mo layer.

3. CHARGE TRANSPORT IN THE Cr–*n*-InP STRUCTURE

The current–voltage (*I*–*V*) characteristics measured at $T = 77$ and 300 K for a typical sample are shown in Fig. 1. The forward portions can be described by the relation

$$J = J_0\left(\exp\frac{qV}{nkT} - 1\right), \tag{1}$$

where n is the ideality factor, and the other symbols retain their conventional meaning. The factor $n = 1.01$–1.2 at $T = 300$ K and increases with decreasing temperature, attaining values of 1.5–2.1 at $T = 77$ K. The reverse-bias characteristics do not tend toward constant values; notably, $J_0 \propto V^{\alpha}$, where $\alpha = 0.7$–0.9. These fea-

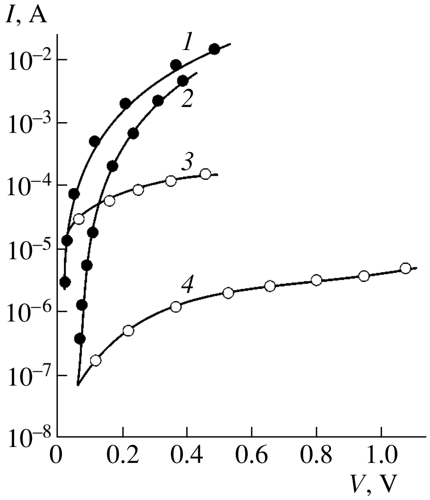

Fig. 1. (*1*, *2*) Forward and (*3*, *4*) reverse-bias current–voltage characteristics of the Schottky Cr–*n*-InP diodes at *T* =77 and 300 K.

tures of the I–V characteristics are indicative of a complex charge-transport mechanism, i.e., of contribution of several types of current, one of them being dominant in various temperature intervals. In the general form, the contribution of different charge-transport mechanisms can be represented as

$$J = \sum_i J_{0i}\left(\exp\frac{qV}{nkT} - 1\right). \quad (2)$$

In our opinion, it is the thermionic emission that contributes predominantly to the charge transport in the samples with $n \approx 1.01$ at $T = 300$ K. An estimate of the Schottky barrier height φ_B from the relation

$$J_{0t} = A^*T^2\exp\frac{q\varphi_B}{kT} \quad (3)$$

yielded $\varphi_B = 0.63$ eV (and $A^* \approx 9$ A/(m^2 K^2) is the effective Richardson constant).

The capacitance–voltage (C–V) characteristics (Fig. 2) yield supplementary data on φ_B and on other parameters of the diode structure. From the cutoff point on the abscissa axis, we determined the values of $\varphi_B = 0.65$ and 0.43 eV for various samples. The former value corresponds to that determined from the I–V data, and the latter one corresponds to the value obtained in [2]. With allowance for the fact that the values of φ_B were obtained in [2] for samples with atomically clean surfaces covered with chromium deposited in ultrahigh vacuum, the larger value of φ_B we obtained can be explained by the presence of an intermediate layer between Cr and n-InP. This fact is corroborated by the estimate of N_d from the slope of the C–V characteristic (equal to $2/q\varepsilon_n N_d$), according to which the value of N_d differs from the Hall value by a factor of 2–5.

If the temperature decreases, the contribution of the generation–recombination component to the total current determined by formula (2) should increase, especially at $T = 77$ K ($n \approx 2$); in this case,

$$J_r = J_{0r}\left(\exp\frac{qV}{2kT} - 1\right), \quad J_{0r} = \frac{qn_iW}{2\tau_r}. \quad (4)$$

In these expressions, W is the width of the space-charge layer, n_i is the intrinsic carrier concentration, and τ_r is the lifetime in the space-charge region. We estimate the contribution from the diffusion and tunneling components of the current. The diffusion component is due to the possible injection of holes into the neutral region. In accordance with the definition of the injection coefficient [3] as

$$\gamma_p \approx \frac{J_p}{J_n} = \frac{qD_pn_i}{N_dLA^*T^2\exp\left(-\frac{q\varphi_B}{kT}\right)} \quad (5)$$

(D_p is the diffusivity of holes, L is the neutral-region width), some contribution of the diffusion current might be expected only for $\varphi_B = 0.65$ eV. However, it follows from (5) that γ_p is negligible even at $T = 300$ K with $n_i \approx 7 \times 10^6$ cm^{-3}.

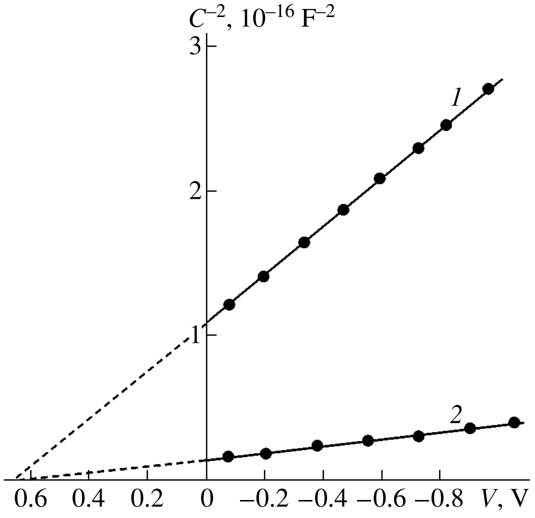

Fig. 2. Voltage–capacitance characteristics of the Schottky Cr–n-InP diodes at $T = 77$ K. *1* for diode 1, and *2* for diode 2.

The possible contribution of the tunnel current J_{tun}, for example, with respect to the thermionic current J_t, can be approximately estimated from the relation

$$J_{tun}/J_t = \exp\left(-\frac{q\varphi_B}{E_{00}}\right)/\exp\left(-\frac{q\varphi_B}{kT}\right), \quad (6)$$

where $E_{00} = \frac{q\hbar}{2}\left(\frac{N_d}{m^*\varepsilon}\right)^{1/2}$. From (6), it can be seen that J_{tun} should be taken into account for $E_{00} > kT$. With allowance for the substrate characteristics, $E_{00}/kT \approx 0.24$ and ≈ 0.9 at $T = 300$ and 77 K, respectively. Thus, the tunnel current contributes negligibly at high temperatures (close to room temperature) and the generation–recombination current (4) predominates at low temperatures. From the above, it follows that the mechanism of charge transport in the investigated Cr–n-InP structures is characterized by the contribution of several types of current in different temperature intervals and can vary, depending on the parameters of the diode structure.

4. CHARGE TRANSPORT IN THE Mo–n-InP STRUCTURES

In Fig. 3, we show the I–V characteristics typical of the Mo–n-InP structure, which are measured at $T = 110$ K in the forward direction. As can be seen from Fig. 3, these dependences are either linear (at low V) or quadratic. From this fact, it follows that there is no emission mechanism caused by the presence of a barrier at the metal–semiconductor interface, nor is the charge transport controlled by recombination in the space-

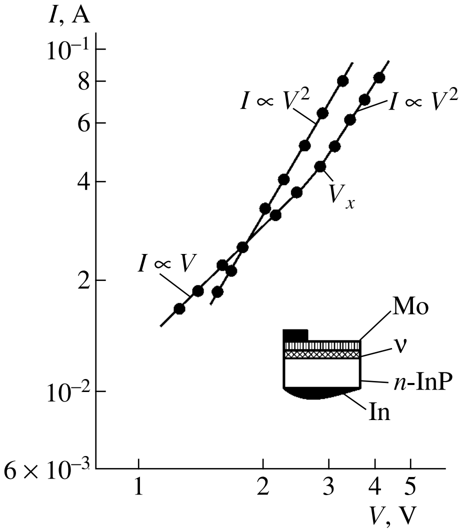

Fig. 3. Forward current–voltage characteristics for two Mo–*n*-InP samples at $T = 110$ K. The inset shows the schematic of the structure (ν is the high-resistance layer).

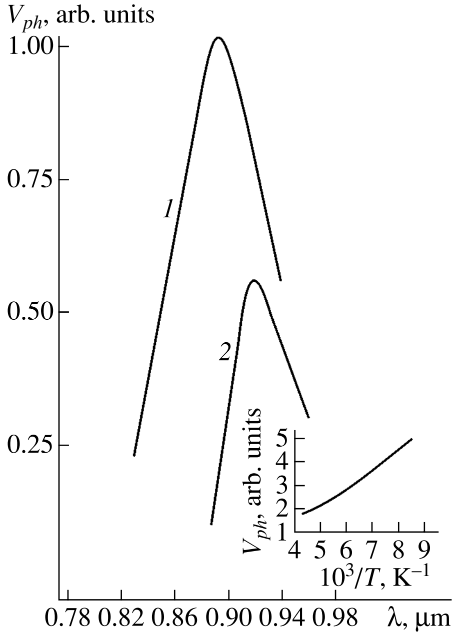

Fig. 4. Spectral photosensitivity of Mo–*n*-InP structures at (*1*) 110 and (*2*) 300 K. The inset shows the temperature dependence of the photovoltage.

charge layer or in the neutral region; i.e., there is no analytical dependence of type (2). In our opinion, the observed character of the *I*(*V*) dependences can be attributed to the double injection of carriers in a high-resistivity semiconductor layer, with the drift transport being predominant. Therefore, the structure under investigation can be represented by the schematic shown in the inset to Fig. 3. During the deposition of molybdenum, the degradation of a thin surface layer occurs. As a result of this degradation, a set of acceptor levels related to defects appear in the band gap of this layer. The acceptor impurities compensate the initial donor centers in this layer, which leads to the formation of a relatively high-resistance layer (ν), and the whole structure has an Mo–ν–*n*-InP form. From the viewpoint of the processing cycle, this degradation is similar to the process of fabricating *p*-InP-based solar cells by sputtering *n*-In_2O_3, where the surface layer of the substrate transforms into a thin *n*-layer [4] as a result of the degradation.

In our case, the application of a forward bias leads to the intense injection of electrons into the compensated ν-region from a good antiblocking contact (*n*-InP) and to the injection of holes from the Mo side. Analytically, this mode can be represented in the form

$$J = q\tau\mu_n\mu_p(n_0 - p_0)\frac{V^2}{W_1^3}, \tag{7}$$

where W_1 is the thickness of the compensated ν-layer. The critical voltage at which the linear portion transforms into a quadratic one $V_x \approx 3$ V (Fig. 3) is related to the transit time of holes $t_p \approx \tau$ as follows:

$$t_p = \frac{W_1^2}{\mu_p V_x}. \tag{8}$$

If we assume the pure Coulomb attraction of holes by negatively charged acceptor centers with a density $N_a \approx 10^{16}$ cm^{-3}, the capture cross section amounts to $S \approx 10^{-11}$ cm^2 at $T = 110$ K; the lifetime $\tau = 1/V_{\text{th}}SN_a$ (V_{th} is the thermal velocity of ~5×10^6 cm/s) is equal to ~2×10^{-12} s, while the ν-layer width $W_1 \approx 2 \times 10^{-5}$ cm for $m_p \approx 60$ cm^2 V^{-1} s^{-1}). The diffusion length of holes $L_p < 2 \times 10^{-5}$ cm, which satisfies the condition for drift transport.

In Fig. 4, we show the spectral-photosensitivity curves measured at $T = 110$ and 300 K for a typical sample. The shift of the descending portion (at $\lambda > \lambda_{\max}$) by 0.07–0.09 eV at the half-maximum $(1/2)V_{\text{ph}}^{\max}$ to the long-wavelength region is characteristic of these curves. This also corroborates that a compensated ν-region is formed because transitions to shallow compensated levels turn out to be possible. The temperature dependence of the photovoltage (Fig. 4, inset) for the case of exposure to light with $\lambda = 0.9$ μm shows slight growth in the range of 110–300 K, which is caused by a weak variation in the lifetime and in other structure parameters.

5. CONCLUSION

The results obtained from investigating charge transport in diode structures based on *n*-InP show that either the thermionic or generation–recombination current (depending on temperature) predominates in the Cr–*n*-InP structures and the double injection of carriers predominates in the Mo–*n*-InP structures; in the latter case, the decisive factor is the degradation of the surface *n*-InP layer.

REFERENCES

1. E. Hökelek and G. J. Robinson, J. Appl. Phys. **54**, 5199 (1983).
2. T. Kendelewicz, N. Newman, R. S. List, *et al.*, J. Vac. Sci. Technol. B **3**, 1206 (1985).
3. E. H. Rhoderick, *Metal–Semiconductor Contacts*, 2nd ed. (Claredon Press, Oxford, 1988; Radio i Svyaz’, Moscow, 1982).
4. Ming-Long Tsai, A. L. Fahrenbruch, and R. H. Bube, J. Appl. Phys. **51**, 2696 (1980).

Translated by V. Bukhanov

Semiconductors, Vol. 37, No. 8, 2003, pp. 940–943. Translated from Fizika i Tekhnika Poluprovodnikov, Vol. 37, No. 8, 2003, pp. 964–967.
Original Russian Text Copyright © 2003 by Bessolov, Zhilyaev, Konenkova, Fedirko, Zahn.

LOW-DIMENSIONAL SYSTEMS

Raman and Infrared Spectroscopy of GaN Nanocrystals Grown by Chloride-Hydride Vapor-Phase Epitaxy on Oxidized Silicon

V. N. Bessolov*, Yu. V. Zhilyaev*, E. V. Konenkova*, V. A. Fedirko, and D. R. T. Zahn*****
** Ioffe Physicotechnical Institute, Russian Academy of Sciences, Politekhnicheskaya ul. 26, St. Petersburg, 194021 Russia*
e-mail: Bes@triat.ioffe.ru
*** State Technological University Stankin, Moscow, 101472 Russia*
**** Institut für Physik, TU Chemnitz, D-09107 Chemnitz, Germany*

Submitted January 27, 2003; accepted for publication January 28, 2003

Abstract—Raman and infrared spectroscopy were applied to study nanocrystalline GaN films grown by chloride–hydride vapor-phase epitaxy on SiO_2/Si(111) substrates at $T = 520°C$. It was ascertained that GaN nanocrystals are formed on the oxidized silicon surface at a rate of 10^{-2} nm/s. It was shown that the peaks in the Raman spectra $E_2(high) = 566$ cm^{-1} and $A_1(LO) = 730$ cm^{-1} correspond to the elastically strained GaN wurtzite structure. It was detected that a peak related to $E_1(TO) = 558$ cm^{-1} arises in the infrared spectra, which shows that elastic stresses in the nanocrystals are insignificant. © *2003 MAIK “Nauka/Interperiodica”.*

Gallium nitride epitaxial films play an important role in the development of short-wavelength devices. The absence of a perfect substrate material is the main hindrance limiting progress in the production of high-efficiency devices based on GaN. Various single crystals (Al_2O_3, SiC, GaAs, Si) are being actively employed as substrates for the heteroepitaxial growth of GaN. Notwithstanding the large misfit between the thermal expansion coefficients and lattice parameters of the epitaxial GaN layer with wurtzite structure and the Si substrate, it is especially attractive to employ the latter in the development of devices due to the integration of GaN into silicon microelectronics.

Recently, much attention has been paid to the technology of producing GaN nanocrystals, as it holds much promise prospective for nanoelectronic devices. Gallium nitride nanocrystals [1, 2] and nanowires [3] have been synthesized by a variety of physical or chemical methods; however, there are no papers devoted to GaN nanostructures on silicon substrates. Epitaxial GaN layers on silicon substrates are grown by various methods: high-vacuum chemical vapor deposition [4], metal–organic chemical vapor deposition (MOCVD) [5], and hydride vapor-phase epitaxy (HVPE) [6]. In low-temperature chloride vapor-phase epitaxy, the formation of a GaN layer on an oxidized silicon substrate begins with the formation of nanocrystalline islands [7].

The optical and electronic properties of GaN layers grown both on Si substrates [8] and GaN nanocrystals have been successfully studied in detail using Raman [3, 9] and infrared (IR) [10] spectroscopy.

This paper is devoted to the study of the properties of GaN nanocrystals grown by chloride–hydride vapor-phase epitaxy on oxidized silicon substrates.

Heteroepitaxy of GaN was carried out on preliminarily oxidized silicon substrates 50 mm in diameter rotating in a hydrogen flow at a frequency of 1 Hz. The ratio of hydrogen and ammonia flows was 2 : 1; the epitaxy temperature $T = 520°C$. After the heteroepitaxy, the pattern of GaN nucleation was studied using atomic-force microscopy (AFM) at room temperature in air.

The Raman spectra were measured in the $Z(X, Y)Z$ geometry, where the Z axis is directed along the wurtzite C axis. As is known, a perfect GaN crystal is characterized by a hexagonal wurtzite structure (space symmetry group C_{6v}^4 At the Γ point, optical phonons are described by the irreducible representation $\Gamma_{opt} = A_1(Z) + 2B + E_1(X, Y) + 2E_2$, where X, Y, and Z are the polarization directions. The $A_1(Z)$, $E_1(X, Y)$, and E_2 modes correspond to Raman active phonons, whereas the B modes are silent. The Raman measurements were carried out at room temperature using a Dilor XY monochromator with a multichannel detector. An Ar laser ($\lambda = 514.5$ nm) was used as the excitation source. The laser-spot size was 1 μm; the spectral resolution was about 2 cm^{-1}. The incident-beam power was about 20 mW.

Infrared spectroscopy measurements were carried out using a Bruker IFS66 instrument.

Heteroepitaxial growth on a preliminarily oxidized silicon substrate at low temperatures begins with three-

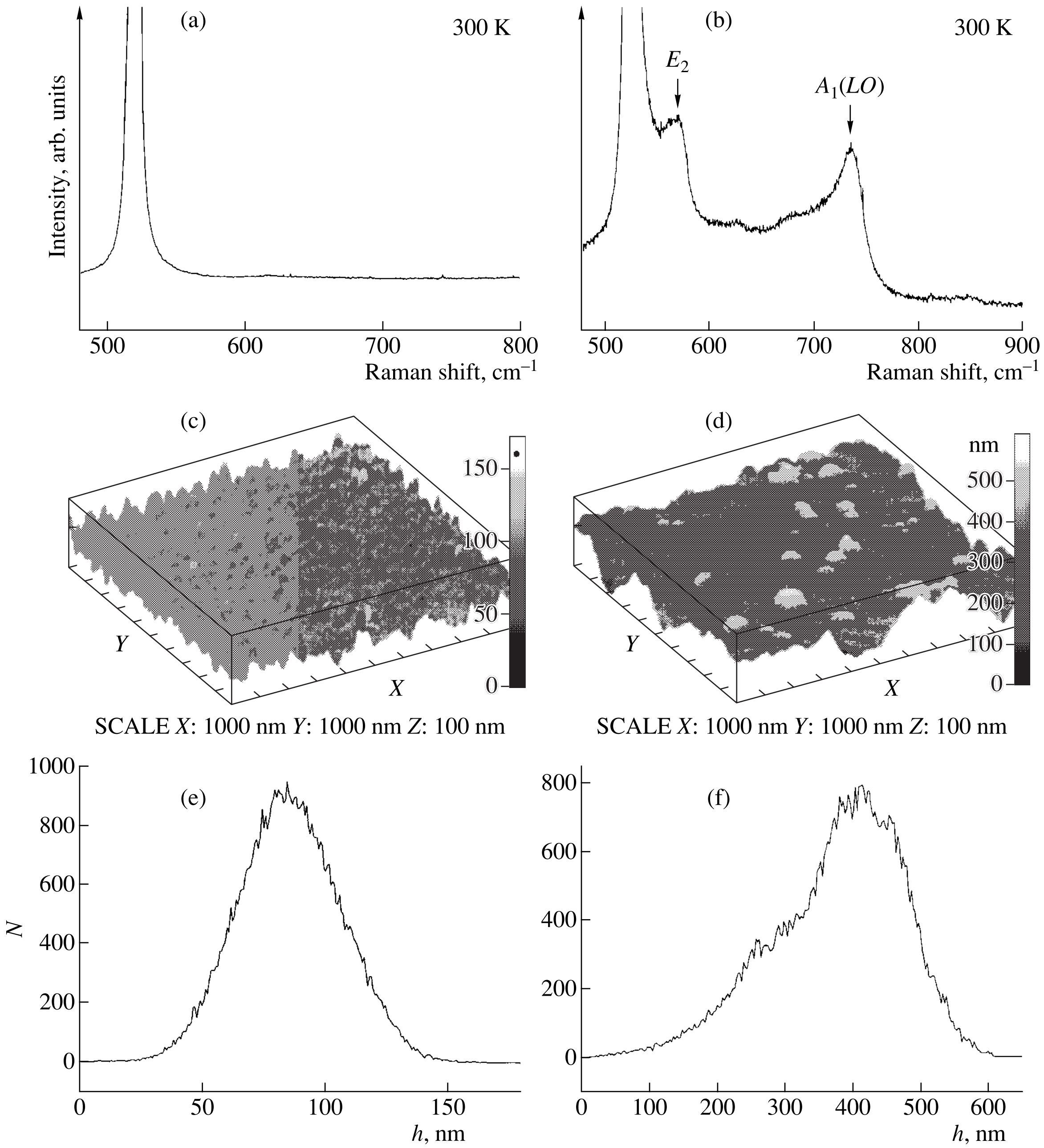

Fig. 1. (a, b) Raman scattering spectra of GaN nanocrystals, (c, d) the GaN/SiO_2 surface profile, and (e, f) the size distribution of GaN nuclei at the growth times of (a, c, e) 100 and (b, d, f) 200 min. The scales (c, d) are 1000 (x), 1000 (y), and 100 (z) nm; T = 300 K.

dimensional nucleation of a GaN island; the height h of an island at the instant of its appearance is comparable to its base radius R [7]. The size distribution of GaN nuclei on the substrate surface varies: the average size h linearly increases from 15 to 400 nm as the growth time increases from 10 to 200 min (see Figs. 1c–1f).

GaN nanocrystals with h = 50, 200, and 400 nm were studied. Infrared spectroscopy showed that the spectra of nanocrystals with $h \approx 200$ and 400 nm are similar and consist of peaks at 1100 and 480 cm^{-1}, which we relate to Si, and a peak at 558 cm^{-1}, due to the $E_1(TO)$ mode (Fig. 2). The latter peak is absent in the spectrum of the nanocrystal with $h \approx 50$ nm.

Raman spectroscopy was applied to reveal the properties of GaN nanocrystals, depending on their sizes, as well as in the course of high-vacuum deposition of silver atoms on the GaN surface. For GaN nanocrystals with $h \approx 400$ nm, peaks at 566 and 730 cm^{-1} were observed, which were due to the E_2 (high) and $A_1(TO)$ modes, respectively, as was a peak at 516 cm^{-1}, which we attribute to Si (Fig. 1b). The spectra of nanocrystals with $h \approx 50$ and 200 nm contained only the peak at 516 cm^{-1} (Fig. 1a). After all of the nanocrystals under study were placed in vacuum and annealed, the Raman spectra initially exhibited only one peak at 516 cm^{-1} (Fig. 3). However, in the course of Ag deposition on the surface, a peak at ~737 cm^{-1} arose, which we attribute to the $A_1(LO)$ mode. After Ag deposition on nanocrystals with $h \approx 200$ and 400 nm, one more peak at 716 cm^{-1} was detected. As Ag atoms were being deposited on the surface, the intensity of the peak at 516 cm^{-1} decreased, whereas the intensities of the peaks at 737 and 716 cm^{-1} initially increased as the Ag-coating thickness grew up to 3 nm, and then decreased.

As is known, at the initial stage of the formation of GaN films, nanocrystalline nuclei arise on the SiO$_2$/Si substrate; these are subject to both elastic and plastic strain with the generation of misfit dislocations. The optical properties of such films may be affected, along with the state of the nanocrystal itself, by the medium between nanocrystals (pores, defects, dislocations) and by the existence of amorphous clusters. Therefore, analysis of Raman and IR spectra is difficult.

The AFM measurements show that new nuclei arise on the SiO$_2$ surface and their size linearly increases at a rate of ~10^{-2} cm/s with the time of film growth increasing (Figs. 1e, 1f). Such a low growth rate of islands is caused by the low epitaxy temperature (520°C) and the high barrier for GaN nucleation on a silicon oxide layer.

The IR absorption spectra for GaN nuclei with $h \approx 50$ nm show (Fig. 2) only the peaks at 480 and 1100 cm^{-1}, which are related to Si [10] (Fig. 2a). In the case of GaN nuclei with $h \approx 200$ and 400 nm, the peak at 558 cm^{-1} arises, which is due to the $E_1(TO)$ mode [10] (Figs. 2b, 2c). A similar peak at 566 cm^{-1} was observed in the IR spectra of GaN layers 0.8 μm thick grown by MOCVD on an Si(001) substrate [10]. The fact that the $E_1(TO)$ peak observed by us is shifted to shorter waves can be explained by weaker elastic stress in nanocrystals 400 nm in size in comparison with the stress in the layers 0.8 μm thick. This is due to the fact that nucleation of nanocrystals occurs on the amorphous layer of silicon oxide, rather than on Si as in [10]. We should note that, according to the theoretical estimates [10], the peak due to the $E_1(TO)$ mode in the spectrum of bulk gallium nitride is at 557 cm^{-1}. Thus, the oxide layer not only prevents the silicon–ammonia interactions with formation of Si$_3$N$_4$, but also reduces the elastic strain in the nanocrystals, caused by the lattice mismatch between Si and GaN.

The Raman spectra of such nanocrystals confirm the IR-spectroscopy data. If the size of GaN nanocrystals is $h \approx 50$ and 200 nm, the Raman spectra exhibit only the peak at 516 cm^{-1} related to Si. If $h \approx 400$ nm, one more peak at 566 cm^{-1} arises, which is due to the $A_1(LO)$ mode. A similar peak at 566.2 cm^{-1} was observed in [8],

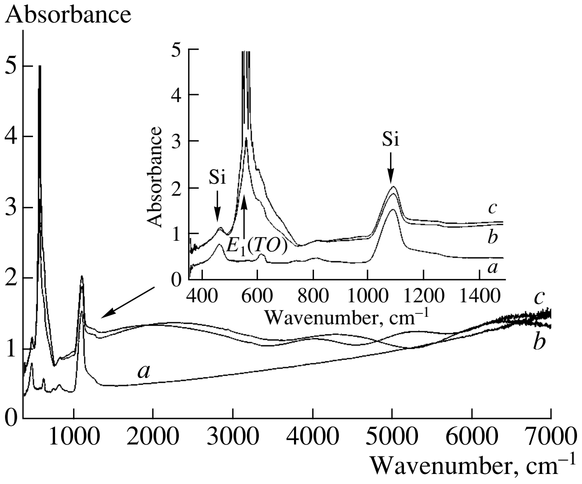

Fig. 2. Infrared absorption spectra of GaN/SiO$_2$/Si nanocrystals with h = (a) 50, (b) 200, and (c) 400 nm.

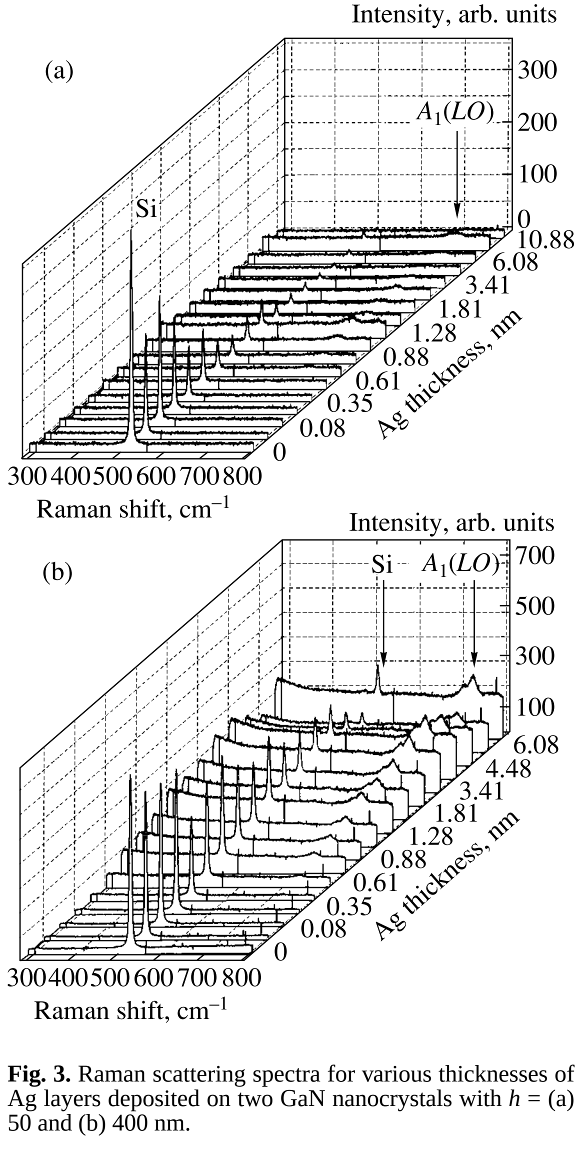

Fig. 3. Raman scattering spectra for various thicknesses of Ag layers deposited on two GaN nanocrystals with h = (a) 50 and (b) 400 nm.

where GaN layers 2 μm thick grown by MOCVD on an Si(111) substrate were studied; this peak was attributed to the elastic stress in the layer. Thus, Raman spectroscopy of GaN nanocrystals with $h \approx 400$ nm grown by HVPE on SiO_2/Si(111) and GaN layers 2 μm thick grown by MOCVD on Si(111) shows similar results, which indicates approximately equal elastic stress.

Raman spectroscopy of GaN nanocrystals with h = 400 nm placed in high vacuum and annealed at T = 600°C shows the disappearance of the peak at 566 cm^{-1}; however, deposition of silver atoms gives rise to the peak at 737 cm^{-1} in all nanocrystals under study, which is also due to the $A_1(LO)$ mode [11] (Fig. 3). As the thickness of the deposited silver layer increased to 3–4 nm, the intensity of the peak at 737 cm^{-1} increased, whereas the intensity of the peak at 516 cm^{-1} decreased. In the course of deposition of silver, one more peak appeared at 716 cm^{-1} in the Raman spectra of nanocrystals with $h \approx 400$ nm; this peak was not identified.

Thus, Raman and IR spectroscopy methods showed that the GaN nanocrystals grown on oxidized silicon exhibit single-crystal properties inherent to the strained wurtzite structure. The low (~10^{-2} cm/s) rate of nanocrystal growth allows one to control the size of nanocrystals and opens up new opportunities for HVPE as applied to gallium nitride nanoelectronics.

ACKNOWLEDGMENTS

This study was supported in part by the Russian Foundation for Basic Research, project no. 03-03-32503, and the federal program of the Ministry of Industry, Science, and Technology of the Russian Federation (state contract 40.012.1.1.1153).

E. V. Konenkova acknowledges the support of the Saxon Ministry of Science and Culture (Germany).

REFERENCES

1. P. Millet, A. Colka, J. S. Williams, and G. J. H. Vantenaar, Appl. Phys. Lett. **63**, 2505 (1993).
2. M. Benaissa, M. Jose-Yacaman, J. M. Hernander, *et al.*, Phys. Rev. B **54**, 17763 (1996).
3. G. S. Cheng, L. D. Zhang, Y. Zhou, *et al.*, Appl. Phys. Lett. **75**, 2455 (1999).
4. M. H. Kim, Y.-C. Bang, N. M. Park, *et al.*, Appl. Phys. Lett. **78**, 2858 (2001).
5. A. Munkholm, C. Thompson, M. V. Raman Murty, *et al.*, Appl. Phys. Lett. **77**, 1626 (2000).
6. Yu. V. Melnik, K. V. Vassilevski, I. P. Nikitina, *et al.*, MRS Internet J. Nitride Semicond. Res. **2**, 39 (1997).
7. V. N. Bessolov, Yu. V. Zhilyaev, E. V. Konenkova, *et al.*, Pis'ma Zh. Tekh. Fiz. **27** (23), 60 (2001) [Tech. Phys. Lett. **27**, 1010 (2001)].
8. M. Benyonul, M. Kuball, B. Benumont, and P. Gibart, Appl. Phys. Lett. **80**, 2275 (2002).
9. Y. G. Cao, X. L. Chen, Y. C. Lan, *et al.*, J. Mater. Res. **15**, 267 (2000).
10. X. Zhang, Y. T. Hou, Z. C. Feng, and J. L. Chen, J. Appl. Phys. **89**, 6165 (2001).
11. S. Tripathy, S. J. Chua, P. Chen, and Z. L. Miao, J. Appl. Phys. **92**, 3503 (2002).

Translated by A. Kazantsev

Semiconductors, Vol. 37, No. 8, 2003, pp. 944–948. Translated from Fizika i Tekhnika Poluprovodnikov, Vol. 37, No. 8, 2003, pp. 968–973.
Original Russian Text Copyright © 2003 by Blank, Gol'dberg, Kalinina, Konstantinov, Posse.

PHYSICS OF SEMICONDUCTOR DEVICES

Ultraviolet Radiation Photodetectors Based on Structures Consisting of a Metal and a Wide-Bandgap Semiconductor

T. V. Blank*, Yu. A. Gol'dberg, E. V. Kalinina, O. V. Konstantinov, and E. A. Posse
Ioffe Physicotechnical Institute, Russian Academy of Sciences, St. Petersburg, 194021 Russia
**e-mail: tblank@delfa.net*

Submitted February 3, 2003; accepted for publication February 11, 2003

Abstract—Recently, much attention has been given to measuring and monitoring ultraviolet radiation from the Sun and artificial sources. Detectors based on various wide-bandgap surface-barrier structures, which are characterized by a linear dependence of the photocurrent on incident power density in the range of 10^{-2}–10^3 W/m^2 and can record various kinds of ultraviolet radiation, are described. For example, GaP detectors with a UFS-6 filter have a spectral photosensitivity range corresponding to that of solar ultraviolet radiation on the Earth's surface. The spectral sensitivity of 4*H*-SiC surface-barrier photodetectors corresponds to the spectral curve of the bactericidal effect produced by ultraviolet radiation. A model has been developed for explaining the process of short-wavelength photoelectric conversion. According to this model, photogenerated electrons and holes can unite into hot excitons, being thus excluded from the photoelectric conversion process. The rise in quantum efficiency with increasing temperature, which has been established experimentally for photodetectors based on Schottky barriers, is attributed to the capture of photogenerated carriers by traps arising from fluctuations of the conduction and valence band edges, with subsequent thermal release of these carriers. These fluctuations are related to imperfections in the surface layer of the semiconductor, which is confirmed by the temperature independence of the quantum efficiency of photodetectors based on *p*–*n* structures. *© 2003 MAIK "Nauka/Interperiodica".*

1. INTRODUCTION

At present, much attention is being given to the monitoring of solar and artificial sources of ultraviolet (UV) radiation in the context of topical issues in medicine, biology, and ecology, in particular, the problem of ozone depletion.

UV radiation (wavelengths λ = 10–380 nm, photon energies $h\nu$ = 3.2–124 eV [1]) covers the following ranges [2–5]: pigmentation radiation, 1.2–4.2 eV, peaked at 2.8–3.3 eV; erythemal (biologically active) radiation, 4.0–6.2 eV, with the first peak at 4.2 eV, a dip at 4.4 eV, and a second peak at 5 eV; vitamin-yielding radiation, 3.9–5.0 eV, peaked at 4.3 eV; and bactericidal radiation, 4.0–5.9 eV, peaked at 4.9 eV.

Wide-bandgap semiconductor structures with a potential barrier and, in particular, a Schottky barrier are most promising for recording UV radiation. This is due to their high sensitivity in the short-wavelength spectral range, linearity of the dependence of the photocurrent on the incident power density, and compatibility with integrated-circuit technology.

This paper reports results obtained from studying the spectral and temperature dependences of the quantum efficiency of photodetectors with Schottky barriers based on wide-bandgap semiconductors, such as GaP, GaN, SiC.

During measurements, the photodetectors studied were placed in a thermostat with quartz windows and illuminated with a mercury or deuterium lamp through a monochromator. The photocurrent was measured in the short-circuit mode at 78–400 K and incident photon energies of 3–6 eV. The photocurrent values were used to determine the quantum efficiency (electron/photon), i.e., the ratio of current sensitivity (A/W) to the energy of photons being detected (eV).

2. PHOTODETECTORS BASED ON GaP, GaN, AND 4*H*-SiC SCHOTTKY BARRIERS

GaP photodetectors were fabricated on Czochralski-grown *n*-GaP wafers with an electron density $n \approx 10^{17}$ cm^{-3} (300 K). An ohmic contact was fabricated on one side of the wafer by alloying with indium, and an optically semitransparent barrier contact, on its other side by chemical deposition of gold. The structure thickness d = 200 μm; the illuminated surface area $S \approx$ 5 mm^2.

The GaP photodetectors were characterized by a spectral sensitivity range of 2.5–6.2 eV with a peak sensitivity at 3.4 eV (Fig. 1), a dark current density less than 10^{-8} A/cm^2 (at a voltage of –1 V), and a time constant of less than 10^{-6} s. With a UFS-6 filter, GaP photodetectors show sensitivity in the spectral range of

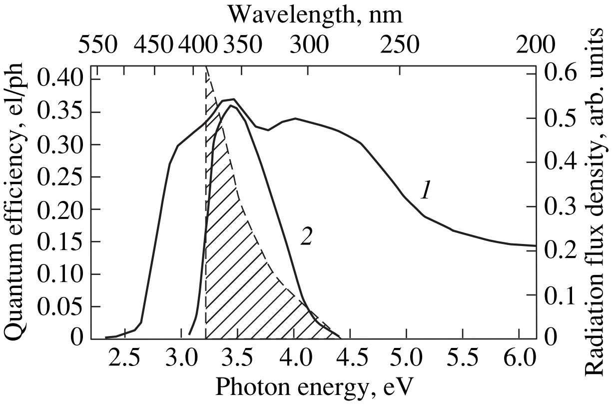

Fig. 1. Spectral dependence of the quantum efficiency of the photoelectric conversion of a GaP photodetector with a Schottky barrier: (*1*) without filter and (*2*) with a UFS-6 filter. The shaded region corresponds to solar UV radiation recorded on the Earth's surface (at Sun elevation of 60°).

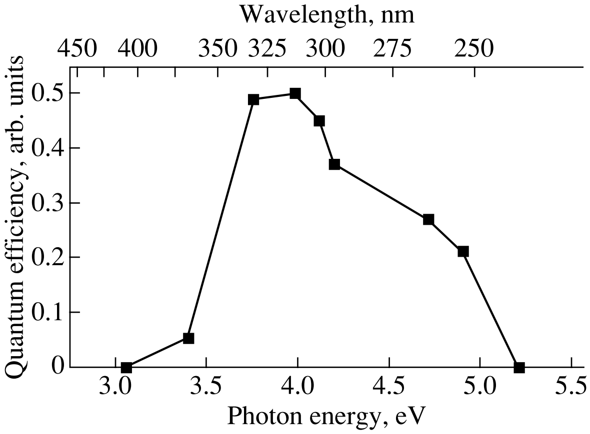

Fig. 2. Spectral dependence of the quantum efficiency of photoelectric conversion of a GaN photodetector with a Schottky barrier.

3.1–4.2 eV, which is close to the spectrum of solar UV radiation on the Earth's surface (Fig. 1). The quantum efficiency of these photodetectors is 0.4–0.5 electron/photon (300 K, no antireflection coating); the photocurrent depends linearly on incident power density in the range 10^{-2}–10^3 W/cm^2. Thus, these structures can be used to measure solar UV radiation.

GaN photodetectors with a Schottky barrier have a spectral sensitivity range of 3.4–5.0 eV, with peak sensitivity at 3.9 eV (Fig. 2), which virtually coincides with the published values for *m–s–m* and *p–n* GaN photodetectors [6–8]. The quantum efficiency γ of these photodetectors is 0.3–0.4 electron/photon at room temperature. The authors believe that GaN and $Al_xGa_{1-x}N$ may be promising materials for selective photodetectors of erythemal UV radiation.

4*H*-SiC layers 25 μm thick with an electron density of 4×10^{15} cm^{-3} (300 K) were grown by CVD on commercial *n*-4*H*-SiC substrates with $n = 10^{19}$ cm^{-3}. The Schottky barrier and ohmic contact were fabricated by thermal evaporation of Cr onto a substrate in different temperature modes. The Schottky barrier was semitransparent to light; the illuminated surface area $S \approx$ 2.25 mm^2.

The spectrum of the quantum efficiency of 4*H*-SiC Schottky photodetectors lies at photon energies of 3.2–5.2 eV (Fig. 3). With increasing photon energy, the quantum efficiency γ grows slowly at $h\nu > 3.2$ eV and more rapidly at $h\nu > 4.2$ eV, reaching a maximum value of ~0.3 electron/photon at 4.9 eV. At $h\nu > 5.0$ eV, the value of γ falls abruptly. 4*H*-SiC surface-barrier photodetectors are characterized by a spectral sensitivity range close to the spectrum of bactericidal UV radiation. Thus, 4*H*-SiC Schottky photodetectors can be used as photodetectors of bactericidal UV radiation. Moreover, photodetectors of this type can operate at elevated temperatures.

The mechanism of photoelectric conversion in structures with a Schottky barrier will now be considered. The long-wavelength threshold of photosensitivity is determined by the energy gap of a semiconductor. For example, no photocurrent is observed for 4*H*-SiC at $h\nu < 3.2$ eV, which is in agreement with published data on the energy gap of 4*H*-SiC ($E_g = 4.2$ eV) [9]. With increasing $h\nu$, the quantum efficiency (at $h\nu > 3.2$ eV) grows slowly at first, which is due to indirect optical transitions (I_1, I_2) between the valence-band top at the Γ point of the Brillouin zone and the conduction-band bottom at the *M* point (Fig. 4). At $h\nu > 4.2$ eV, when optical transitions become direct at the center of the Brillouin zone (D_1, D_2), the quantum efficiency grows more rapidly and reaches a maximum at 4.9 eV. At $h\nu >$ 5 eV, the quantum efficiency falls abruptly. The photosensitivity spectra of GaP and GaN photodetectors exhibit similar behavior.

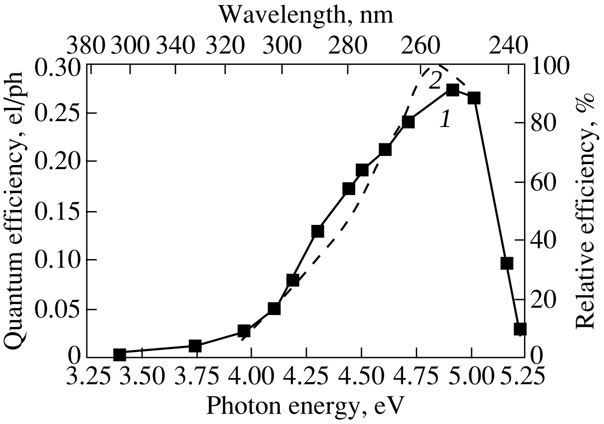

Fig. 3. (*1*) Spectral dependence of the quantum efficiency of photoelectric conversion of a 4*H*-SiC photodetector with a Schottky barrier and (*2*) spectrum of the relative effectiveness of bactericidal UV radiation for a human being.

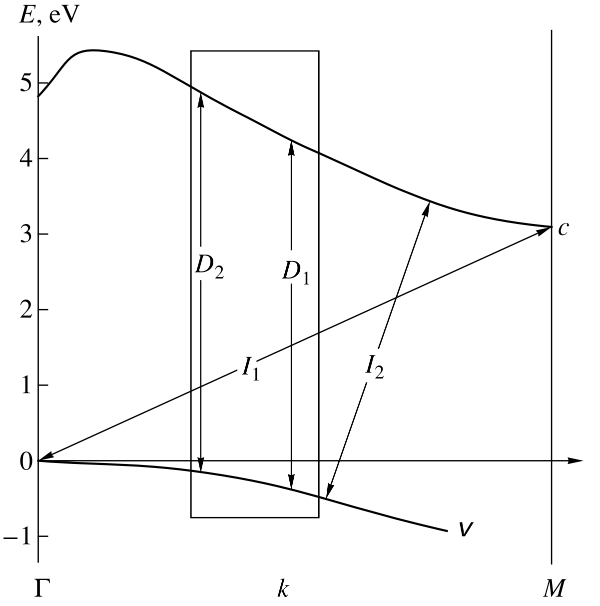

Fig. 4. Band structure of 4*H*-SiC and schematic of optical transitions.

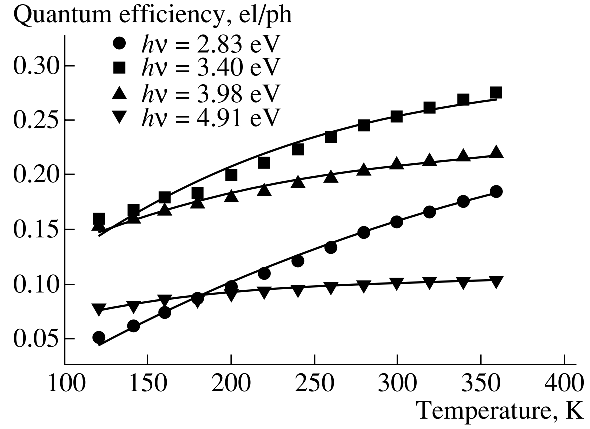

Fig. 5. Temperature dependence of the quantum efficiency of UV photodetectors based on GaP Schottky barriers at different photon energies.

The photosensitivity of detectors with a Schottky barrier has a falloff in the short-wavelength part of the spectrum (5–6 eV), which corresponds to the range of fundamental absorption of the semiconductor. This falloff can be explained in terms of a hot exciton model based exclusively on the intrinsic properties of a semiconductor, particularly, on the structure of the Brillouin zone. All of the semiconductors considered have regions of the Brillouin zone in which the conduction- and valence-band edges are virtually parallel, and the curvature of the dispersion curve is low. For GaP, these regions lie in the vicinity of the *X* point of the Brillouin zone, with the energy of band-to-band transitions equal to ~3.9 eV [10]. For 4*H*-SiC, this is the region between the Γ and *M* points of the Brillouin zone, with the energy of band-to-band transitions equal to ~4.9 eV (Fig. 4). When the energy of photons being detected becomes close to the energy of band-to-band transitions in these regions of the Brillouin zone, a photogenerated electron and hole move in the same direction at similar velocities and may form a hot exciton as a result of Coulomb interaction. The formation of such an exciton has been predicted theoretically [11]. In view of the low curvature of the dispersion curves, the exciton has a large effective mass and binding energy, weakly dissociates in the contact electric field, and weakly interacts with optical phonons, which leads to its long mean free path. Thus, it seems possible that hot excitons can pass across the entire space charge layer, reach the metal or the quasi-neutral bulk of the semiconductor, and recombine there. Therefore, the photogenerated hot electron and hole which form the hot exciton are excluded from further photoelectric conversion processes and the quantum efficiency decreases with increasing photon energy in the short-wavelength region.

3. TEMPERATURE DEPENDENCE OF THE QUANTUM EFFICIENCY OF UV PHOTODETECTORS

Figure 5 shows the temperature dependences of the quantum efficiency of UV photodetectors based on GaP Schottky structures for different photon energies. The experimental results are as follows: the quantum efficiency grows with increasing temperature at any energy of photons being detected; the increase in the quantum efficiency with temperature is weaker the higher the photon energy; raising the temperature by a factor of 3 leads to an increase in the quantum efficiency by a factor of 3.2 at an incident photon energy of 2.83 eV and by a factor of 1.4 at an incident photon energy of 3.98 eV; the temperature dependence of the quantum efficiency levels off at high temperatures (T > 300 K) and high photon energies ($h\nu$ > 3.4 eV).

It is noteworthy that similar temperature dependences are observed for GaAs detectors with a Schottky barrier [12].

Figures 6a and 6b show the temperature dependences of the quantum efficiency of UV photodiodes based on 4*H*-SiC Schottky barriers for different photon energies. The experimental results are as follows: at low temperatures (80–175 K), the quantum efficiency grows with increasing temperature over the entire range of photon energies under investigation; at medium temperatures (200–300 K), the temperature dependence of the quantum efficiency tends to level off with increasing temperature and energy of photons being detected; at higher photon energies, leveling-off is observed at lower temperatures; at high temperatures (300–400 K), the run of the temperature dependence varies with photon energy: in the case of the long-wavelength photoelectric effect (a photon energy of 3.2–4.5 eV), a second region of rising quantum efficiency at $T > 300$ K after the leveling-off portion (the higher the photon energy, the weaker the rise) and a second region of slower rise with a tendency toward leveling-off are observed; in the case of the short-wavelength photoelectric effect (a photon energy of 4.9–5.3 eV), the second region of rising quantum efficiency is not observed and the quantum efficiency is virtually temperature-independent at $T > 300$ K.

The rise with temperature of the long-wavelength quantum efficiency at low temperatures can be accounted for by a shift of the absorption edge and an increase in the diffusion length of holes with increasing temperature. According to the authors' estimates, the diffusion length of holes grows from 0.5 μm at 80 K to 1.5 μm at 400 K, although the authors believe that the main reason for the rise in the quantum efficiency is the shift of the absorption edge. In the case of a short-wavelength photoelectric effect, these factors cannot account for the rise in quantum efficiency with temperature.

It is noteworthy that the temperature dependence of the quantum efficiency of photodetectors based on Si and GaAs *p–n* structures in the short-wavelength region markedly differs from the above dependences for photodetectors with a Schottky barrier [13, 14]: for *p–n* detectors, the quantum efficiency is virtually temperature independent at photon energies of 1.4–6 eV (Si photodetectors) and 1.8–6 eV (GaAs photodetectors). In this case, measurement error does not exceed 1.5% and, therefore, it can be concluded that the quantum efficiency varies in these spectral ranges by no more than 0.01%/°C.

The rise with temperature of the quantum efficiency of photodetectors with a Schottky barrier can only be understood in terms of the fluctuation trap model. The authors believe that the reason for the significant rise in quantum efficiency is the high density of imperfections in the surface layer of the semiconductor. Such imperfections may give rise to fluctuations in the conduction- and valence-band edges. In the absence of an electric field, fluctuations of this kind lead to localization of only a single kind of carriers. However, the electric field of the space charge region simultaneously converts these fluctuations into traps for electrons and holes. Thus, carriers of different signs are the localized within a small region of space and, in the course of time, recombine via tunneling. Varying the temperature leads to a change in the concentration of free thermalized photogenerated carriers because of their partial capture by, and release from, fluctuation traps. With increasing temperature, the concentration of free thermalized photogenerated carriers grows because of the thermal dissociation of electron–hole pairs captured by traps and, consequently, the quantum efficiency of photoelectric conversion grows with temperature until the traps become completely depopulated.

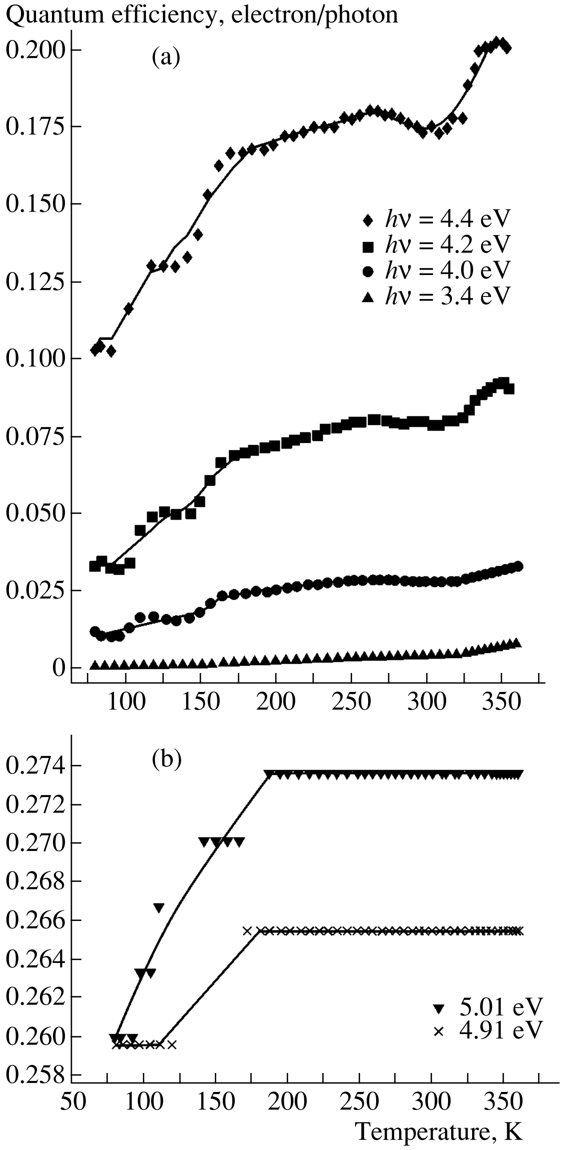

Fig. 6. Temperature dependence of the quantum efficiency of UV photodetectors based on 4*H*-SiC Schottky barriers at different photon energies for the cases of (a) the long-wavelength photoelectric effect ($h\nu$ = 3.4–4.4 eV) and (b) the short-wavelength photoelectric effect ($h\nu$ = 4.91–5.01 eV).

The quantum efficiency γ is equal to the product of probabilities of a number of successive events: the incidence of a photon on the semiconductor $(1 - R)$; the generation of an electron–hole pair by the photon, η; the thermalization of this pair in the space charge region, $(1 - \delta_{hot})$; the separation of the thermalized electron–hole pair by an electric field $(1 - \delta_{therm})$:

$$\gamma = (1-R)\eta(1-\delta_{hot})(1-\delta_{therm}).$$

Here, R is the reflection coefficient; η, the internal quantum efficiency; δ_{hot} and δ_{therm}, the loss factors for hot and thermalized photogenerated carriers.

The value of δ_{therm} depends only on the concentration ratio of trapped ($n_{\rm loc}$) and free (n_f) photogenerated carriers:

$$\delta_{therm} = \frac{n_{loc}}{n_f + n_{loc}}.$$

If it is assumed that $\eta = 1$ and the release of carriers from traps with an activation energy ΔE occurs in accordance with the Boltzmann statistics,

$$1 - \delta_{therm} = \exp(-\Delta E/kT),$$

then

$$\gamma = (1-R)(1-\delta_{hot})\exp(-\Delta E/kT).$$

Interpolation of the experimental data with the use of the suggested theoretical dependence made it possible to determine the activation energy of the fluctuation traps. The activation energy was virtually temperature-independent and equal to 10 meV for GaP photodetectors and 15 meV for 4*H*-SiC photodetectors.

In the case of the long-wavelength photoelectric effect, the second region of rise and leveling-off of the quantum efficiency of 4*H*-SiC photodetectors can be accounted for by specific features of the band structure of 4*H*-SiC. The minimum of the 4*H*-SiC conduction band lies at the point Γ of the Brillouin zone. With increasing photon energy, the optical transition of an electron occurs first indirectly (with phonon absorption) and then as directly (without phonon absorption). The probability of an indirect optical transitions grows with increasing density of phonons, i.e., with increasing temperature. If the characteristic energy of a phonon is taken to be 30 meV, then the corresponding characteristic temperature at which the rise in quantum efficiency must cease will be ~350 K, and it is precisely this value that is observed in experiment. The photon energy at which the rise with temperature ceases is the limiting energy of direct optical transitions. Thus, the absorption in the spectral range of the short-wavelength photoelectric effect at photon energies exceeding 4.9 eV involves direct optical transitions, and at $h\nu \geq$ 4.9 eV a second range of rise in quantum efficiency is not observed. It follows from obtained the experimental data that the energy of direct optical transitions is 4.9 eV for 4*H*-SiC, which is in agreement with published calculated data [9].

The temperature stability of photodetectors based on *p*–*n* structures in the short-wavelength region confirms the model of fluctuation traps. In *p*–*n* structures, the space charge region lies deep in the crystal bulk. Imperfections in the surface layer (in particular, fluctuation traps) are not subject to the electric field of the space charge region and cannot simultaneously serve as traps for electrons and holes. Therefore, the quantum efficiency of *p*–*n* photodetectors is independent of the density of defects in the surface layer and virtually temperature independent.

To conclude, it should be noted that investigations of structures based on a metal and a wide-gap semiconductor were initiated by Professor D.N. Nasledov in the 1970s.

REFERENCES

1. *Photometry. Terms and Definitions*, GOST-26148-84, Appendix 1 (1992).
2. L. R. Koller, *Ultraviolet Radiation* (Wiley, New York, 1965).
3. K. L. Coulson, *Solar and Terrestrial Radiation* (Academic, New York, 1975).
4. E. E. Anderson, *Fundamentals of Solar Energy Conversion* (Addison-Wesley, Reading, MA, 1983).
5. *WHO, Environmental Hygienic Criterions 1984. Ultraviolet Radiation*, *WHO Environmental Health Criterion* 160 (International Fadiation Protection Association and WHO, Geneva, 1994).
6. Q. Chen, J. W. Yang, A. Osinsky, *et al.*, Appl. Phys. Lett. **70**, 2277 (1997).
7. E. Monroy, T. Palacios, O. Hainaut, *et al.*, Appl. Phys. Lett. **80**, 3198 (2002).
8. J. M. van Hove, R. Hickman, J. J. Klaassen, *et al.*, Appl. Phys. Lett. **70**, 2282 (1997).
9. *Properties of Advanced Semiconductor Materials*, Ed. by M. Levinshtein, S. Rumyantsev, and M. Shur (Wiley, New York, 2000).
10. *Landolt-Burnstein. New Series*, Ed. by O. Madelung (Springer, New York, 1982), Vol. 17a.
11. R. F. Kazarinov and O. V. Konstantinov, Zh. Éksp. Teor. Fiz. **40**, 936 (1961) [Sov. Phys. JETP **13**, 654 (1961)].
12. Yu. A. Goldberg, O. V. Konstantinov, O. I. Obolensky, *et al.*, J. Phys.: Condens. Matter **11**, 455 (1999).
13. Yu. A. Gol'dberg, V. V. Zabrodskiĭ, O. I. Obolenskiĭ, *et al.*, Fiz. Tekh. Poluprovodn. (St. Petersburg) **33**, 344 (1999) [Semiconductors **33**, 343 (1999)].
14. Yu. A. Gol'dberg, O. V. Konstantinov, V. N. Lantratov, *et al.*, Fiz. Tekh. Poluprovodn. (St. Petersburg) **33**, 876 (1999) [Semiconductors **33**, 804 (1999)].

Translated by M. Tagirdzhanov

Semiconductors, Vol. 37, No. 8, 2003, pp. 949–954. Translated from Fizika i Tekhnika Poluprovodnikov, Vol. 37, No. 8, 2003, pp. 974–979.
Original Russian Text Copyright © 2003 by Andreev, Il'inskaya, Kunitsyna, Mikhaĭlova, Yakovlev.

PHYSICS OF SEMICONDUCTOR DEVICES

High-Efficiency GaInAsSb/GaAlAsSb Photodiodes for 0.9- to 2.55-μm Spectral Range with a Large-Diameter Active Area

I. A. Andreev, N. D. Il'inskaya, E. V. Kunitsyna, M. P. Mikhaĭlova, and Yu. P. Yakovlev

Ioffe Physicotechnical Institute, Russian Academy of Sciences, St. Petersburg, 194021 Russia

Submitted February 10, 2003; accepted for publication February 17, 2003

Abstract—The results of a study aimed at the fabrication of high-sensitivity photodiodes for the 0.9- to 2.55-μm spectral range with a photosensitive area diameter as large as 1–3 mm are presented. A large range of photodiodes based on GaSb/GaInAsSb/GaAlAsSb heterostructures with a long-wavelength edge of spectral sensitivity $\lambda = 2.4$ and $\lambda = 2.55$ μm have been developed. The special features of the photodiodes are their high monochromatic current sensitivity in the spectral peak, high operating speed, and low reverse dark current density. The detectivity of photodiodes estimated from the measured noise level and monochromatic current sensitivity in the spectral peak reaches $D^*(\lambda_{\max}, 1000, 1) = (0.8\text{–}1.0) \times 10^{11}$ Hz$^{1/2}$ cm W^{-1}. *© 2003 MAIK "Nauka/Interperiodica".*

1. INTRODUCTION

The spectral range of 0.9–3.0 μm attracts the considerable interest of those designing instruments for use in laser diode spectroscopy of gases and molecules, laser ranging and location, medicine, and environmental monitoring [1–4]. The principal problem in these areas is the detection of an optical signal with minimum possible intensity. Therefore, the threshold characteristics defining the lowest intensity signals detected at the noise level are of principal importance. To provide minimum noise level, a photodiode must have low dark current and, respectively, high dark resistance in the photovoltaic mode. When a photodiode is used with a preamplifier, the conditions of low noise level and broad bandwidth lead to the demand for the lowest possible capacitance of the photodiode. Further, the specific detectivity of a photodiode increases with increasing diameter of the active area. A large size of the active area imposes strict constraints on the surface homogeneity and the quality of heterointerfaces between the semiconductor epitaxial structures forming the photodiode.

Using liquid-phase epitaxy (LPE) the laboratory of IR optoelectronics of the Ioffe Physicotechnical Institute has designed and fabricated high-performance LEDs [5], and also lasers [6] and photodiodes with matching spectral sensitivity [7], including avalanche diodes [8] based on multicomponent $Ga_{1-x}In_xAs_ySb_{1-y}$ narrow-gap solid solutions. LPE provides for the production of high-quality bulk epitaxial layers, and its relative simplicity and low cost still make it an attractive method in the fabrication of optoelectronic devices.

In this report, the specific features of the production of GaInAsSb/GaAlAsSb photodiode heterostructures lattice-matched with GaSb, as well as the physical processes underlying the operation of these photodiodes, are examined. The principal characteristics of photodiodes for the spectral sensitivity range of 0.9–2.55 μm with an active area 1–3 mm in diameter are presented.

2. PRODUCTION OF GaSb/$Ga_{1-x}In_xAs_ySb_{1-y}$/$Ga_{1-x}Al_xAs_ySb_{1-y}$ LATTICE-MATCHED HETEROSTRUCTURES

GaSb/$Ga_{1-x}In_xAs_ySb_{1-y}$/$Ga_{1-x}Al_xAs_ySb_{1-y}$ photodiode heterostructures were grown by LPE on (100) *n*-GaSb substrates doped with Te to $(1\text{–}5) \times 10^{17}$ cm^{-3}. The binary compounds InSb, GaSb, and InAs were used as stock components for GaInAsSb epitaxial layers. For the growth of GaAlAsSb, we used Ga of 99.999 wt % purity, GaSb and Al of 99.999 wt % purity, and saturating GaAs substrate intended for introducing As into the liquid phase. The equilibrium mole fractions in liquid and solid phases at fixed temperature and overcooling were calculated using the thermodynamic method [9]. To obtain solid solutions lattice-matched with the substrate, the liquid-phase composition determined from calculation was ascertained experimentally. The chemical composition of solid solutions at the surface and its variation across the thickness (normal to the heterointerface plane) were determined by quantitative X-ray fluorescence analysis using a JXA-5 CAMEBAX X-ray microanalyzer.

In this way, epitaxial layers of $Ga_{0.78}In_{0.22}As_{0.18}Sb_{0.82}$ solid solutions were reproducibly grown at the miscibility gap boundary from the liq-

Parameters of $Ga_{1-x}In_xAs_ySb_{1-y}$ and $Ga_{1-x}Al_xAs_ySb_{1-y}$ epitaxial layers

Solid solution	Growth temperature, °C	Thickness, µm	Band gap E_g, eV; $T = 300$ K
$Ga_{0.78}In_{0.22}As_{0.18}Sb_{0.82}$	600	2.2–2.8	0.53
$Ga_{0.76}In_{0.24}As_{0.21}Sb_{0.79}$	600	2.2–2.8	0.51
$Ga_{0.66}Al_{0.34}As_{0.025}Sb_{0.975}$	599	1.5–2.0	1.1
$Ga_{0.50}Al_{0.50}As_{0.04}Sb_{0.96}$	599	1.5–2.0	1.3

uid phase of the molecular composition at $T = 600$°C with overcooling $\Delta T = 3$°C. When (111)B GaSb substrate was used, the indium content in solid phase increased to $x = 0.24$ under the same technological conditions and liquid phase composition. A wide-bandgap "window" of the photodiode heterostructures was formed by $Ga_{0.66}Al_{0.34}As_{0.025}Sb_{0.975}$ layers grown at $T = 599$°C. The average growth rate was 3.0–4.0 and 1–1.5 µm min^{-1} for the GaInAsSb and GaAlAsSb solid solutions, respectively. The parameters of the obtained epitaxial layers are listed in the table.

According to X-ray diffraction data, the lattice mismatch between the layer and the substrate was positive in all samples: $\Delta a/a = (2–8) \times 10^{-4}$ at room temperature. The FWHM of the diffraction reflections was 15″–20″ for the layers and 10″–12″ for the substrate, which indicates high structural perfection of the epitaxial layers and planarity of the layer–substrate interface. The FWHM of the photoluminescence (PL) peaks (Fig. 1) for the $Ga_{0.78}In_{0.22}As_{0.18}Sb_{0.82}$ epitaxial layers was $\Delta h\nu = 16–18$ meV at $T = 80$ K, which is typical of solid solutions with a homogeneous composition. The energy gap of solid solutions (see table) determined in the study of PL and transmission spectra (Figs. 1, 2) correlate well with the data calculated from a semi-empirical relation, where E_g of the quaternary solid solution for direct transitions was determined by interpolation of the energy gaps of the binary compounds with the use of the bowing parameters for ternary compounds [10].

3. PHOTODIODES WITH A 2.40- TO 2.55-µm LONG-WAVELENGTH EDGE OF SPECTRAL SENSITIVITY

To produce high-efficiency long-wavelength photodiodes based on $Ga_{1-x}In_xAs_ySb_{1-y}$ solid solutions, it is necessary to resolve a series of additional technical problems, such as the reduction of the majority carrier density in the active region of high-speed devices, suppression of leak currents, fabrication of ohmic contacts, and achievement of high linearity of the output signal.

We have produced and thoroughly studied photodiodes based on n-GaSb/n-$Ga_{1-x}In_xAs_ySb_{1-y}$/p^+-$Ga_{1-x}Al_xAs_ySb_{1-y}$ heterostructures grown on (100) and (111)B GaSb substrates (see table). The active region was Te-doped in a wide range of densities $n = (0.2–20) \times 10^{16}$ cm^{-3}, and the wide-bandgap window was Ge-doped to $p = 8 \times 10^{18}$ cm^{-3}. Mesa-photodiodes with an active area 1–3 mm in diameter were formed on the grown layers by standard photolithography. The ohmic contacts to the p-GaAlAsSb and n-GaSb substrates were AuGe/Ni/Au and Cr/Au/Ni/Au, respectively.

The solid line in Fig. 3 shows the spectral distribution of sensitivity for a typical $Ga_{0.78}In_{0.22}As_{0.18}Sb_{0.82}/Ga_{0.66}Al_{0.34}As_{0.025}Sb_{0.975}$ photo-

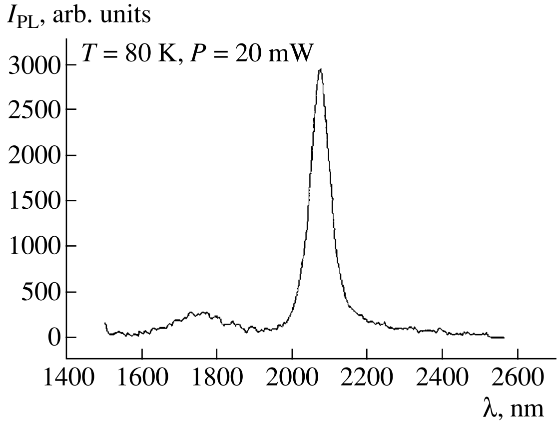

Fig. 1. PL spectrum of $Ga_{0.78}In_{0.22}As_{0.18}Sb_{0.82}$ epitaxial layer at $T = 80$ K. Parameters of the intensity peak I_{PL}: $\lambda_{max} = 2.075$ µm, $\Delta h\nu = 17.3$ meV.

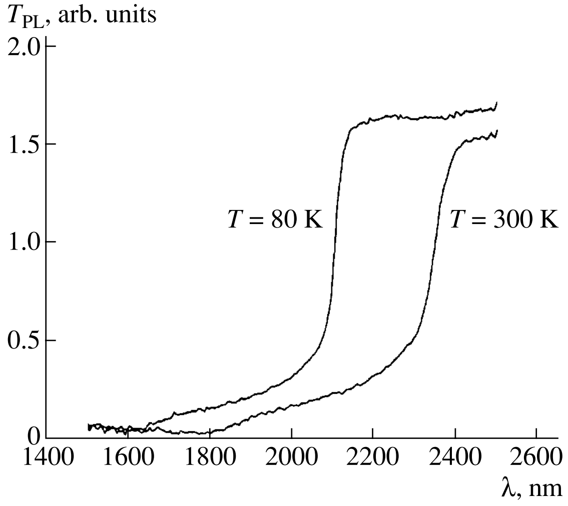

Fig. 2. Transmission spectra of $Ga_{0.78}In_{0.22}As_{0.18}Sb_{0.82}$ epitaxial layer (thickness ~2 µm).

diode at room temperature. As seen, at $T = 300$ K the long-wavelength edge lies at 2.4 μm. The energy gap of the narrow-gap $Ga_{0.78}In_{0.22}As_{0.18}Sb_{0.82}$ solid solution determined from the wavelength corresponding to a twofold decrease in sensitivity is 0.53 eV at $T = 300$ K, which correlates with the data obtained in studies of the PL and transmission spectra (table). When the active region is $Ga_{0.76}In_{0.24}As_{0.21}Sb_{0.79}$, the long-wavelength edge of the diode spectral sensitivity is red-shifted to $\lambda = 2.55$ μm (Fig. 3, line *3*). The short-wavelength cutoff of the photosensitivity is due to strong absorption of the short-wavelength radiation in the wide-bandgap window. The presence of the window essentially reduces the loss of light-generated carriers via surface recombination. The choice of material for this layer offers an additional means to modify the position of the short-wavelength edge of the spectral sensitivity and reverse dark current in a structure. Thus, the short-wavelength edge of the diode spectral sensitivity is defined by the energy gap of the window material and lies at 0.9 μm for $Ga_{0.66}Al_{0.34}As_{0.025}Sb_{0.975}$ (Fig. 3, solid line), 0.8 μm for $Ga_{0.50}Al_{0.50}As_{0.04}Sb_{0.96}$ (Fig. 3, curve *1*), and 1.6 μm for GaSb (Fig. 3, curve *2*).

Figure 4 shows temperature dependences of the long-wavelength edge of spectral sensitivity for a $Ga_{0.78}In_{0.22}As_{0.18}Sb_{0.82}/Ga_{0.66}Al_{0.34}As_{0.025}Sb_{0.975}$ photodiode. The temperature coefficient of the energy gap of the narrow-gap $Ga_{0.78}In_{0.22}As_{0.18}Sb_{0.82}$ solid solution was found to be $\alpha = -3.8 \times 10^{-4}$ eV K^{-1} in the temperature range $T = -40$–60°C. The estimated temperature shift of the long-wavelength edge of spectral sensitivity at the wavelength $\lambda_{(1/2)\max}$ equals 1.6 nm K^{-1}. The monochromatic current sensitivity in the spectral peak ($\lambda_{\max} = 2.0$–2.2 μm) is $S_\lambda = 1.0$–1.1 A W^{-1}, which corresponds to a quantum efficiency of 0.6–0.7 without a special antireflection coating. The deposition of antireflection SiO_2 and Si_3N_4 films allowed us to reach an increase in sensitivity by nearly 30% at a wavelength of about $\lambda = 2.0$ μm. However, in this case, the reverse dark current also substantially increased, so the signal/noise ratio was adversely affected.

The study of capacitance–voltage characteristics has shown that the impurity distribution in a heterostructure is sharp and that the majority carrier density in the active region may vary, depending on the doping level, in a wide range, $n = (2–200) \times 10^{15}$ cm^{-3}, (Fig. 5). A high operating speed demands minimum intrinsic capacitance of a photodiode; thus, the majority carrier density must be low. It is necessary to keep in mind that dark current has a local minimum at the density $n = (8–20) \times 10^{15}$ cm^{-3}, which should be regarded as optimum in this case. The required content of Te in the melt is $N_{Te} = 1.67 \times 10^{-5}$ at. % (Fig. 5).

The operating speed of the photodiode is defined by three processes: the time of carrier transit across the active region ($t_{tr} = 10^{-11}$–10^{-12} s); the time of generated carrier diffusion to the space charge region (in our case, carriers originate directly in the space charge region); and, lastly, the *RC* constant. The operating speed of the discussed photodiodes is determined by the *RC* constant; in the operating mode with a load $R_l = 50\ \Omega$ and

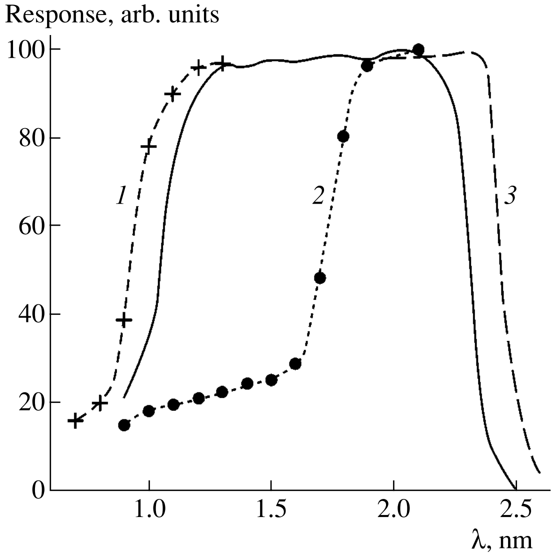

Fig. 3. Spectral distribution of photosensitivity of GaInAsSb photodiodes at $T = 300$ K: (solid line) $Ga_{0.78}In_{0.22}As_{0.18}Sb_{0.82}$ active region and $Ga_{0.66}Al_{0.34}As_{0.025}Sb_{0.975}$ wide-gap window; (*1*) $Ga_{0.50}Al_{0.50}As_{0.04}Sb_{0.96}$ window; (*2*) GaSb window; (*3*) $Ga_{0.76}In_{0.24}As_{0.21}Sb_{0.79}$ active region.

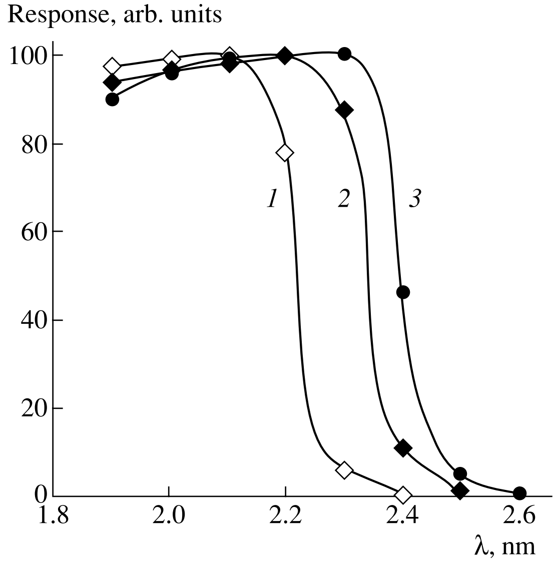

Fig. 4. The long-wavelength edge of spectral sensitivity of the $Ga_{0.78}In_{0.22}As_{0.18}Sb_{0.82}/Ga_{0.66}Al_{0.34}As_{0.025}Sb_{0.975}$ photodiode at temperatures of (*1*) –40, (*2*) 20, and (*3*) 60°C.

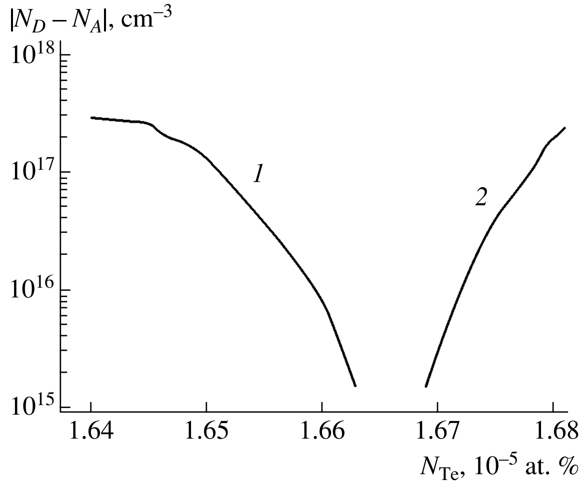

Fig. 5. The density $|N_D – N_A|$ in the GaInAsSb epitaxial layer as a function of the Te content N_{Te}, at. %, in the liquid phase for (*1*) *p*-type and (*2*) *n*-type conduction.

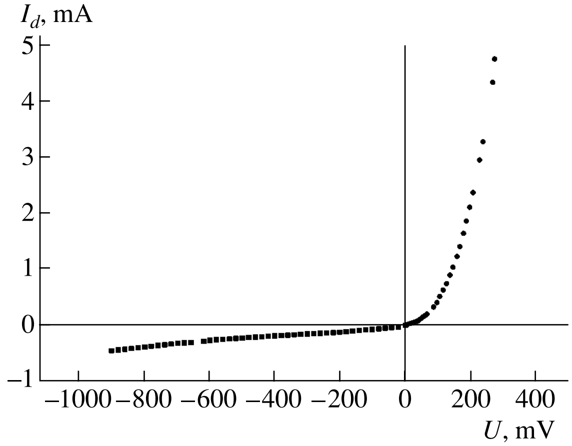

Fig. 6. *I–V* characteristic of the GaInAsSb/GaAlAsSb photodiode with an active area 2 mm in diameter, $T = 300$ K.

a photodiode intrinsic capacitance $C = 1000–2000$ pF, it does not exceed $t_{0.1–0.9} = 120–250$ ns, which is a good result for a photodiode whose active area has such a large diameter.

As mentioned above, special restrictions are imposed on the reverse dark current of a photodiode, because the detectivity is defined by the dark current I_d (photodiode operation mode) or by the shunting resistance $R_0 = (dU/dU)_{U=0}$ (photovoltaic mode). Figure 6 shows an example of a current–voltage (*I–V*) characteristic of a typical photodiode with an active area 2 mm in diameter, and Figure 7 shows the temperature dependence of the shunting resistance R_0. Both the dark current and shunting resistance are strongly dependent on the energy gap of the solid solution and the mechanism of dark current transport:

$$I_d \propto \exp(-E_g/nkT), \quad (1)$$

where n is the parameter defined by the dark current origin; it varies from $n = 1$ (band-to-band recombination) to $n = 2$ (generation–recombination mechanism). For this situation, it was necessary to study the nature of dark current in the *n*-GaSb/*n*-GaAlAsSb/p^+-GaAlAsSb structure. We have studied forward and reverse *I–V* characteristics at different temperatures. Figure 8a shows typical dependences of the dark current on the reverse bias in a photodiode with a 2-mm active-region diameter at different temperatures. Figure 8b shows the temperature dependence of the reverse current at a bias $U = –0.2$ V, as well as the calculated temperature dependences for the generation–recombination (G–R) and diffusion mechanisms of current transport. It is evident that the experimental data correlate better with the dependence for the G–R current. The temperature dependence of this current is expressed by $I \propto T^{3/2}\exp(-E_g/2kT)$. The activation energy for this dependence is $E_A^* = 0.3$ eV, which is close to half the energy gap of the active region material (GaInAsSb, $E_g(0) \approx 0.6$ eV). The deviation of the experimental dependence from that calculated for the G-R current at low temperatures is due to the increase of the tunnel component in the dark current [11]; this component is characterized by a weaker temperature dependence, so it becomes dominant in narrow-gap materials under high bias and at low temperatures.

At room temperature, the $I(U)$ dependence under a reverse bias over 0.2–0.5 V is weak ($I \propto W \propto U^{1/2}$); it is described by the relation

$$I_{G-R} = qn_iWA/\tau_{eff}, \quad (2)$$

where q is the elementary charge, A is the *p*–*n*-junction area, W is the space charge layer width, n_i is the intrin-

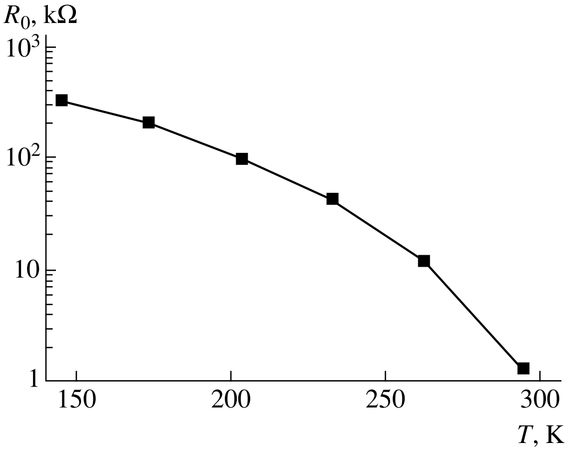

Fig. 7. Temperature dependence of the shunting resistance R_0 of the GaInAsSb/GaAlAsSb photodiode 2 mm in diameter.

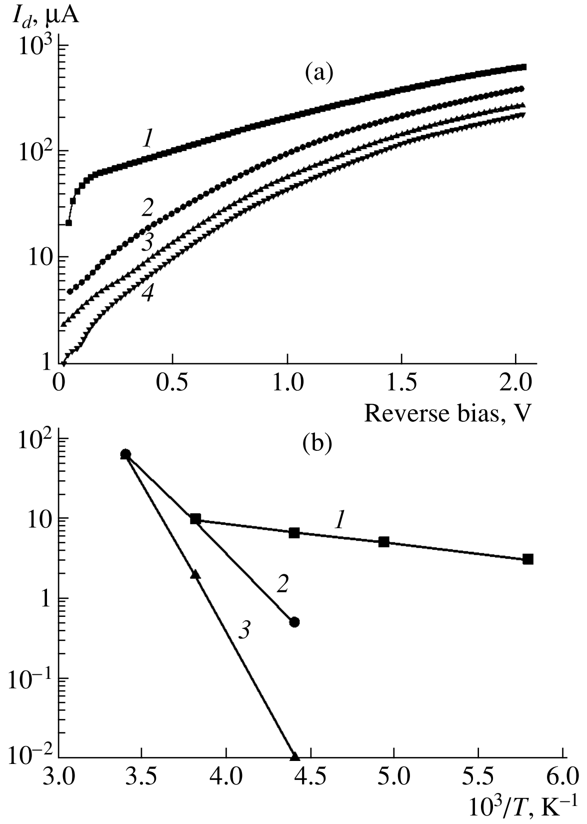

Fig. 8. The reverse dark current I_d of the GaInAsSb/GaAlAsSb photodiode with the long-wavelength edge of spectral sensitivity λ = 2.4 μm, 2 mm in diameter: (a) *I–V* characteristics at temperatures of (*1*) 22, (*2*) –10, (*3*) –70, and (*4*) –100°C. (b): (*1*) temperature dependences under a reverse bias $U = -0.2$ V; calculated dependences for (*2*) generation-recombination and (*3*) diffusion current.

sic carrier density, and τ_{eff} is the effective lifetime of minority carriers. At $n_i = 4 \times 10^{14}$ cm^{-3} and $W \approx 1$ μm, it can be found from the experimental value of current that $\tau_{\mathrm{eff}} = (1.8\text{–}9) \times 10^{-7}$ s, which considerably exceeds the data in the literature and is close to the radiative lifetime for GaInAsSb solid solutions. In the best diodes, the reverse dark current density was $j = 3 \times 10^{-3}$ A cm^{-2} under a reverse bias $U = -(0.2\text{–}1.0)$ V. Analysis of forward *I–V* characteristics has shown that current can be presented in an analytical form as $I \propto \exp(qU/nkT)$, where n increases from $n = 1.9$ to $n = 2.8$ with temperature decreasing. This indicates that the mechanism of dark current changes from generation-recombination to tunneling.

Thus, according to our study, the bulk component of the reverse dark current in $Ga_{0.78}In_{0.22}As_{0.18}Sb_{0.82}/Ga_{0.66}Al_{0.34}As_{0.025}Sb_{0.975}$ photodiodes has two components: generation-recombination and tunneling. Further reduction of the dark current can be attained by improving the fabrication technology of photodiode structures, e.g., by growing the active region with the inclusion of rare-earth elements to reduce the background density of impurities [12], or by using lead as a solvent in the growth of GaInAsSb [13]. These methods substantially improve the quality of the epitaxial layer by reducing the density of defects and background impurities, which results in a lengthening of the effective lifetime of carriers in the active region and, consequently (see (2)), in a decrease in the reverse dark current. Further, the surface component of the reverse dark current, which is related to surface leakage, can be reduced by choosing the optimal technique of surface mesa-structure formation [14] or by sulfide passivation of the lateral surface of the mesa in GaSb/GaInAsSb/GaAlAsSb photodiode structures [15].

The photodiode detectivity, estimated from the measured noise level and the current sensitivity, reaches, in the spectral peak, the value $D^*(\lambda_{\max}, 1000, 1) = (0.8\text{–}1.0) \times 10^{11}$ Hz$^{1/2}$ cm W^{-1}. The nonlinearity of the output signal does not exceed 0.1%.

4. CONCLUSION

High-efficiency high-speed GaInAsSb/GaAlAsSb photodiodes with a long-wavelength edge of the spectral sensitivity λ = 2.4 and 2.55 μm with a large-diameter active area have been produced and studied. In the best diodes, the density of the reverse dark current is as low as $j = 3 \times 10^{-3}$ A cm^{-2} at a bias $U = -(0.2\text{–}1.0)$ V. The investigation of the nature of dark current has shown that the bulk component of the reverse dark current in the diodes under study consists of generation-recombination and tunneling components.

ACKNOWLEDGMENTS

We are grateful to Ya. V. Terent'ev and T. B. Popova for their assistance with the experiment and helpful discussions.

REFERENCES

1. A. I. Nadezhdinski and A. M. Prokhorov, Proc. SPIE **1724**, 2 (1992).
2. R. J. Becherer, Laser Focus World **29**, 71 (1993).
3. R. Martini, C. Bethear, F. Capasso, *et al.*, in *Abstracts Book of 5th International Conference on MID-IR Optoelectronic Materials and Devices (MIOMD-V)* (Annapolis, Maryland, 2002), pp. 04–05.
4. T. L. Troy and S. N. Thennadil, J. Biomed. Opt. **6** (2), 167 (2001).
5. K. D. Moiseev, M. P. Mikhailova, B. I. Zhurtanov, *et al.*, Appl. Surf. Sci. **142**, 257 (1999).
6. A. N. Baranov, E. A. Grebenshchikova, B. E. Dzhurtanov, *et al.*, Pis'ma Zh. Tekh. Fiz. **14**, 1839 (1988) [Sov. Tech. Phys. Lett. **14**, 798 (1988)].

7. I. A. Andreev, M. A. Afrailov, A. N. Baranov, *et al.*, Pis’ma Zh. Tekh. Fiz. **15** (7), 20 (1989) [Sov. Tech. Phys. Lett. **15**, 253 (1989)].
8. I. A. Andreev, A. N. Baranov, M. V. Voznitskiĭ, *et al.*, Opt. Mekh. Prom., No. 7, 19 (1991).
9. A. M. Litvak and N. A. Charykov, Zh. Fiz. Khim. **64**, 2331 (1990).
10. F. Karota, H. Mani, J. Bhan, *et al.*, Rev. Phys. Appl. **22**, 1459 (1987).
11. J. L. Moll, *Physics of Semiconductors* (McGraw-Hill, New York, 1964).
12. A. T. Gorelenok, A. V. Kamanin, and N. M. Shmidt, Microelectronics J. **26**, 705 (1995).
13. E. V. Kunitsyna, I. A. Andreev, N. A. Charykov, *et al.*, Appl. Surf. Sci. **1–4**, 371 (1999).
14. E. V. Kunitsyna, I. A. Andreev, M. P. Mikhailova, *et al.*, Proc. SPIE **4340**, 244 (2000).
15. I. A. Andreev, E. V. Kunitsyna, V. M. Lantratov, *et al.*, Fiz. Tekh. Poluprovodn. (St. Petersburg) **31**, 653 (1997) [Semiconductors **31**, 556 (1997)].

Translated by D. Mashovets

Semiconductors, Vol. 37, No. 8, 2003, pp. 955–959. Translated from Fizika i Tekhnika Poluprovodnikov, Vol. 37, No. 8, 2003, pp. 980–984.
Original Russian Text Copyright © 2003 by Zotova, Kizhaev, Molchanov, Voronina, Lagunova, Pushnyĭ, Yakovlev.

Characterization of Light-Emitting Diodes Based on InAsSbP/InAsSb Structures Grown by Metal-Organic Vapor-Phase Epitaxy

N. V. Zotova, S. S. Kizhaev*, S. S. Molchanov, T. I. Voronina, T. S. Lagunova, B. V. Pushnyĭ, and Yu. P. Yakovlev

Ioffe Physicotechnical Institute, Russian Academy of Sciences, Politekhnicheskaya ul. 26, St. Petersburg, 194021 Russia
**e-mail: serguie@mail.ru*

Submitted February 10, 2003; accepted for publication February 17, 2003

Abstract—Light-emitting diodes for the wavelength range λ = 3.3–4.5 μm were fabricated on the basis of InAsSbP/InAsSb heterostructures grown by metal–organic vapor-phase epitaxy. The use of vapor-phase epitaxy made it possible to appreciably increase the phosphorus content in barrier layers (up to 50%) in comparison with that attainable in the case of liquid-phase epitaxy; correspondingly, it was possible to improve confinement of charge carriers in the active region of the structures. Photoluminescent properties of InAsSb layers, electroluminescent properties of light-emitting diodes, and dependences of the emission power on current were studied. Two types of light-emitting diodes were fabricated: (i) with extraction of emission through the substrate (type *A*) and (ii) with extraction of emission through the epitaxial layer (type *B*). The light-emitting diodes operating in the pulse mode (with a relative pulse duration of 20) had an emission power of 1.2 mW at room temperature.

1. INTRODUCTION

At present, there is a need for devices that monitor the level of contamination of the enviroment with noxious gases. To this end, we need efficient and reliable infrared emitters which operate at room temperature. Nowadays, the majority of measuring systems that operate in the wavelength range of 3–5 μm employ lamp-based infrared sources. Infrared lamps have an appreciable time lag, which complicates their use in practical applications. Light-emitting diodes (LEDs) and lasers offer the following two advantages: low power consumption and a high modulation frequency. Compounds based on lead salts (the IV–VI compounds) [1] and narrow-gap HgCdTe solid solutions (II–VI compounds) [2] feature a low thermal conductivity and appreciable metallurgical instability, which makes these compounds less suitable for the production of infrared emitters compared to III–V compounds. At present, laser diodes designed for the wavelength range of 3–5 μm operate stably only at temperatures close to 295 K [3–5]. In addition, gas-monitoring setups based on laser diodes require an elaborate system for stabilization, as the narrow spectrum of laser radiation is very sensitive to variations in temperature, which can significantly reduce the accuracy of measurements. Compared to lasers, LEDs operate reliably at temperatures as high as 180°C [6] and a LED’s broad spectrum is less sensitive to temperature variations. Liquid-phase epitaxy (LPE) is the most-used method for growing LED structures designed for the aforementioned range of wavelengths [6–9]. An optical-emission power of 50 μW at a wavelength λ = 5.5 μm was reported by Matveev *et al.* [8]. The dependence of the quantum efficiency of LEDs based on an $InAs/AlAs_{0.16}Sb_{0.84}$ heterostructure grown by molecular-beam epitaxy (MBE) was studied by Kane *et al.* [10]. The quantum efficiency was equal to 24% at low currents and at a concentration of charge carriers (holes) in the active region $p = 5 \times 10^{17}$ cm^{-3}. Antimony-containing strained quantum-confinement structures have been used in the active region in order to suppress nonradiative Auger processes [11–13]. The LEDs designed for a wavelength of 4.3 μm have been developed on the basis of quantum-confinement cascade InAsSb structures grown by metal–organic vapor-phase epitaxy (MOVPE) [12]. Strained MBE-grown InAs/InAsSb superlattices were used to fabricate LEDs with an emission wavelength of 4.2 μm and optical-emission power of 100 μW at a current of 2 A.

Studies concerned with the development of LEDs based on diffused *p–n* InAs structures emitting in the region of ~3.3 μm were initiated by D.N. Nasledov and N.V. Zotova as far back as 1970 [14]. This study is a continuation of previous investigations and is concerned with the development of light-emitting MOVPE-grown heterodiodes for the aforementioned spectral region [15]. Our aim is to refine the MOVPE growth technology for InAsSbP/InAsSb heterostructures and improve the characteristics of previously developed LEDs in order to make LEDs more suitable for applications in systems for ecological monitoring.

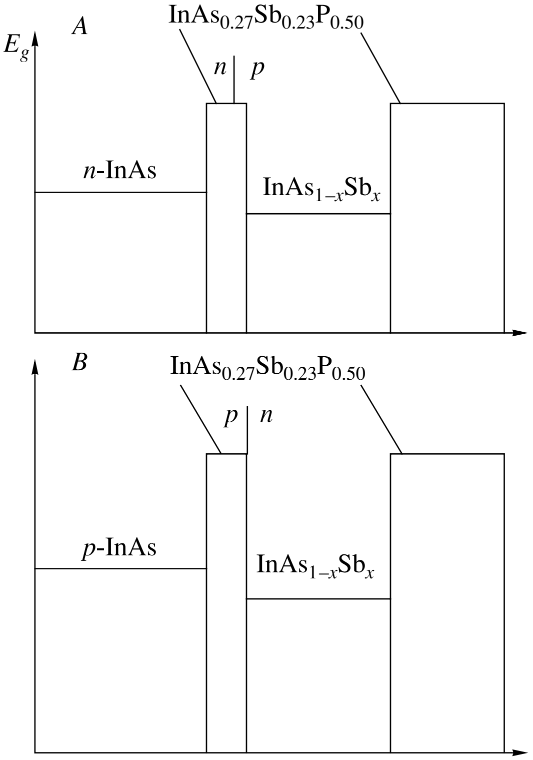

Fig. 1. Energy-band diagrams for light-emitting heterodiode structures of types *A* and *B*. E_g stands for the band gap.

2. EXPERIMENTAL

The InAsSbP/InAsSb heterostructures were grown in a horizontal reactor under atmospheric pressure. The InAs substrates were positioned on a molybdenium substrate holder with resistive heating. The total hydrogen flow through the reactor amounted to 18 l/min. As sources, we used trimethyl indium (TMIn), trimethyl antimony (TMSb), diethyl zinc (DeZn), biscyclopentadienyl magnesium $(C_5H_5)_2Mg$, and hydrides, i.e., phosphine PH_3 and arsine AsH_3, both diluted by 20% with hydrogen. In all experiments, containers with TMIn, TMSb, DeZn, and $(C_5H_5)_2Mg$ were kept at temperatures of 28, –6, 5, and 20°C, respectively. When growing the structures, we used the *n*-InAs:S or *p*-InAs:Zn substrates with carrier concentrations of $n \approx 2 \times 10^{18}$ cm^{-3} and $p \approx 5 \times 10^{18}$ cm^{-3}, respectively. The *n*-type substrates were treated in an HCl : H_2O : CrO_3 mixture prior to growth; the *p*-type substrates did not require additional treatment.

The lattice mismatch between the epitaxial layer and the substrate was estimated from the results of X-ray diffraction analysis. The elemental composition of the layers was measured using a CAMEBAX electron-microprobe analyzer produced by the CAMECA company. The concentrations of impurities in epitaxial layers were determined using secondary-ion mass spectrometry (SIMS). The optical properties of InAsSb layers were studied using an analysis of photoluminescence (PL) spectra measured at 77 K. Emission was detected using a cooled InSb photodiode. An IKM-1 monochromator was used as the dispersive system. The PL was excited using a GaAs diode laser (radiation wavelength $\lambda = 0.8$ μm, luminous power of 10 W in the pulse mode, pulse duration $\tau = 5$ μs, and pulse-recurrence frequency $f = 500$ Hz). Electroluminscence (L) of the LEDs was studied in the pulsed and quasi-continuous modes at room temperature. The emission power was measured using a calibrated system (produced by OPHIR Ltd.) equipped with a 2A-SH thermocouple unit.

3. GROWTH OF STRUCTURES AND FABRICATION OF LIGHT-EMITTING DIODES

Type-*A* LEDs consisted of an *n*-InAs substrate which was overgrown first with a 0.7-μm-thick undoped $InAs_{0.27}Sb_{0.23}P_{0.50}$ barrier layer, then with a 2.5-μm-thick active undoped $InAs_{1-x}Sb_x$ layer, and finally with a 2-μm-thick *p*-$InAs_{0.27}Sb_{0.23}P_{0.50}$ barrier layer doped with Zn or Mg. Subsequent measurements by the induced-current method showed that the *p–n* junction was located within the first $InAs_{0.27}Sb_{0.23}P_{0.50}$ barrier layer at a distance of 0.5 μm from the *n*-InAs substrate.

B-type LED structures included a *p*-InAs:Zn substrate ($p \approx 5 \times 10^{18}$ cm^{-3}) and an undoped $InAs_{1-x}Sb_x$ active region located between the Zn-doped and undoped $InAs_{0.27}Sb_{0.23}P_{0.50}$ barrier layers with thicknesses of 0.5 and 2 μm, respectively. The *p–n* junction was located at the interface between the $InAs_{0.27}Sb_{0.23}P_{0.50}$:Zn barrier layer and the $InAs_{1-x}Sb_x$ active layer. The energy-band diagrams of the *A*- and *B*-type LED structures are shown schematically in Fig. 1.

The $InAs_{0.27}Sb_{0.23}P_{0.50}$ layers were grown at a temperature of 520°C. The hydrogen that flows through the containers with TMIn and TMSb were equal to 600 and 20 ml/min, respectively. The flows of AsH_3 and PH_3 were equal to 2 and 80 ml/min, respectively. The doping level of $p \approx 4 \times 10^{18}$ cm^{-3} was attained at hydrogen flows of 25 ml/min through the container with DeZn and 9 l/min through the container with $(C_5H_5)_2Mg$. The charge-carrier concentration was determined from the measurements of the magnitude of the Hall effect in InAsSbP layers grown on semi-insulating GaAs substrates. The details of the doping of the epitaxial layers with magnesium and zinc will be given later. The magnitude of the lattice mismatch between the $InAs_{0.27}Sb_{0.23}P_{0.50}$ layer and the InAs substrate $\Delta a/a$ was no larger than 6×10^{-4}.

The InAsSb layers were grown at temperatures of 575–610°C. In order to calculate the ratios [V]/[III] and [TMSb]/([TMSb] + [AsH_3]) in the gaseous phase, we used vapor-pressure values of 3 Torr for TMIn (at 28°C) and 22.43 Torr for TMSb (at –6°C). InAs layers of higher quality were obtained at [V]/[III] = 40, a growth temperature of 610°C, and a growth rate of 0.4 μm/h. The PL band of InAs layers at 77 K had a full width at half-maximum $\Delta h\nu_{1/2}$ = 10 meV; the band was peaked at 408 meV. A superlinear increase in the emission power (Fig.2) and narrowing of the band are observed with increasing excitation intensity. The SIMS was used to ascertain that the concentration of background impurities, such as carbon and oxygen, in InAs layers was below the sensitivity threshold of the measurement system (~5×10^{15} cm^{-3}). For InAsSb, the growth temperature was lowered to 575°C. The dependence of Sb content in the solid phase on the ratio [TMSb]/([TMSb] + [AsH$_3$]) in the gaseous phase is shown in Fig. 3. If TMSb concentrations in the gaseous phase were higher than those shown in Fig. 3, Sb droplets were observed on the surface.

The LEDs were fabricated using conventional photolithography. *A* chips were mounted with the epitaxial side faced downward, whereas *B* chips were mounted with the substrate faced downward; otherwise, there were no differences between the structures of both chips. The point contacts on the upper side of the chips were 100 μm in diameter. The contacts were formed by vacuum-evaporation deposition of gold and tellurium on the *n*-type layer and of gold and zinc on the *p*-type layer. A chip's area was 500 × 500 μm^2 and its thickness was 200 μm; the rear side of a chip was mounted on a standard case. A parabolic reflector designed to narrow the directivity pattern of emission to 10°–12° was additionally mounted on the case.

Layers with dissimilar compositions (InAs, $InAs_{0.935}Sb_{0.065}$, $InAs_{0.895}Sb_{0.105}$, and $InAs_{0.843}Sb_{0.157}$) were used in the active region in order to obtain LEDs designed for different wavelengths. The positions of the peaks in the PL spectra were 408 meV for InAs, 364 meV for $InAs_{0.935}Sb_{0.065}$, 335 meV for $InAs_{0.895}Sb_{0.105}$, and 326 meV for $InAs_{0.843}Sb_{0.157}$. The PL spectra of the solid solutions under consideration are shown in Fig. 4. The temperature dependence of EL spectra is governed by the temperature dependence of the band gap, i.e.,

$$E_g(T) = E_g(0) - \alpha T^2/(T + \beta), \qquad (1)$$

where α = 0.25 meV/K and β = 80 K.

In Fig. 5, we show the EL spectra of the type-*A* LEDs, which emit at various wavelengths at room temperature. The injection current was equal to 50 mA in the quasi-steady mode. The positions of the peaks remained constant in the current range of 0–200 mA. The EL intensity decreased and the band widths increased with increasing content of Sb in the active layer. The increasing lattice mismatch between the epitaxial structure and the substrate and the increasing role of nonradiative Auger processes are the most probable causes of the aforementioned behavior. The position of

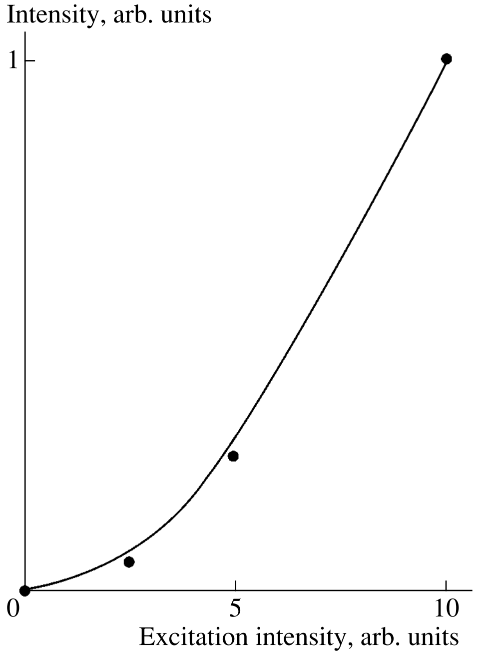

Fig. 2. Dependence of photoluminescence intensity in InAs layers on excitation power.

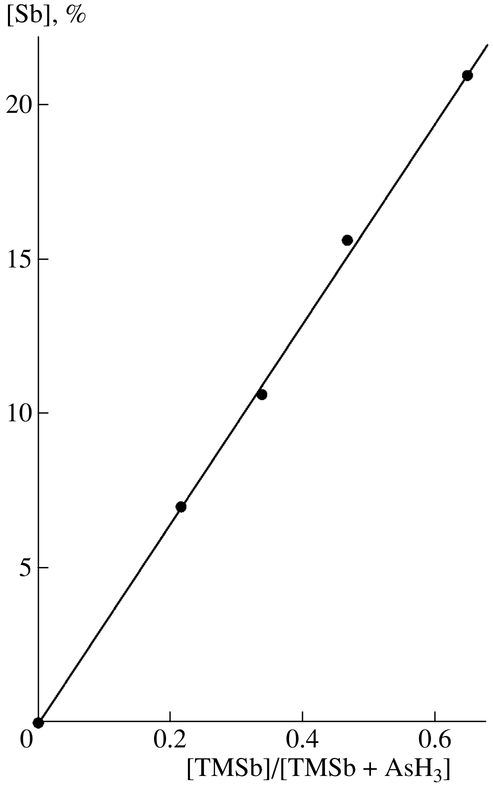

Fig. 3. Dependence of Sb content in the solid phase on the ratio [TMSb]/([TMSb] + [AsH$_3$]) in the gaseous phase.

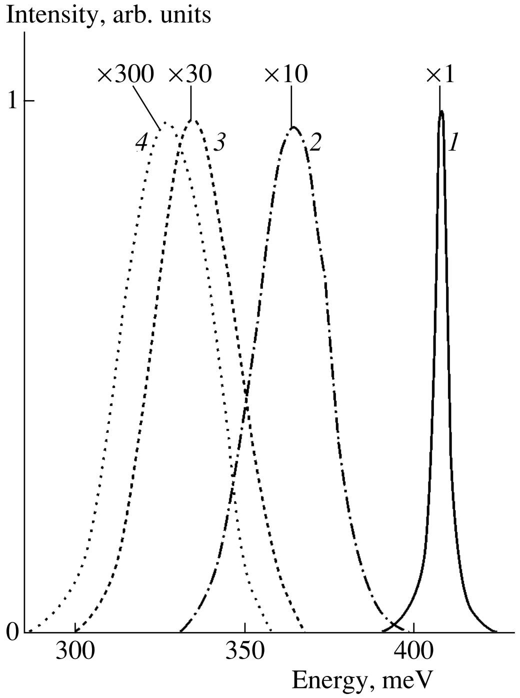

Fig. 4. Photoluminescence spectra of $InAs_{1-x}Sb_x$ solid solutions with x = (*1*) 0 (InAs), (*2*) 0.065, (*3*) 0.105, and (*4*) 0.157.

the peak in the EL spectra of LEDs with an InAs active layer depends on the structure type; the peak is located at 3.45 μm for an *A*-type structure and at 3.38 μm for a *B*-type structure. This variation in the peak position is apparently caused by the difference in the conductivity type of the active layer. In *p*-InAs, radiative recombination occurs with the involvement of acceptor levels, which are located above the valence-band top; as a result, the peak of emission shifts to longer wavelengths. It follows from the results obtained that the zinc diffusion from the solid phase is negligible and the active region in the *B*-type structures features the *n*-type conductivity. The EL spectra for the *A*- and *B*-type structures were virtually identical for LEDs with other emission wavelengths; it is difficult to determine the precise position of the peak owing to strong absorption of emission by carbon dioxide at a wavelength of 4.25 μm. The measurements of induced current show that the position of the *p*–*n* junction is independent of the Sb content in the active region for the composition range under consideration. The mechanism of recombination is probably the same for any structure with InAsSb and InAs active layers. Detailed data on the behavior of impurities (zinc and magnesium) will be reported later.

The dependence of the optical-emission power of LEDs on the current in the pulse mode is shown in Fig. 6. The type-*A* structure ensures better heat removal; as a result, the emission power of *A*-type LEDs is about twofold higher at high injection currents. In the current range of 0–200 mA, the *B*-type LEDs are more efficient than the *B*-type LEDs owing to a higher probability of radiative recombination in *n*-InAs than in *p*-InAs [16]. The dependence of the emission power for

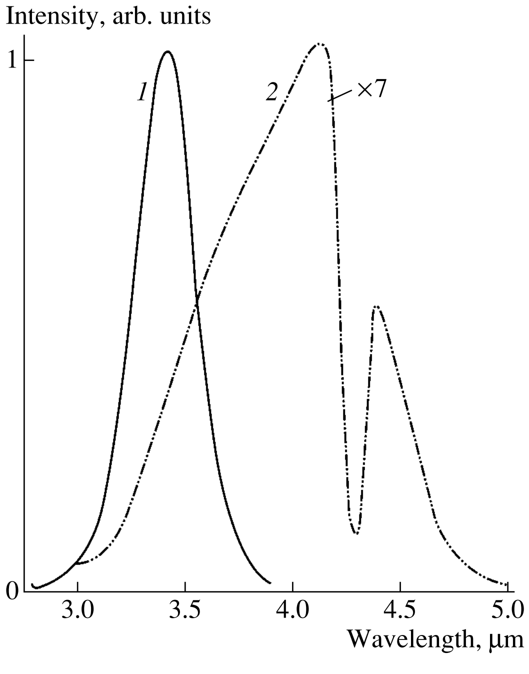

Fig. 5. Electroluminescence spectra of type-*A* light-emitting diodes with emission bands peaked at (*1*) λ = 3.45 μm and (*2*) λ = 4.25 μm at room temperature.

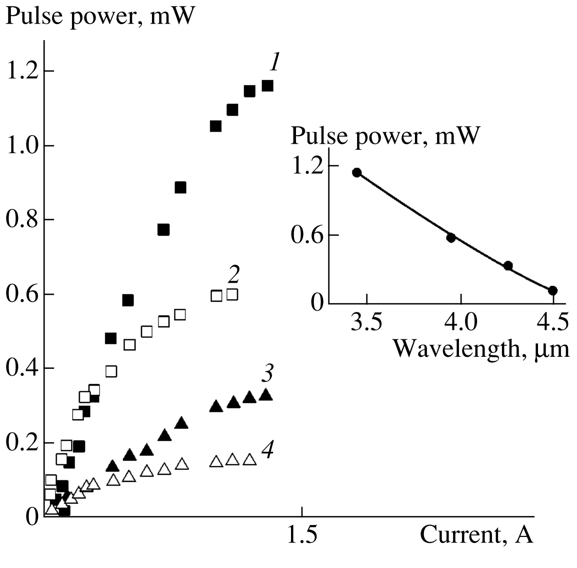

Fig. 6. Dependences of emission power of light-emitting diodes on current in the pulse mode at τ = 100 μs and *f* = 500 Hz. (*1*, *3*) Light-emitting diodes of type *A*; (*2*, *4*) light-emitting diodes of type *B*. The emission wavelength λ = (*1*) 3.45, (*2*) 3.38, and (*3*, *4*) ~4.25 μm. The emission power of type-*A* light-emitting diodes as a function of wavelength in the pulse mode at a current of 1.3 A is shown in the inset.

the *A*-type LEDs on the wavelength for the injection current of 1.3 A is shown in the inset to Fig. 6.

The nonradiative Auger recombination, heating of the structure, and mismatch of the lattice parameters are probably the factors that limit the performance of LEDs. Possible methods for increasing LED efficiency include the growth of InGaAsSb or AlGaAsSb barrier layers with a more efficient confinement of charge carriers and the use of quantum-confinement structures in the active region with the aim of suppressing the nonradiative Auger processes and obtaining the emission at longer wavelengths.

4. CONCLUSION

We fabricated light-emitting diodes (LEDs) which operated in the wavelength range of 3.3–4.5 μm and were based on InAsSbP/InAsSb heterostructures grown by MOVPE. We studied the photoluminescence of InAs and $InAs_{1-x}Sb_x$ solid solutions with $x \approx 0$, 0.065, 0.105, and 0.157. Light-emitting diodes of two types (*A* and *B*) were fabricated. The electroluminescence spectra and optical-emission power of the LEDs were measured. It is ascertained that nonradiative Auger recombination, mismatch of lattice parameters, and Joule heating are the main factors limiting the performance of light-emitting diodes. The light-emitting diodes of type *B* are preferable in the injection-current range of 0–200 mA, whereas the light-emitting diodes of type A are preferable at currents higher than 200 mA. The measured values of the optical-emission power in the pulse mode are 1.2 mW ($\lambda = 3.45$ μm), 0.6 mW ($\lambda = 3.95$ μm), 0.3 mW ($\lambda = 4.25$ μm), and 0.1 mW ($\lambda = 4.5$ μm).

ACKNOWLEDGMENTS

This study was supported in part by the Microelectronics Science and Technology Center at the Ioffe Physicotechnical Institute, the Russian Foundation for Basic Research (project no. 00-02-17047), and the Ministry of Science of the Russian Federation. S.S. Kizhaev thanks the Robert Haveman Foundation for support during pursuance of this study.

REFERENCES

1. Z. Feit, D. Kostyk, R. J. Woods, and P. Mak, Appl. Phys. Lett. **58**, 343 (1991).
2. E. Hadji, J. Bleuse, N. Magnea, and J. L. Pautrat, Appl. Phys. Lett. **67**, 2591 (1995).
3. H. K. Choi, S. J. Eglash, and W. G. Turner, Appl. Phys. Lett. **64**, 2474 (1994).
4. T. C. Hasenberg, R. H. Miles, A. R. Kost, and L. West, IEEE J. Quantum Electron. **33**, 1403 (1997).
5. H. Lee, L. J. Olafsen, R. J. Menna, *et al.*, Electron. Lett. **35**, 1743 (1999).
6. B. A. Matveev, N. V. Zotova, S. A. Karandashev, *et al.*, IEE Proc.: Optoelectron. **149**, 33 (2002).
7. A. A. Popov, V. V. Sherstnev, Yu. P. Yakovlev, *et al.*, Electron. Lett. **33**, 86 (1997).
8. B. Matveev, N. Zotova, S. Karandashov, *et al.*, IEE Proc.: Optoelectron. **145**, 254 (1998).
9. V. V. Sherstnev, A. M. Monahov, A. Krier, and G. Hill, Appl. Phys. Lett. **77**, 3908 (2000).
10. M. J. Kane, G. Braithwaite, M. T. Emeny, *et al.*, Appl. Phys. Lett. **76**, 943 (2000).
11. A. Stein, D. Puttjer, A. Behres, and K. Heime, IEE Proc.: Optoelectron. **145**, 257 (1998).
12. R. M. Biefeld, A. A. Allerman, S. R. Kurtz, and K. C. Baucom, J. Cryst. Growth **195**, 356 (1998).
13. M. J. Pullin, H. R. Hardaway, J. D. Heber, *et al.*, Appl. Phys. Lett. **74**, 2384 (1999).
14. O. A. Allaberenov, N. V. Zotova, D. N. Nasledov, and L. D. Neuĭmina, Fiz. Tekh. Poluprovodn. (Leningrad) **4**, 1939 (1970) [Sov. Phys. Semicond. **4**, 1662 (1970)].
15. S. S. Kizhayev, N. V. Zotova, S. S. Molchanov, and Y. P. Yakovlev, IEE Proc.: Optoelectron. **149**, 33 (2002).
16. N. P. Esina and N. V. Zotova, Fiz. Tekh. Poluprovodn. (Leningrad) **14**, 316 (1980) [Sov. Phys. Semicond. **14**, 185 (1980)].

Translated by A. Spitsyn

Semiconductors, Vol. 37, No. 8, 2003, pp. 960–970. Translated from Fizika i Tekhnika Poluprovodnikov, Vol. 37, No. 8, 2003, pp. 985–995.
Original Russian Text Copyright © 2003 by Astakhova, Danilova, Imenkov, Kolchanova, Yakovlev.

PHYSICS OF SEMICONDUCTOR DEVICES

Single-Mode Fast-Tunable Lasers for Laser-Diode Spectroscopy

A. P. Astakhova*, T. N. Danilova, A. N. Imenkov, N. M. Kolchanova, and Yu. P. Yakovlev
Ioffe Physicotechnical Institute, Russian Academy of Sciences,
Politekhnicheskaya ul. 26, St. Petersburg, 194021 Russia
**e-mail: dap@iropt4.ioffe.ru*

Submitted February 10, 2003; accepted for publication February 17, 2003

Abstract—Physical mechanisms leading to the suppression of instability in the electron–hole plasma under conditions of population inversion and, thus, promoting single-mode lasing and drive-current-controlled tuning were studied; in particular, nonuniform injection and spatial oscillations of laser flux were considered. Transient times typical of current- and heat-aided tuning are measured. The effective time constant is estimated as ~1 μs for heat-controlled tuning; by contrast, it is at least one order of magnitude shorter for current tuning. The tuning range does not exceed several angstroms and is as wide as 100 Å in the case of heat- and current-aided tuning, respectively. A single-mode fast-tunable heterolaser which is capable of operating within the 2.8–3.6 μm wavelength range at 12–120 K and is designed for laser-diode spectroscopy is developed. The results of using the laser for the detection of absorption spectra in OCS, NH_3, CH_3Cl, CH_4, N_2O, and H_2O vapors are reported. *© 2003 MAIK "Nauka/Interperiodica".*

INTRODUCTION

The physics of diode lasers originated at laboratories of the Ioffe Physicotechnical Institute by D.N. Nasledov, A.A. Rogachev, S.M. Ryvkin, and B.V. Tsarenkov, who managed to obtain amplification in an electron–hole channel instead of common absorption [1]. This effect was achieved due to the production of population inversion, which implies that the population of lower levels in the conduction band is higher that of the upper levels in the valence band. The population inversion appeared as a result of applying short powerful forward-current pulses to the *p*–*n* junction. The US scientific team headed by Hall ensured positive feedback by installing a *p*–*n* junction in an optical cavity and attained stimulated emission at the wavelength of maximum amplification [2]; i.e., a diode laser was produced.

Almost all III–V semiconductors intended for diode lasers have been synthesized and studied under the guidance of Nasledov. Direct-gap materials were used as the electron band-to-band transitions in them imply no energy loss via lattice oscillations, in contrast to the case of indirect-gap semiconductors. A wide variety of III–V semiconductors with different band gaps and refractive indices predetermined their use as a basis for solid solutions and heterojunctions and enabled a reduction of the drive current required for lasing by several hundred times.

Heterojunctions have become the area of scientific interest to Zh.I. Alferov, whose contribution to this field was rewarded by a Nobel prize [3].

Superinjection, optical and electronic confinement of the area of excitation, and almost complete elimination of nonradiative recombination are examples of phenomena obtained in heterojunctions. Tunnel-permeable thin-layer heterojunctions and semiconductors with foreign quantum-size inclusions gave rise to the physics of semiconductor nanostructures and greatly improved the performance characteristics of injection lasers. As a result, commercially produced diode lasers appeared for the purposes of optoelectronic communication, as well as for the reading and processing of information.

The advantages of a heterojunction laser manifest themselves in full measure in the case of a double heterostructure. The inner layer of such a structure is characterized by a narrower band gap and a higher refractive index than those in adjacent layers. Radiation is generated in the inner layer. The outer layers confine the electron–hole plasma and act as the lateral walls of the optical cavity. The outer crystal surfaces perpendicular to heteroboundaries act as cavity's edge walls. Standing waves appear between the edge walls, the resonance frequencies of which are given by

$$\nu_i = \frac{ic}{2nL}, \quad (1)$$

where *i* is an integer, *c* is the speed of light, *L* is the distance between the edge walls, and *n* is the refractive index. Lasing occurs at the resonance frequency at which the amplification in the active medium balances all the losses via the absorption, scattering, and escape of radiation. In early studies on diode lasers, it was suggested that the dependence of the refractive index on temperature [4] or hydrostatic pressure [5] might be used for frequency tuning. Current-induced change of laser temperature was considered promising for diode-laser spectroscopy applications [6].

By concentrating the stimulated radiation in one spectral line, one can make its half-width as small as several megahertz [7, 8], which is 100 times smaller than the typical width of absorption lines in gases. Scanning over these lines by diode-laser radiation allows highly accurate determination of their shape. This circumstance served as a basis for high-resolution laser-diode spectroscopy. Lasers intended for this purpose must emit only one spectral line and be tunable within the range of no less than 10 Å. However, the first diode lasers, including those developed in Nasledov's laboratory, emitted about 10 spectral lines and were practically untunable, which naturally followed from the instability of electron–hole plasma in the conditions of population inversion and optical feedback. Thus, the problem arose of diminishing the electron–hole plasma instability.

Under the supervision of Rogachev, the successor of Nasledov as head of the laboratory, prime attention was concentrated on the investigation of lasers for the middle infrared (IR) spectral region, which includes the absorption lines of gas molecules. For the first time [9], lasers of a new type were developed on the basis of self-aligned quantum wells that form at heteroboundaries of type II when the offsets of the conduction band and the valence band are equally directed. These lasers were used in pioneering studies in the area of laser spectroscopy carried out in collaboration with Moscow colleagues V.G. Avetisov, A.I. Nadezhdinskiĭ, and A.N. Khusnutdinov [10]. The narrow-gap layer of the double heterostructures was made of a quaternary solid solution, GaInAsSb, and the confining layers, of AlGaAsSb. Lasers whose narrow-layer had a different composition emitted in the range $\lambda = 1.8$–2.4 μm. Frequency tuning occurred as current pulses heated the laser from the initial temperature ($T = 90$–250 K) by ~2 K. Smooth single-frequency tuning occurred at ~5 Å as the current varied from $1.1I_{\mathrm{th}}$ to $1.5I_{\mathrm{th}}$ (I_{th} is the threshold current). The laser linewidth ranged from 3.3 to 80 MHz. The overtones of the absorption lines in H_2O and CO_2 were detected.

Another spectral range was covered with the advent [11] of lasers with InAsSb narrow-gap and InAsSbP wide-gap layers, which allowed the detection of the main absorption lines within the range $\lambda = 3.0$–3.6 μm, depending on the composition of the narrow-gap layer. The range of tuning due to rising temperature during the current pulse did not exceed 5 Å. The working temperature varied from 80 to 100 K.

A drawback of heat-governed tuning is the necessity to choose the amplitude and duration of the pulse so that the laser heats up by 1–5 K and remains in a single-frequency mode. At low temperatures, the pulse duration must be increased considerably because of a drop of the threshold current. This circumstance leads to a corresponding decrease in the speed of recording the absorption spectra of gases. It should be noted here that, at a high quantum yield of radiative recombination and low losses of radiation in the crystal bulk, the laser heating should be insignificant. Only the excess (due to the useful loss of radiation leaving the crystal) of the difference between quasi-Fermi levels for electrons and holes over the photon energy by an order of thermal energy kT may cause appreciable heating of the active region.

This situation called for the design of lasers operating on inertia less effects so as to exclude thermal inertia. Quantum phenomena leading to the self-focusing of laser radiation could form a basis of inertia-free tuning [12]. This study contributes to the development of tunable diode lasers, which is being carried out at the infrared optoelectronics laboratory of the Ioffe Physocotechnical Institute and is concerned with the design and investigation of a single-mode fast-tunable laser for diode-laser spectroscopy.

The possibility of tuning a diode laser was suggested for the first time by P.G. Eliseev and A.P. Bogatov [13, 14] when they took into consideration the dependence of the refractive index on the concentration of nonequilibrium carriers and revealed the dependence of this concentration on the lasing intensity. In special experiments with GaAlAs/GaAs/GaAlAs nonstripe lasers [15], a speckled structure was observed in the near zone with a 10–30% excess of current over the threshold value, thus indicating the formation of an optical waveguide in the plane of the *p*–*n* junction. In the far zone, the beam broadened due to its self-focusing in the middle of the waveguide. The absence of laser radiation at the periphery results in an increase in the concentration of nonequilibrium carriers and a corresponding decrease in the refractive index, which turns out to be sufficient for the onset of optical confinement. We should also note the observed spatial self-focusing instability of the laser channel and the multimode lasing.

SELF-FOCUSING IN A STRIPE LASER

Self-focusing was observed [16] with the use of specially designed mesa-stripe lasers based on *n*-$InAsSb_{0.17}P_{0.35}$/*n*-$InAsSb_{0.05}$/*p*-$InAsSb_{0.17}P_{0.35}$ double heterostructures (Fig. 1), which featured highly uniform electrical and optical properties and uniform pump density over the active region. The structures were grown by liquid-phase epitaxy on *n*-InAs substrates with (100) crystallographic orientation. The active layer was nominally undoped and had an electron concentration of 10^{16} cm^{-3}. The confining *n*- and *p*-type layers were doped with Sn to an electron concentration of 2×10^{18} cm^{-3} and with Zn to a hole concentration of 10^{18} cm^{-3}, respectively. The thickness of the active region was 1 μm, and the thickness of the confin-

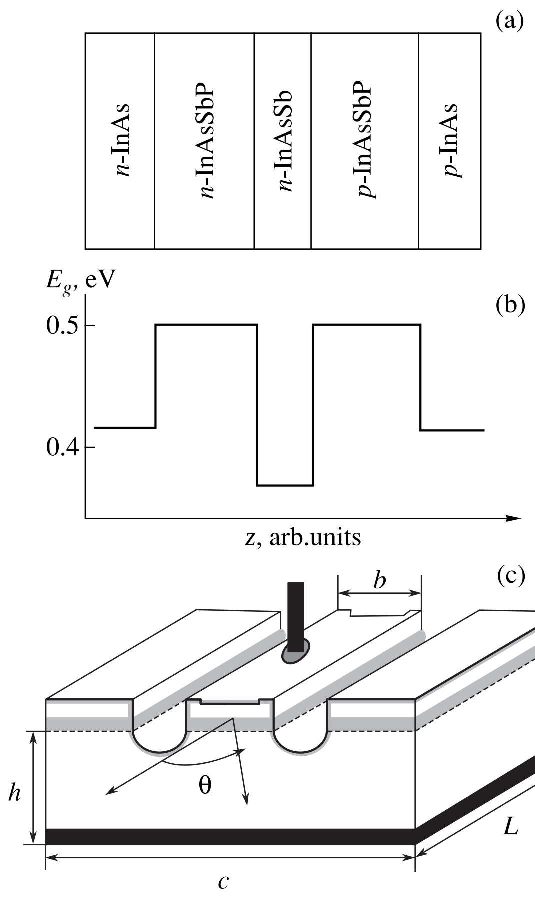

Fig. 1. The diode laser structure: (a) the arrangement of epitaxial layers, (b) the corresponding profile of the band-gap E_g, and (c) the structure of the mesastripe laser diode.

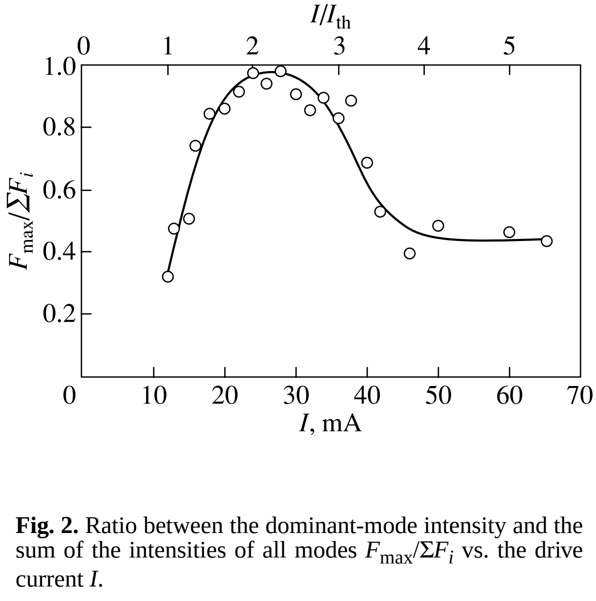

Fig. 2. Ratio between the dominant-mode intensity and the sum of the intensities of all modes $F_{max}/\Sigma F_i$ vs. the drive current I.

ing layers was 2 μm. The stripe width ranged from 10 to 20 μm. The cavity length was L = 275–350 μm. The experiments were performed at a temperature of 78 K.

For currents within the range $I = (1.3–4)I_{th}$, the intensity of one dominant mode F_{max} (Fig. 2) exceeded the total intensity of all other modes F_i. When excess current over the threshold was approximately twofold, the observed lasing was virtually single-mode. As the drive current grew, the half-height width of the directivity diagram Δθ (Fig. 3) first decreased and, after twofold excess over the threshold value, steadily grew.

Both the initial narrowing and the subsequent broadening of the radiation pattern with an increase in current can be attributed to the effect of the emitted radiation on the refractive index. An increase in current extinguishes first the weak transverse modes, which can broaden the radiation pattern; at large currents, the self-focusing of a dominant longitudinal mode manifests itself. Near the lateral walls of the cavity, permittivity decreases with current due to an increase in the nonequilibrium carrier concentration as a consequence of the low lasing intensity in this region; at the same time, in the middle of the cavity, the permittivity remains close to its value at the threshold N_{th}. Radiation can no longer penetrate to the lateral walls of the cavity; i.e., the effective cavity width decreases and the lasing wavelength decreases accordingly. If we assume for the sake of simplicity that the distribution of field amplitude across the effective cavity width remains close to the cosine function, then the variation of the wavelength (Δλ) with a change in the ratio between current and the threshold current (j) can be expressed as

$$\Delta\lambda \approx \frac{d\varepsilon}{dN}\frac{\lambda}{2\varepsilon}N_{th}(j-1), \qquad (2)$$

where ε is the permittivity and N is the nonequilibrium-carrier concentration. When $d\varepsilon/dN = 2 \times 10^{-18}$ cm^3 [17], λ = 3 μm, ε = 13, and $N_{th} = 5 \times 10^{16}$ cm^{-3}, formula (2) yields $d\Delta\lambda/dj$ = 115 Å. In reality, the values of $d\Delta\lambda/dj$ are lower because of the influence of the crystal boundaries at small currents and because of the deviation of the amplitude distribution from the cosine function at large currents. At a twofold increase in current, the value Δλ = 50 Å is attained [18].

The time constant characterizing a change in the wavelength with current should be equal to the effective lifetime of nonequilibrium carriers, which amounts to 10^{-8}–10^{-9} s in the diode laser under consideration.

In this way, fast-operating tunable laser diodes were developed for the needs of spectroscopy studies of the middle-infrared spectral region.

SPATIAL OSCILLATIONS OF LASER FLUX ACROSS THE CAVITY

Laser radiation patterns obtained in [19] with the cavity width >18 μm (Fig. 4) are split by an angle of

~11°, which is two times less than that expected for the first transverse spatial cavity mode. A possible reason for this is the presence of two antiphase radiation fluxes 17 μm apart. By using the conformal transformation, we calculated the distribution of current across the cavity, which revealed a higher density of injection near the cavity walls than in the middle. This increase in the nonequilibrium carrier concentration in the direction from the middle towards the cavity walls resulted in the formation of a smooth optical waveguide. Laser flux generated in the medium with population inversion could travel in such a waveguide from one lateral wall of the cavity to another and back, i.e., to execute spatial oscillations. Antiphase and in-phase fluxes might also coexist, which would ensure better correlation between the flux density and the injection density.

Analyzing the wave equation [18, 19] for the laser flux showed the absence of transverse modes, a fact which is highly important for providing single-mode lasing.

SINGLE-MODE LASING

It has been noticed that, in lasers with a short (~200 μm) cavity, the current-induced onset of single-mode lasing is accompanied by the abrupt enhancement of the radiation intensity [10]. In contrast lasers with long cavities (500 μm) show no rise in intensity and the number of modes grows with current (Fig. 5) due to the emergence of modes with longer wavelengths. Both the longitudinal mode and the transverse spatial modes are generated. Lasers with a short cavity (~200 μm) usually generate only one longitudinal mode, the wavelength of which decreases with increase drive current (Fig. 6).

The observed dependences have recently been explained of as follows [20]. The intensity of odd transverse modes varies from zero in the middle of the cavity to the maximum value at the lateral walls. Thus, the odd transverse modes disturb the formation of a gradient-concentration waveguide and the long-cavity lasers turn out to be virtually untunable. The fact that the wavelengths of the longitudinal mode and the first transverse mode are close to each other gives rise to the dynamic phase grating of the refractive index, which increases the gain at the long-wavelength side from the stronger mode and lowers it at the short-wavelength side [21, 22]. As the drive current grows, the modes with still larger wavelengths are excited in addition to the already existing short-wavelength modes, which also remain. As a result, several tens of modes support each other.

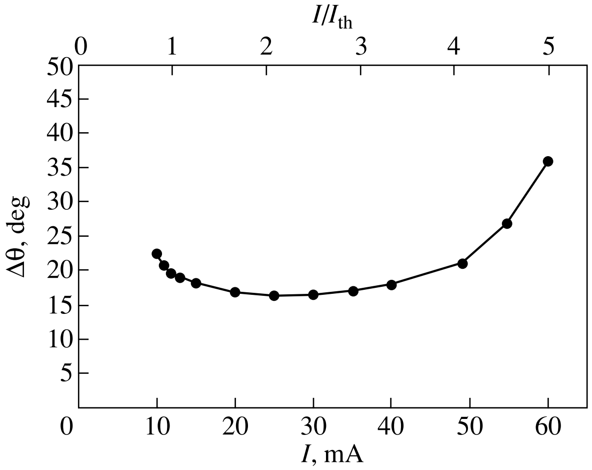

Fig. 3. Width of the radiation pattern in the *p*–*n* junction plane vs. the drive current.

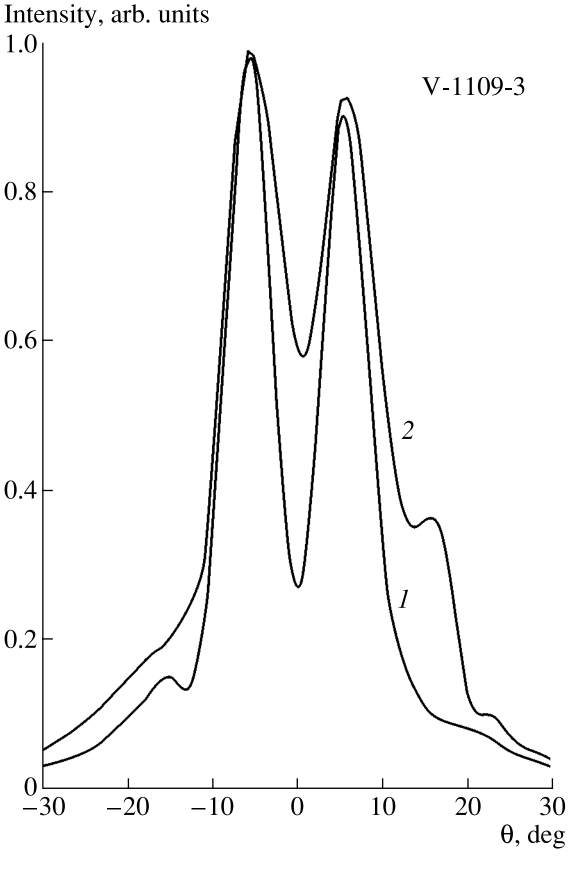

Fig. 4. Radiation patterns in the *p*–*n*-junction plane at (*1*) 14% and (*2*) 80% excess of the drive current over the threshold value.

The most favorable cavity length for a gradient-concentration waveguide to appear is the length at which the first transverse modes fall between the longitudinal ones, so that

$$L = \frac{2\varepsilon b^2}{n^* 3\lambda}, \tag{3}$$

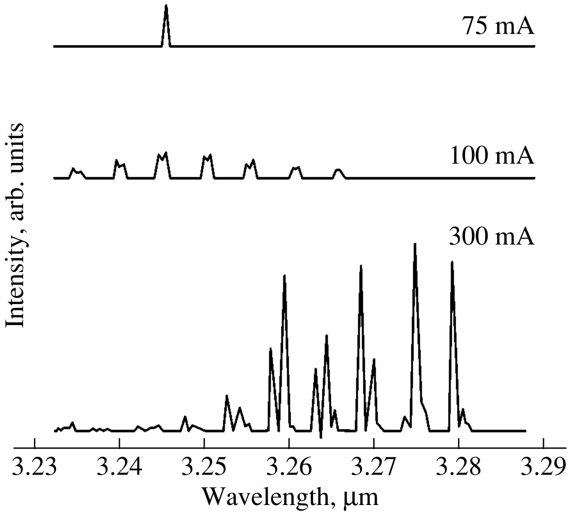

Fig. 5. Emission spectra of poorly tunable laser with a cavity length of 500 μm and a threshold current 70 mA at several drive currents.

where b is the cavity width and

$$n^* = n\left(1 - \frac{\lambda}{n}\frac{dn}{d\lambda}\right).$$

There is a certain value of current for which the spectral position of the amplification peak coincides with that of the longitudinal mode. In this case, the longitudinal mode reduces the carrier concentration in the middle of the cavity and does not hamper its increase near the lateral wall. A smooth waveguide appears in which the spatial oscillations of flux completely suppress the transverse modes. The above-mentioned dielectric grating becomes smoother by a factor of 10^3, since the frequency of spatial oscillations (10^{12} Hz) is three orders of magnitude higher than the inverse effective lifetime of carriers in a laser. Finally, only the spectral line that is nearest to the amplification peak survives. This line and the amplification peak shift in the same direction. Therefore, the tuning range may exceed the mode spacing. The disappearance of mode coupling accompanied with the generation of highly absorbed difference and sum harmonics leads to the above-mentioned increase in the quantum yield of radiation.

Thus, the formation of a gradient-concentration waveguide and the elimination of transverse oscillations from the radiation flux are shown to be favorable for the single-mode lasing with the current-induced shift of the mode to shorter wavelengths. The widest tuning range is attained by choosing the temperature at which the amplification peak shifts with current at the same rate as the generated cavity mode.

Realizing the spatial oscillations of laser flux at an appropriate choice of working temperature enables one to expand the tuning range to 100 Å or more.

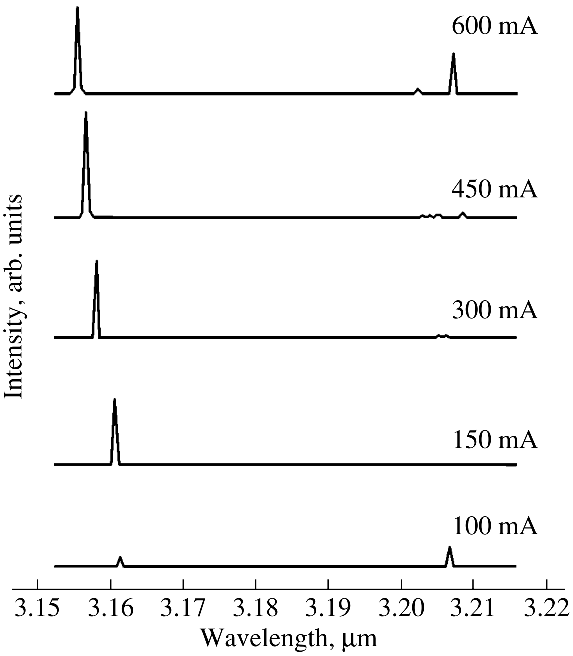

Fig. 6. Emission spectra of tunable laser with a cavity length of 230 μm and a threshold current of 90 mA at several drive currents.

TUNING RESPONSE SPEED

The speed of the laser response to tuning was studied with current pulses whose tops have a positive slope (Fig. 7). The duration of pulses τ varied from several to hundreds of microseconds, and their shape remained the same. The amplitude of a pulse was appreciably larger than its variation. The measurements were carried out at a laser temperature of 78 K. The emitted radiation was passed through a 1.1-cm-thick silicon

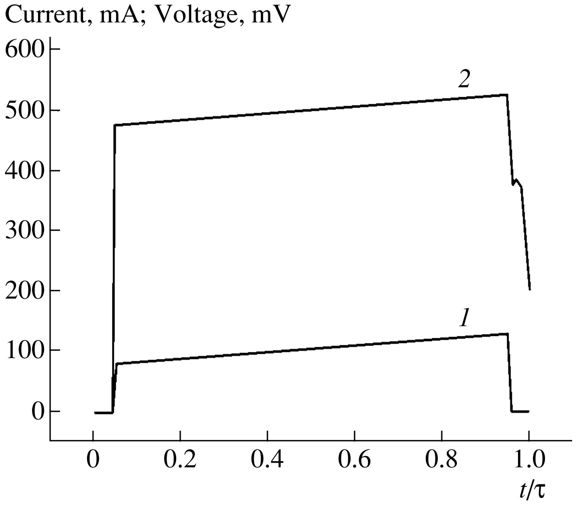

Fig. 7. The inclined-top pulses of (*1*) current and (*2*) laser voltage.

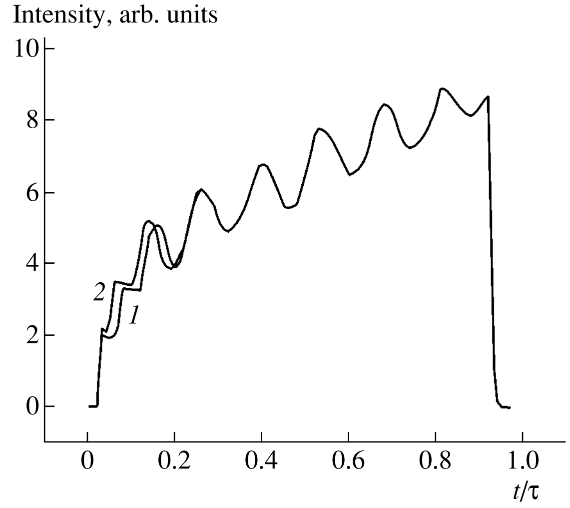

Fig. 8. Pulse shapes after passing the silicon Fabry–Perot cavity for the pulse duration τ = (*1*) 4.5 and (*2*) 9 μs.

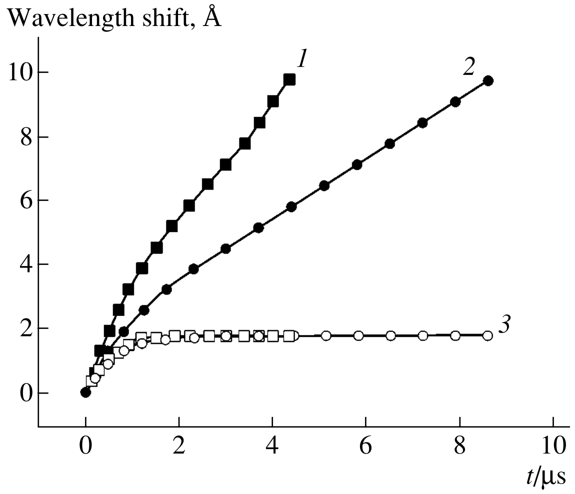

Fig. 9. Temporal variation in the lasing wavelength in a laser driven by pulses with duration τ = (*1*) 4.5 and (*2*) 9 μs and (*3*) the thermal component.

Fabry–Perot cavity where it became sine-modulated due to a change in the wavelength during the pulse (Fig. 8). One sinusoid period corresponded to a change in the wavelength by 1.5 Å.

The time dependence of a change in the wavelength (Fig. 9) consists in a linear component and a leveling-off component. The leveling-off component has the same shape for any pulse duration and, hence, may be considered as originating from heating after the switching-on of the pulse, since a change in the pulse amplitude is much smaller than its magnitude. The leveling-off component reaches 63% of its peak value in 0.9 μs. This value coincides with the effective time constant calculated under the assumption that heat is emitted in the active region and expands over the crystal and then reaches the laser holder. The estimation can be made by the following formula:

$$\tau_3^* = \frac{c_p\rho}{3\kappa}b^2\left(\pi - \frac{4h}{D}\right)^{-2}\ln^2\frac{4h}{b}, \qquad (4)$$

where c_p = 0.018 cal/(g K) is the heat capacity; ρ = 6 g/cm^3 is the density; κ = 1 W/(cm K) is the thermal conductivity; b = 18 μm is the cavity width; and D = 500 μm and h = 100 μm are the width and the thickness of crystal, respectively. The formula is obtained when $2h/D \ll 1$ and $2h/b \gg 1$. A more general expression is presented in [23].

It would seem that considerable nonradiative spontaneous recombination should be presumed to account for heat release in the active region. The above-threshold part of the current is considerably smaller than the threshold value, and the tuning range during the progress of a pulse is appreciably wider than that in the beginning. Consequently, the linear component should be attributed to an increase in current rather than having a thermal origin. The wavelength varies with current for all pulse durations (Fig. 8). The angular frequency of sinusoids are $\omega_s = 10^7$ Hz at a pulse duration of 4.5 μs. Therefore, the response time of the current-induced tuning is no longer than $1/\omega_s = 10^{-7}$ s.

Thus, it is shown that current-induced tuning has a wider range with a smaller interval of currents as compared to thermal tuning and provides a response time no longer than 10^{-7} s.

LASING LINEWIDTH IN TUNABLE DIODE LASERS

The spectral linewidth is the most important characteristic of a laser used for highly accurate spectroscopic studies of vibrational–rotational spectra of gas molecules. The linewidth of radiation emitted by current-tuned lasers based on InAsSbP/InAsSb/InAsSbP was analyzed in [24–26]. The lasers were driven by sawtooth-modulated direct current in the interval from one to five threshold values in the temperature range from 12 to 100 K. The emission corresponding to the mode was passed through the gas under study or through the reference cavity. The detected signal was fed to both the differentiating *RC* filter and one of the digital oscilloscope channels. The filter time constant τ_f amounted to 20 μs, which was two orders of magnitude longer than the rise time of the signal in the detection system. The oscillograms in Fig. 10 show the signal U of the laser radiation passed through CH$_3$Cl (curve *1*) and the derivative of this signal dU/dt (curve *2*). From the time interval between the two minima, which corresponded to the known lines of absorption in CH$_3$Cl, we determined the value of ν', which is the rate of change in the wave number ν with time. When using a single line of absorption, the rate ν was obtained from the eigenfrequencies of the reference cavity. The second channel of the oscillo-

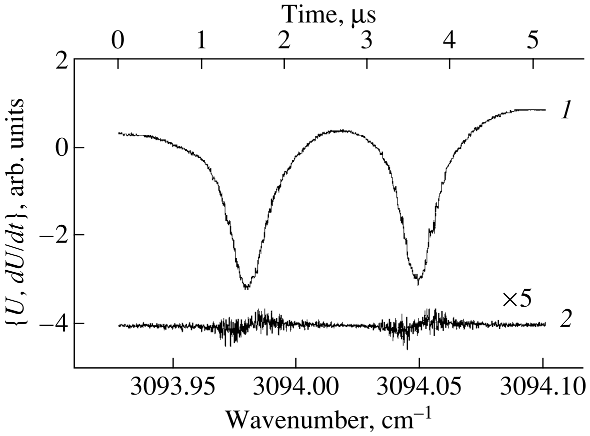

Fig. 10. Oscillograms of (*1*) signal U proportional to the intensity of laser radiation transmitted through CH_3Cl and (*2*) its time derivative dU/dt obtained after *RC* differentiation; the drive current is sawtooth-modulated.

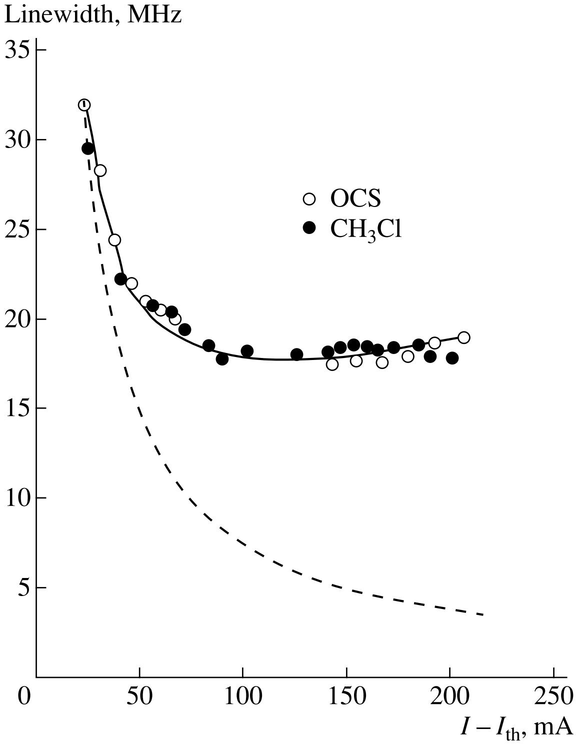

Fig. 11. The experimental linewidths Δf of the V-12191-3 laser at different currents as obtained from the lines of absorption in CH_3Cl and OCS gases (circles) and the calculated dependences of Δf on current under the assumption of a current-independent concentration of nonequilibrium carriers (dashed line) and under the assumption of growing concentration of nonequilibrium carriers with current (solid line).

scope was used to measure the linearly averaged derivative U_R and the root-mean-square deviation $\langle U_\mu \rangle$. These values were measured at the inflection points of curve *1*, where they are maximal, and averaged. The half-height width of the laser radiation peak was calculated from the formula

$$\Delta f = 2c\tau_f \nu' \langle U_\mu \rangle / U_R. \quad (5)$$

The experimental values of the linewidth Δf depend on the drive current I (Fig. 11). There is a certain value of current, $I = I_{min}$, corresponding to the minimum lasing linewidth. At currents $I < I_{min}$, an increase in Δf with current is sharp; if $I > I_{min}$, it is gradual ($I_{min} = (3–4)I_{th}$). In the laser under consideration, Δf remains within 32–18 MHz. In multimode lasers, the spread in the widths of several simultaneously generated modes is no more than 20%. If temperature deviations from the optimal value (at which the tuning range is maximum) are within ±10 K, a change in the lasing linewidth at a fixed difference $I–I_{th}$ follows the direction of temperature variation, but is less pronounced.

Along with the experimental points, Fig. 11 shows two analytical curves. The dashed curve is the lasing linewidth calculated for the studied V-12191-3 laser according to the expression derived by Henry [8]:

$$\Delta f = R(1 + \alpha_n^2)/4\pi P, \quad (6)$$

where R is the mean rate of spontaneous emission, α_n is the ratio between the variations of the real and imaginary parts of the refractive index, and P is the number of photons in the cavity. It is assumed in Henry's theory that, starting from a certain value N_{th}, the average concentration of nonequilibrium carriers N is independent of current. In this case, the values of R, α_n, and Δf are governed by the change in the number of photons in the cavity P, and Δf is attributed to the fluctuations of spontaneous emission into the mode, which is consistent with both the basic theory developed by Shawlow and Townes [27] and its applied version suggested by Yamada [28]. A hyperbolic decrease in Δf with $I - I_{th}$ is observed only at small currents (Fig. 11) [29]. In tunable lasers, the nonequilibrium carrier concentration grows with current. Another factor that affects the lasing linewidth is the fluctuations of cavity eigenfrequencies due to the fluctuations in the number of carriers in the cavity and the corresponding change in the refractive index.

In the absence of laser radiation, the probability distribution function of the cavity eigenfrequencies has the width

$$\Delta f_0 = 2\frac{f}{n}\left|\frac{dn}{dN}\right|\sqrt{\frac{2}{V}(N_{th} + \delta N)}, \quad (7)$$

where V is the volume of the active region and δN is the excess of nonequilibrium carrier concentration over the threshold value; we relate this excess to the lasing frequency deviation δf from the value at the threshold current:

$$\delta N = \frac{\delta f}{f}\frac{n}{(-dn/dN)}. \tag{8}$$

In the presence of laser radiation, the distribution function narrows by the same factor as decreases the carrier lifetime (from τ_0 to τ_p). Therefore, the linewidth can be expressed as

$$\Delta f = \Delta f_0 \frac{\tau_p}{\tau_0}. \tag{9}$$

Considering the velocity equation for a change in N at given injection and amplification rates in the conditions of bimolecular recombination typical of lasers, we have

$$\frac{\tau_0}{\tau_p} = 1 + \frac{(I/I_{\text{th}}) - (1 + \delta N/N_{\text{th}})^2}{2(1 - N_0/N_{\text{th}})(1 + \delta N/N_{\text{th}})}, \tag{10}$$

where N_0 is the nonequilibrium carrier concentration at the threshold of population inversion for the given mode and $N_0/N_{\text{th}} = 0.75$–0.80. The solid curve in Fig. 11 represents the values of Δf calculated by formulas (7)–(10) at $n = 3.6$, $dn/dN = 0.25 \times 10^{-18}$ cm^3, and $N_{\text{th}} = 9.4 \times 10^{16}$ cm^{-3}; good correlation with the experimental data is seen. In the case where the lasing linewidth and its dependence on current are defined by the fluctuations of cavity eigenfrequencies associated with the fluctuations in the number of carriers, the lasing linewidth is inversely proportional to the square root of the volume of the active region. This circumstance enables the reduction of the lasing linewidth by increasing the cavity width. In lasers with a cavity width of 100 μm [25], the lasing linewidth was made as narrow as 10 MHz. When the working temperature is between 15 and 20 K, it has been possible to attain a linewidth of 7 MHz [26]. This value is 15–50 times smaller than the linewidths typical of lines of absorption in gases. In the temperature range from 60 to 80 K, the laser operated in a single-mode regime; the wavenumber could be tuned within 2–4 cm^{-1}. Being able to attain single-mode operation with a narrow line in lasers with a wide cavity indicates high crystal perfection of the epitaxial layers grown by liquid-phase epitaxy and makes such lasers promising for applications in spectroscopy due to their high power and small lasing linewidth. Using our tunable lasers, we were able to measure the absorption lines of the following gases: N_2O [18], CH_3Cl [24, 25, 29, 30], H_2O [29, 30], OSC [25, 30], and NH_3 [30].

THE ABSORPTION SPECTRA OF GASES

The current-tuned diode laser described above was used to study the absorption spectra in gaseous CH_3Cl, N_2O, OCS, NH_3, HCl, CH_4, CO_2, and H_2O in a wide frequency range (Figs. 12–17). The aim of these experiments was to investigate the potential of the proposed laser spectrometer and to find out whether it is capable of revealing the molecules of harmful gaseous pollutants.

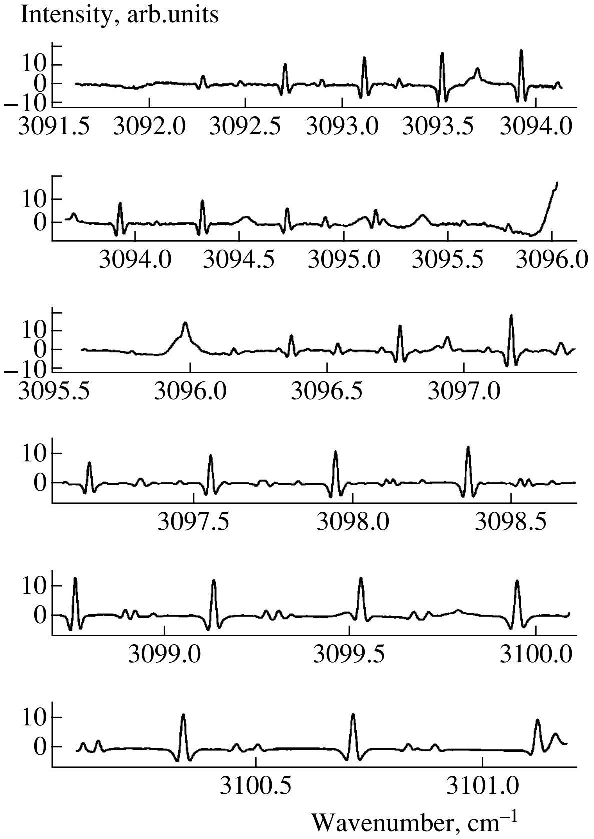

Fig. 12. OCS transmission spectra obtained by the laser-beam scanning.

As a first step, we detected the reference spectrum, which contained a variety of absorption lines in the spectral region under examination. To identify the reference spectrum, we used the atlas [31]. Based on the reference, we corrected the calibration of the laser. Then, the gas to be tested was admitted into the working chamber.

The spectrometer was tested in laboratory conditions. The gases CH_3Cl, OCS, and H_2O were of main interest to us. First of all we calibrated the laser and monochromator on the basis of gases that have been thoroughly studied in the spectral range under consideration. We found that the OSC gas is the most useful for calibration due to a diversity of vibrational lines, which are observed in its spectrum within 3090–3100 cm^{-1} (Fig. 12) (7O) (2C) and can be used for the identification of lines obtained in experiment. The correctness of our identification of the absorption lines according to the HITRAN catalogue [31] was verified with the CH_3Cl gas (Fig. 13). The frequency calibration of the spectrometer (Fig. 18) was carried out using OCS lines within six spectral ranges. The CH_3Cl spectrum obtained with the use of the reference data for OCS was then compared to that provided by HITRAN. It turned

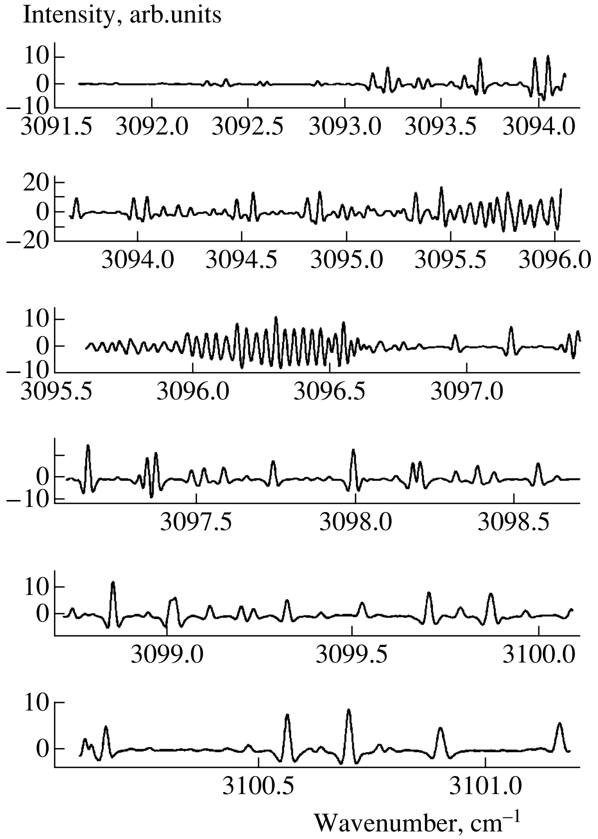

Fig. 13. CH_3Cl transmission spectra obtained by the laser-beam scanning.

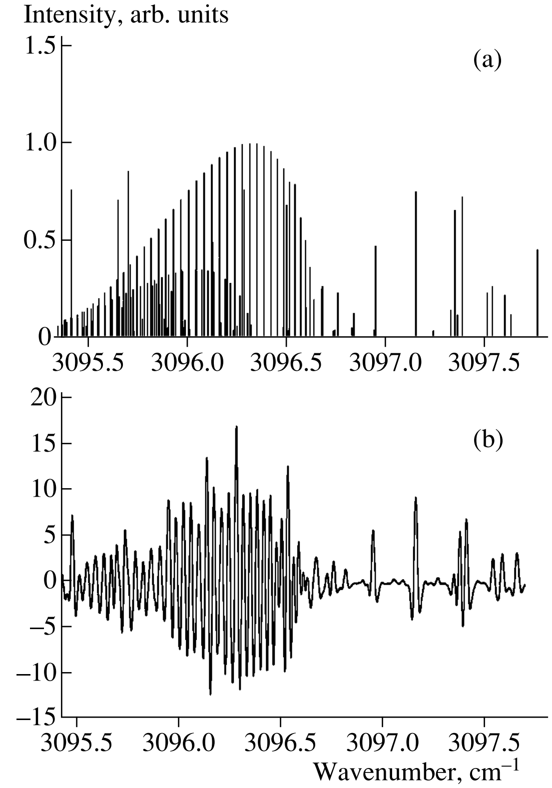

Fig. 14. CH_3Cl transmission spectra near the characteristic *Q* portion of the vibrational–rotational spectrum (3095.5–3096.5 cm^{-1}) according to (a) HITRAN and (b) our experiment.

out that the experimental spectrum of CH_3Cl coincided with the spectrum given in the catalogue within 0.003 cm^{-1}. Insignificant shifts of the wavelengths (0.01 cm^{-1}) were observed only for comparatively high injection currents (above 250 mA), when the drive-current heating of laser resulted in a nonlinear dependence of the frequency shift on current. However, in the middle of the tuning range (3091–3097 cm^{-1}), the shift of the wavelength is still a linear function of current in this case. Figures 14a and 14b show the same part of the spectrum taken either from HITRAN or recorded by a laser-diode spectrometer, respectively. A characteristic *Q* portion of the vibrational–rotational spectrum (3095.5–3096.5 cm^{-1}) is seen. A comparison between these spectra shows good agreement between the absorption bands detected by our spectrometer and those reported in the literature.

The presence of atmospheric water (Fig. 15) (vibrational lines of the 2ν2 bands) (14C) exerts some influence on the spectral background. This effect is particularly pronounced in the OCS spectrum, where it leads to the broadening of the line at 3096 cm^{-1} (Fig. 12).

By means of the same laser, we made a detailed recording of the absorption spectrum of NH_3 within the range of 100 Å (Fig. 16) and of a separately located group of absorption lines of CH_4 (Fig. 17).

CONCLUSION

The idea of developing a laser monochromator had appeared even before stimulated radiation in *p–n* junction was obtained by Nasledov, Rogachev, Ryvkin, and Tsarenkov. However, the first diode lasers, including those developed at Nasledov's laboratory, emitted about ten spectral lines and were virtually untunable—a natural consequence of the instability of electron–hole plasma in the conditions of population inversion. Smoothing of the spatial periodic inhomogeneities in plasma density undoubtedly favors single-mode lasing as it provides the conditions by which the lasing line gains maximum amplification within a wide range of drive currents. The spatial width of the laser flux decreases with the drive current, since the flux is expelled from the lateral walls of the cavity as the refractive index becomes lower there with an increase in nonequilibrium carrier concentration. The narrowing of flux accelerates its propagation; i.e., the lasing line shifts to shorter wavelengths. Simultaneously, the peak of amplification also shifts in the same direction. By properly choosing the design parameters of the laser

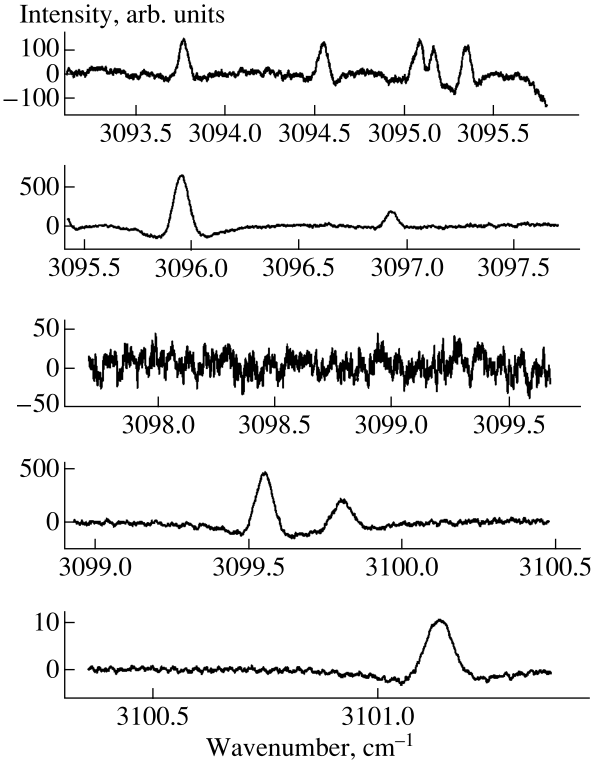

Fig. 15. H_2O transmission spectra obtained by laser-beam scanning.

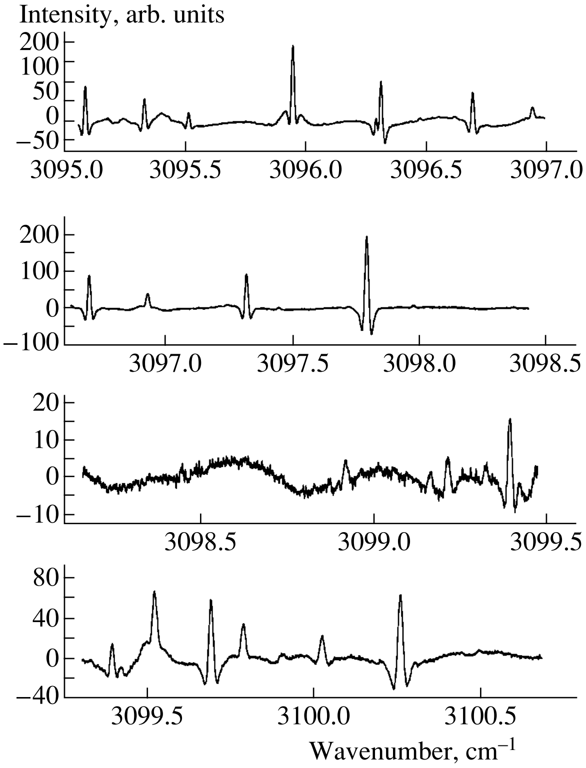

Fig. 16. NH_3 transmission spectra obtained by laser-beam scanning.

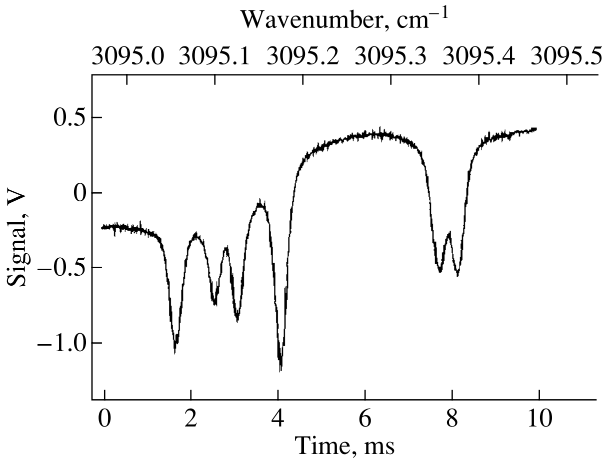

Fig. 17. A separately located group of absorption lines of CH_4 recorded by the digital oscilloscope during 10 ms.

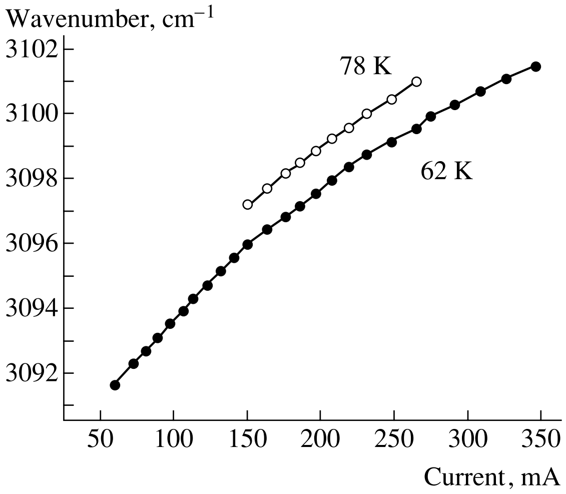

Fig. 18. Wavenumber of V-12191-3 laser emission vs. the drive current at a temperature of 62 and 78 K.

and the working temperature, one can make the rate of the shift of the amplification-peak equal the rate of the laser-line shift and, thus, obtain a fairly wide tuning range.

A higher injection density near the lateral walls of the cavity than in its center facilitates the compression of flux at small currents. It becomes possible for the compressed flux to travel between the cavity walls and to smoothen periodic inhomogeneities in the spatial distribution of electron–hole plasma. As a result, the amplification turns out to be sufficient for lasing at a single cavity mode but insufficient for any other line to be generated.

The above principles were realized in the design of laser diodes based on InAsSbP/InAsSb/InAsSbP double heterostructures; these lasers operated at wavelengths of 2.8–3.6 μm and temperatures of 12–120 K. The single spectral line emitted by these lasers has a width from 7 to 30 MHz and can be tuned within 100 Å, with an average variation of current from approximately 30 to 300 mA. The characteristic time constant of tuning is no greater than 10^{-7} s.

The developed lasers allowed us to detect the absorption lines for a number of noxious industrial gases (OCS, NH_3, CH_3Cl, CH_4, N_2O, and H_2O) and to record up to 20 lines. Such a large number of lines is convenient for their identification using the data available in catalogues. The lasers are capable of operating both in a neutral gas medium and in vacuum, a circumstance which enables their application to both terrestrial and outer-space conditions.

REFERENCES

1. D. N. Nasledov, A. A. Rogachev, S. M. Ryvkin, and B. V. Tsarenkov, Fiz. Tverd. Tela (Leningrad) **4**, 1062 (1962) [Sov. Phys. Solid State **4**, 782 (1962)].
2. R. N. Hall, G. E. Fenner, J. D. Kingsley, *et al.*, Phys. Rev. Lett. **9**, 366 (1962).
3. Zh. I. Alferov, in *Physics Today and Tomorrow*, Ed. by V. M. Tuchkevich (Nauka, Leningrad, 1973).
4. W. E. Engler and M. Garfinkel, J. Appl. Phys. **34**, 2746 (1963).
5. J. Feinleib, S. Grows, W. Paul, and R. Zallen, Phys. Rev. **131**, 2070 (1963).
6. S. Siahatav and V. E. Hochuli, IEEE J. Quantum Electron. **5**, 295 (1969).
7. D. Wolford and A. Mooradian, Appl. Phys. Lett. **40**, 865 (1982).
8. C. N. Henry, IEEE J. Quantum Electron. **18**, 259 (1982).
9. A. N. Baranov, B. E. Dzhurtanov, A. N. Imenkov, *et al.*, Fiz. Tekh. Poluprovodn. (Leningrad) **20**, 2217 (1986) [Sov. Phys. Semicond. **20**, 1385 (1986)].
10. V. G. Avetisov, A. N. Baranov, A. N. Imenkov, *et al.*, Pis'ma Zh. Tekh. Fiz. **16** (14), 66 (1990) [Sov. Tech. Phys. Lett. **16**, 549 (1990)].
11. A. N. Baranov, T. N. Danilova, O. G. Ershov, *et al.*, Pis'ma Zh. Tekh. Fiz. **18** (22), 6 (1992) [Sov. Tech. Phys. Lett. **18**, 725 (1992)].
12. W. W. Anderson, IEEE J. Quantum Electron. **1** (6), 165 (1965).
13. P. G. Eliseev, Preprint No. 33, FIAN (Physical Institute, USSR Academy of Sciences, Moscow, 1970).
14. P. G. Eliseev, A. P. Bogatov, and V. V. Mamutin, Kvantovaya Élektron. (Moscow) **3**, 1609 (1976).
15. H. Bachert, P. G. Eliseev, and A. P. Bogatov, Kvantovaya Élektron. (Moscow) **5**, 603 (1978).
16. A. N. Baranov, T. N. Danilova, O. G. Ershov, *et al.*, Pis'ma Zh. Tekh. Fiz. **19** (17), 30 (1993) [Tech. Phys. Lett. **19**, 543 (1993)].
17. T. N. Danilova, O. I. Evseeko, A. N. Imenkov, *et al.*, Fiz. Tekh. Poluprovodn. (St. Petersburg) **31**, 662 (1997) [Semiconductors **31**, 563 (1997)].
18. A. N. Imenkov, N. M. Kolchanova, P. Kubat, *et al.*, Fiz. Tekh. Poluprovodn. (St. Petersburg) **36**, 622 (2002) [Semiconductors **36**, 592 (2002)].
19. A. P. Danilova, T. N. Danilova, A. N. Imenkov, *et al.*, Fiz. Tekh. Poluprovodn. (St. Petersburg) **33**, 1088 (1999) [Semiconductors **33**, 991 (1999)].
20. A. P. Astakhova, T. N. Danilova, A. N. Imenkov, *et al.*, Fiz. Tekh. Poluprovodn. (St. Petersburg) **36**, 1388 (2002) [Semiconductors **36**, 1303 (2002)].
21. P. G. Eliseev and A. P. Bogatov, Tr. Fiz. Inst. im. P. N. Lebedeva, Akad. Nauk SSSR, No. 166, 15 (1986).
22. A. P. Bogatov, P. G. Eliseev, and B. N. Sverdlov, Kvantovaya Élektron. (Moscow) **1**, 2286 (1974).
23. A. P. Astakhova, A. N. Baranov, A. Viset, *et al.*, Fiz. Tekh. Poluprovodn. (St. Petersburg) **37**, 502 (2003) [Semiconductors **37**, 485 (2003)].
24. A. N. Imenkov, N. M. Kolchanova, P. Kubat, *et al.*, Fiz. Tekh. Poluprovodn. (St. Petersburg) **34**, 1468 (2000) [Semiconductors **34**, 1406 (2000)].
25. A. N. Imenkov, N. M. Kolchanova, P. Kubat, *et al.*, Fiz. Tekh. Poluprovodn. (St. Petersburg) **35**, 375 (2001) [Semiconductors **35**, 360 (2001)].
26. A. N. Imenkov, N. M. Kolchanova, P. Kubat, *et al.*, Fiz. Tekh. Poluprovodn. (St. Petersburg) **36**, 622 (2002) [Semiconductors **36**, 592 (2002)].
27. A. L. Shawlow and C. H. Townes, Phys. Rev. **112**, 1940 (1958).
28. M. Yamada, IEEE J. Quantum Electron. **30**, 1511 (1994).
29. S. Civis, A. N. Imenkov, A. P. Danilova, *et al.*, Spectrochim. Acta A **56**, 2125 (2000).
30. A. P. Danilova, T. N. Danilova, A. N. Imenkov, *et al.*, Fiz. Tekh. Poluprovodn. (St. Petersburg) **34**, 243 (2000) [Semiconductors **34**, 237 (2000)].
31. G. Guelachvili and K. Narahary Rao, *Handbook of Infrared Standarts II: with Spectral Coverage of 1.4–4 μm and 6.2–7.7 μm* (Academic, New York, 1993).

Translated by A. Sidorova

Semiconductors, Vol. 37, No. 8, 2003, pp. 971–984. Translated from Fizika i Tekhnika Poluprovodnikov, Vol. 37, No. 8, 2003, pp. 996–1009.
Original Russian Text Copyright © 2003 by Stoyanov, Zhurtanov, Astakhova, Imenkov, Yakovlev.

PHYSICS OF SEMICONDUCTOR DEVICES

High-Efficiency LEDs of 1.6–2.4 μm Spectral Range for Medical Diagnostics and Environment Monitoring

N. D. Stoyanov*, B. E. Zhurtanov, A. P. Astakhova, A. N. Imenkov, and Yu. P. Yakovlev

Ioffe Physicotechnical Institute, Russian Academy of Sciences, St. Petersburg, 194021 Russia
**e-mail: ns@iropt6.ioffe.ru Fax: (812) 2470006*

Submitted February 10, 2003; accepted for publication February 17, 2003

Abstract—High efficient LED structures covering the spectral range of 1.6–2.4 μm have been developed on the basis of GaSb and its solid solutions. The electroluminescent characteristics and their temperature and current dependences have been studied. The radiative and nonradiative recombination mechanisms and their effect on the quantum efficiency have been investigated. A quantum efficiency of 40–60% has been obtained in the quasi-steady mode at room temperature. A short-pulse optical power of 170 mW was reached. *© 2003 MAIK “Nauka/Interperiodica”.*

1. INTRODUCTION

Over the last decade, the requirements for permanent environment monitoring have been increasing. Sensors for determining natural gas (methane) leaks and concentrations of carbon dioxide, carbon monoxide, and other pollutants are being demanded in all rooms in every house. In spite of definite progress in the development of chemical and adsorption gas sensors, optical sensors offer evident advantages, such as high selectivity, corrosive stability, and high operating speed.

As is known, quite a number of important chemical compounds have characteristic absorption bands in the mid-IR spectral range. Among these are water in liquid and vapor forms (1.94, 2.75–2.85 μm), methane (1.65, 2.3, 3.3 μm), CO_2 (2.65, 4.27 μm), CO (2.34, 4.67 μm), acetone (3.4 μm), ammonium (2.25, 2.94 μm), and many other inorganic and organic substances. A new promising application of optical sensors is in the design of devices for noninvasive medical diagnostics. These devices usually include a linear array of emitters for various wavelengths in the IR range. The processing of time-separated signals generated by different sources and partially absorbed by the medium under study and comparison of these signals with standard values make possible, for example, the monitoring of sugar and other substances in blood. In this case, an optical head is simply brought in contact with the patient’s skin at points with abundant blood circulation. This type of device is still being developed.

Dispersive IR sources (incandescent lamps) emitting in a very wide spectral range in accordance with Planck’s law are currently widely used in optical sensor devices. The necessary band is selected with special optical filters. However, the compactness of such a device is limited by the necessity to use additional filters and modulators and also by its high dissipated thermal power.

The optimal way to eliminate all these deficiencies would be to develop high-power, high-speed light-emitting diodes (LEDs) for the mid-IR range, which would emit in a narrow spectral range. Systematic studies in this area first started at the Laboratory of IR optoelectronics of the Ioffe Physicotechnical Institute more than 20 years ago. These investigations were preceded by the creation of a GaAs fast-response IR source by D.N. Nasledov *et al.* [1]. Over the last decade, several groups around the world have been performing active studies in this area [2–4]. Here, we present an extension of studies performed at the IR Optoelectronics Laboratory of the Ioffe Institute [5–8]; it is devoted to the improvement of the efficiency of 1.6–2.4 μm LEDs.

2. LED DESIGN FEATURES

To produce a series of highly efficient LEDs covering the spectral range of 1.6–2.4 μm, we fabricated and performed a detailed study of LED structures for eight discrete wavelengths: 1.65, 1.75, 1.85, 1.95, 2.05, 2.15, 2.25, and 2.35 μm. A 0.1-μm interval was chosen on the basis of the minimum half-width of the LED spectrum, which was 0.12 μm, so as to cover the whole spectral range.

LED heterostructures were grown by LPE. Quaternary GaInAsSb solid solutions with an In content ranging from 5 to 22% were used in the active layer of LEDs for wavelengths exceeding 1.8 μm. In 1.75-μm LEDs, the GaSb binary compound was used, and for λ = 1.65 μm the active layer consisted of quaternary AlGaAsSb solid solution with 3% Al.

Structures with one-sided and double-sided confinement of carriers were produced (Fig. 1). The confining layers were quaternary AlGaAsSb solid solutions with

1063-7826/03/3708-0971$24.00 © 2003 MAIK “Nauka/Interperiodica”

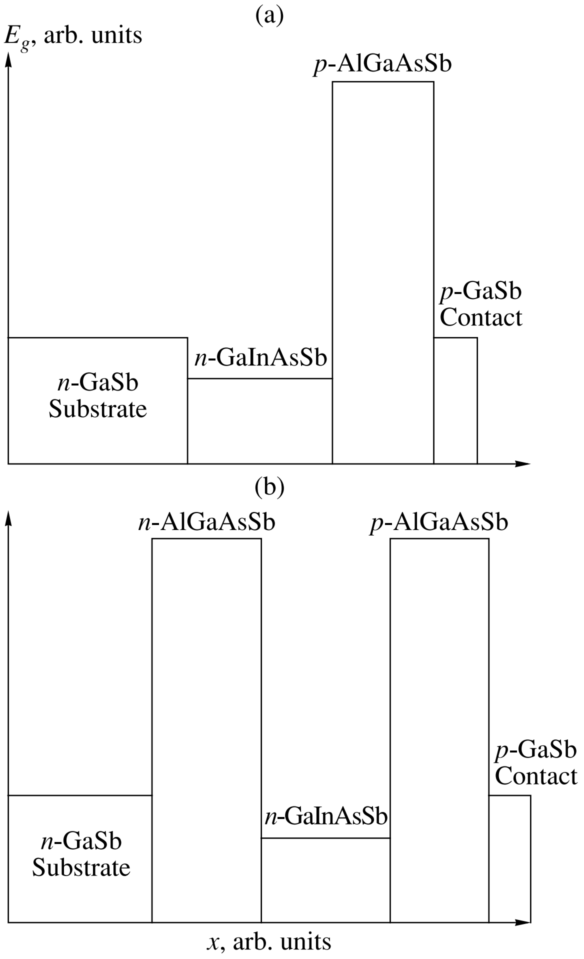

Fig. 1. Energy diagrams of LED structures with (a) one-sided and (b) double-sided confinement of carriers.

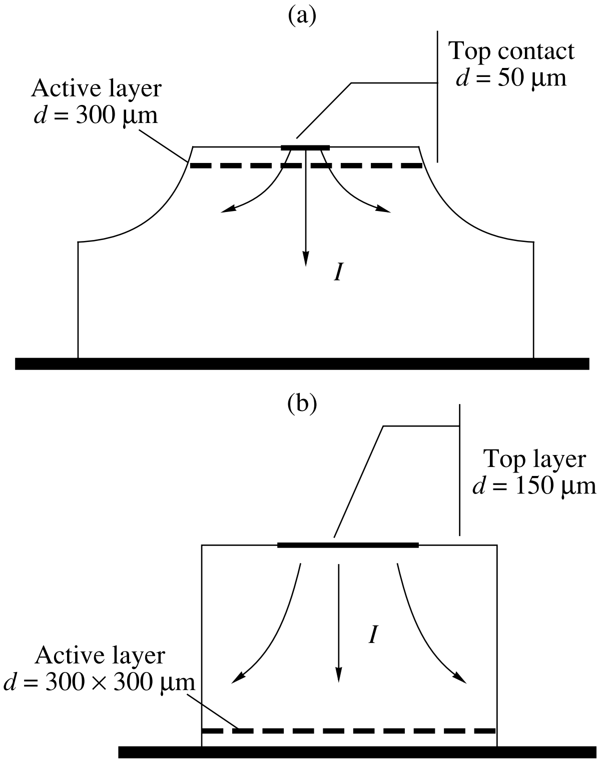

Fig. 2. (a) Schematic of a standard LED mesa-structure, and (b) the design used in the present study.

an Al content of 34% (E_g = 1.1 eV) and 64% (E_g = 1.2 eV). In all cases, (100) *n*-GaSb substrates with an electron density of 2×10^{16} cm^{-3} were used. A series of experiments was performed to define the optimal contact systems for *n*- and *p*-type materials and the optimal modes of contact burning-in. A four-layer Cr/(Au+Te)/Ni/Au system was applied to *n*-substrates. An upper gold layer was additionally grown by electroplating to a thickness of 1.5 μm. A compact contact with a similar four-layer Cr/(Au+Zn)/Ni/Au system was deposited by vacuum evaporation onto the *p*-layer.

To reduce Joule heating in the active layer, we used a novel LED design (Fig. 2b), which is fundamentally different from the design presented in [7, 8]. Our design provides a uniform spread of current over the whole area of the *p*–*n*-junction and a very low thermal resistance, because the active layer lies only 2 μm away from the LED package. In the quasi-steady mode with a current amplitude of 300 mA, the active region temperature was 7–9 degrees above the ambient temperature, whereas in the mesa structure shown in Fig. 2a, there was overheating by 30–40 degrees. The guarantee of high-quality, nearly ideal contacts with minimum thermal resistance, and maximum homogeneity of current flow in the produced LED structures are of great importance, because stability and reliability are fundamental parameters for devices primarily intended for metrology and medical diagnostics.

For a simple cubic-shaped chip, the fraction of emission leaving the crystal is smaller, but more predictable than in the case of a mesa structure. This fact allowed us to calculate the internal quantum efficiency of emission with higher precision.

The spectral characteristics of LEDs were studied at different currents, in different pulse modes, and at various temperatures. An original, specially derived method allowed us to make corrections to the shapes of spectra; determine the spectral density of the power and integral power; and determine the dependences of the integral power on current, off-duty factor, and temperature. This method takes into account all parameters of the measuring setup: the spectral dependence of the detectivity of a cooled InSb photodetector, the spectral dependences and bandwidths of the diffraction gratings, the frequency response of data acquisition and amplification systems, etc. Finally, the recorded spectrum is multiplied by the correction coefficient $K(\lambda)$, and the spectral density of the LED power $P_{\mathrm{den}}(\lambda)$ is obtained. The integral of this function over the whole spectrum yields the integral LED power $P(\lambda)$. A com-

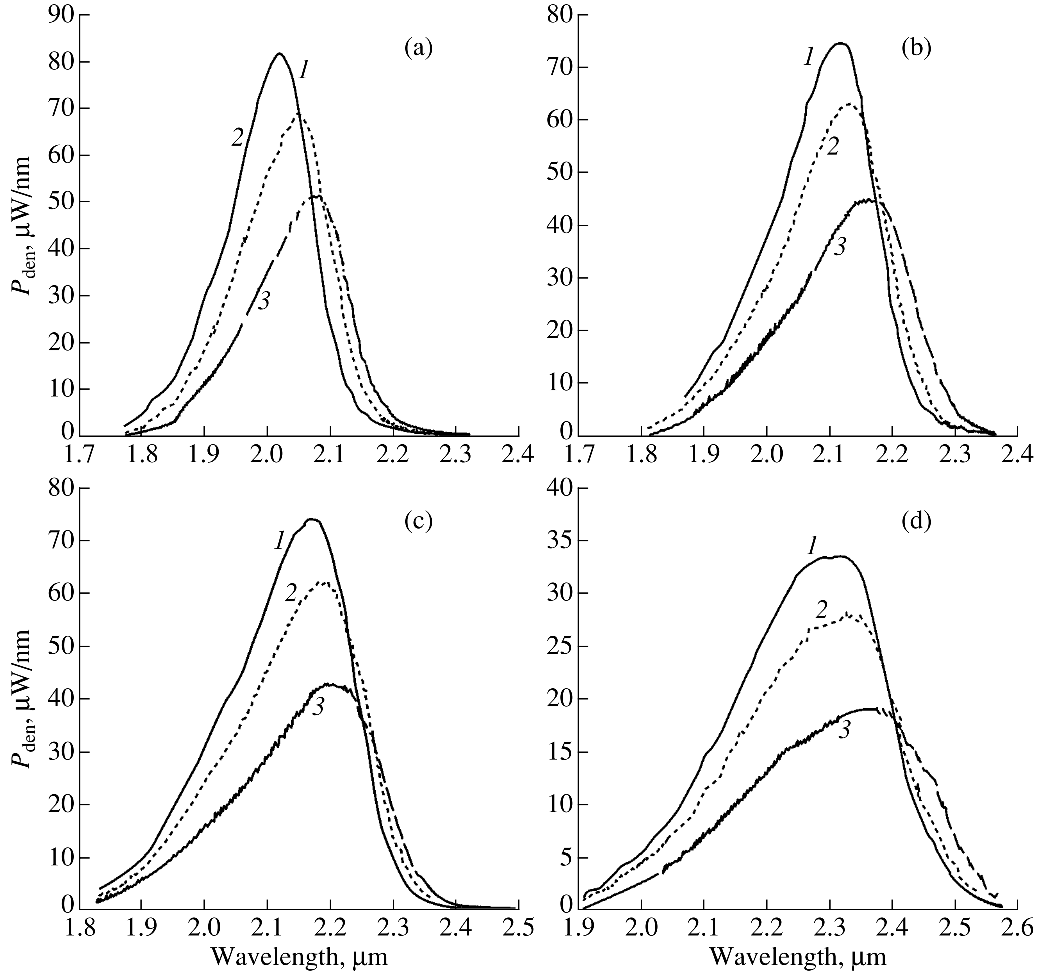

Fig. 3. Spectral power density P_{den} for four LED structures of the 2.0- to 2.4-μm spectral range: (a) LED20, (b) LED21, (c) LED22, and (d) LED23. The temperature of measurement: (*1*) 10, (*2*) 22, and (*3*) 55°C. Parameters of measurement: the frequency f = 500 Hz, off-duty factor Q = 2, current I = 200 mA.

parison of the data of measured power obtained by our group with the data obtained for the same LEDs in the United States (Instrumentation Metrics Inc.) and France (Montpelier University) showed perfect agreement. The obtained values of the integral power differed by no more than 10%.

3. OPTICAL CHARACTERISTICS OF 2.0- TO 2.4-μm LEDS

First of all, we will discuss LED structures with emission peaks at 2.05, 2.15, 2.25, and 2.35 μm. At these wavelengths, the absorption in the GaSb substrate is minimum, since its absorption edge lies at λ = 1.72 μm. Therefore, circular contacts 150 μm in diameter were formed on the substrate side by photolithography. Chips 300 × 300 μm^2 were mounted in standard TO-18 packages with the active layer faced down. The emission output occurred through the substrate. For thermal measurements, the LED chips were mounted on frigistors in TO-5 packages 9 mm in diameter.

Figures 3a–3d show the spectral power density distributions for four LED structures with emission peaks at approximately 2.05, 2.15, 2.25, and 2.35 μm, at three different temperatures.

One of the fundamental specific features of these structures is the existence of type II heterojunctions formed by the GaSb substrate and GaInAsSb active layer, which exerts an influence on the recombination processes. Heterostructures with double-sided, wide-bandgap confinement were also studied, but making the technology more complex did not improve the radiative recombination conditions for these wavelengths, because the *p*-AlGaAsSb layer (see the structure in Fig. 4) provides very good confinement for electrons, whereas the introduction of the additional wide-bandgap layer does not raise the barrier for holes.

Figure 5 shows the power density distributions as functions of the photon energy for four structures at T = 22°C. The emission peaks correspond to 0.608 eV (for LED20), 0.583 eV (LED21), 0.568 eV (LED22), and

0.534 eV (LED23). These data correlate with the energy gap values calculated for four compositions of the active layers: LED20 12% In, E_g = 0.610 eV; LED21 16% In, E_g = 0.575 eV; LED22 19% In, E_g = 0.550 eV; LED23 22% In, E_g = 0.526 eV.

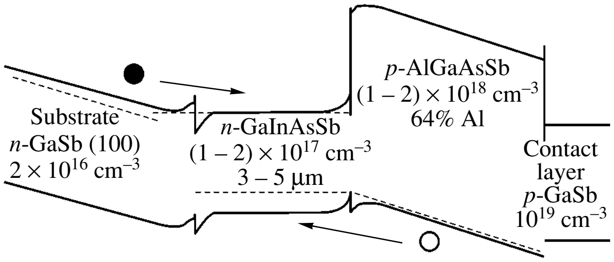

Fig. 4. Energy-band diagrams of LED structures LED20, LED21, LED22, and LED23 under forward bias.

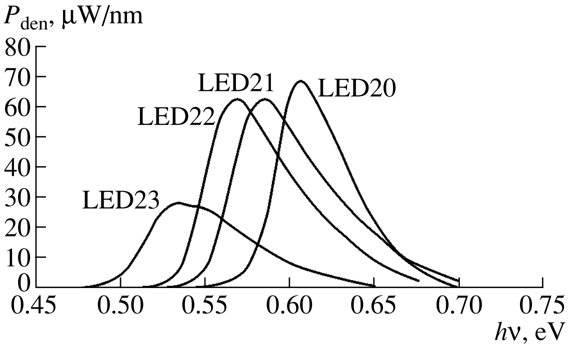

Fig. 5. Spectral power density P_{den} vs. the photon energy for four LED structures at room temperature (T = 22°C). The measurement parameters are the same as in Fig. 3.

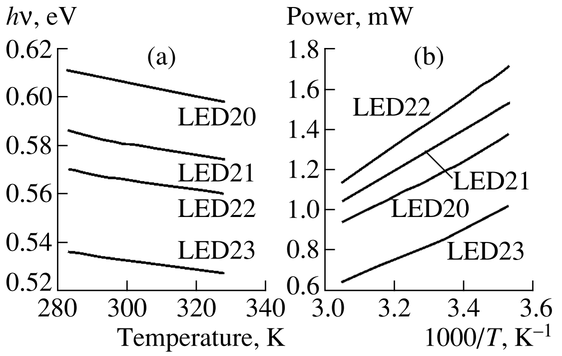

Fig. 6. Temperature dependences of (a) photon energy in the emission peak and (b) integral optical power for LED structures of the 2.0- to 2.4-μm range.

Figure 6a shows temperature dependences of photon energies in the emission peak for four LED structures. The temperature coefficient of photon energies in the emission peak near room temperature was determined. For structures LED20–LED23 the values were -2.9×10^{-4}, -2.6×10^{-4}, -2.2×10^{-4}, and -1.8×10^{-4} eV K^{-1}, respectively. For comparison, the temperature coefficient of the GaSb energy gap equals -3.78×10^{-4} eV K^{-1}.

Figure 6b shows temperature dependences of the integral optical power. With temperature rising, the power decreases as $\exp(T_0/T)$. In LED20, the maximum spectral density of the optical power is higher than in LED21 and LED22 (Fig. 5), but, since the spectrum is broadened from 160 nm for LED20 to 280 nm for LED23, the maximum integral power is observed in LED22. The LED23 structure is substantially inferior to the other three structures in its peak power spectral density, as well as in its integral power. The active region composition in LED23 (22% In) lies near the miscibility gap for the GaSb–InAs system, which results in a higher density of defects raising the nonradiative recombination rate.

We will now look at the current dependences of the spectral power density and integral power in more detail, using the LED20 structure as an example.

In the course of measuring the light–current characteristics, LED structure heating by driving current was compensated by a built-in frigistor. In this way, the temperature of the chip remained constant, which is also confirmed by the fact that the peak wavelength does not shift (Fig. 7). At currents below 100 mA, the power increases superlinearly (Fig. 8a); between 100 and 250 mA, the rise in power is virtually linear; and only above 250 mA is a slight deviation toward sublinearity observed.

The external quantum efficiency of emission was determined using the relation

$$\eta_{\text{ext}} = \frac{P}{I}\frac{q}{h\nu}, \tag{1}$$

where P is the optical power, I is the current across the structure, $h\nu$ is the photon energy, and q is the elementary charge. In current range of 200–250 mA, the external quantum efficiency was 1.35–1.37%. The well-known relation between the internal and external quantum efficiencies of emission through a single facet has the form [10]

$$\frac{\eta_{\text{ext}}}{\eta_{\text{in}}} = \frac{1}{n(n+1)^2}, \tag{2}$$

where n = 3.95 is the GaSb refractive index and yields $\eta_{\text{ext}}/\eta_{\text{in}}$ = 0.82%. Taking into account the ratio between the emission through the top and side faces of a chip and the absorption by contacts, in our case, we determined that $\eta_{\text{in}} = 43.6\eta_{\text{ext}}$. The dependences of the internal quantum efficiency on current were calculated for the LED20–LED23 samples (Fig. 8b). At currents of 200–250 mA, the maximum internal quantum efficiency at T = 22°C was 60% for LED22, 53% for LED21, 50% for LED20, and 35% for LED23. The dependence of the quantum efficiency on current can be analyzed in terms of the known equation for overall recombination in IR-optoelectronic materials [3]:

$$R_{\text{tot}} = q(A_{\text{SRH}}n_{\text{ac}} + B_{\text{rad}}n_{\text{ac}}^2 + C_{\text{Auger}}n_{\text{ac}}^3)h, \qquad (3)$$

where n_{ac} is the carrier density in the active region and h is the active region thickness. The total recombination rate R_{tot} includes recombination via levels in the band gap $A_{\text{SRH}}n_{\text{ac}}$ (Shockley–Read–Hall), radiative recombination $B_{\text{rad}}n_{\text{ac}}^2$, and Auger recombination $C_{\text{Auger}}n_{\text{ac}}^3$. At currents below 100 mA, nonradiative Shockley–Read–Hall recombination is substantial. At currents of 150–250 mA, the contribution of radiative recombination, which is proportional to the squared carrier density, increases and, consequently, the quantum efficiency grows. At currents above 250 mA, the quantum efficiency slightly decreases. As mentioned above, this decrease is not associated with a rise in the temperature of the structure, rather, it can be attributed to the increasing contribution of the nonradiative Auger recombination, which is proportional, as a first approximation, to the cubed carrier density in the active region.

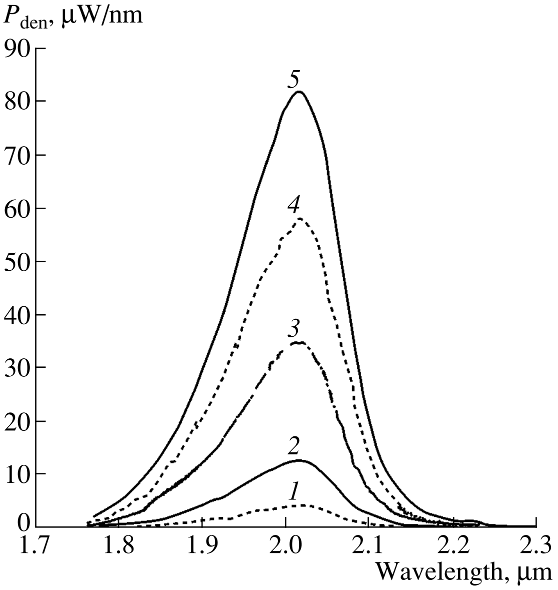

Fig. 7. Spectral power density P_{den} measured at different currents in the quasi-steady mode (Q = 2, f = 500 Hz, T = 22°C). I: (*1*) 25, (*2*) 50, (*3*) 100, (*4*) 150, and (*5*) 200 mA.

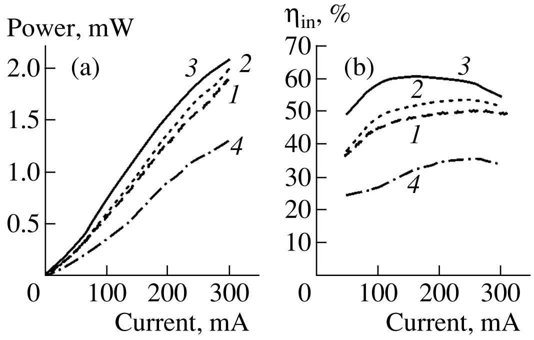

Fig. 8. Dependences of (a) integral optical power and (b) internal quantum efficiency on current for LED structures: (*1*) LED20, (*2*) LED21, (*3*) LED22, and (*4*) LED23.

4. OPTICAL CHARACTERISTICS OF 1.6- TO 2.0-μm LEDS AND REASONS FOR THEIR LOWER EFFICIENCY AS COMPARED WITH 2.0- TO 2.3-μm LEDS

In the first version of the linear array of LEDs, we used the same structure and design as for the LED20–LED23 series to fabricate LED19 and LED18 diodes emitting at 1.95 and 1.85 μm, respectively. A GaSb substrate almost entirely absorbs the 1.65 and 1.75 μm emission; thus, in the design of LED16 and LED17, we used heterostructures with double-sided wide-bandgap confinement and an emission output through the top p-layer instead of through the substrate. Figures 9a–9d show the spectral distribution of the power density P_{den} for the four LED structures with emission peaks at 1.65, 1.75, 1.85 and 1.95 μm, respectively, at three different temperatures; and the power density distributions for the four samples as functions of the photon energy at T = 22°C are shown in Fig. 10. The spectra of the LED16 and LED19 diodes have one peak and a normal FWHM of about 120–140 nm. The spectrum of LED17 exhibits a second peak, which shifts from 1850 nm at T = 10°C to 1900 nm at T = 55°C. A separate second peak is not observed in the LED18 spectrum, but the FWHM of the peak is 180 nm at T = 22°C, which is 40 nm broader than that for LED19. For the LED16–LED19 diodes, the room-temperature emission peaks correspond to 0.758, 0.733, 0.667, and 0.638 eV, respectively. The temperature coefficients of the photon energy (Fig. 11a) were in the range –(3.6–4.0) × 10^{-4} eV K^{-1}, which correlates with the temperature dependence of the energy gap in these materials.

The emission power of all four LED structures in the 1.6- to 2.0-μm range is significantly less than in the 2.0- to 2.4-μm diodes. To account for this fact, as well as for the specific features of the LED17 and LED18 spectra, we will discuss the band diagrams of the structures (Fig. 12) in more detail. With the In content in the active region raised from 0 to 20%, the energy spacing between the valence band and Γ valley of the conduction band decreases from 0.726 to 0.55 eV. The gap between the valence band and L valley of the conduction band decreases more weakly, from 0.81 to 0.76 eV.

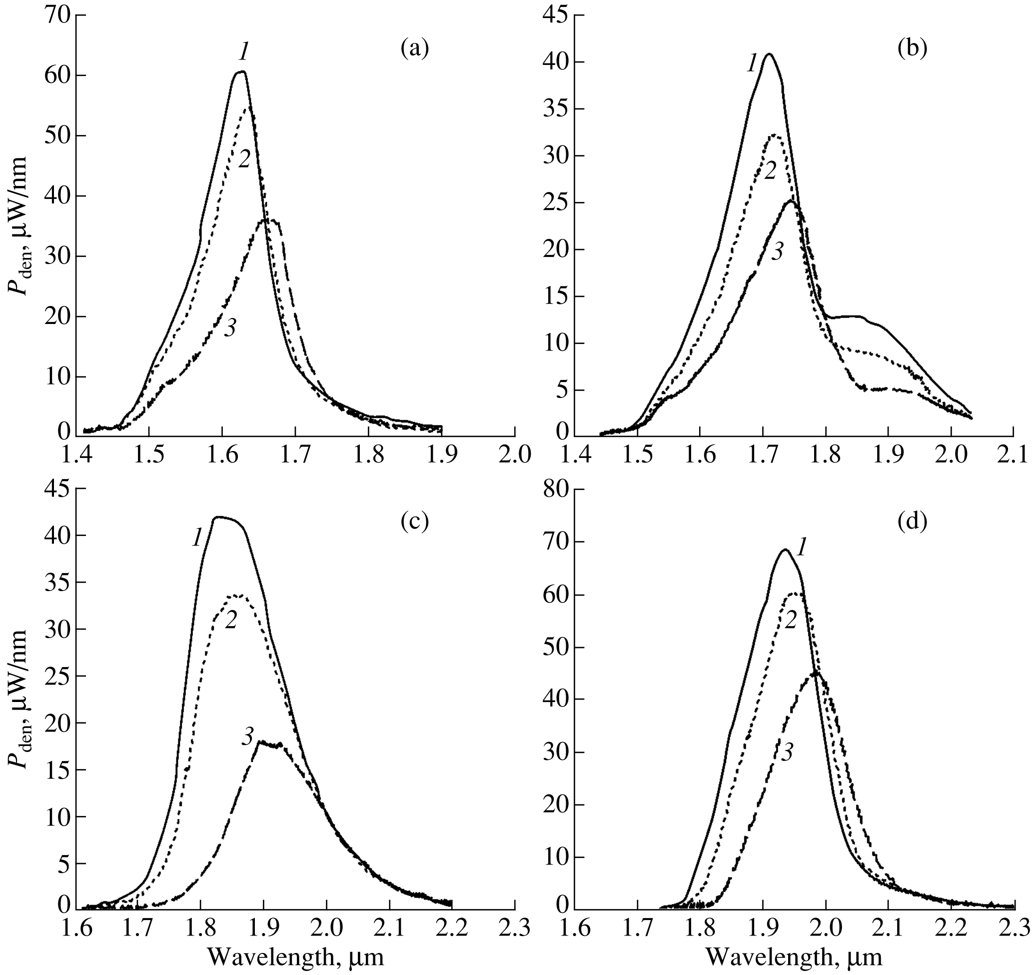

Fig. 9. Spectral power density for four LED structures of the 1.6- to 2.0-μm range: (a) LED16, (b) LED17, (c) LED18, and (d) LED19. The temperature of measurement *T*: (*1*) 10, (*2*) 22, and (*3*) 55°C. Parameters of measurement: *f* = 500 Hz, *Q* = 2, *I* = 200 mA.

Earlier thorough investigations of GaSb and quaternary GaInAsSb solid solutions [13] showed that three acceptor levels always exist in Czochralski-grown, unintentionally doped GaSb: a shallow level with an activation energy E_1 = 11–17 meV and two deep levels with E_2 = 30–35 meV and E_3 = 70–90 meV, which can be attributed to double-charged structural defects in the crystal lattice, i.e., gallium vacancy and Ga at the Sb site

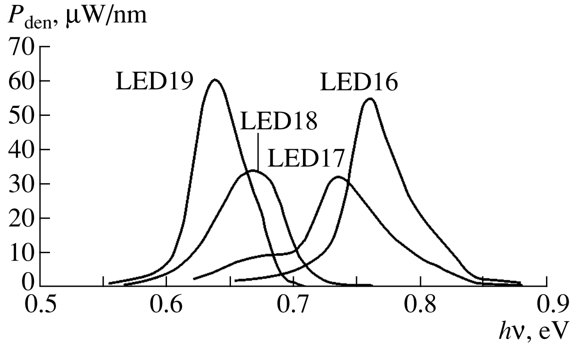

Fig. 10. Spectral power density P_{den} vs. the photon energy for four LED structures of the 1.6- to 2.0-μm range at room temperature (*T* = 22°C). For the measurement parameters, see Fig. 9.

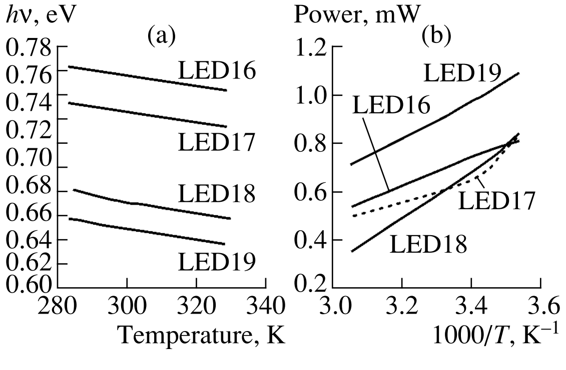

Fig. 11. Temperature dependences of (a) the photon energy in the emission peak and (b) the integral optical power for LEDs of the 1.6- to 2.0-μm range.

($V_{Ga}Ga_{Sb}$). In quaternary solid solutions, the probability of structural defect formation decreases when Ga atoms are replaced with In and when the density of deep acceptor levels in the crystals decreases.

The lifetime of minority carriers, which is determined from the characteristic time of emission decay upon switching the current off and from the amount of charge extracted upon switching from forward to reverse current [5], decreased by an order of magnitude, from 50 ns for LEDs with $\lambda = 1.8$ μm to 3–5 ns for LEDs with $\lambda = 2.4$ μm (Fig. 13).

We can offer two reasons for the substantial decrease in the quantum efficiency (Fig. 14) and in the maximum emission power on passing from the LED22 structure emitting at 2.25 μm (Fig. 8) to shorter-wavelength structures, especially LED18 and LED17 (Fig. 15).

(i) Deep levels of a double-charged structural defect in the crystal lattice of GaSb and closely similar solid solutions act as trapping levels for injected minority carriers in the *n*-type active region. This effect raises the lifetime of radiative recombination, which has been confirmed by direct measurements, and reduces the quantum efficiency in accordance with the relation

$$\eta_{\text{in}} = \frac{\tau_{nr}}{\tau_r + \tau_{nr}}. \tag{4}$$

As mentioned above, the density of deep levels in a solid solution decreases with increasing In content (or Al for the $\lambda = 1.65$ μm LED). Obviously, the presence of the second peak in the LED17 spectrum and the broadening of the LED18 spectrum are related to radiative recombination via acceptor levels.

(ii) The energy spacing between *L* and the Γ valleys of the GaSb conduction band is only 84 meV. Furthermore, the electron mass and, hence, the density of states in an *L* valley is an order of magnitude higher than in Γ. The spacing between *L* and Γ valleys increases as the In content rises; thus, the ratio of electron densities in *L* and Γ valleys changes in favor of the Γ valley.

5. NATURE OF SPONTANEOUS ELECTROLUMINESCENCE OF 1.8- TO 2.4-μm LEDS IN 77–300 K TEMPERATURE RANGE

All diodes can be arbitrarily classified into two groups according to their electroluminescence (EL) properties: short-wavelength, with emission at $\lambda <$ 2 μm; and long-wavelength, with emission at $\lambda > 2$ μm. The room-temperature emission spectra of all LEDs have the form of a band with a FWHM of 0.04–0.06 eV, with the peak energy $h\nu_{\max}$ close to the energy gap E_g of the narrow-gap layer. Along with the spectral and power characteristics, we studied the lifetime of nonequilibrium carriers in relation to current and temperature. The lifetime of nonequilibrium carriers was assumed to be equal to the characteristic time of emission decay on switching the current off. The measurements were done in the 77–300 K temperature range at currents of 0.3–1000 mA. As the temperature changes from 300 to 77 K, the emission spectra of the long-wavelength LEDs ($\lambda \geq 2$ μm) do not exhibit qualitative

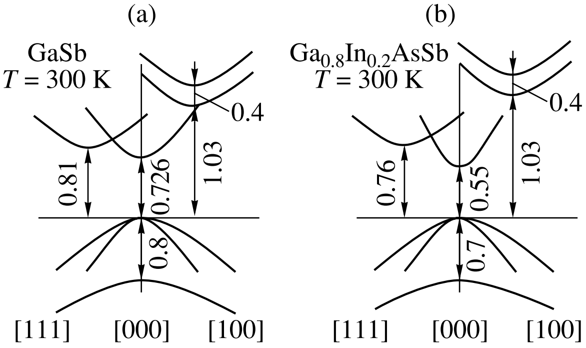

Fig. 12. Energy-band diagrams of (a) GaSb and (b) GaInAsSb with 20% In (LED22). The transition energies are given in electronvolts.

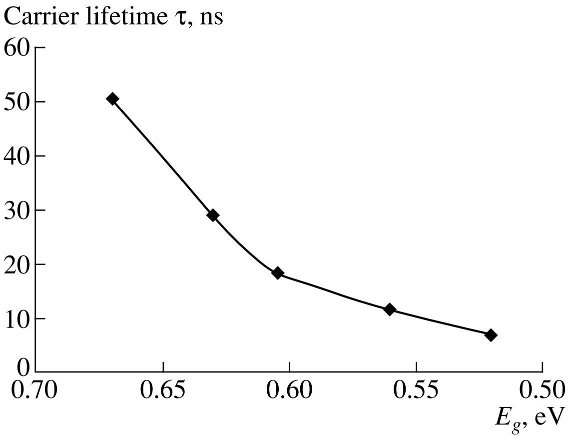

Fig. 13. The emission decay time constant vs. the E_g of the active region.

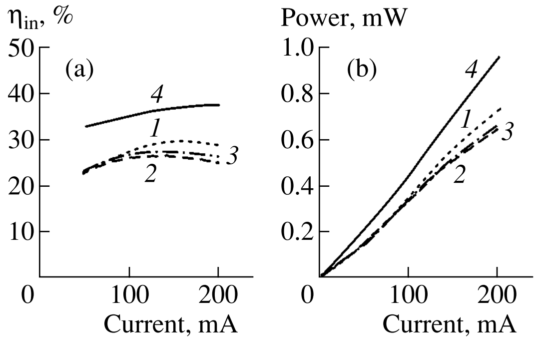

Fig. 14. Dependences of (a) the integral optical power and (b) the internal quantum efficiency on current for LEDs: (*1*) LED16, (*2*) LED17, (*3*) LED18, and (*4*) LED19.

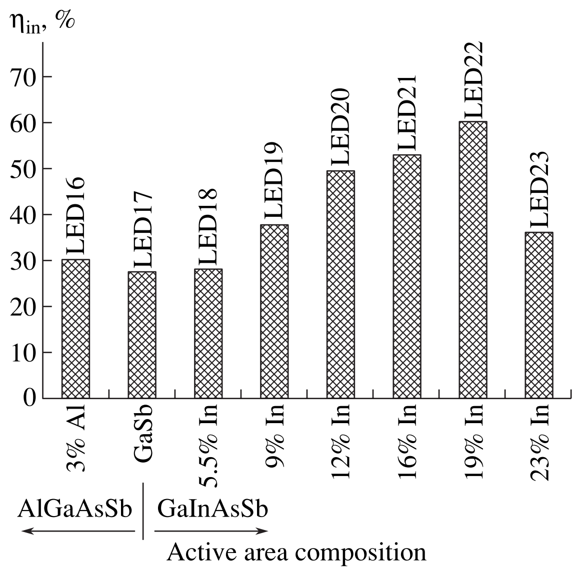

Fig. 15. The internal quantum efficiency for eight LED structures.

changes: they remain single-band, but the peak energy $h\nu_{max}$ is 10–30 meV lower than E_g and it depends on current. When the temperature changes from 300 to 77 K, the spectra of short-wavelength LEDs ($\lambda < 2$ μm) become multiband; they contain several bands, *A*, *B*, and *C*. The energies of the *B* and *C* bands are, respectively, 20 and 80 meV lower than E_g, and their intensity strongly depends on current. The emission of the longer wavelength bands *C* and *B* dominates at small currents. As the current rises, the emission intensity of these bands tends toward a limiting value (*C* band), whereas the dependence of intensity in the short-wavelength band on current gradually varies from superlinear to linear (*A* band). The contribution of the *A* band in the short-wavelength LEDs increases with rising temperature, and it is this band that becomes predominant at room temperature. The external quantum efficiency is at a maximum (up to 6%) in 2.0- to 2.2-μm LEDs and decreases gradually to η= 1–2% for both shorter and longer wavelength (2.4 μm) diodes. At a fixed current of 30 mA, the external quantum efficiency decreases with rising temperature in all of the structures. In the range of 77–150 K, the temperature dependence of η is weak; at higher temperatures, it is strong.

The transient characteristics of EL observed upon applying a rectangular pulse of forward current (I = 200 mA) depend on the LED emission wavelength. The minority carrier lifetime determined from the characteristic time of emission decay on switching the current off, and also from the amount of charge extracted on switching from forward to reverse current, was the highest (50 ns) for λ = 1.8 μm LEDs and decreased gradually by an order of magnitude to 3–5 ns for λ = 2.4 μm diodes.

We will now analyze the obtained experimental data.

All of the LEDs demonstrate properties typical of semiconductor luminescent devices: the peak energy of the emission bands is close to the energy gap, the FWHM of bands exceeds kT, the external quantum efficiency of emission η_{ext} decreases with rising temperature (Fig. 16a), and the speed of radiative response depends on temperature.

We analyzed the calculated radiative (τ_r) and nonradiative (τ_a) lifetimes of minority carriers and compared them with the experimentally observed lifetimes (Fig. 16b). In the calculations, we used the expression

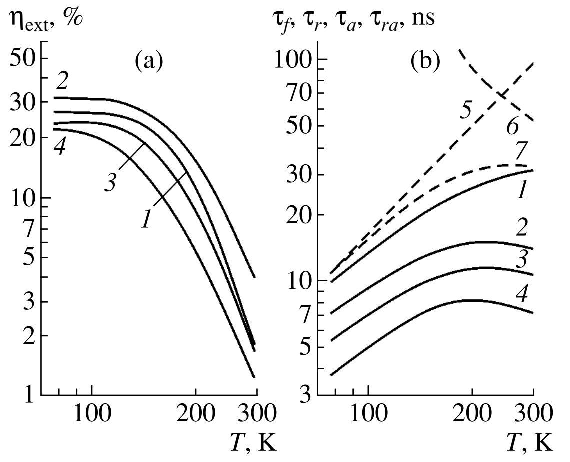

Fig. 16. Temperature dependences of (a) the external quantum efficiency η_{ext} for LEDs: (*1*) LED18, (*2*) LED19, (*3*) LED22, and (*4*) LED23; (b) lifetime of carriers: solid lines *1*–*4*, the experimental data; dashed lines *5*–*7*, calculated.

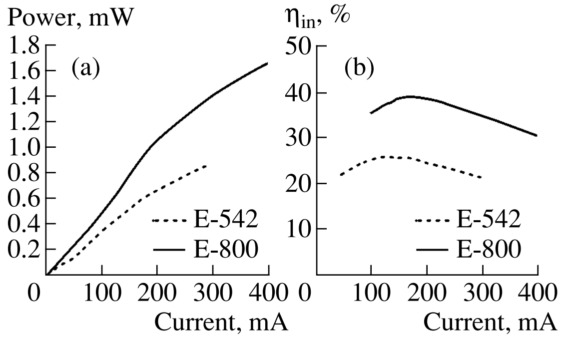

Fig. 17. Dependences of (a) integral optical power and (b) internal quantum efficiency on current for 1.85-μm LEDs grown with (E-800) and without (E-542) a buffer layer.

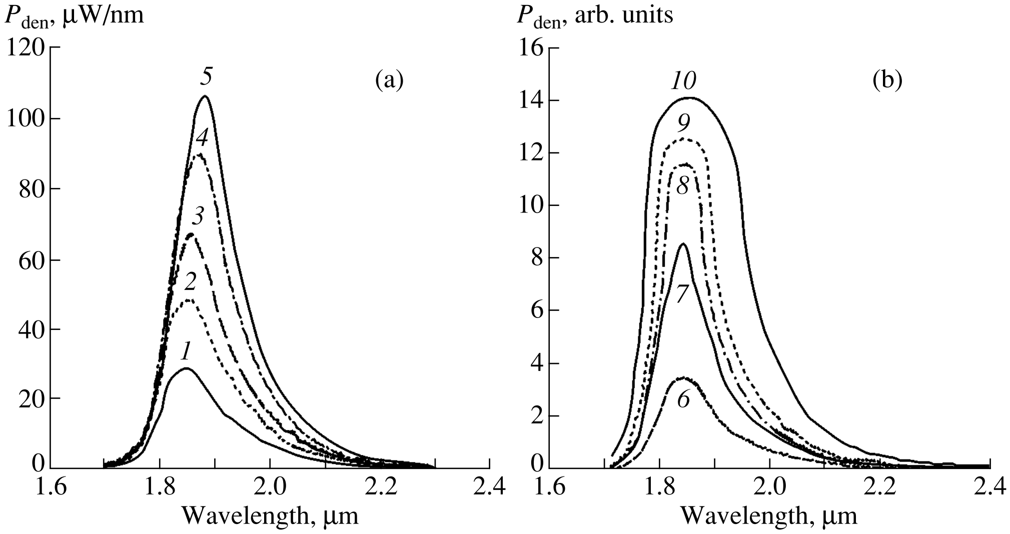

Fig. 18. Spectra of E-800 LED structure recorded in different pulsed modes ($f = 500$ Hz): (a) the off-duty factor $Q = 2$, $\tau = 1$ ms and (b) $Q = 1000$, $\tau = 200$ ns. The current, I: (*1*) 0.1, (*2*) 0.15, (*3*) 0.2, (*4*) 0.3, (*5*) 0.4, (*6*) 1, (*7*) 2, (*8*) 3, (*9*) 4, and (*10*) 10 A.

obtained by Gel'mont and Zegrya [11], taking into account the nonparabolicity of energy bands and the spin-orbit splitting of the valence band.

It seems that, at 77 K, the radiative lifetime τ_r exceeds the experimental value only by ~20%, which indicates good agreement between the calculated and experimental data. With temperature rising, the calculated τ_r increases as $T^{3/2}$, whereas the experimental dependence is substantially weaker, which implies the contribution of other recombination channels at higher temperatures.

We will now discuss the nonradiative lifetime of minority carriers. As is known, band-to-band nonradiative Auger recombination dominates in narrow-gap materials. The most probable process in *n*-type semiconductors is the Auger process in which minority holes recombine with electrons and the excess energy is transferred to another electron in the conduction band (CHCC process).

The nonradiative time for holes τ_a in this process was calculated the same way as in [12]. At a temperature of 300 K, the calculated τ_a value is higher than the experimental one by a factor of 1.5 and twice as small as the calculated radiative time τ_r. With temperature falling, τ_a strongly increases. The total time

$$\tau_{ra} = \frac{\tau_a - \tau_r}{\tau_a + \tau_r}$$

exceeds the experimental value of τ only by 10–25% (satisfactory agreement); thus, we may conclude that, at low temperatures, radiative recombination dominates in short-wavelength LEDs, and, at $T > 200$ K, the nonradiative Auger recombination of the CHCC type makes a significant contribution which is comparable to the radiative recombination. The calculated internal quantum efficiency of emission η_{in} is 98% at 77 K, and with temperature rising it decreases to 35% at 300 K. The experimental external quantum efficiency of emission differs from the calculated one: it is 30–40% at 77 K, and strongly decreases to 1–2% as the temperature rises to 300 K.

We will now move on to an analysis of long-wavelength LED properties. According to [12], the radiative lifetime under band-to-band bulk recombination must increase by 40% with E_g decreasing from 0.7 to 0.5 eV independently of temperature, whereas the nonradiative lifetime at 300 K should decrease by a factor of 2. However, the experimental lifetime does not increase, rather, it decreases in the entire temperature range by a factor of 2.5–5, with E_g decreasing from 0.68 to 0.53 eV. This leads to the assertion that band-to-band

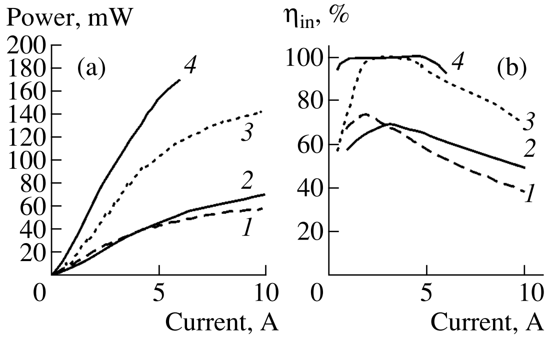

Fig. 19. Dependences of (a) power and (b) internal quantum efficiency on current for optimized LED structures emitting at the 1.6- to 2.0-μm wavelength in the short-pulse mode ($\tau = 200$ ns, $Q = 1000$). Structures: (*1*) E-800, (*2*) E-816, (*3*) E-832, and (*4*) E-833.

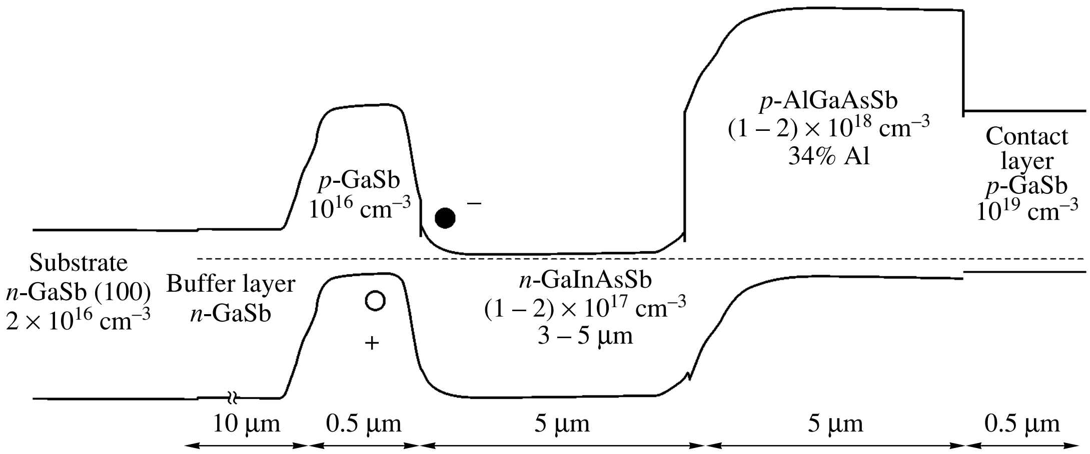

Fig. 20. The energy-band diagram of the *E*-816 LED structure.

recombination in the bulk does not dominate in long-wavelength LEDs.

The predominance of radiative recombination at low temperatures is confirmed by the fact that the external quantum efficiency of emission in long-wavelength LEDs at 77 K is 20–35%, which corresponds to the domination of radiative recombination if the absorption of emission is taken into account. At room temperature, η_{ext} is an order of magnitude smaller than at 77 K and, correspondingly, the lifetime is defined by the nonradiative process.

Thus, radiative recombination dominates in long-wavelength ($\lambda \geq 2$ μm) LEDs at the temperature of liquid nitrogen, whereas, at room temperature, the contribution of nonradiative Auger recombination at the heterointerface is significant.

6. RAISING THE QUANTUM EFFICIENCY OF 1.85-μm LEDS BY THE INSERTION OF A BUFFER LAYER

To raise the quantum efficiency of 1.85-μm LEDs, it was necessary, first of all, to reduce the negative effect of deep levels related to double-charge structural defects in the crystal lattice. The concentration of structural defects in GaSb substrates reached 2×10^{17} cm^{-3}. Nearly the same defect density was observed in GaSb or quaternary solution layers with a low (<6%) In content and which were grown directly on these substrates. The density of natural structural defects related to stoichiometry depends on the ratio of the Ga to Sb content in the melt. A method for modifying this ratio by introducing Pb as a neutral solvent was suggested in [13]. Using this method, the density of deep acceptor levels can be reduced to 2×10^{16} cm^{-3}.

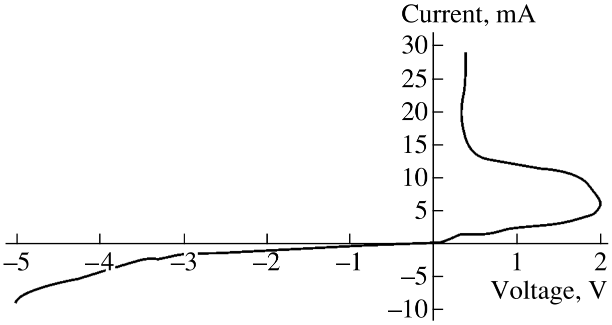

Fig. 21. Current–voltage characteristic of the *E*-816 LED structure at *T* = 22°C.

In this study, a minimum defect density in the active region was obtained by growing an *n*-GaSb buffer layer 6 to 10 μm thick on *n*-GaSb substrate. Lead was used as a neutral solvent in the epitaxial process. Further, a 1.5-μm-thick $Ga_{0.95}In_{0.05}AsSb$ active layer doped with Te to $n \approx 10^{17}$ cm^{-3} was grown on top of the buffer layer. The LED structure also included a p-$Al_{0.34}Ga_{0.66}AsSb$ layer (3 μm), acting as a wide-bandgap barrier for electrons, and a contact GaSb layer (0.5 μm) doped to $p \approx 10^{19}$ cm^{-3}.

As is seen in Fig. 17, the E-800 LED structure with a thick buffer layer surpasses the initial E-542 structure by 13% in internal quantum efficiency and by two times in the integral operating power. At the same time, the spectral FWHM is 130 nm for the E-800 structure and 180 nm for the E-542 structure. This indicates that we have succeeded in reducing not only the density of deep acceptor levels in the active region, which are responsible for the increase in the lifetime of radiative recombination, but also the density of shallow acceptor states; it also indicates that we have depressed the density-of-state tails responsible for the broadening of the spectrum. The increase in the spectral FWHM as the current exceeds 3 A in pulsed mode (Fig. 18b) is most probably related to the fact that the radiative recombination process involves not only the carriers near the conduction-band bottom and the valence-band top, but also the carriers with higher energies, since the current density at

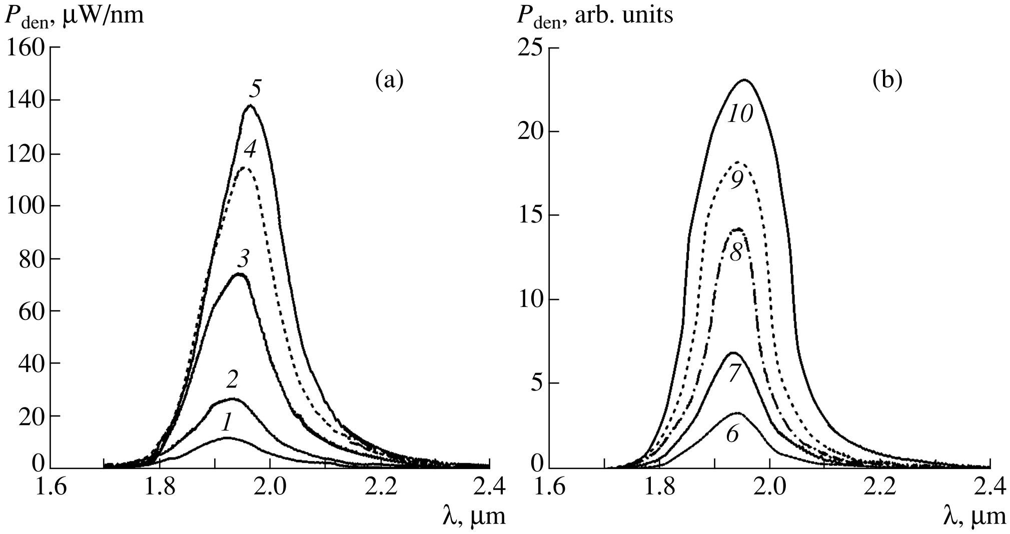

Fig. 22. Spectra of the E-816 LED structure recorded in different pulsed modes: (a) $Q = 2$, $\tau = 1$ ms and (b) $Q = 1000$, $\tau = 200$ ns. The current, I: (*1*) 0.05, (*2*) 0.1, (*3*) 0.2, (*4*) 0.3, (*5*) 0.4, (*6*) 1, (*7*) 2, (*8*) 3, (*9*) 5, and (*10*) 10 A.

$I = 10$ A was 111 A cm^{-2}. The maximum internal quantum efficiency (Fig. 19) reached 82% at a current of 2 A ($Q = 1000$).

In addition to the rise in the share of the Auger recombination, the operation of LEDs at high currents in real structures is limited by possible breakdown or overheating due to local inhomogeneities in the crystal or chip surface. The quality of the E-800 structure allowed us to substantially raise the operating power of the LEDs owing to the increase in currents at which LED operation was stable. For example, an optical power $P = 1.66$ mW was obtained at a current of 400 mA in the quasi-steady mode ($Q = 2$) and $P = 60$ mW at 10 A in pulsed mode ($Q = 1000$, $\tau = 200$ ns).

7. RAISING THE QUANTUM EFFICIENCY OF 1.95-μm LEDS WITH A THYRISTOR STRUCTURE

In the design of the 1.95-μm LED structure with increased quantum efficiency (E-816), we applied the same buffer-layer growth technology as in the E-800 structure. The buffer layer was 10 μm thick. However, one more new element was used here. A 0.5-μm-thick *p*-GaSb layer was introduced between the buffer and the active layer (Fig. 20).

The shape of the current–voltage characteristic of the obtained *n*–*p*–*n*–*p*-structure was typical of a thyristor structure (Fig. 21). The turn-on voltage was 1.9 V. In the "on" state, the voltage sharply decreased to 0.45 V. As is known from the theory of thyristor structures, the height of a barrier subject to reverse bias drops sharply due to the electron and hole charge that accumulates on both sides of the interface (in our case, it was a type-II heterointerface between *p*-GaSb and *n*-GaInAsSb), which is a positive charge in *p*-type and a negative one in an *n*-type semiconductor. The processes in this complex structure demand more detailed discussion. We note only that, in all probability, the interface between *p*-GaSb and *n*-GaInAsSb makes a positive contribution to radiative recombination.

Figure 22 shows the spectra of the E-816 structure recorded in (a) quasi-steady and (b) pulsed modes, and Fig. 23 compares (a) light–current characteristics and (b) the dependences of the internal quantum efficiency on current for two 1.95-μm LED structures, E-729 and E-816. A maximum internal quantum efficiency was obtained in the E-816 structure; it was 52% in the quasi-steady mode at a current of 250 mA and 77% in the pulsed mode at 3 A ($Q = 1000$). The maximum output optical power was 2.5 mW at an off-duty factor $Q = 2$ and 71 mW at $Q = 1000$.

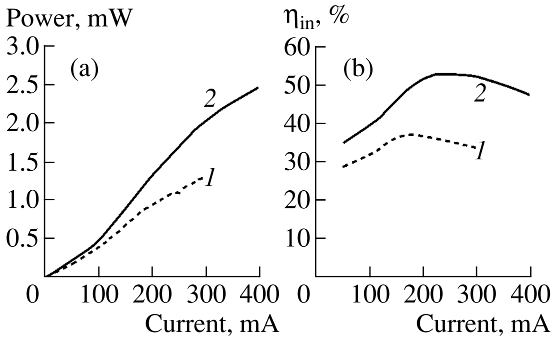

Fig. 23. Dependences of (a) the output power and (b) the internal quantum efficiency on current for two 1.95-μm LED structures: (*1*) E-729 and (*2*) E-816.

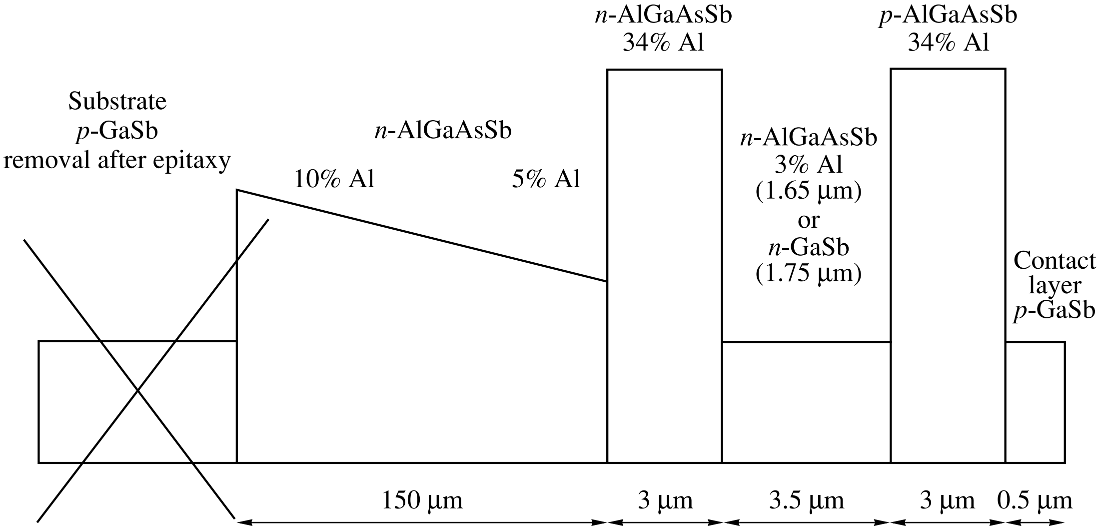

Fig. 24. The energy-band diagram of LED structures with increased quantum efficiency, emitting at 1.75 μm (E-832) and 1.65 μm (E-833).

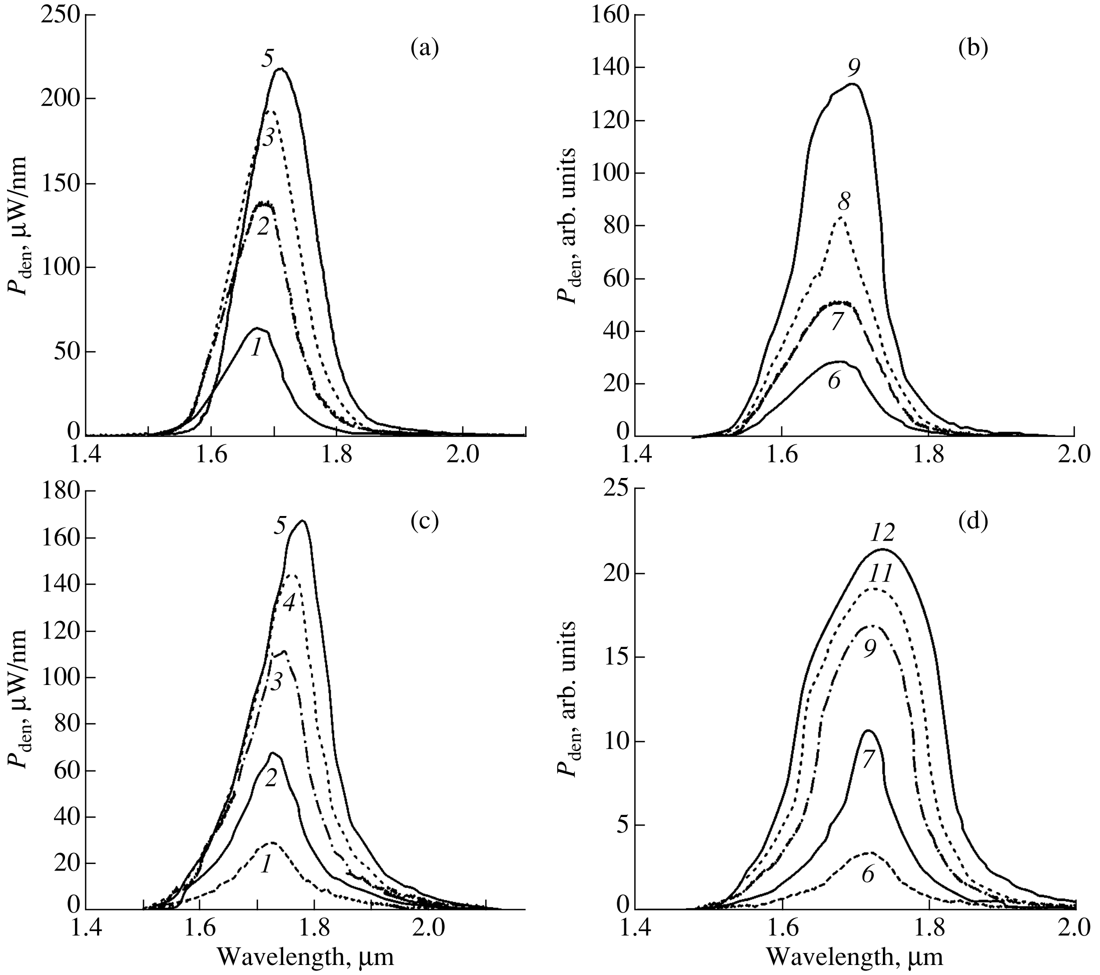

Fig. 25. Spectral power density for LED structures (a, b) E-833 and (c, d) E-832 in (a, c) quasi-steady (Q = 2) and (b, d) pulsed (Q = 1000) modes.

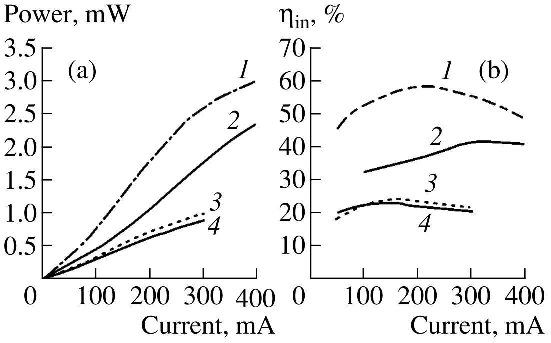

Fig. 26. The comparison of dependences of (a) power and (b) internal quantum efficiency on current for LED structures emitting at 1.65- and 1.75-μm wavelengths: (*1*) E-833, (*2*) E-832, (*3*) E-444, and (*4*) E-651.

8. HIGH-EFFICIENCY LED STRUCTURES EMITTING AT 1.65 AND 1.75 μm

As mentioned above, all LED structures for the 1.8- to 2.4-μm spectral range were grown on *n*-GaSb substrates and mounted with their active layer facing down on the package, with emission output through the substrate. This provided a sufficient heat sink for a LED even at currents of about 10 A (a current density over 100 A cm^{-2}). However, this approach is inapplicable in the design of LEDs emitting at wavelengths below 1.75 μm, because photons with an energy above 0.72 eV are completely absorbed by the GaSb substrate. The only possible principal solution to this problem is to fabricate a specially grown substrate with a wider energy gap, grow a LED heterostructure on it, and then remove the GaSb substrate (Fig. 24).

After the removal of the GaSb substrate, chips were mounted onto packages with the *p*-GaSb contact layer facing down. Emission output took place through a thick (150 μm) *n*-AlGaAsSb layer. The structural perfection of this thick layer was much higher than that of the GaSb substrate. Correspondingly, the active region was free of deep acceptor levels related to crystal structure defects.

The spectra were single-band at all currents. The FWHM of the emission band in the quasi-steady mode was 130 nm for the E-833 structure (Fig. 25a) and 140 nm for the E-832 structure (Fig. 25c). The internal quantum efficiency reached 60% (Fig. 26). In the short-pulse mode, the spectra were broadened at a current over 4 A (Figs. 25b, 25d). We believe that, similar to the E-800 and E-816 structures, the increase of FWHM is related to the contribution of higher energy carriers to the radiative recombination, but this problem demands further investigation.

The integral optical power was measured in the short-pulse mode (the off-duty factor $Q = 1000$); it was 140 mW and 170 mW for the E-832 and E-833 structures, respectively (Fig. 19a). In both structures, the internal quantum efficiency in this mode reached 100% (Fig. 19b). At currents of 1–5 A, the rate of radiative recombination in the E-833 structure substantially exceeded the rates of nonradiative Shockley–Read and Auger recombination processes. In the E-832 structure, this range of currents was narrower (2.5–4 A). Figure 27 shows the final values of the internal quantum efficiency, which was measured at room temperature in the quasi-steady mode ($Q = 2$, $f = 500$ Hz) for eight LED structures emitting in the spectral range of 1.6–2.4 μm. We are planning to improve the design of LED chips in future investigations, with the goal of raising the external quantum efficiency and the output optical power.

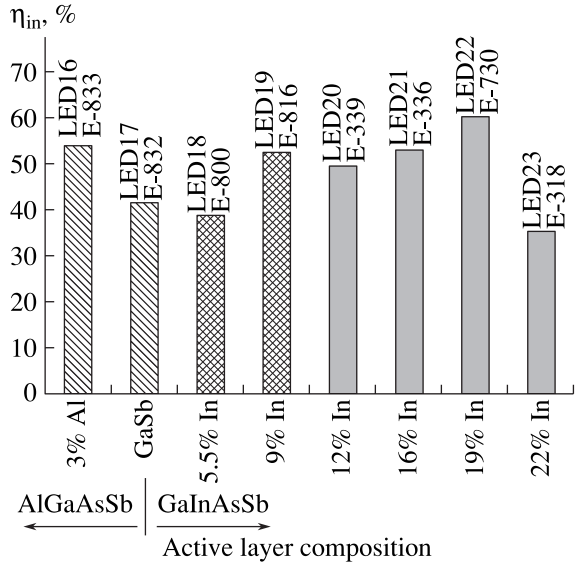

Fig. 27. The final values of the internal quantum efficiency measured at room temperature in the quasi-steady mode ($Q = 2$, $f = 500$ Hz) for eight LED structures emitting in the spectral range of 1.6–2.4 μm.

9. CONCLUSION

In this study, LED structures completely covering the 1.6- to 2.4-μm spectral range were designed and investigated. The mechanisms leading to a decrease in the internal quantum efficiency have been studied. In *n*-GaSb and quaternary solid solutions used as an active region, the CHCC Auger process occurs and becomes more important with decreasing energy gap and temperature rising. This process is responsible for the decrease in quantum efficiency at high currents in all of the structures. It has been shown that the decreasing internal quantum efficiency of LED structures with the energy gap increasing from 0.56 to 0.72 eV is due to the fact that the radiative recombination lifetime becomes longer. Deep levels of double-charged structural defects of the crystal lattice in GaSb and closely related solid solutions act as trapping levels for the injected minority carriers in the *n*-type active region. This reduces the radiative recombination rate. Based on these conclusions, we have developed new LED structures for 1.65-, 1.75-, 1.85-, and 1.95-μm wavelengths with increased quantum efficiency. An internal quantum efficiency of 40–60% was achieved in the structures under study. A high peak power of 170 mW and 100% internal quantum efficiency were attained in the short-pulse operation mode. These LEDs can be widely applied in environmental monitoring and medical diagnostics.

ACKNOWLEDGMENTS

We are grateful to M.P. Mikhailova for her assistance in interpreting the experimental data.

REFERENCES

1. A. A. Gutkin, A. A. Rogachev, V. E. Sedov, and B. V. Tsarenkov, Prib. Tekh. Éksp., No. 4, 187 (1963).
2. Y. Mao and A. Krier, J. Electron. Mater. **23**, 503 (1994).
3. A. Krier, H. H. Gao, V. V. Sherstnev, and Yu. P. Yakovlev, Appl. Phys. **32**, 3117 (1999).
4. X. Gong, H. Kan, T. Makino, *et al.*, Jpn. J. Appl. Phys. **39**, 5039 (2000).
5. A. A. Andaspaeva, A. N. Baranov, A. A. Guseĭnov, *et al.*, Pis'ma Zh. Tekh. Fiz. **15** (18), 71 (1989) [Sov. Tech. Phys. Lett. **15**, 734 (1989)].
6. A. A. Andaspaeva, A. N. Baranov, A. A. Guseĭnov, *et al.*, Fiz. Tekh. Poluprovodn. (Leningrad) **24**, 1708 (1990) [Sov. Phys. Semicond. **24**, 1067 (1990)].
7. A. A. Popov, V. V. Sherstnev, and Yu. P. Yakovlev, Pis'ma Zh. Tekh. Fiz. **23** (20), 19 (1997) [Tech. Phys. Lett. **23**, 783 (1997)].
8. A. A. Popov, V. V. Sherstnev, Yu. P. Yakovlev, *et al.*, Electron. Lett. **33** (1), 86 (1997).
9. *Handbook Series on Semiconductor Parameters*, Ed. by M. Levinshtein, S. Rumyantsev, and M. Shur (World Sci., Singapore, 1996).
10. T. Ashley, C. T. Elliott, N. T. Gordon, *et al.*, Appl. Phys. Lett. **64**, 2433 (1994).
11. B. A. Gel'mont and G. G. Zegrya, Fiz. Tekh. Poluprovodn. (Leningrad) **25**, 1381 (1991) [Sov. Phys. Semicond. **25**, 1216 (1991)].
12. A. R. Beattie and P. T. Landsberg, Proc. R. Soc. London **249** (1256), 16 (1959).
13. T. I. Voronina, B. E. Dzhurtanov, T. S. Lagunova, *et al.*, Fiz. Tekh. Poluprovodn. (St. Petersburg) **32**, 278 (1998) [Semiconductors **32**, 250 (1998)].

Translated by D. Mashovets

Semiconductors, Vol. 37, No. 8, 2003, pp. 985–991. Translated from Fizika i Tekhnika Poluprovodnikov, Vol. 37, No. 8, 2003, pp. 1010–1016.
Original Russian Text Copyright © 2003 by Moiseev, Mikhaĭlova, Yakovlev.

Special Features of Spontaneous and Coherent Emission of IR Lasers Based on a Single Type-II Broken-Gap Heterojunction

K. D. Moiseev*, M. P. Mikhaĭlova, and Yu. P. Yakovlev
Ioffe Physicotechnical Institute, Russian Academy of Sciences, St. Petersburg, 194021 Russia
**e-mail: mkd@iropt2.ioffe.rssi.ru*

Submitted February 11, 2003; accepted for publication February 17, 2003

Abstract—The electroluminescence characteristics of a single type-II p-$Ga_{0.84}In_{0.16}As_{0.22}Sb_{0.78}$/$n$-$In_{0.83}Ga_{0.17}As_{0.80}Sb_{0.20}$ heterostructure have been studied in the temperature range 77–300 K. A new advanced laser structure based on a type-II broken-gap p-GaInAsSb/n-InGaAsSb heterojunction as the active region has been suggested and fabricated. Single-mode lasing at wavelength $\lambda = 3.14$ μm under a threshold current density $j_{th} = 400$ A/cm^2 ($T = 77$ K) was obtained. The domination of TM- over TE-polarization, observed both in the spontaneous and coherent modes of operation of the novel laser structure, can be accounted for by involvement of light holes, tunneling across the heterointerface, in radiative recombination. *© 2003 MAIK "Nauka/Interperiodica".*

1. INTRODUCTION

In recent years, considerable attention has been drawn to the design and study of mid-IR ($\lambda = 2$–5 μm) diode lasers based on III–V compounds. These devices have multiple important applications, such as the remote monitoring of atmospheric contamination by gases, laser ranging in the wavelength range safe for the eyes, monitoring in the high-tech industry, and medical diagnostics [1, 2]. Another possible application can be optical communications in free space, in the 3- to 5-μm window of atmospheric transparency. For the majority of applications, it is important that diode lasers be able to operate at room temperature.

The design of long-wavelength lasers operating at high temperatures is in progress at several leading scientific centers [3–6]. To date, only uncooled injection GaInAsSb/GaAlAsSb lasers operating at $\lambda < 2.7$ μm [3], quantum-cascade lasers emitting at $\lambda > 5$ μm [4], and lasers based on type-II quantum-confinement heterostructures with optical pumping [5] have been reported. However, there are still no long-wavelength ($3 < \lambda < 5$ μm) lasers operating on band-to-band transitions at room temperature. IR lasers based on narrow-gap InAsSb/InAs, GaInAsSb/InAs, AlGaAsSb/InAsSb heterostructures grown by LPE, MBE, and MOCVD operate at temperatures up to $T = 120$ K in the CW-mode and up to $T = 255$ K in the pulsed mode [6].

The high-temperature operation of long-wavelength lasers based on III–V compounds has several fundamental limitations. The principal factors defining the limiting temperature of laser operation are the following: (i) Auger recombination, (ii) intraband absorption of radiation, and (iii) heating of carriers. The strongest influence upon the temperature dependence of the threshold current is exerted by Auger recombination. This process dominates over radiative recombination in bulk narrow-gap semiconductors, such as InAs and GaAs and their solid solutions, whose energy bands have a "resonance" structure, in which the energy gap E_g is close to the spin–orbit splitting of the valence band Δ_{so} [7]. An important factor which must also be taken into account is the leakage of carriers from the active region of a laser based on InAs-rich compositions; this leakage results from the low height of potential barriers at the heterointerfaces with InAsSbP confining layers, in contrast to the system of AlGaAs(Sb)/GaAs(Sb) solid solutions.

Several original physical approaches have been suggested recently to suppress Auger recombination in narrow-gap heterostructures and improve the temperature characteristics of IR diode laser structures based on type-II heterojunctions [8, 9]. Quaternary $Ga_{1-x}In_xAs_ySb_{1-y}$ solid solutions are promising materials for the production of efficient optoelectronic devices, because they form both staggered and broken-gap type-II heterojunctions and completely cover the 2- to 5-μm IR spectral range.

The specific feature of type-II broken-gap GaInAsSb/InAs heterojunctions is such a mutual position of bands at the interface at which the valence band of the wide-gap GaInAsSb solid solution lies 60–100 meV above the conduction band of the narrow-gap material (InAs) [10]. In thermodynamic equilibrium, the band bending at the heterointerface between two semiconductors gives rise to a deep potential well for electrons on the InAs side. Electrons are contained at the heterointerface by the internal electric field created by holes localized in a self-consistent potential well on the solid solution side. This results in the formation of a quantum-confined semimetallic channel of spatially separated carriers localized on opposite sides of the heterointerface. When a negative voltage is applied to *p*-InAs, the depth of wells increases due to the inflow of external carriers to such an extent that one or even two occupied levels can be formed in the electron quantum well (QW). In such a structure, tunnel transitions of carriers across the heterointerface with their subsequent radiative recombination become probable.

Earlier, we suggested a new physical approach to the design of a semiconductor diode laser for the mid-IR range which relies upon the tunnel injection of carriers across the type-II interface in a single broken-gap *p*-GaInAsSb/*p*-InAs heterojunction. In this heterostructure, asymmetrical band offsets of the conduction and valence bands ($\Delta E_C \approx 0.64$ and $\Delta E_V \approx 0.42$ eV) give rise to potential barriers for electron and hole quantum confinement simultaneously, which results in the strong accumulation of carriers in the active region and enhances the recombination efficiency for spatially separated electrons and holes near the heterointerface [11]. In this case, the driving current can be maintained by tunnel injection of electrons from the bulk of the narrow-gap semiconductor.

High-intensity electroluminescence (EL) was observed in the spectral range 0.3–0.7 eV. At $T = 77$ K, the EL spectra exhibited two distinct emission bands with peak photon energies $h\nu_A = 0.314$ eV and $h\nu_B = 0.378$ eV. A blue shift of the second band was observed as the current increased through the structure. A third high-energy band $h\nu_C = 0.633$ eV, which was broader and had a lower intensity, was observed only at a high injection level because of the recombination of Auger electrons from the QW with holes from the bulk of the $Ga_{0.84}In_{0.16}As_{0.22}Sb_{0.78}$ solid solution ($E_g = 0.635$ eV [12]). This band indicates that the height of the effective potential barrier for electrons in an isotype *p*–*p* heterostructure is considerably less than the conduction band offset at the heterointerface ($V_e < 0.4$ eV).

We have also studied and produced a novel tunnel-injection laser with an isotype type-II broken-gap *p*-$Ga_{0.84}In_{0.16}As_{0.22}Sb_{0.78}$/*p*-$In_{0.83}Ga_{0.17}As_{0.80}Sb_{0.20}$ heterojunction in the active region [13]. Single-mode lasing was obtained in the temperature range 77–125 K. At $T = 77$ K, the wavelength of the stimulated emission was $\lambda = 3.26$ μm and the threshold current density reached $j_{th} = 2$ kA cm^{-2}. In this laser structure, the Auger recombination at the heterointerface was suppressed and the temperature dependence of the threshold current was weaker: a high characteristic temperature $T_0 = 60$ K was reached in the temperature range 80–110 K, which indicated good prospects for the improvement of the operating characteristics of IR lasers based on a type-II broken-gap heterojunction.

Further studies of the temperature and threshold characteristics of these lasers have revealed several principal factors limiting their operation at higher temperatures. The first, and the main one, is a high leakage of carriers from the laser active region. Holes from the valence band of the wide-gap semiconductor move to the valence band of the narrow-gap one across the narrow barrier at the heterointerface; the appearance of this barrier is due to the energy diagram of a *p*–*p* heterostructure under reverse bias. Moreover, electrons from the QW on the narrow-gap solid solution side move to the conduction band of the wide-gap solution layer via Auger-electron emission over the potential barrier V_e at the heterointerface. Second, the minority carriers, electrons in the given case, are localized near the heterointerface because of the occurrence of the zero-threshold Auger process [14]; this localization enhances intraband absorption, which depends exponentially on temperature.

In this study, radiative recombination in a type-II broken-gap *p*-GaInAsSb/*n*-InGaAsSb heterojunction was analyzed as a promising kind of laser active region. We have studied the EL in the temperature range of 77–300 K and the specific features of coherent emission, including luminescence polarization characteristics, from an asymmetrical *p*-$Ga_{0.84}In_{0.16}As_{0.22}Sb_{0.78}$/*n*-$In_{0.83}Ga_{0.17}As_{0.80}Sb_{0.20}$ laser structure.

2. EXPERIMENT

In view of the specified problem, a model *p*-$Ga_{0.84}In_{0.16}As_{0.22}Sb_{0.78}$/*n*-$In_{0.83}Ga_{0.17}As_{0.80}Sb_{0.20}$ single heterostructure was fabricated on the basis of undoped layers of a quaternary GaInAsSb solid solution, wide-gap *p*-$Ga_{0.84}In_{0.16}As_{0.22}Sb_{0.78}$ with a hole density $p = 2 \times 10^{16}$ cm^{-3}, and narrow-gap *n*-$In_{0.83}Ga_{0.17}As_{0.80}Sb_{0.20}$ ($E_g = 0.395$ eV at $T = 77$ K) with an electron density $n = 10^{16}$ cm^{-3}. The lattice-matched heterostructure was grown by liquid-phase epitaxy (LPE) on undoped (100) *n*-InAs ($n = 2 \times 10^{16}$ cm^{-3}) substrate. The epitaxial structures produced under conditions of thermodynamic equilibrium in the phase diagram of the melt and the layers grown were unstrained and characterized by a high quality of the sharp heterointerface, as confirmed by X-ray diffraction analysis. The lattice mismatch between the epitaxial layers and the substrate did not exceed $\Delta a/a \approx 2 \times 10^{-3}$ [15].

The solid solutions produced form an almost-staggered type-II heterojunction (Fig. 1). The estimated overlap between the valence band of the wide-gap semiconductor and the conduction band of the narrow-gap one is, according to our estimates, about $\Delta \approx 10$–20 meV. The energy Δ was calculated by linear interpolation of the electron affinities of binary compounds constituting the quaternary GaInAsSb solid solution. Due to comparatively small band bending at the interface, the potential barrier in the conduction band was high, $V_e \approx \Delta E_C = 0.6$ eV, which ensured the quantum

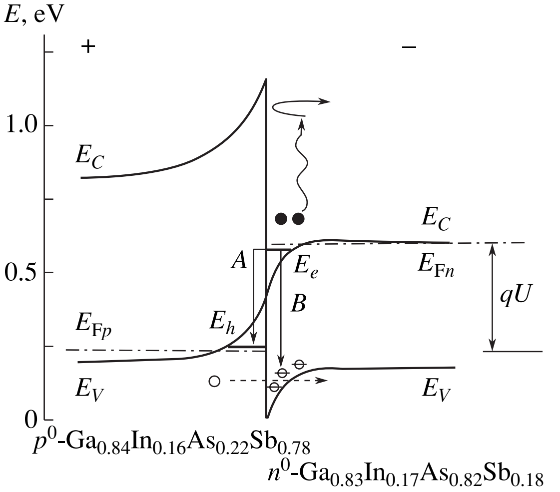

Fig. 1. Band diagram of the type-II p-$Ga_{0.84}In_{0.16}As_{0.22}Sb_{0.78}$/$n$-$In_{0.83}Ga_{0.17}As_{0.80}Sb_{0.20}$ heterojunction under an external bias U. Arrows indicate possible radiative transitions.

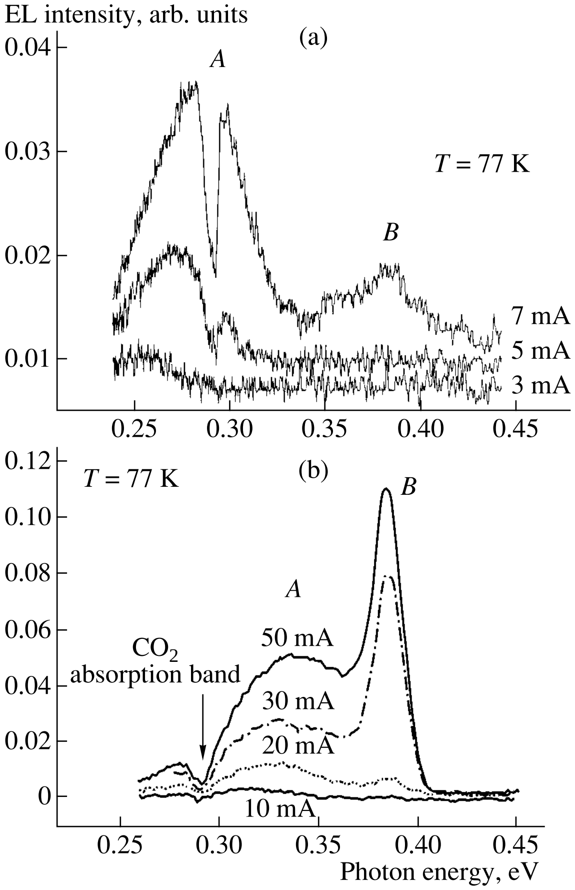

Fig. 2. EL spectra of the single type-II p-$Ga_{0.84}In_{0.16}As_{0.22}Sb_{0.78}$/$n$-$In_{0.83}Ga_{0.17}As_{0.80}Sb_{0.20}$ heterostructure under forward bias at T = 77 K for different current values at (a) low and (b) high injection levels. The arrow indicates the absorption band of atmospheric CO_2 ($\lambda \approx 4.25$ μm).

confinement of the electron gas and suppressed the Auger processes involving emission of hot electrons to the conduction band of the p-GaInAsSb solid solution. A good ohmic contact to the epitaxial heterostructure was provided by a reversely biased type-II broken-gap p-$Ga_{0.84}In_{0.16}As_{0.22}Sb_{0.78}$/$n$-InAs heterojunction.

3. RESULTS AND DISCUSSION

When external bias was applied in such a way that the negative potential was at the n-GaInAsSb epitaxial layer, and the positive potential, at n-InAs, high-intensity spontaneous emission was observed in the spectral range 0.24–0.45 eV in a wide temperature interval, up to room temperature (Figs. 2 and 3). As is seen in Fig. 2, the EL spectra at T = 77 K exhibit two clearly pronounced emission bands with peak photon energies $h\nu_A = 0.280$ and $h\nu_A = 0.383$ eV. It is necessary to note that the spectral position of the observed bands nearly coincides with the position of EL bands for the p-GaInAsSb/p-InAs heterostructure, which suggests a common nature of recombination transitions that is determined by the influence of the type-II heterointerface.

Similarly to the spectra of the p–p structure, the EL spectra are dominated at low (I < 10 mA) injection levels by a low-energy band A ($h\nu_A = 0.250$ eV, FWHM 50 meV) (Fig. 2 a). With the driving current I rising, the peak of this emission band shifts to higher energies and reaches 0.345 eV, while the position of the high-energy band B with an FWHM of 18 meV is virtually current-independent (Fig. 2 b). A further rise in current does not induce a noticeable shift of the A peak, because it could be overlapped by the low-energy tail of a B peak having a higher intensity. A B band appears at even higher injection levels (I = 7 mA), its intensity grows steeply with increasing current through the structure, and at $I \gtrsim$ 30 mA it dominates in the EL spectra. Both bands have a similarly asymmetric peak shape: an abrupt high-energy edge and a tail exponentially decreasing into the range of lower photon energies.

If the dependence of the EL intensity is represented as

$$\Phi_m \propto I^n,$$

where Φ_m is the EL intensity and I is the current across the structure, then two portions can be distinguished in the dependence of the EL intensity on current for the A band

$$\Phi_m \propto I^2$$

for small currents I < 20 mA, which is transformed into a linear portion

$$\Phi_m \propto I$$

at I > 30 mA. In the entire current range under study, the emission intensity in the B band peak increases as $\Phi_m \propto$

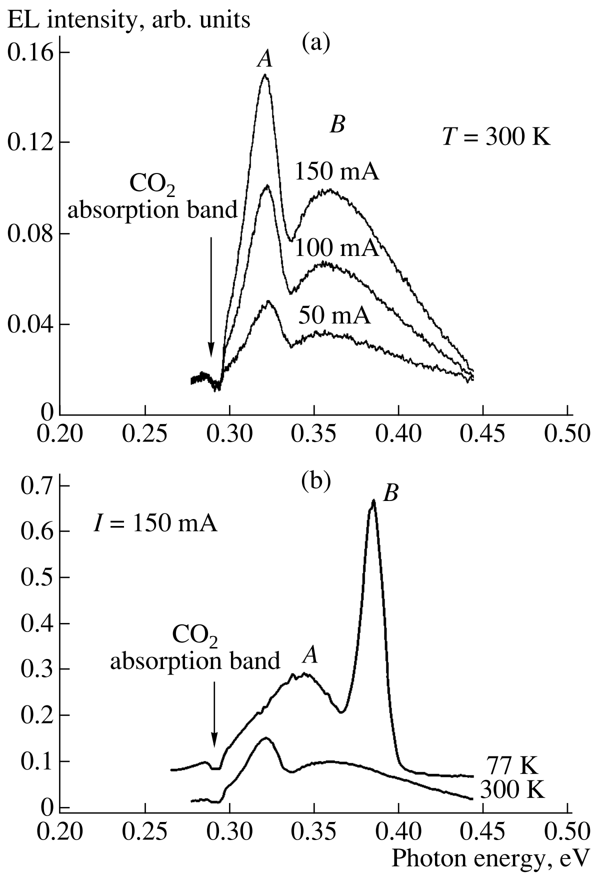

Fig. 3. EL spectra of the single type-II p-$Ga_{0.84}In_{0.16}As_{0.22}Sb_{0.78}$/$n$-$In_{0.83}Ga_{0.17}As_{0.80}Sb_{0.20}$ heterostructure under forward bias (a) at $T = 300$ K and different currents across the heterostructure and (b) at $T = 77$ and 300 K and a current of 150 mA. The arrow indicates the absorption band of atmospheric CO_2 ($\lambda \approx 4.25$ μm).

I^{η}, with the parameter $\eta > 1$. This complicated dependence of intensity on current can be accounted for by the simultaneous contribution of several mechanisms of current transport across the structure near the heterointerface. The EL spectra of the *p*–*n* structure does not contain a high-energy band of the type $h\nu_C = 0.633$ eV, which was observed earlier in the *p*–*p* structure and was attributed to Auger recombination in the bulk of the wide-gap GaInAsSb solid solution. This fact confirms our assumption that the electron containment in the active region of the heterostructures under study has been improved.

The blue shift of the *A* band with rising current and its larger half-width can be attributed to the filling of the potential well for holes on the side of the wide-gap GaInAsSb layer. A high injection level and, consequently, a higher bias across the structure, create the conditions for the formation of quantum levels of hole localization, which is manifested in the experiment by the stabilization of the position of the *A* band ($h\nu_A$ = 0.345 eV). In its turn, the position of the *B* band remains unchanged with current rising, which is accounted for by the contribution to recombination from transitions via surface levels at the heterointerface.

The most impressive fact is that high-intensity EL was observed at room temperature (Fig. 3). In this case, the EL spectra also contain two emission bands but, in contrast with the low-temperature case ($T = 77$ K), a redistribution of intensity between *A* and *B* peaks is obvious. At $T = 300$ K, an *A* band with a peak photon energy $h\nu_A = 0.320$ eV and an FWHM of 26 meV dominates in the spectrum, whereas a *B* peak is seen as a weaker and broader band with $h\nu_B = 0.355$ eV and an FWHM of 68 meV. The observation of EL at $T = 300$ K in the *A* band demonstrates the possibility of fabricating high-efficiency emitting devices operating near room temperature and which are based on type-II broken-gap heterostructures. At higher temperatures ($T > 200$ K), the p-$Ga_{0.84}In_{0.16}As_{0.22}Sb_{0.78}$/$n$-$In_{0.83}Ga_{0.17}As_{0.80}Sb_{0.20}$ heterojunction becomes of the broken-gap type and, from the very beginning, we have a semimetallic channel at the interface; this channel is filled with carriers. Applying a small external bias gives rise to high-intensity interfacial EL ($h\nu_A = 0.320$ eV), which dominates over the bulk luminescence manifested by the *B* band ($h\nu_B = 0.355$ eV).

The novel laser structure contains a type-II p-$Ga_{0.84}In_{0.16}As_{0.22}Sb_{0.78}$/$n$-$In_{0.83}Ga_{0.17}As_{0.80}Sb_{0.20}$ heterojunction; as an active layer its band diagram is shown in Fig. 1. Figure 4 shows a five-layer structure with separate quantum confinement, which was grown by LPE on (100)*p*-InAs substrate. Quaternary $InAs_{1-y-x}Sb_yP_x$ ($x = 0.30$) solid solutions were used as capping layers. Mesa-stripe laser diodes with a stripe width $d = 60$ μm and a cavity length $L = 400$ μm (Fig. 4c) were produced by standard photolithography. The laser chips were mounted on a copper heat sink. The output emission was measured at the front working face.

Spontaneous and coherent emission was observed in this structure. Single-mode lasing was obtained at a wavelength $\lambda = 3.14$ μm under a threshold current density $j_{th} = 400$ A cm^{-2} at $T = 77$ K (Fig. 5a). Stimulated emission arose at the high-energy wing of the spontaneous emission spectrum. For comparison, the same figure shows the EL spectrum of a round mesa-structure based on a single p-$Ga_{0.84}In_{0.16}As_{0.22}Sb_{0.78}$/$n$-$In_{0.83}Ga_{0.17}As_{0.80}Sb_{0.20}$ heterojunction grown directly on *n*-InAs substrate. It may be concluded that the lasing relies upon recombination transitions at the heterointerface.

The principal mechanism of radiative recombination in this heterojunction is tunneling radiative recombination via the quantum states at the type-II heterointerface. This is why we anticipated the suppression of the Auger recombination and the achievement of a weaker temperature dependence for the threshold current as compared with the results of [13], in which an

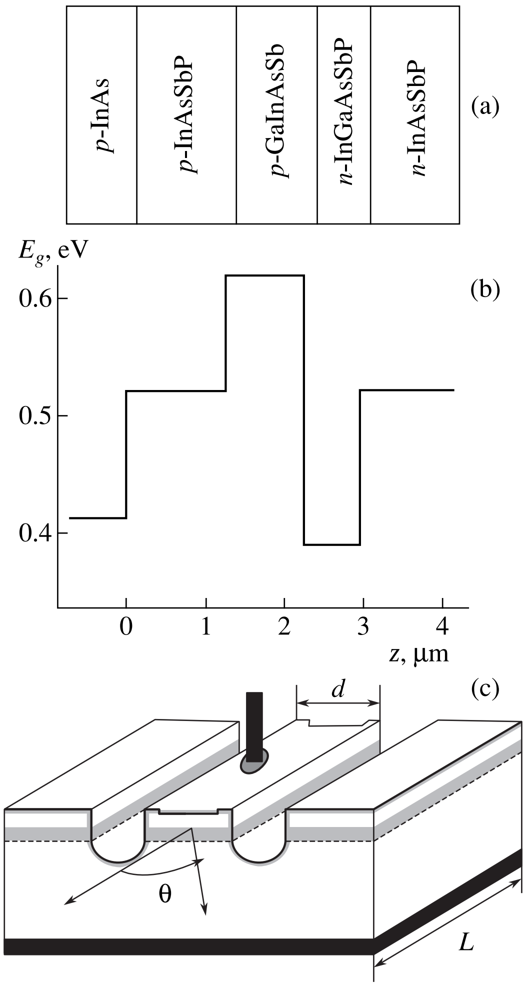

Fig. 4. (a) Composition of layers, (b) the layer-by-layer profile of the band gap in the novel laser structure with the type-II p-$Ga_{0.84}In_{0.16}As_{0.22}Sb_{0.78}$/$n$-$In_{0.83}Ga_{0.17}As_{0.80}Sb_{0.20}$ heterojunction in the active layer, and (c) the working front face of a laser chip.

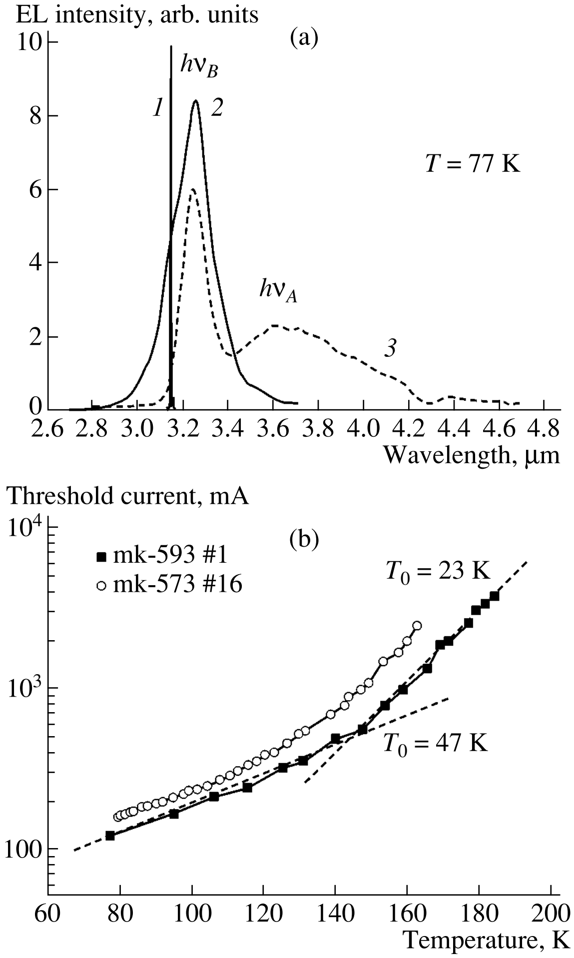

Fig. 5. (a) Spectra of (*1*) lasing emission and spontaneous emission from (*2*) stripe laser and (*3*) round mesa; (b) temperature dependences of the threshold current for novel laser structures with a type-II *p*–*n* heterojunction in the active region.

isotype type-II broken-gap *p*–*p* heterojunction was used as the active region, where the threshold current was rather high owing to a large leakage of carriers (both electrons and holes) across the heterointerface. Indeed, the threshold current observed in the new structures was a factor of 5 lower than in the laser structure with a type-II broken-gap *p*–*p* heterojunction in the active region studied earlier. As can be seen in Fig 5b, in the new laser, we succeeded in extending the region of a weak temperature dependence of the threshold current in the pulsed mode (τ = 200–500 ns) to T = 140–150 K, in contrast to T = 110 K in the laser with the *p*–*p* junction. We also obtained a higher characteristic temperature, T_0 = 47 K at T = 77–140 K and T_0 = 23 K in the range of 150–200 K. The limiting working temperature of the laser was raised to T = 195 K. As the working temperature rose above 150 K, the threshold current increased considerably (T_0 = 23 K), which can be accounted for by the contribution of the Auger process involving both the transition of hot holes to the spin–orbit-split band (CHHS) and the absorption of radiation by free carriers within the valence band. Recent advancements in the design of new hybrid (III–V)/(II–VI) laser structures have shown possible ways to achieve quantum confinement of hole gas and contain holes in the active region of a laser [16].

The study of polarization of light in the spontaneous and coherent modes has shown the dominance of TM- over TE-polarization for the luminescence related to the type-II heterojunction in the structures under study (Fig. 6). This fact is indicative of the tunneling origin of the optical radiative transitions across the type-II heterointerface. As is seen in Fig. 6a, maximum emission intensity is obtained when the polarizer vector is normal to the heterojunction plane (TM-polarization mode). When the polarizer is rotated by 90°, the laser

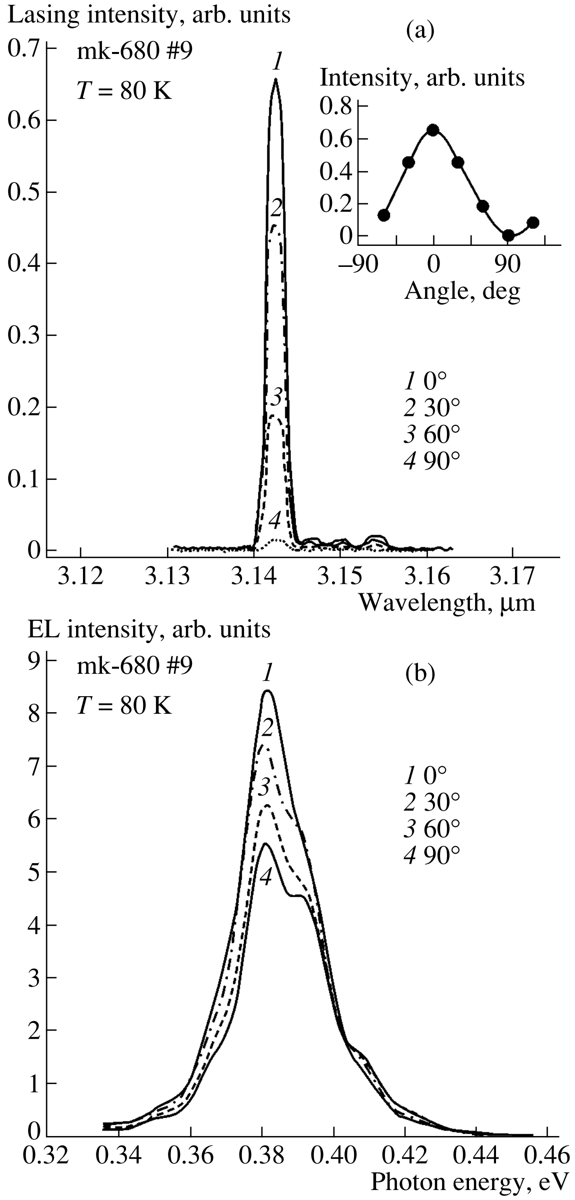

Fig. 6. The degree of polarization of (a) coherent emission and (b) spontaneous EL recorded from the front face of the stripe of the novel laser structure with a type-II *p*–*n* heterojunction in the active region.

emission nearly vanishes, whereas the intensity of the *B* band in the spectrum of spontaneous EL obtained near the lasing threshold at T = 80 K decreases by a factor of 2 (Fig. 6b). Moreover, an additional band $h\nu_C$ = 0.410 eV appears, the polarization dependence of intensity of which is opposite to that for the *A* and *B* emission bands observed earlier. It seems most likely that this band is related to radiative transitions in the bulk of the narrow-gap *n*-InGaAsSb solid solution. Previously, the TM-polarization of emission from a GaSb/GaInAsSb staggered type-II heterojunction was attributed [17] to the subbarrier tunneling of light holes from the *p*-GaSb valence band across the heterojunction, with their subsequent recombination with electrons in the *n*-GaInAsSb layer.

Thus, in the proposed novel laser structure we have achieved good electron confinement and containment of electrons in the active region. However, there remains the essential problem of hole leakage across a weak potential barrier associated with the valence band offset at the type-II p-$\mathrm{Ga_{0.84}In_{0.16}As_{0.22}Sb_{0.78}}$/$n$-$\mathrm{In_{0.83}Ga_{0.17}As_{0.80}Sb_{0.20}}$ heterointerface. In our opinion, the *A* band originates from the tunneling of electrons and holes from the localization levels in self-consistent QWs across the heterointerface due to strong overlap of the wave functions, whereas the *B* band is related to radiative transitions in the narrow-gap *n*-InGaAsSb solid solution involving electrons from the QW and holes tunneling via the bound states at the heterointerface.

4. CONCLUSION

We have studied the EL characteristics of a single type-II p-$\mathrm{Ga_{0.84}In_{0.16}As_{0.22}Sb_{0.78}}$/$n$-$\mathrm{In_{0.83}Ga_{0.17}As_{0.80}Sb_{0.20}}$ heterostructure in the temperature range of 77–300 K and demonstrated the prospects for designing IR laser structures based on type-II broken-gap heterostructures which operate on tunneling radiative recombination transitions across the heterointerface. A novel improved laser structure was suggested and fabricated on the basis of a type-II broken-gap *p*-GaInAsSb/*n*-InGaAsSb heterojunction in the active region. Single-mode lasing was observed at a wavelength $\lambda = 3.14$ μm under a threshold current density $j_{\mathrm{th}} = 400$ A cm^{-2} (T = 77 K). A high characteristic temperature T_0 = 47 K was obtained, and a limiting working temperature T = 195 K of the laser in the pulsed mode was achieved. The predominance of TM- over TE-polarization of the emission in both the spontaneous and coherent operation modes was observed. This fact can be attributed to recombination with light holes tunneling across the heterointerface.

To improve the characteristics and raise the working temperature of InAs-based lasers to room temperature, further optimization of the laser structure design is necessary, and this would need to include the study of fundamental mechanisms of nonradiative losses (Auger processes, heat loss in the confining layers of the structure, and intraband absorption and the related heating of carriers).

ACKNOWLEDGMENTS

This study was supported in part by the Ministry of Industry, Science, and Technology of the Russian Federation Program “Physics of Solid-State Nanostructures” and the Russian Foundation for Basic Research (project no. 02-02-17633).

REFERENCES

1. A. I. Nadezhdinski and A. M. Prokhorov, Proc. SPIE **1724**, 2 (1992).
2. A. N. Imenkov, N. M. Kolchanova, P. Kubat, *et al.*, Fiz. Tekh. Poluprovodn. (St. Petersburg) **35**, 375 (2001) [Semiconductors **35**, 360 (2001)].
3. D. Garbuzov, M. Maiorov, H. Lee, *et al.*, Appl. Phys. Lett. **74**, 2990 (1999).
4. J. Faist, F. Capasso, D. L. Sivco, *et al.*, Electron. Lett. **30**, 865 (1994).
5. D. W. Stokes, L. J. Olafsen, W. W. Bewley, *et al.*, J. Appl. Phys. **86**, 4729 (1999).
6. A. Wilk, M. E. Gazouli, M. E. Skouri, *et al.*, Appl. Phys. Lett. **77**, 2298 (2000).
7. M. P. Mikhaĭlova, A. A. Rogachev, and I. N. Yassievich, Fiz. Tekh. Poluprovodn. (Leningrad) **10**, 1460 (1976) [Sov. Phys. Semicond. **10**, 866 (1976)].
8. A. A. Allerman *et al.*, Electron. Lett. **34**, 369 (1998).
9. Yu. P. Yakovlev, T. N. Danilova, A. N. Imenkov, *et al.*, Proc. SPIE **3001**, 237 (1997).
10. M. P. Mikhaĭlova, I. A. Andreev, T. I. Voronina, *et al.*, Fiz. Tekh. Poluprovodn. (St. Petersburg) **29**, 678 (1995) [Semiconductors **29**, 353 (1995)].
11. M. P. Mikhaĭlova, G. G. Zegrya, K. D. Moiseev, *et al.*, Fiz. Tekh. Poluprovodn. (St. Petersburg) **29**, 687 (1995) [Semiconductors **29**, 357 (1995)].
12. K. D. Moiseev, A. A. Toropov, Ya. V. Terent’ev, *et al.*, Fiz. Tekh. Poluprovodn. (St. Petersburg) **34**, 1432 (2000) [Semiconductors **34**, 1376 (2000)].
13. K. D. Moiseev, M. P. Mikhaĭlova, O. G. Ershov, and Yu. P. Yakovlev, Pis’ma Zh. Tekh. Fiz. **21** (12), 83 (1995) [Tech. Phys. Lett. **21**, 482 (1995)].
14. G. G. Zegrya and A. D. Andreev, Appl. Phys. Lett. **67**, 2681 (1995).
15. K. D. Moiseev, A. A. Sitnikova, N. N. Faleev, and Yu. P. Yakovlev, Fiz. Tekh. Poluprovodn. (St. Petersburg) **34**, 1438 (2000) [Semiconductors **34**, 1381 (2000)].
16. Yu. P. Yakovlev, S. V. Ivanov, A. M. Monakhov, *et al.*, Proc. SPIE **4651**, 203 (2002).
17. N. S. Averkiev, A. N. Baranov, A. N. Imenkov, *et al.*, Pis’ma Zh. Tekh. Fiz. **13**, 332 (1987) [Sov. Tech. Phys. Lett. **13**, 135 (1987)].

Translated by D. Mashovets

Semiconductors, Vol. 37, No. 8, 2003, pp. 992–997. Translated from Fizika i Tekhnika Poluprovodnikov, Vol. 37, No. 8, 2003, pp. 1017–1022.
Original Russian Text Copyright © 2003 by Domashevskaya, Terekhov, Kashkarov, Turishchev, Molodtsov, Vyalykh, Vinokurov, Ulin, Shishkov, Arsent'ev, Tarasov, Alferov.

LOW-DIMENSIONAL SYSTEMS

Synchrotron Investigations of an Electron Energy Spectrum in III–V-Based Nanostructures

É. P. Domashevskaya*, [1], V. A. Terekhov*, V. M. Kashkarov*, S. Yu. Turishchev*,
S. L. Molodtsov, D. V. Vyalykh***, D. A. Vinokurov****, V. P. Ulin****, M. V. Shishkov****,**
I. N. Arsent'ev**, I. S. Tarasov****, and Zh. I. Alferov******

**Voronezh State University, Universitetskaya pl. 1, Voronezh, 394893 Russia*
[1]e-mail: root@ftt.vsu.ru
***Institut für Oberfläshen- und Mikrostrukturphysik, TU Dresden, Germany*
****Institut für Experimentalphysik, Freie Universität Berlin, Berlin, Germany*
*****Ioffe Physicotechnical Institute, Russian Academy of Sciences,*
Politekhnicheskaya ul. 26, St. Petersburg, 194021 Russia

Submitted February 11, 2003; accepted for publication February 17, 2003

Abstract—Using synchrotron radiation, the spectra of an X-ray absorption near-edge structure in a region of $P\text{-}L_{2,3}$ edges of a band spectrum are obtained for the first time. The spectra give insight into the local density of states in the conduction band for MOCVD-grown nanostructures with InP quantum dots on GaAs(100) substrates and for porous InP layers obtained by anodic pulse electrochemical etching of single-crystal InP(100) wafers. For all of the nanostructures, quantum-confinement effects are observed, which manifest themselves in the emergence of an additional level 3.3 eV above the conduction band bottom, as well as in variation in the band gap of the materials under investigation upon the dimensional quantization of the electron spectrum. A band-to-band origin of the luminescence spectra for the nanostructures investigated is assumed. *© 2003 MAIK "Nauka/Interperiodica".*

1. INTRODUCTION

In recent years, researchers have paid serious attention quantum-well III–V structures owing to their unusual properties. The formation of self-organized low-dimensional semiconductor layers on III–V single crystals has turned out to be especially promising due to the possibility of achieving the dimensional quantization of electronic states in homogeneous and stable (dislocation-free) clusters. Self-organized MBE- and MOCVD-grown heterostructures, in contrast to nanodimensional structures formed using photolitography, are characterized by a high density of electronic states (caused by the dimensional quantization), an atomlike structure of the electron energy spectrum, and high emission efficiency due to a low defect density [1].

In addition, porous quantum-confinement III–V materials can be used as matrices for obtaining nanodimensional structures of the quantum-wire type.

To date, however, there is very little known about local partial density of states in the conduction bands of these materials. We, at any rate don't know of any available data on the X-ray absorption in the near-edge region of the $L_{2,3}$ bands even for III–V single crystals. The purpose of this study is to show that synchrotron investigations are promising for the examination of the local density of states in III–V nanostructures. Of prime importance is to investigate the energy structure of the conduction band for the III–V porous materials and nanostructures with InP quantum dots (QDs) buried in the InGaP matrix and grown on GaAs substrates.

It is known that the spectrum of the electron quantum yield corresponds to the spectrum of the X-ray absorption near-edge structure (XANES) [2] and reflects the distribution of the local partial density of states (LP DoS). This density corresponds to unoccupied states in the conduction band with the accuracy to a probability factor equal to the squared matrix element of the electron transition from the core level to free states in the conduction band [3]:

$$\mu(E) \propto \nu^3 \sum_f |M_{fi}|^2 \delta(E_f - E_i - h\nu), \qquad (1)$$

where

$$M_{fi} = \int \varphi_f^* H' \varphi_i dr$$

is the matrix element of probability of the electron transition from the core level with the wave function φ_i and the eigenvalue E_i to the states in the conduction band with the wave function φ_f, H'] is the perturbation operator, and $h\nu$ is the energy of the absorbed quantum of synchrotron radiation (SR).

We correlated the obtained XANES spectra with ultrasoft X-ray emission spectra (USXES). The USXES spectra allow one to determine the LP DoS of occupied states in the valence band of the material under investigation:

$$I(E) \propto \nu^3 \sum_j |M_{ij}|^2 \delta(E_i - E_j - h\nu), \qquad (2)$$

where

$$M_{ij} = \int \varphi_i^* H' \varphi_j dr$$

is the matrix element of probability of the electron transition from the valence band with the wave function φ_j and the eigenvalue E_j to the vacancy of the inner level with the wave function φ_i.

The correlation between the XANES and USXES spectra in the unified energy scale relative to the core 2*p* level for the $L_{2,3}$ spectra permits one to estimate the band gap from the distribution of partial ($s + d$) states.

2. EXPERIMENTAL

The XANES investigations were carried out using a Russia–Germany channel of a BESSY II synchrotron. An X-ray optical scheme of XANES measurements includes four Au-coated mirrors and four Au-coated gratings with 600 grooves per mm. The energy resolution is 0.03 eV. The thickness of an informative layer of the samples under investigation, which is limited by the depth of electron escape, was no larger than ~20 nm.

The USXES were obtained using a PSM-500 laboratory X-ray spectrometer–monochromator with a spherical mirror and a spherical grating with 600 groves per mm with the excitation by an electron beam. The energy resolution of the spectrometer is 0.3 eV in the region of the $P\text{-}L_{2,3}$ spectrum. The analysis depth for the electron beam (1–2 keV) was ~10–20 nm. The residual pressure in an X-ray tube during measurements of the X-ray emission spectrum was ~2 × 10^{-6} Torr.

The samples with InP QDs were grown by the MOCVD technique using an Epiquip VP 50-RP installation under a pressure of 100 mbar and with microwave heating of the substrate. Self-organized nanodimensional InP clusters were grown in an $In_{0.5}Ga_{0.5}P$ matrix on GaAs(100) substrate [4]. A schematic drawing of a similar structure is given in the inset to Fig. 1. The nanostructures thus obtained contained nanocrystalline InP layers with effective thicknesses varying from three to ten monolayers (ML), which were buried under a wide-gap $In_{0.5}Ga_{0.5}P$ layer 20 nm thick.

The surface profile of the QD-containing nanostructures was investigated using a Philips EM-420 high-resolution electron microscope with an accelerating voltage of 120 kV.

The porous InP samples were prepared under pulse anodic electrochemical etching of the *n*-InP(100) single-crystal substrate in HF-, HCl-, or HBr-containing electrolytes.

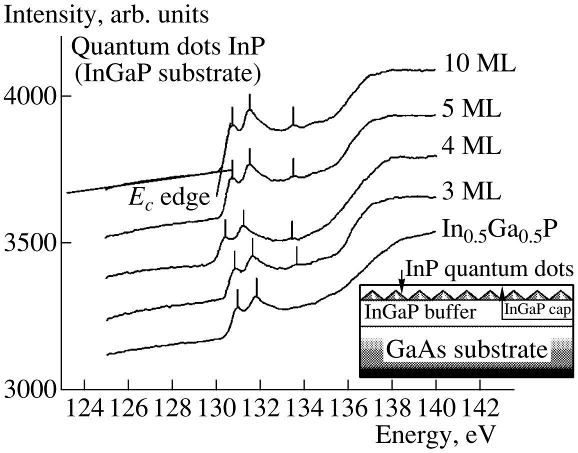

Fig. 1. $P\text{-}L_{2,3}$ XANES spectra for the nanostructures with InP quantum dots with various number of monolayers and the spectrum for the $In_{0.5}Ga_{0.5}P$ solid solution (E_c is the conduction-band bottom). The schematic representation of the structure with InP quantum dots in the $In_{0.5}Ga_{0.5}P$ matrix on the GaAs(100) substrate is in the inset.

3. RESULTS AND DISCUSSION

3.1. III–V Nanostructures with InP Quantum Dots

The $P\text{-}L_{2,3}$ XANES spectra in the *p* region for the III–V structures with InP QDs grown on GaAs(100) single-crystal wafers and for the $In_{0.5}Ga_{0.5}P$ solid solution are shown in Fig. 1. The XANES spectra reflect the partial density of electron states in the conduction band. In this case, these will be the ($s + d$) states of P in accordance with dipole transitions from the $2p_{1/2,3/2}$ to the ($s + d$) states of the conduction band (E_c is the conduction-band bottom).

The USXES $P\text{-}L_{2,3}$ of the $In_{0.5}Ga_{0.5}P$ solid solution reflects the local partial density of occupied states in the valence band of the material under investigation (E_v is the valence band top).

As was mentioned above, to date there is no data on the edges of X-ray absorption for the $L_{2,3}$ region even for the III–V single crystals. However, using SR, we were able to record the $P\text{-}L_{2,3}$ XANES spectra for the nanostructures with InP QDs, as well as the spectrum of the $In_{0.5}Ga_{0.5}P$ solid solution. We were also able to show that these spectra feature a clearly pronounced fine structure with two main peaks at ~131 and ~132 eV (Table 1).

All of the spectra that are shown in Fig. 1 are very similar both in the energy position of their main features (Table 1) and in the intensity ratio of their two main peaks. A main distinction between the XANES spectra of QD-containing nanostructures and the $In_{0.5}Ga_{0.5}P$ solid solution is the presence of a weakly pronounced additional peak at 133.5 eV (in the case of QDs). Despite the presence of a $In_{0.5}Ga_{0.5}P$ protective coating, which covers the InP QDs, the intensity of this

Table 1. Energy positions of the main features of the XANES and USXES spectra for the nanostructures with InP quantum dots

Sample, number of monolayers (ML)	Position of band edges, eV		Energies of spectral features, eV		
	USXES, E_V	XANES, E_c			
Quantum dots InP, 3 ML	–	130.3	130.9	131.6	133.6
Quantum dots InP, 4 ML	–	129.9	130.4	131.2	133.5
Quantum dots InP, 5 ML	–	130.2	130.8	131.5	133.5
Quantum dots InP, 10 ML	–	130.2	130.8	131.5	133.5
Solid solution $In_{0.5}Ga_{0.5}P$	128.5	130.4	130.9	131.8	–

additional peak increases as the number of InP monolayers increases from three to ten. It seems likely that the presence of the additional peak at 133.5 eV is associated with stresses induced at the interface between the InP QDs and the matrix and which propagate throughout the entire $In_{0.5}Ga_{0.5}P$ protective layer.

Figure 3 shows the transmission electron microscopy (TEM) image of the QDs for the nanostructures with three InP MLs coated with the 40-nm-thick $In_{0.5}Ga_{0.5}P$ protective layer. The average QD size is about 80 nm with an average QD density of 3×10^9 cm^{-2}. The TEM data (Fig. 3) show the emergence of dark zones whose diameter is close to the effective QD section of ~80 nm.

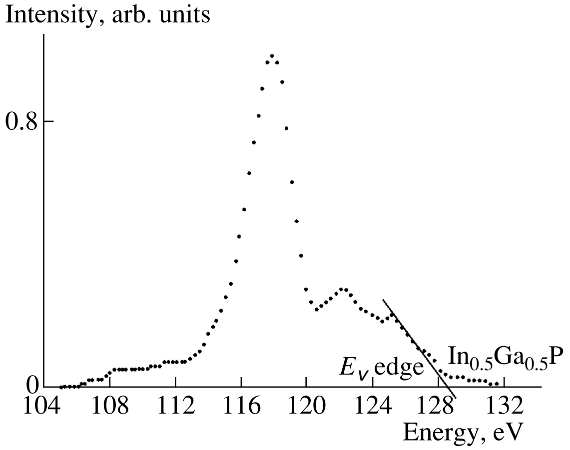

Fig. 2. P-$L_{2,3}$ USXES for the $In_{0.5}Ga_{0.5}P$ solid solution (E_V is the valence-band top).

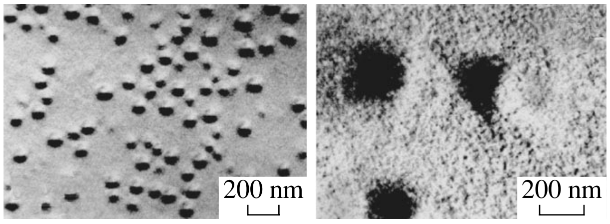

Fig. 3. TEM images of the InP quantum dots with an effective thickness of three monolayers at different magnifications.

The correlation between the band gap of ~1.9 eV for the $In_{0.5}Ga_{0.5}P$ solid solution and the PL peak energy (Fig. 4 in [4]) shows good agreement between the methods used. The band gap of the solid solution is defined as the difference between the energy position of the valence-band top E_V and the conduction-band bottom E_c (Table 1). For the nanostructures with InP QDs, an average decrease in the energy position of the conduction-band bottom by 0.2 eV is observed (Table 1), which should lead to a decrease in the band gap for the nanostructures under consideration. Thus, we may conclude that, both for the solid solution and for the QD-containing nanostructures, the PL peak has a band-to-band origin.

3.2. Porous III–V Phosphides

The AFM images of the surface profile of the porous InP (*por*-InP) under investigation are shown in Fig. 5 (AFM is the atomic-force microscopy).

The P-$L_{2,3}$ XANES spectra of *por*-Si, grown on single-crystal InP(100) wafers using anodic pulse electrochemical etching in HF-, HCl-, or HBr-containing electrolytes, are shown in Fig. 6.

The USXES spectra of HCl-etched *por*-Si are shown in Fig. 7, along with the spectrum of single-crystal InP (*c*-InP). The energy positions of the main features, as well as of the edges of the conduction bands E_c (XANES), and of the valence bands E_V (USXES) for the samples investigated are listed in Table 2.

Comparison of all of the data obtained (Figs. 1 and 6, Tables 1 and 2) shows that the fine structure of the XANES spectra observed for *por*-InP virtually coincides with the XANES spectra of the InP QD-containing nanostructures in the position of their energy peaks. However, the peaks of XANES spectra for *por*-Si, obtained by etching in HCl, have a pronounced quasi-molecular character (Fig. 6). We attribute this fact to the formation of clusters or quasi-molecules of InP, which cover the surface of pores. The fine structure of this

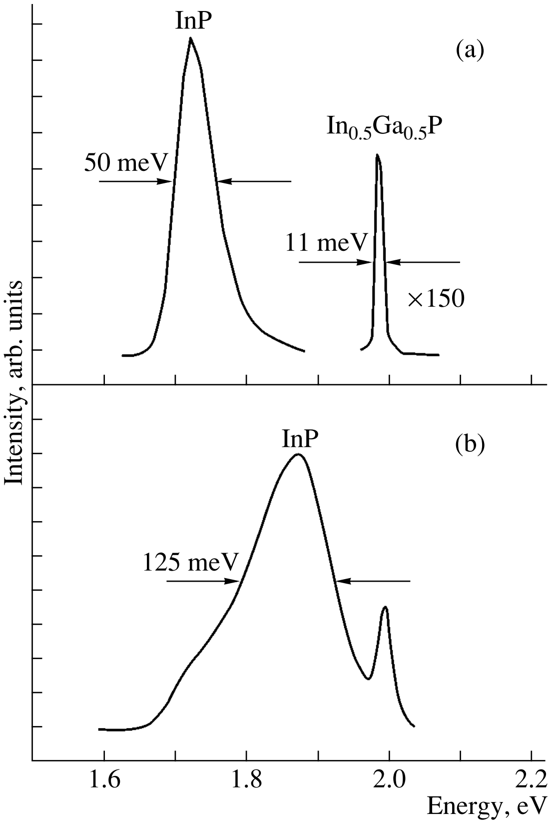

Fig. 4. Photoluminescence spectra (T = 77 K) for the nanostructures with InP quantum dots (three monolayers). The pump power is (a) 100 W/cm^2 and (b) 5 kW/cm^2 [4].

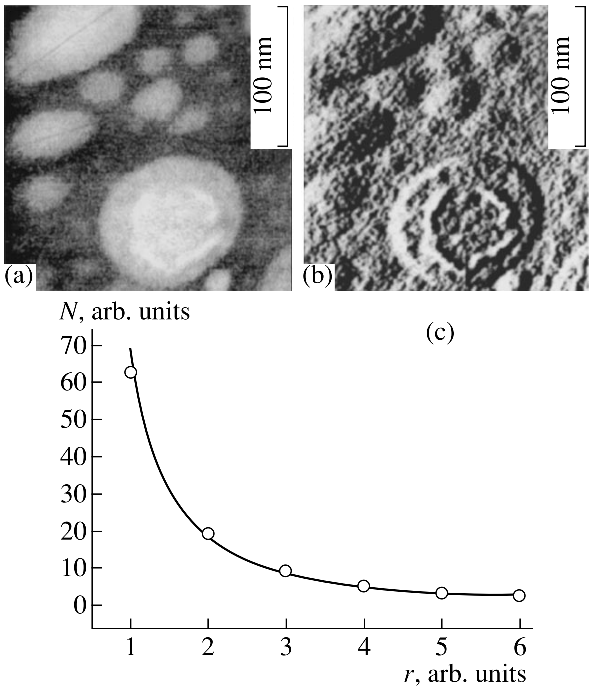

Fig. 5. AFM images of porous InP: (a) aged and (b) refreshed in the etchant, as well as (c) the pore size distribution law.

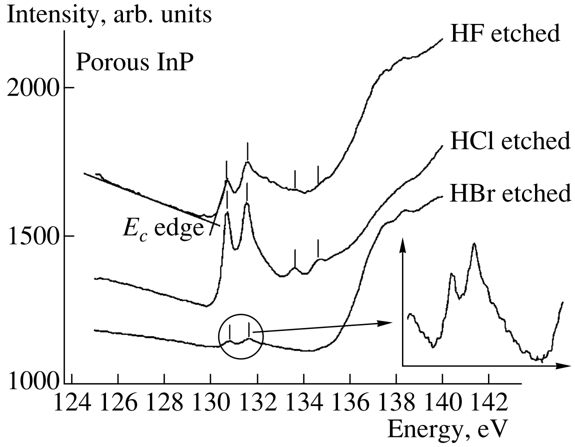

Fig. 6. P-$L_{2,3}$ XANES spectra of porous InP obtained by substrate etching in various electrolytes (E_c is the conduction-band bottom).

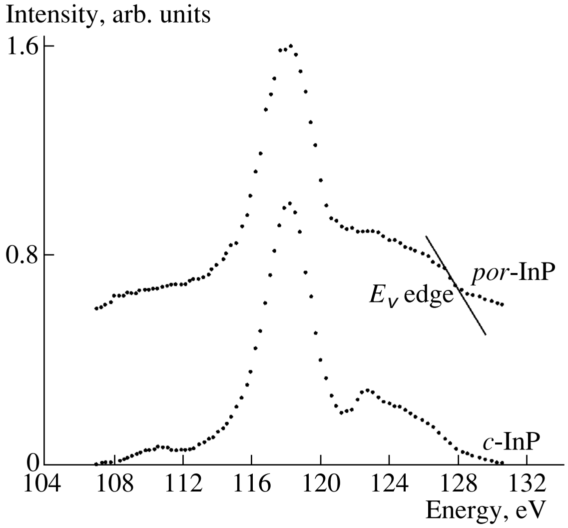

Fig. 7. P-$L_{2,3}$ USXES of porous InP obtained by substrate etching in HCl solution and of single-crystal InP (E_v is the valence-band top).

sample is most pronounced in comparison with the samples obtained by etching in the HF- and HBr-containing solutions. These distinctions may be attributed to the smaller dimensions of the InP clusters which emerge in the products of interaction with chloride solutions. This conclusion correlates with the data of

Table 2. Energy positions of main features of the XANES and USXES spectra for porous InP

Sample (electrolyte)	Position of band edges, eV		Energies of spectral features, eV			
	XANES, E_c	USXES, E_v				
Porous InP (HCl)	128.5	130.3	130.7	131.5	133.5	134.6
Porous InP (HF)	–	130.1	130.7	131.6	133.7	134.9
Porous InP (HBr)	–	130.2	130.8	131.6	–	–

comparative chemical analysis of porous layers obtained in fluoride-, chloride-, and bromide-containing electrolytes [5]. Furthermore, it is known that chlorine ions are most reactive with crystalline InP [6].

Our previous XANES investigations of *por*-InP [7] show (Fig. 7) that the main peak of the P-$L_{2,3}$ spectrum, which reflects the density of the $P3s$ states, is ~25% broader for *por*-InP than for crystalline InP. This observation points to considerable disordering of In–P bonds in the surface layer of *por*-InP or to the formation of dangling bonds at the surface of quasi-molecules. This is precisely the circumstance in connection with which considerably greater suppression of the fine structure in the upper part of the valence band of *por*-InP occurs compared with *c*-InP, in which sp^3 hybridization of the III–V compounds manifests itself.

Furthermore, the density of localized states above the valence-band top E_v is considerably higher for *por*-InP than for *c*-InP (Fig. 7), which also characterizes the partial disordering of the In–P bonds in the surface layer of *por*-Si. However, in this case, the USXES and XANES data indicate that phosphorus in the surface quasi-molecules remains bonded mainly with In and virtually unbound to oxygen [8].

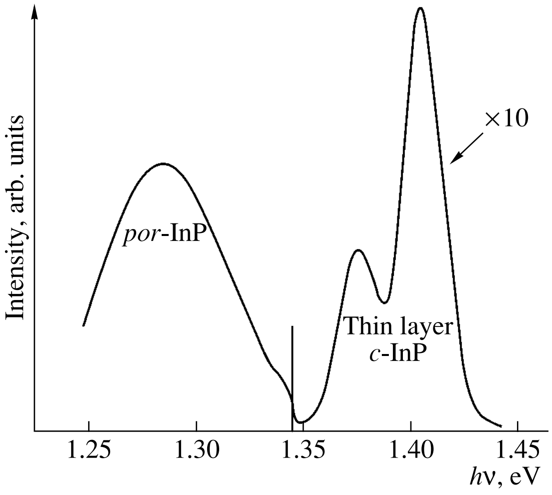

Fig. 8. Photoluminescence spectrum (T = 77 K) of a thin single-crystal InP film grown on porous InP.

In the PL spectrum in Fig. 8, a high-energy peak at $h\nu$ = 1.4 eV is attributed to the *c*-InP film covering the *por*-InP layer, whereas the left-hand peak at $h\nu$ = 1.27 eV is related directly to the porous layer. A considerable decrease in the energy of the left-hand peak when it has a band-to-band origin may be attributed to the existence of a high density of localized states in the band gap, above the E_v top (Fig. 7, upper curve), which narrows the band gap of *por*-InP.

4. CONCLUSION

For the first time, the spectra of an X-ray absorption near-edge structure (XANES) close to the P-$L_{2,3}$ edge for nanostructures with InP quantum dots (QDs), an $In_{0.5}Ga_{0.5}P$ solid solution, and porous InP were obtained using the BESSY II synchrotron. The XANES data on the local density of states in the conduction band combined with the data of ultrasoft X-ray emission spectra (USXES) on the local density of states in the valence band are in good agreement with the photoluminescence (PL) spectra. This points to the band-to-band origin of PL peaks.

The fine structure of X-ray absorption spectra for all samples investigated is characterized by two peaks 0.7–0.9 eV apart. This may be associated with the spin–orbit splitting of the P-$L_{2,3}$ level. An additional peak at 133.5 eV, which is found at a distance of ~3.3 eV from the conduction-band bottom E_c, is caused by quantum-confinement effects.

The XANES spectra of porous InP show the narrowest peaks of local density of states with a quasi-molecular character. This observation is associated with the formation of InP quasi-molecules in the surface layers of porous InP.

ACKNOWLEDGMENTS

We thank the Director, the Administration, and the Committee on the Distribution of the Operating Time of the Channels of the BESSY II Synchrotron, and the Coordinators of the Russia–Germany channel of the BESSY II synchrotron for supporting our study.

REFERENCES

1. N. N. Ledentsov, V. M. Ustinov, V. A. Shchukin, *et al.*, Fiz. Tekh. Poluprovodn. (St. Petersburg) **32**, 385 (1998) [Semiconductors **32**, 343 (1998)].
2. T. M. Zimkina and V. A. Fomichev, *Ultrasoft X-Ray Spectroscopy* (Leningr. Gos. Univ., Leningrad, 1971).
3. A. S. Vinogradov, E. O. Filatova, and T. M. Zimkina, Pis'ma Zh. Éksp. Teor. Fiz. **15** (1), 84 (1989) [JETP Lett. **15**, 35 (1989)].
4. D. A. Vinokurov, V. A. Kapitonov, O. V. Kovalenkov, *et al.*, Fiz. Tekh. Poluprovodn. (St. Petersburg) **33**, 858 (1999) [Semiconductors **33**, 788 (1999)].
5. P. Schmuki, L. Santinacci, T. Djenzian, and D. J. Lockwood, Phys. Status Solidi A **182**, 51 (2000).
6. A. Liu, Nanotechnology **12**, L1 (2001).
7. É. P. Domashevskaya, V. A. Terekhov, V. M. Kashkarov, *et al.*, in *Abstracts of 5th Russia Conference on the Physics of Semiconductors* (Nizhni Novgorod, 2001), Vol. 2, p. 383.
8. A. J. Nelson, T. van Buuren, C. Bostedt, *et al.*, http://alspubs.1b1.gov/AbstractsManager/uploads/99062.pdf.

Translated by N. Korovin